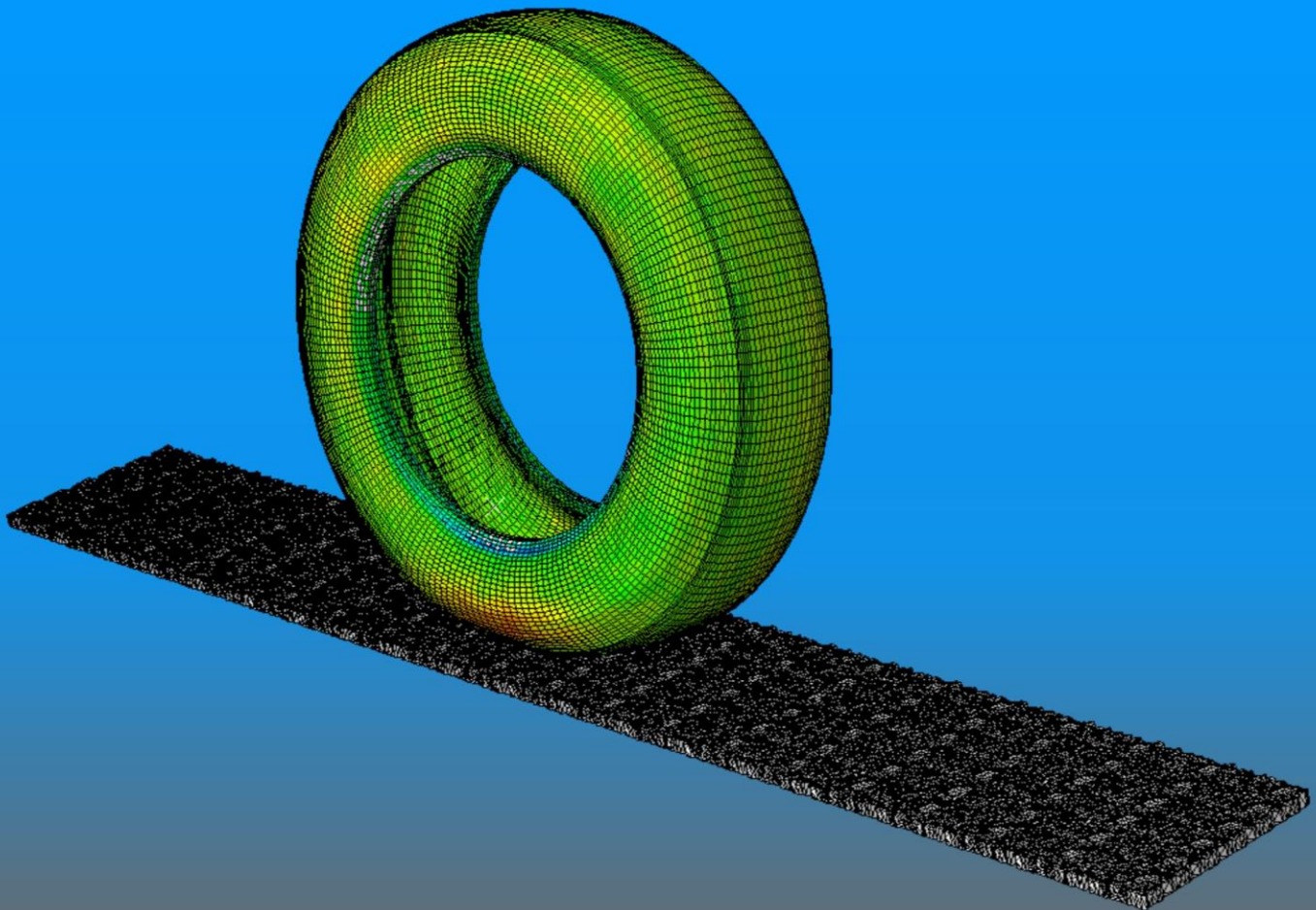


Numerical Simulation of Tire-Pavement Interaction



Numerical Simulation of Tire-Pavement Interaction

Santosh Kumar Srirangam

The research described in this thesis was performed in the section of Road and Railway Engineering, Faculty of Civil Engineering and Geosciences, Delft University of Technology, Stevinweg 1, 2628 CN, Delft, The Netherlands. This work was supported by the European Union Seventh Framework Program, Theme: Safety and Security by Design, in the context of the project: SKIDSAFE and by the Dutch Ministry of Infrastructure and Environment, Rijkswaterstraat, in the context of the project: Grip op Wegen.

Numerical Simulation of Tire-Pavement Interaction

Proefschrift

ter verkrijging van de graad van doctor
aan de Technische Universiteit Delft,
op gezag van de Rector Magnificus Prof.ir. K.C.A.M. Luyben,
voorzitter van het College voor Promoties,
in het openbaar te verdedigen op
14 September 2015 om 15:00 uur

Door

Santosh Kumar SRIRANGAM

Master of Engineering in Civil Engineering,
National University of Singapore.

geboren te Kakinada, Andhra Pradesh, Indië

This dissertation has been approved by the

promoter: Prof. dr. A. Scarpas

Composition of the doctoral committee:

Rector Magnificus	Delft University of Technology, Netherlands, chairperson
Prof. dr. A. Scarpas	Delft University of Technology, Netherlands, promoter

Independent members:

Prof. dr. ir. S.M.J.G. Erkens	Delft University of Technology, Netherlands
Prof. dr. I.L. Al-Qadi	University of Illinois at Urbana-Champaign, USA
Prof. dr. E. Masad	Texas A &M University at Qatar, Qatar
Prof. dr. A. Loizos	National Technical University of Athens, Greece
Prof. dr.-ing. habil. M. Oeser	RWTH Aachen University, Germany

Reserve member:

Prof dr. ir. R.P.B.J. Dollevoet	Delft University of Technology, Netherlands
---------------------------------	---

Published and distributed by:

Santosh Kumar Srirangam
Email: S.K.Srirangam@tudelft.nl

Copyright ©2015 by Santosh Kumar Srirangam

Printed by CPI Koninklijke Wöhrmann

ISBN 978-94-6203-873-8

All rights reserved. No part of the material protected by this copyright notice may be reproduced or utilized in any form or by any means, electronic or mechanical, including photocopying, recording or by any information storage and retrieval system, without written consent from the publisher.

To

My wife PURNA

&

my Children PINKY and KARTHIK

Acknowledgements

According to Vedas (Sacred Hindu Transcripts), the Guru is described as follows:

अज्ञानतिमिरान्धस्य ज्ञानाञ्जनशालाकया ।

चक्षुरुन्मीलितं येन तस्मै श्रीगुरवे नमः ॥

Ajnyaana Timira Andhasya Jnyaana Aajana Shaalaakayaa |

Chakssur Unmiilitam Yena Tasmai Shri Gurave Namah ||

it means

Salutations to the Guru who removes the darkness of ignorance from our (inner) eyes by applying the collyrium of the light of knowledge |

By whom our (inner) eyes are opened; salutations to that Guru ||

These are the words come to my mind to describe my mentor, Prof. Dr. Tom Scarpas, Chair of the Pavement Engineering, CITG, TU Delft. Ever since, I started working on my PhD topic, Prof. Scarpas has supported me not only by providing a research assistantship and top-notch research facilities, but also intellectually and emotionally through the rough road to finish this thesis. He always has time for his students. I bow to his relentless pursuit in making his students as specialists in their respective fields and projecting their work to the local and international venues. Also, I would like to thank Mrs. Maureen Scarpas for her motherly care and constant encouragement.

After my mentor, I would like to express my gratitude to two persons, Dr. Kumar Anupam and Ir. Cor Kasbergen. Both of them possess qualities of great human-beings. They always treated my problems as their problems whether they are professional or personal. Anupam is my best friend, my guide and my counselor. His expertise in tire-pavement interaction, his problem solving skills and his way of looking at the problem out of the box kept me motivated to deal with the problem which initially I thought impossible. Coming to Cor, the back-bone of our pavement engineering group, imparted me the knowledge of continuum and contact mechanics and mathematics which is important to come up with rational solutions to the problems that I dealt with. Without these two guys, perhaps, I would never be able to finish my PhD. Thank you guys.

One always needs a great working environment and great colleagues to make his/her working life pleasant and memorable. Dr. Xueyan Liu comes as the first of this list. I'm very much benefited from his knowledge of mechanics and materials. His critical questions made me to think better. He always treated me like his kid brother and never hesitated to extend any help whenever I needed. Thank you Dr. Xueyan. During the middle of my PhD journey, I'm fortunate to have acquaintance with Prof. Dr. Ir. Sandra Erkens who provided me with her invaluable guidance and support in completing this thesis. She's always been accessible and open to discussions. Thank you Prof. Sandra.

Next comes in my thank list, my lovely and fabulous friends and colleagues, Jinlong Li, George Tzimiris, Katerina Varveri, Stavros, Alieh Alipour, Sayeda Nahar and Zahid, Mirella Villani and

Alexander Schmets. Ladies and Gentlemen, you all have been a source of love and energy throughout my journey. Thank you very much. I would also like to thank Dr. Niki Kringos, Yani Sutjiadi and Marjon van der Perk who made my initial days in Delft comfortable with their invaluable suggestions professionally and personally and their friendly nature. I also would like to thank Jacqueline Barnhoorn and Anneke Meijer for their constant cooperation to deal with the administration issues. Thank you Ladies.

A special group of friends who are just like my family members and who made Delft a home away from my home. My sincere gratitude to Dr. Malleswara Rao and Kalyani, Prithivi, Deepthi and their cute daughter Kittu, Meenakshi Bhabi (Anupam's better half) and lovely Amya. I sincerely thank you all for your care, love and moral support that you provided me and my family throughout this journey. Thank you all.

I would like to thank fabulous persons of my previous company HSL constructor Pte Ltd., Mr. Lim Choo Leng, Mr. Charles Quek and Mrs. Grace Quek. Thank you very much for providing me your moral support and financial help whenever I'm in need. I specially thank Dr. Dharmendra Singh, who encouraged me to embark on this difficult task of pursuing PhD. Thank you Mr. Charles and Dharmendra for your unconditional help and constant encouragement throughout this journey.

I would like to express my gratitude to family. I thank my wife, Purna, who always stood by me in all hardships. She took upon all the burden and stress and only give me love and warmth in turn. Without her encouragement and support, it is next to impossible to finish this thesis. Then come along in my life, my two wonderful kids, Pinky and Karthik. I love you Children, I love you more than anything in my life.

Thanks is a small word for my angel mother who sacrificed everything for me. She never expected anything from me except my wellbeing. I would like to thank my sister, Sri Devi and my brother-in-law, Suresh, my brother, Swamy and my sister-in-law, Aruna who took care of my mother in my absence and always encouraged me in this journey. I also would like to thank my best friend Vasu and his wife, Lalitha for their constant encouragement, love and care throughout my journey.

Last but not least, I would like to thank my late maternal grandparents, who brought me up and educated me. I wouldn't be anything without them.

Santosh Kumar Srirangam
Delft (Netherlands), September 2015.

Contents

Acknowledgements	viii
Contents.....	i
1 Introduction.....	1
1.1 Background	1
1.2 Basic terminology	2
1.2.1 Tire.....	2
1.2.2 Pavement surface texture	7
1.3 Friction mechanisms	8
1.3.1 Adhesion	10
1.3.2 Hysteresis.....	11
1.3.3 Remarks	11
1.4 Computational contact mechanics models	12
1.5 Temperature generation in tires	14
1.5.1 Internal energy dissipation.....	14
1.5.2 Thermal State of a Tire	18
1.6 Parameters influencing tire-pavement friction.....	18
1.6.1 Tire factors	19
1.6.2 Pavement surface factors	23
1.6.3 Environmental factors	25
1.7 Research objectives.....	28
1.8 Thesis outline	28
2 Determination of Rheological Properties of Rubber Materials	31
2.1 Introduction.....	31
2.2 Concepts of viscoelasticity.....	31
2.2.1 Terminology.....	31
2.2.2 DSR test	33
2.2.3 Master curve construction.....	34
2.3 Laboratory DSR test results	34
2.4 Visco-elastic parameter determination procedure.....	38
2.5 Summary	46
3 FE Modelling of Pneumatic Tires and Pavement Surfaces.....	47
3.1 Introduction.....	47
3.2 Laboratory static load-deflection tests	47

3.2.1	PIARC test tire	48
3.2.2	Wheel load test facility	49
3.2.3	Load-deflection tests	49
3.3	FE modeling of a PIARC test tire	52
3.3.1	Step 1: two dimensional cross section generation	52
3.3.2	Step 2: three dimensional tire model generation.....	56
3.3.3	Step 3: 3D model calibration	57
3.3.4	Fourth step: footprint analysis	60
3.4	Development of FE asphalt pavement mesh.....	61
3.4.1	Asphalt mix compositions.....	62
3.4.2	FEM mesh generation	63
3.5	Summary	66
4	FE Modeling of Thermo-Mechanical Tire-Pavement Interaction	67
4.1	Introduction.....	67
4.2	FE modeling of tire-asphalt surface interaction	68
4.2.1	Deformation module	68
4.2.2	Dissipation module	75
4.2.3	Thermal module	78
4.3	Validation of temperature distribution.....	80
4.4	FE Model Tests	83
4.4.1	Temperature development in a test tire.....	83
4.4.2	Temperature rise and cool down in the tire body.....	84
4.4.3	Temperature development in different regions of a fully rolling tire	85
4.4.4	Relation between tire band temperature and combined pavement and ambient temperatures	86
4.4.5	Effect of friction coefficient on the temperature development	86
4.5	Summary	87
5	Tire-Pavement Interaction Under Different Operating Conditions	89
5.1	Introduction.....	89
5.2	FE Model parameters	89
5.3	Validation.....	91
5.4	Analysis of Straight-line Braking Tire.....	93
5.4.1	Effect of tire band temperature on the hysteretic friction	93
5.4.2	Effect of Pavement Temperature on the Hysteretic Friction	97
5.4.3	Effect of Ambient Temperature on the Hysteretic Friction	101

5.4.4	Effect of Contained Air Temperature on the Hysteretic Friction	105
5.4.5	Effect of Pavement Surface Texture on the Hysteretic Friction	106
5.4.6	Effect of Tire Slip Conditions on the Hysteretic Friction	108
5.4.7	Relative Effects of PT, AT, CAT, Pavement Texture and Slip Ratios ..	108
5.5	Analysis of Cornering Tire	109
5.5.1	Applied Load on Tire vs. Cornering Friction Coefficient.....	109
5.5.2	Inflation Pressure vs. Cornering Friction Coefficient	112
5.5.3	Speed vs. Cornering Friction Coefficient	114
5.5.4	Side-slip Angle vs. Cornering Friction Coefficient	115
5.5.5	Pavement Surface Texture vs. Cornering Friction Coefficient	115
5.6	Summary	116
6	Hydroplaning	117
6.1	Introduction.....	117
6.2	Three Zone Concept.....	117
6.2	Manifestations of Hydroplaning	118
6.2.3	Detachment of tire footprint.....	118
6.2.4	Hydrodynamic ground pressure	119
6.2.5	Spin-down of unbraked wheel	119
6.2.6	Suppression of tire bow wave	119
6.2.7	Scouring action of escaping fluid in tire-ground footprint region	119
6.2.8	Peaking of fluid displacement drag.....	119
6.2.9	Loss in braking traction	120
6.2.10	Loss in directional stability and control.....	120
6.3	Factors Influencing Hydroplaning Speed.....	120
6.3.3	Tire parameters	120
6.3.4	Fluid parameters.....	127
6.3.5	Pavement surface parameters.....	130
6.4	Empirical Equations to Determine Critical Hydroplaning Speed	133
6.4.3	NASA equations	133
6.4.4	Gallaway's hydroplaning equation	133
6.4.5	Wambold's hydroplaning equation.....	134
6.4.6	PAVDRN hydroplaning equation	134
6.5	Analytical/Numerical Modeling of Hydroplaning	134
6.6	Computational Formulation of Hydroplaning.....	138
6.6.3	CEL method.....	138

6.7	Summary	146
7	Finite Element Simulations of Tire-Wet Pavement Interaction.....	147
7.1	Introduction.....	147
7.2	FE Simulation of Tire Hydroplaning on Smooth Pavement Surface	148
7.2.1	Study parameters of proposed hydroplaning model.....	148
7.2.2	Salient features of proposed hydroplaning model.....	148
7.3	Validation of 3D Hydroplaning Model	150
7.4	Analysis of Hydroplaning	151
7.4.1	Effect of tire groove depth and surface water depth on hydroplaning speed.....	151
7.4.2	Effect of slip ratio on hydroplaning speed	151
7.4.3	Effect of yaw angle on hydroplaning speed.....	153
7.4.4	Effect of slip ratio on longitudinal friction force	154
7.4.5	Effect of yaw angle on cornering force.....	154
7.5	Relation Between Asphalt Mix Design and Wet Friction.....	155
7.5.1	Study Parameters	155
7.5.2	Field Measurements of Wet Friction and Hydroplaning.....	157
7.5.3	Description of Numerical Model	159
7.5.4	Calibration of Numerical Model against Experiment Data.....	162
7.5.5	Results and Discussion	164
7.6	Conclusions.....	168
8	Conclusions and Recommendations	169
8.1	FE Modeling of Tire-Pavement Interaction	169
8.2	FE thermo-mechanical tire-asphalt pavement interaction model.....	169
8.2.1	Model Development.....	169
8.2.2	Model Capabilities	169
8.2.3	Conclusions.....	170
8.2.4	Recommendations.....	170
8.3	FE tire-water-asphalt pavement interaction model	171
8.3.1	Model Development.....	171
8.3.2	FE Model Capabilities	171
8.3.3	Conclusions.....	171
8.3.4	Recommendations.....	172
	Appendices	173
	Nomenclature	181

References	185
Publications	198
Summary	200
Samenvatting	202
Curriculum Vitae	204

1 Introduction

1.1 Background

Vehicle accidents, where the state of the road surface plays an important role, are known to account for at least 25% of all European road fatalities (ERTRAC, 2006). The main reason for this is low levels of friction at the interface between the pavement and the car tire. Depending on the rotational speed of the wheel and the characteristics of the road surface, after the maximum friction level is reached, the wheel may start **skidding**. A direct consequence of skidding is a dramatic loss of braking power and steering capability of the vehicle which leads to damage of the pavement and may result to human casualties. The problem is aggravated further in the presence of water, due to the phenomenon of hydroplaning.

Therefore, a precise investigation of micro-mechanical factors controlling the friction at the tire-pavement interface is of utmost importance in understanding the fundamental properties of friction. In the present study, finite element (FE) tools were developed for the investigation of the influence of asphalt mix characteristics and, in particular, pavement surface morphology on tire-asphalt friction and hydroplaning.

As shown in Figure 1.1a, friction originates primarily from the interaction of the asperities of the road surface with the morphological characteristics of the car tire. **Skid resistance** describes the contribution of the road surface to the development of friction at the tire-road interface. It is an important requirement in the design of safe pavements. Unfortunately, with time and traffic, the asperities of the road surface diminish and, as a consequence, skid resistance diminishes as well.

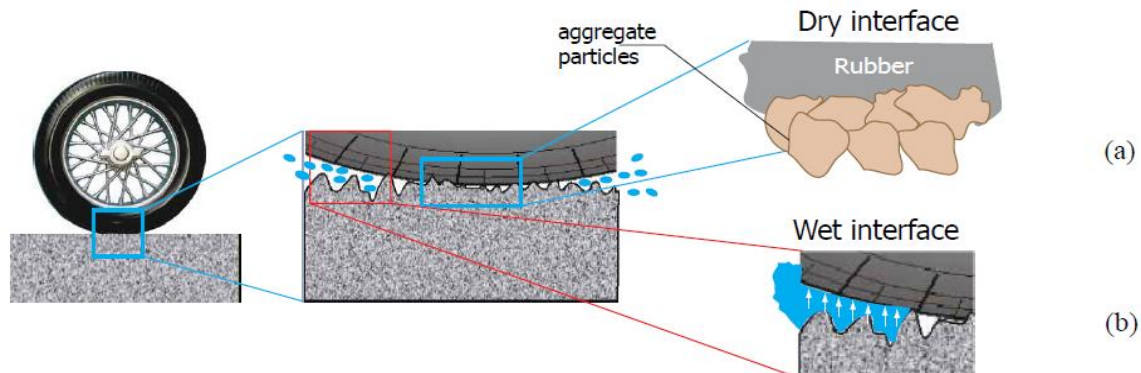


Figure 1.1 (a) Factors influencing skid resistance at the tire-pavement interface, (b) hydrodynamic stresses at the tire-pavement interface

Moisture on the road surface also contributes largely to diminishing skid resistance, because it can act as a lubricant at the tire-pavement interface. Larger amounts of water in the form of puddles can additionally cause the partial or complete separation of the tire from the pavement because of the development of hydrodynamic stresses, Figure 1.1b, in front of the tire. These counterbalance a part of the tire load and result to significant reduction of steering and braking forces. This phenomenon is known as hydroplaning and its likelihood increases as the pavement surface deteriorates and large permanent deformations develop.

In the recent past, several significant developments have been made in tire design and

manufacturing, aiming at improved performance. At the same time, the advent of computational techniques has enabled the development of powerful algorithms which enable simulation of interfacial contact phenomena. Nevertheless, in the vast majority of studies on the topic of tire-pavement interaction, the pavement has been simulated as either a rigid substrate or by means of very simplistic constitutive assumptions and emphasis has been placed on the response of the tire. Yet, it is common knowledge in interfacial science that interfacial response is determined by the characteristics of both contacting bodies.

At European level, a significant initiative was taken in the framework of the project HERMES (2007-2010) which was a round robin study for the purpose of comparing all European skid resistance measuring equipment and developing a procedure for harmonization. HERMES made no attempt to focus on the fundamental aspects of the phenomenon. Nevertheless, at the conclusion of the project the need was realized and a call was made for the development of a new device which can address some of the shortcomings of the existing ones. On the other hand, the SKIDSAFE project (2009-2013) which was a consortium led by TU Delft, was an attempt to examine at a more fundamental level the processes taking place at the interface between the pavement surface and the tire and, to develop laboratory and computational tools for their evaluation. The present thesis is a part of the SKIDSAFE project and it focuses mainly on tire-asphalt pavement interaction.

Under the umbrella of the SKIDSAFE project, the current thesis shall describe a procedure to integrate state-of-the-art constitutive models, tire models with rolling contact algorithms, thermo-mechanical coupling algorithms and hydrodynamic algorithms for simulation of all major physical processes contributing to friction in the interfacial zone between the pavement surface and the tire but, also, in the bulk body of the pavement.

One of the significant findings of this thesis is the crucial influence on friction of the temperature at the tire rubber-asphalt interface. Especially, during braking manoeuvres, temperature increases significantly and at high rates in the body of the tire affecting thus the mechanical characteristics of the rubber materials and the area of the tire footprint and, hence, the developed friction at the interface. Another important finding is the influence of asphalt mix design on the propensity to hydroplaning and in particular, the importance of wearing course drainage as a crucial feature to alleviate the hydroplaning risk in flooded pavement conditions.

The following subsequent sections serve as an introduction to the topic of tire-pavement interaction under various operating conditions. First, basic terminology concerning tires and pavement surfaces is discussed in section 1.2, followed by friction mechanisms in section 1.3. State-of-art contact models are discussed in section 1.4 followed by tire temperature in section 1.5. Section 1.6 discusses the parameters influencing tire-pavement friction. This chapter concludes with the research objectives in section 1.7 and a general outline of the thesis in section 1.8.

1.2 Basic terminology

1.2.1 Tire

The modern passenger car tire is a complex load carrying structure and numerical modeling of such structure is a challenging task. The major difficulties in numerical simulation include the material nonlinearity as shown in Figure 1.2, incompressibility constraint on the deformation of tire rubber, and the nonlinear contact boundary conditions (Yan, 2001). Moreover, the external

loads may cause the tire to undergo very large deformations, even though the resulting strains may be small (Parikh, 1977). For a given load magnitude, tire inflation pressure and tire structure are the two important factors that influence contact area and contact pressure at the tire-pavement interface.

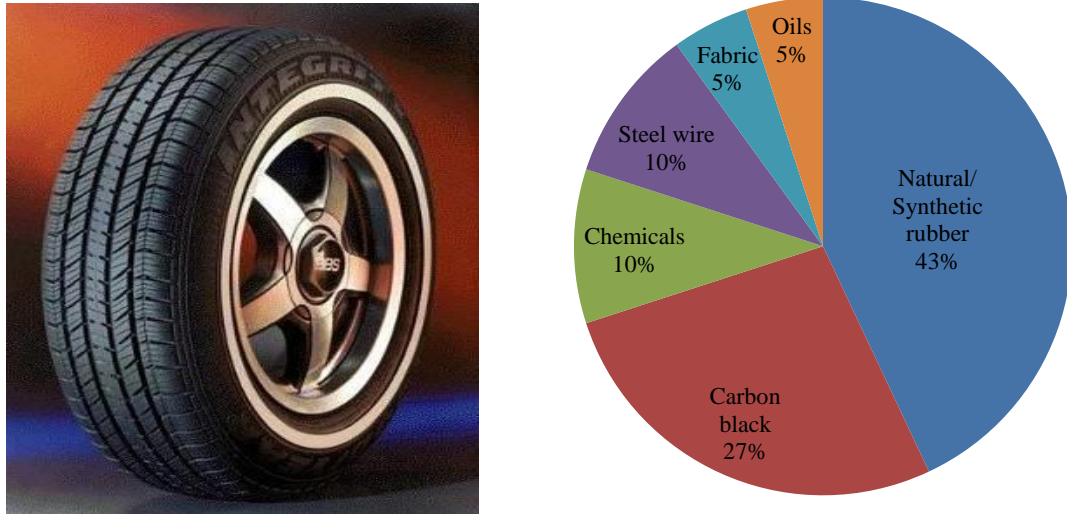


Figure 1.2 Components of a pneumatic tire

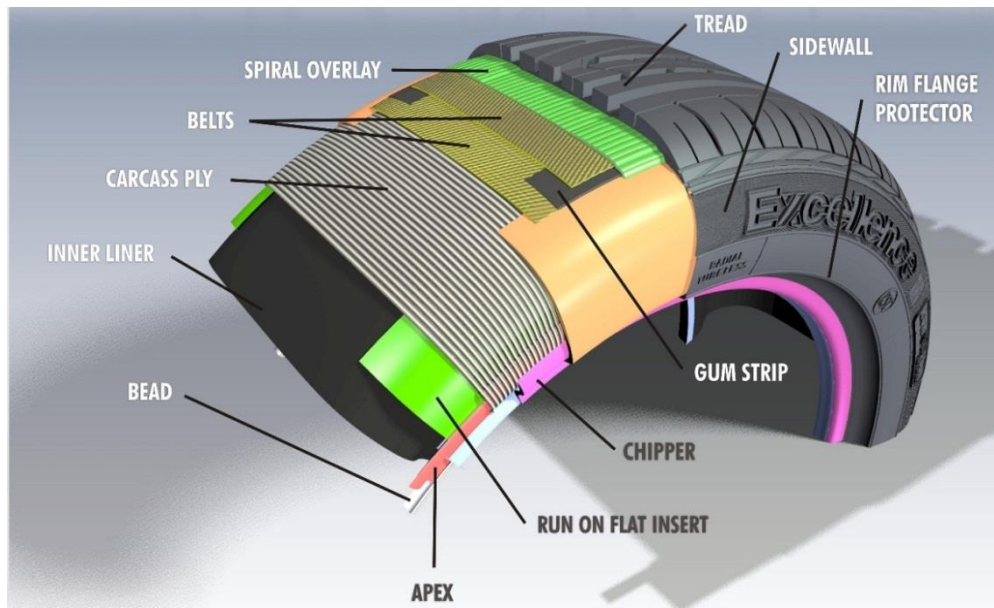


Figure 1.3 Cross sectional geometry of a pneumatic tire (Goodyear)

A pneumatic tire is made of vulcanized rubber and a carcass along with other reinforcing components as shown in Figure 1.3. It is a highly anisotropic, temperature dependent, hyper-elastic or viscoelastic structure. The accurate assessment of the contact area of a deformed tire, known as footprint, has drawn much attention worldwide because it characterizes tire performance issues such as contact pressure, wear, noise, skid resistance and hydroplaning (Clark, 1982).

1.2.1.1 Tire types

1.2.1.1.1 Diagonal bias tires

The body ply cords of these tires lay at angles substantially less than 90° to the tread centerline, Figure 1.4. The advantages of such kind of tires are: (a) simple in construction, and, (b) ease of manufacturing. However, as the tire deflects, shear occurs between the body plies which generates heat. Also these tires have poor wear characteristics due to tread motion.

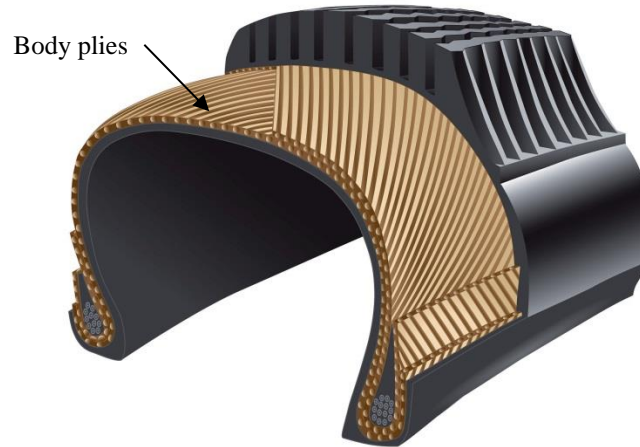


Figure 1.4 Diagonal bias tires (Speciality Equipment Market Association US)

1.2.1.1.2 Belted (bias) tires

For this type of tires, belts are added in the tread region and these belts restrict expansion of the body carcass, Figure 1.5. The main advantages of these tires are improved wear and handling due to added stiffness in the tread area. However, these tires generate more heat due to the shear deformations between body plies. Also they require higher material and manufacturing cost.

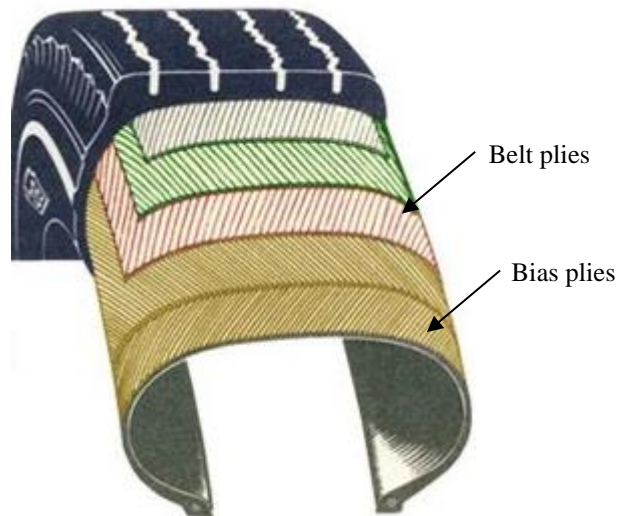


Figure 1.5 Belted bias tires (Salsons Automotive Tyres)

1.2.1.1.3 Radial tires

The radial tire is a carcass of layers of cord ply going over each other from bead to bead. The tread is then strengthened with a belt of diagonal design, Figure 1.6. The side walls are thinner and softer providing comfort but are generally more sensitive to damage. The soft tire wall area in conjunction with the belt gives a larger contact area and lower rolling resistance. Other advantages are good properties at high speed, good grip and comfort on an even surface, low heat buildup and low rolling resistance. However, complex radial construction increases material and manufacturing costs.

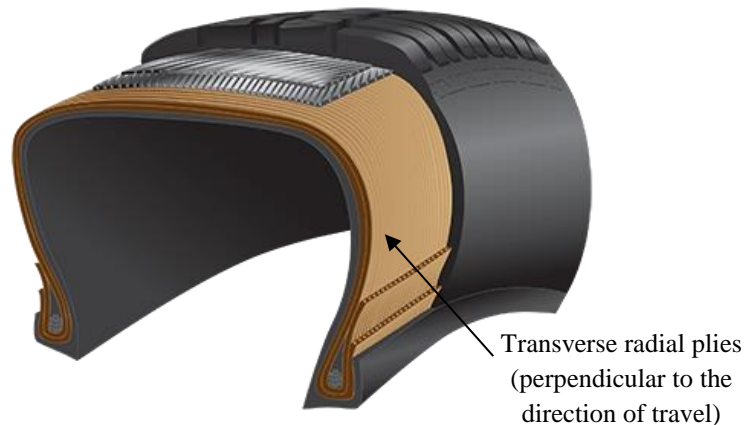


Figure 1.6 (Speciality Equipment Market Association US)

1.2.1.2 Tire components

1.2.1.2.1 Tire rubber compounds

Beyond the visible tread and sidewalls, there are more than a dozen specially formulated compounds that are used in the interior of a tire rubber. The following are the basic ingredients of tire rubber:

- Polymers: backbone of rubber compounds
- Fillers: reinforce rubber compounds
- Softeners: used mainly as processing aids
- Anti-degradents: helps to protect tires against deterioration by ozone, oxygen and heat
- Curatives: to transform the viscous compounds into strong, elastic materials

In general, a typical car tire uses around 60 raw materials.

1.2.1.2.2 Tire reinforcement materials

Tire reinforcement materials like tire cord and bead wire are the predominant load carrying members of the cord-rubber composite. They provide strength and stability to the sidewall and sustain the air pressure. Nylon, polyester, rayon, aramid, steel cord, bead wire are different types of reinforcement material available, Figure 1.7.



Figure 1.7 Tire bead wire (Zhangjiagang City Shengda Steel Wire Rope Co.,Ltd)

1.2.1.2.3 Other tire components

- Inner liner : improves air retention
- Body plies: provide the strength to contain the air pressure and provide for sidewall impact resistance
- Bead bundles: serve to anchor the inflated tire to the wheel rim
- Abrasion gum strip: provides a layer of rubber between the body plies and the wheel rim for resistance against chafing
- Sidewall: protects the body plies from abrasion, impact
- Sidewall reinforcements: some tires feature lower sidewall reinforcements to improve handling or stability
- Stabilizer plies (belts): to restrict the expansion of the body ply cords, stabilize the tread area and provide impact resistance
- Belt wedges: to reduce the inter-ply shear at the belt edge as the tire rolls and deflects
- Shoulder inserts: to help maintain a smooth belt contour and insulate the body plies from the belt edges
- Tread: provides the necessary grip or traction for driving, braking and cornering
- Subtread: improves rolling resistance, fine-tunes driving quality, noise, and handling
- Undertread: boosts adhesion of the tread to the stabilizer plies during tire assembly and covers the ends of the cut belts.
- Nylon cap/cap strips: To further restrict expansion from centrifugal forces during high speed operation

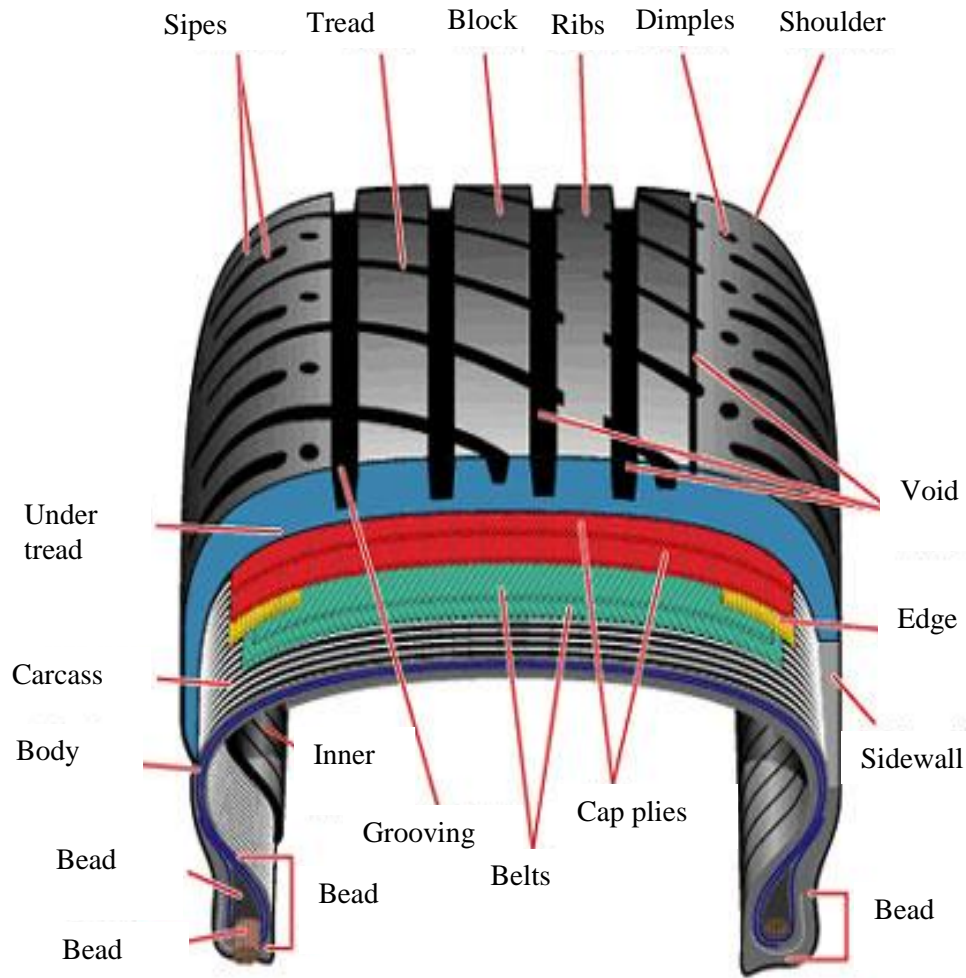


Figure 1.8 Radial tire components (after YOKOHAMA)

1.2.2 Pavement surface texture

Pavement surface texture is defined as the deviations of the pavement surface from a true planar surface. These deviations are grouped at three distinct levels of scale: microtexture, macrotexture and megatexture, each defined within a range of wavelength (λ) and peak-to-peak amplitude (A), Figure 1.9. Such asperities may range from the micro-level roughness contained in individual aggregate particles to a span of unevenness stretching several feet in length.

The three levels of texture, as established by the Permanent International Association of Road Congresses (PIARC, 1987), are as follows:

Microtexture ($\lambda < 0.02$ in [0.5mm], $A = 0.04$ to 20 mils [1 to 500 μm]) –

Surface roughness quality at the sub-visible or microscopic level. It is a function of the surface properties of the aggregate particles contained in the asphalt or concrete paving material.

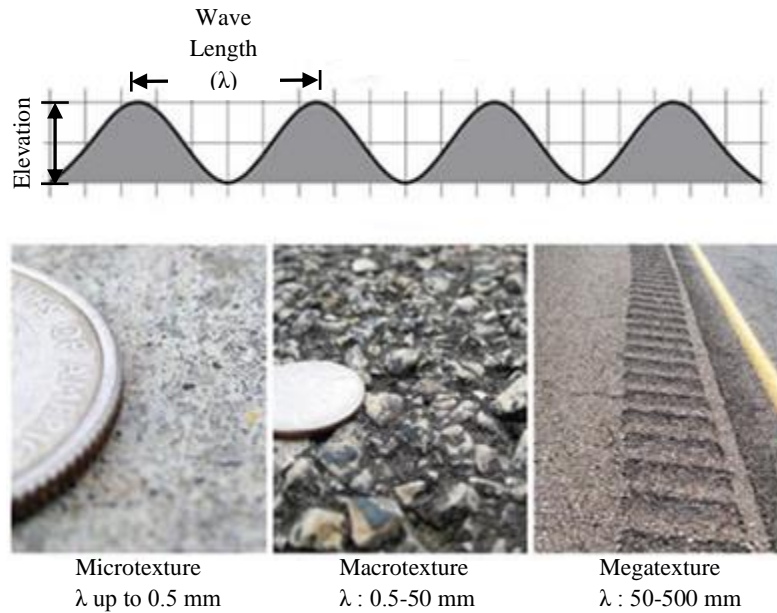


Figure 1.9 Schematic of pavement surface texture (cenews, 2013)

Macrottexture ($\lambda < 0.02$ to 2 in [0.5 to 50 mm], $A = 0.0054$ to 0.8 in [0.1 to 20 mm]) –

Surface roughness quality defined by the mixture properties (shape, size, and gradation of aggregate) of asphalt paving mixtures and the method of finishing/texturing (dragging, grooving, depth, width, spacing and orientation of channels/grooves) used on a concrete paved surface.

Megattexture ($\lambda = 2$ to 20 in [50 to 500 mm], $A = 0.005$ to 2 in [0.1 to 50 mm]) –

Texture with wavelengths in the same order of size as the pavement-tire interface. It is largely defined by the distress, defects, or “waviness” on the pavement surface.

1.3 Friction mechanisms

Friction is the force that resists the relative motion between a vehicle/aircraft tire and a pavement surface. This resistant force, illustrated in Figure 1.10 is generated when the tire rolls or slides over friction, μ , which is the ratio of the tangential friction force (F) between the tire tread rubber and the pavement surface to the perpendicular force or vertical load (F_w).

$$\mu = \frac{F}{F_w} \quad (1.1)$$

Two distinct modes of operation can be identified: free-rolling and full skidding. In the free rolling mode (no braking at all), the relative speed between the tire circumference and the pavement, referred to as the slip speed—is zero. At full skidding, the circumferential tire speed is zero and the slip speed is equal to the speed of the vehicle. In typical braking conditions, the slip speed varies between these two extremes (Meyer, 1982).

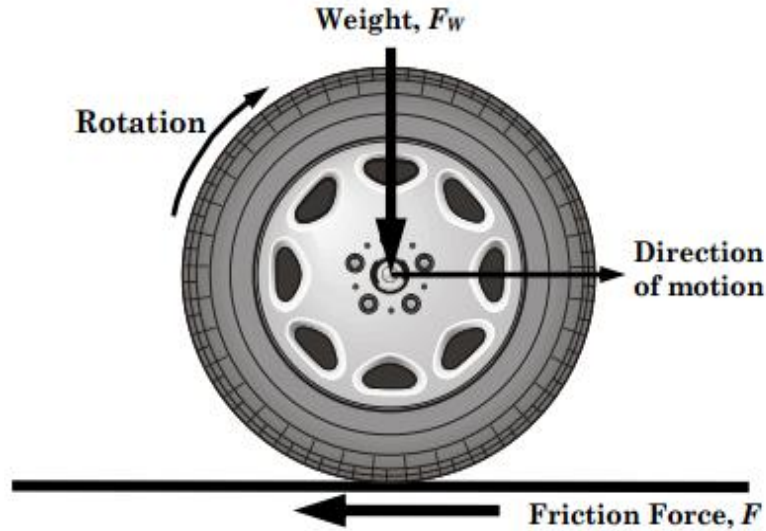


Figure 1.10 Simplified diagram of forces acting on a rotating wheel (NCHRP, 2009)

Hence it holds

$$S = V - V_p \quad (1.2)$$

where: S = Slip speed; V = Vehicle speed; V_p = Average peripheral speed of the tire.

A locked-wheel state is referred to as a 100 per cent slip ratio and the free-rolling state is a zero per cent slip ratio. The slip ratio is defined as the ratio of the slip speed to the vehicle speed and is given by

$$SR = \frac{S}{V} \times 100\% \quad (1.3)$$

Similarly, the side-force coefficient (SFC) is the ratio of the force perpendicular to the plane of the rotating tire to the vertical load on the tire when the plane of the tire is maintained at a fixed angle with respect to the forward velocity vector

$$SFC(V, \alpha) = \frac{F_s}{F_w} \times 100 \quad (1.4)$$

where V is the test speed, α is the angle between the plane of the test tire and the forward velocity vector, F_w is the normal (vertical) load on the test tire, and F_s is the force perpendicular to the plane of the test tire.

The coefficient of friction between a tire and the pavement changes with varying slip, as shown in Figure 1.11. It increases rapidly with increasing slip to a peak value that usually occurs between 10 and 20 percent slip (critical slip). Beyond that, it decreases continuously up to a value known as the coefficient of sliding friction, which occurs at 100 percent slip. The difference between the peak and the sliding coefficients of friction may be up to 50 percent of the sliding value and is much larger on wet pavements than on dry pavements.

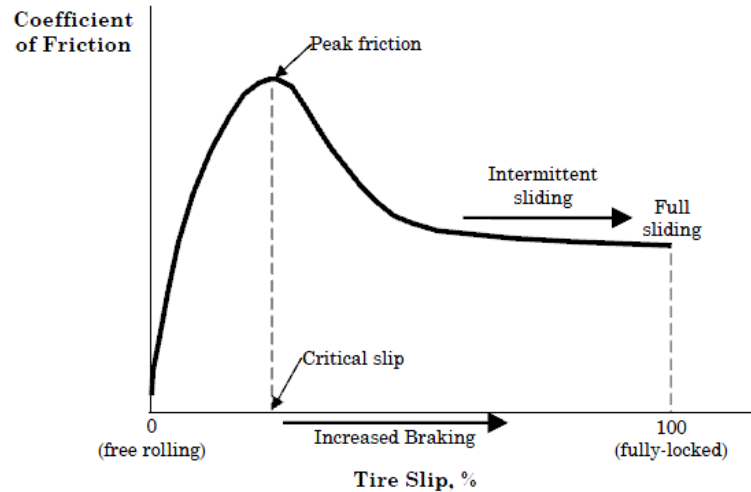


Figure 1.11 Pavement longitudinal friction versus slip (Henry, 2000)

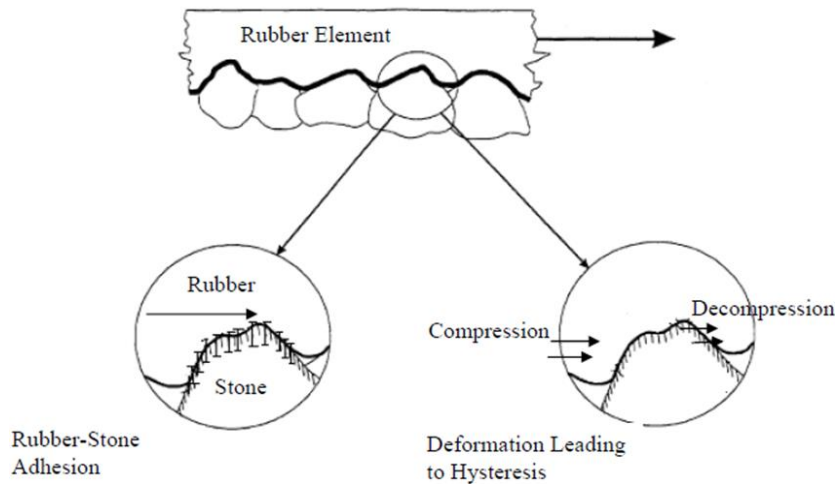


Figure 1.12 Schematic of hysteresis and adhesion (Choubane et al., 2004)

Many empirical models have been developed in an attempt to provide prediction of friction by taking into account the above factors. Friction between the tire and the pavement has two distinct force components: adhesion and hysteresis (Kummer and Meyer, 1963). During skidding, a complex interplay between adhesion and hysteresis contributes to vehicle stopping distance. A schematic of hysteresis and adhesion can be seen in Figure 1.12.

1.3.1 Adhesion

The adhesion component of friction is the result of molecular bonds that are formed when two material surfaces come in contact. The strength of these bonds depends on the natural affinity between the materials. The breaking of the bonds requires some energy. This energy is the work done by the adhesion forces. Therefore, adhesive friction results from the binding forces between the rubber surface and the substrate under the action of draping. The draping mechanism of the tire rubber about the individual asperities of the surface is time dependent, so that, slower speeds permit a greater draping effect and thus ensure a distinctly higher adhesion.

It is generally believed that microtexture governs the adhesion component (Priyantha and Gary, 1995). In the lower speed range and in the case of a wet pavement surface, microtexture breaks through the thin water film creating contact with the rubber and hence adhesion forces. The mechanism is complex because it affects the molecular and electric interactions between the contacting surfaces (Kummer, 1966, Moore, 1969; Moore, 1972). Studies by Roberts (1988) and Persson (1998) also showed that the adhesion component is reduced when particles or water film are present at the contact surface. Similarly, the adhesion component can disappear if the surface is completely covered by a lubricant (Highway Research Board, 1972). A theoretical explanation on adhesion friction in tire-pavement interaction is offered by Moore, (1972).

1.3.2 Hysteresis

The hysteresis friction arises when pavement surface asperities, at the macrotexture level, produce appreciable deformation in the bulk of the rubber (Grosch, 1963). It is associated with energy differences that occur as the rubber is alternately compressed and expanded while it slides over the surface asperities. Since the commercially available tire rubbers are viscoelastic in nature, hysteretic energy losses occur during sliding and, hence, the friction associated with this process is termed hysteresis friction. The influence of surface roughness on the interaction between rubber and pavement surface has been studied by many researchers (Johnson et al., 1971; Fuller & Tabor, 1975; Persson et al., 2002, 2004). Kluppel and Heinrich (2000) presented an analytical formulation of rubber friction on rough, rigid surfaces that relates the frictional energy losses of the rubber. Bui and Ponthot (2002) conducted FE analyses to estimate the influence of adhesion between rubber and rigid pavement surfaces and the energy losses arising from the deformation of rubber bulk to the sliding resistance. Persson (1998) presented rubber friction development on rough surfaces due to the viscoelastic deformations of rubber. Palasantzas (2003) and Gal et al. (1995) investigated friction behavior of sliding of a rubber body on a rough self-affined surface to describe the load dependent hysteretic friction of elastomers. The micromechanical analysis of the contact problem of rough surfaces were proposed by Panagiotopoulos et al. [15] and Haraldsson and Wriggers (2001).

Saka and Araki (1998) presented a theory which states that under severe conditions of tire rubber sliding, significant heat is generated at the tire-pavement contact region. As a result a thin film of melted asphalt and rubber develops which virtually annihilates the development of any adhesive forces. Consequently, the mechanism of adhesion is unlikely to play any important role in the development of tire-pavement friction forces at high skid velocities. Hence, hysteretic friction is the predominantly friction component at the tire-pavement interface (Kummer, 1966), (Greenwood & Tabor, 1958). In view of the above it is logical that tire materials with large damping coefficients have a high coefficient of friction due to increased hysteresis (Heiing et al., 2011) and that, increases in tire temperature result to decreases in friction since the rubber stiffness decreases (Subhi & Farhad, 2005).

1.3.3 Remarks

It is generally believed that both adhesion and hysteresis components depend largely on pavement surface characteristics, the contact between tire and pavement, and the properties of the tire. Usually, adhesion governs the overall friction on smooth-textured and dry pavements, while hysteresis is the dominant component on wet and rough-textured pavements (Hall et al., 2009). Also because tire rubber is a visco-elastic material, temperature and sliding speed affect both categories (Hall et al., 2009).

1.4 Computational contact mechanics models

The interaction between a rolling tire and a pavement surface is a very challenging problem because of its nonlinearity due to various factors. The day to day tire-pavement interaction applications comprise of all the facets of tribology, including friction, lubrication, adhesion and wear. Modern treatment of contact mechanics problems can be found in the research works of Laursen and Simo (1993), Shimizu and Sano (1995), Christensen et al. (1998), Simo Zavarise et al. (1998), Simo and Hughes (1998), Chenot and Fourment (1998), Wriggers and Panagiotopoulos, (1999), Pietrzak and Curnier (1999), Zavarise and Wriggers (1999), Laursen (2002), Wriggers (2006) etc.

In general, implicit time integration algorithms are often applied for the solution of the contact problem together with a fine discretization of tire with huge numbers of finite elements. For the simulation of rolling contact problems on real pavement surfaces and including phenomena such as heat generation and conduction, hydroplaning, noise etc. a combination of implicit and explicit time integration schemes have to be employed.

For simulation of the contact between two surfaces, Coulomb's law is introduced via an inequality involving the normal (\mathbf{R}_N) force and the tangential reaction force (\mathbf{R}_T) (Wriggers, 2006):

$$f(\mathbf{R}_N, \mathbf{R}_T) = |\mathbf{R}_T| + \mu |\mathbf{R}_N| \leq 0 \quad (1.5)$$

In this inequality the constitutive parameter μ is the friction coefficient. By making use of the Equation (1.5), stick and slip phenomena can be defined as follows:

stick occurs when

$$|\mathbf{R}_T| < -\mu \mathbf{R}_N \quad (1.6)$$

In this case, no relative tangential displacement can occur between two bodies in contact.

slip occurs when

$$|\mathbf{R}_T| = -\mu \mathbf{R}_N \quad (1.7)$$

In this case, a relative tangential displacement may occur between two bodies in contact.

The above inequalities can be combined and expressed in the form of Kuhn–Tucker conditions as:

$$|\mathbf{u}_T| \geq 0; f \leq 0 \text{ and } |\mathbf{u}_T| f = 0 \quad (1.8)$$

where \mathbf{u}_T is the tangential displacement. Figure 1.13 portrays in a schematic way the above relations between tangential (i.e. frictional) loading and the corresponding tangential displacements.

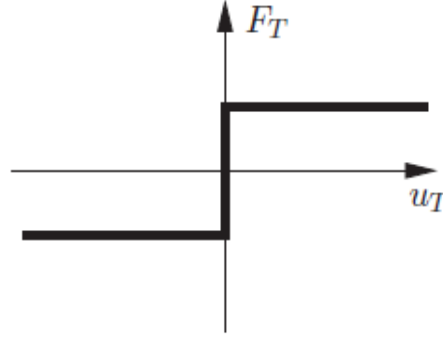


Figure 1.13 Load-displacement diagram for frictional contact (Abaqus, 2010)

In terms of finite element technology, contact is addressed via either of two main formulations: (1) the Lagrange multiplier method or (2) the penalty method. The Lagrange multiplier method is used to add constraints to the system which are equivalent to external constraint forces. Their contribution to the total energy Π_c^{LM} is expressed as (Wriggers & Zavarise, 2004):

$$\Pi_c^{\text{LM}} = \int_{\Gamma_c} (\lambda_N g_N + \lambda_T \cdot g_T) dA \quad (1.9)$$

where λ_N and λ_T are the Lagrange multipliers and g_N and g_T are termed the normal and tangential gap functions representing the associated displacement between the two contacting surfaces in the contact region.

The variation formulation of Equation (1.9) is:

$$C_c^{\text{LM}} = \int_{\Gamma_c} (\lambda_N \delta g_N + \lambda_T \cdot \delta g_T) dA + \int_{\Gamma_c} (\delta \lambda_N g_N + \delta \lambda_T \cdot g_T) dA \quad (1.10)$$

where δg_N and δg_T are the variations of the normal and the tangential gap functions, respectively. The first integral is associated with the virtual work of the Lagrange multipliers along the variation of the gap functions in the normal and the tangential directions. The second integral describes the enforcement of the constraints. Because the Lagrangian multipliers are treated as additional unknown variables, their addition to the overall structural system of equations increases its size and has also been known to result to ill-conditioning due to the “rigid” nature of the constraints.

The Penalty method adds penalty terms to the system which can be interpreted as contact springs with a certain stiffness. The following equation shows the contribution due to penalty contact constraint to the total energy (Wriggers & Zavarise, 2004):

$$\Pi_c^{\text{P}} = \frac{1}{2} \int_{\Gamma_c} (\varepsilon_N (\bar{g}_N)^2 + \varepsilon_T g_T \cdot g_T) dA, \quad \varepsilon_N, \varepsilon_T > 0 \quad (1.11)$$

ε_N and ε_T represent the penalty parameters.

The variation of Equation (1.11) yields

$$C_c^P = \int_{\Gamma_c} (\varepsilon_N \bar{g}_N \delta \bar{g}_N + \varepsilon_T g_T \cdot \delta g_T) dA, \quad \varepsilon_N, \varepsilon_T > 0 \quad (1.12)$$

Because the “spring” is deformable, an approximate solution is obtained and interpenetration may occur. The choice of the spring stiffness is critical since a high penalty parameter leads to an ill-conditioned problem and a low penalty parameter leads to large penetration (Schutte, 2011).

A special formulation, called perturbed Lagrange method developed by Oden (1981), can be used to combine the features of both, the penalty and the Lagrange multipliers methods in a mixed formulation (Wriggers & Zavarise, 2004) :

$$\Pi_c^{PL} = \int_{\Gamma_c} \left(\lambda_N g_N - \frac{1}{2\varepsilon_N} \lambda_N^2 + \lambda_T \cdot g_T - \frac{1}{\varepsilon_T} \lambda_T \cdot \lambda_T \right) dA \quad (1.13)$$

The tire-pavement contact problems are usually come under any one of the analyses:

- *Steady-state analysis*, also called *mixed Lagrangian/Eulerian* approach, in which, for an observer in the reference frame, the tire is a fixed set while materials flow through the refined stationary mesh. Frictional effects, inertia effects and history effects in the material are accounted for. The mesh can deform due to these effects. The steady-state analysis is not often used for rolling tires, since, this type of analysis is not efficient in solving changing contact conditions. The nonlinear equation solving process is expensive due to the Newton iterations, and if the equations are very nonlinear, as in the case of changing contact, it may be difficult to obtain a solution.
- *Transient analysis*, also called *Lagrangian* approach, in which, for an observer in the reference frame, the tires rolls and, turn after turn, the elements touch and leave the contact area. The displacements and velocities are calculate din terms of quantities that are known at the beginning of the increment and no iterations and no tangential stiffness matrix are required unlike steady-state method. However, it requires a very small time step increment.

1.5 Temperature generation in tires

Temperature is generated in a pneumatic tire as it rolls under various operating conditions like braking, slipping and cornering. If the resulting temperatures are high enough, they can seriously degrade the strength of a tire causing it to fail and, also, can result to traction performance degradation over time.

1.5.1 Internal energy dissipation

The temperature dependence of the viscoelastic properties of tire rubber has a significant influence on its hysteretic friction. Many researchers had shown that the coefficient of friction of viscoelastic tires skidding/rolling against pavement macrotexture varies with temperature, (Grosch K. A., 1963); (Grosch & Schallmach, 1970). Various attempts have been made to determine the temperature distribution in the various components of a tire due to energy dissipation. Browne, Wicker, & Segalman (1980) presented the earliest finite element method (FE) based work. They proposed a general model for power loss in pneumatic tires. Yandell et al. (1983) presented a mathematical study which demonstrates the dependency of sideway force or locked wheel friction on the tire temperatures.

When a sinusoidal strain is imposed on VE materials such as rubber, the stress varies sinusoidally with a phase angle δ as shown in Figure 1.14a. The area confined by the hysteresis loop of the stress-strain plot corresponds to the dissipated energy density caused by cyclic loading as seen in Figure 1.14b.

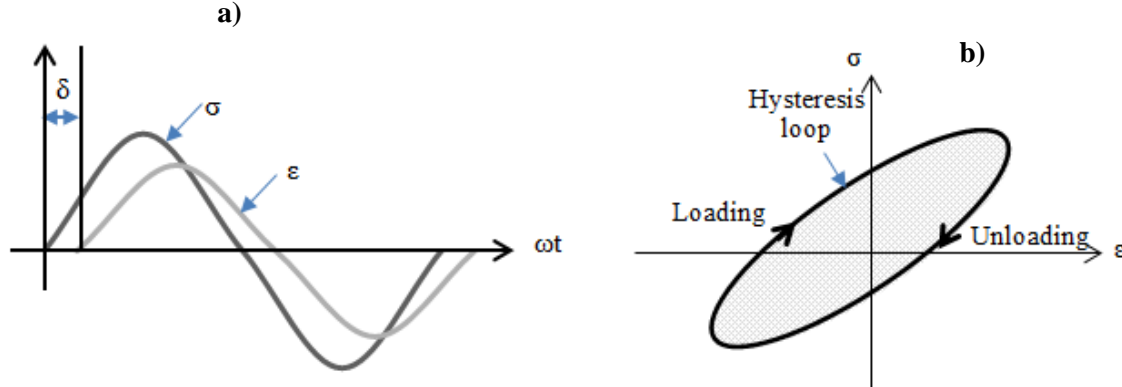


Figure 1.14 Typical stress-strain curve of a material illustrating hysteretic loss

When the stress σ and the strain ε of the VE material assumed to vary sinusoidally, they can be expressed using the phase lag δ :

$$\sigma(t) = \sigma_0 \sin(\omega t + \delta) \quad (1.14)$$

$$\varepsilon(t) = \varepsilon_0 \sin(\omega t) \quad (1.15)$$

The energy dissipated in one cycle is

$$E = V \int_{\text{cycle}} \sigma(t) d\varepsilon \quad (1.16)$$

$$= \pi \cdot V \cdot \sigma_0 \cdot \varepsilon_0 \sin \delta$$

$$W = \frac{E}{V} = \pi \cdot \sigma_0 \cdot \varepsilon_0 \sin \delta \quad (1.17)$$

where, V is the volume of the VE material, σ_0 is the amplitude of the stress, ε_0 is the amplitude of the strain, δ is the VE phase lag between stress and strain and W is the work done per unit volume.

The stress and strain evaluated at the continuous elements along the circumferential direction are considered to be the time history of the stress and strain at any point of the rolling tire. Thus, the time t which is a parameter representing the variation, may be replaced by an angle θ which represents the circumferential position of a tire. Then, the stress profile $\sigma(\theta)$ and strain profile $\varepsilon(\theta)$ are obtained from the toroidal element groups located along the circumferential direction with the same cross-sectional coordinates. Next the VE phase lag (δ) is imposed on the stress profile $\sigma(\theta)$. However, since the general profile of the stress and strain is impulsive rather than sinusoidal as shown in Figure 1.15, it is not possible to apply the phase angle in the form of Equation (1.14).

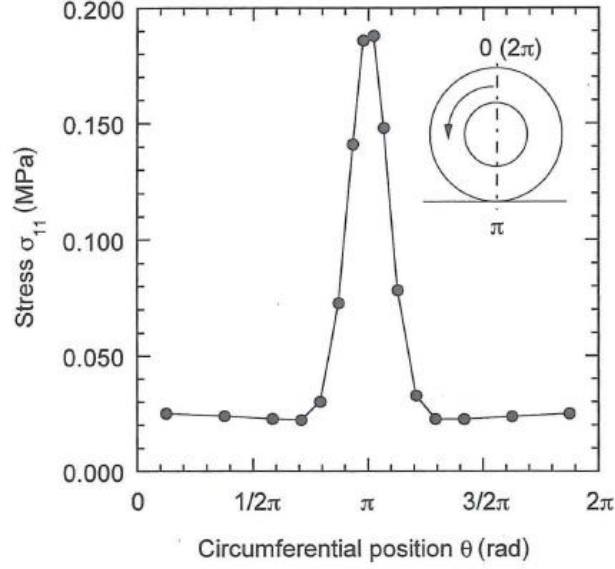


Figure 1.15. Stress profile of the sidewall in the circumferential direction (Shida et al., 1998)

(Shida et al., 1998) presented the stress profile $\sigma(\theta)$ and the strain profile $\varepsilon(\theta)$ in the form of Fourier series of order N using amplitude A_n and phase ϕ_n as follows:

$$\sigma(\theta) = a_0^\sigma + \sum_{n=1}^N \left\{ A_n^\sigma \sin(n\theta + \phi_n^\sigma) \right\} \quad (1.18)$$

$$\varepsilon(\theta) = a_0^\varepsilon + \sum_{n=1}^N \left\{ A_n^\varepsilon \sin(n\theta + \phi_n^\varepsilon) \right\} \quad (1.19)$$

where $A_n = \sqrt{a_n^2 + b_n^2}$ and $\phi_n = \tan^{-1}(b_n/a_n)$.

when the VE phase lag δ is imposed on the stress profile $\sigma(\theta)$, the shifted profile $\hat{\sigma}(\theta)$ is expressed as

$$\hat{\sigma}(\theta) = a_0^\sigma + \sum_{n=1}^N \left\{ A_n^\sigma \sin(n\theta + \phi_n^\sigma + \delta_n) \right\} \quad (1.20)$$

From the strain profile $\varepsilon(\theta)$ and the phase-shifted stress profile $\hat{\sigma}(\theta)$, the area of hysteresis loop is calculated. By applying Equations (1.19) and (1.20) to Equation (1.16), the energy dissipation can be computed as:

$$E = \sum_{n=1}^N \left[\pi \cdot n \cdot V \cdot A_n^\sigma \cdot A_n^\varepsilon \sin(\phi_n^\sigma - \phi_n^\varepsilon + \delta_n) \right] \quad (1.21)$$

The energy dissipation of one circular element group is obtained by integrating each energy dissipation with the six components of stress and strain vectors. Furthermore, the total energy dissipation of the entire tire is calculated by integrating the energy dissipation at each toroidal

element group. Therefore the total energy dissipation is obtained as presented below:

$$E = \sum_{l=1}^{n_{ele}} \sum_{m=1}^6 \sum_{n=1}^N \left[\pi \cdot \mathbf{n} \cdot \mathbf{V}_l \cdot \mathbf{A}_{lmn}^\sigma \cdot \mathbf{A}_{lmn}^\varepsilon \sin(\phi_{lmn}^\sigma - \phi_{lmn}^\varepsilon + \delta_{lmn}) \right] \quad (1.22)$$

where, l is element number, m is the component of the stress and strain, \mathbf{n} is the harmonic order and n_{ele} is the total number of elements in the tire cross section.

Relating to this, Park et al. (1997) proposed a technique to approximate the stress and strain profiles using cubic polynomials, and a VE phase lag is imposed on the approximate stress:

$$\sigma_{ij}^{k,m}(t) = a_{ij}^{k,m} t^3 + b_{ij}^{k,m} t^2 + c_{ij}^{k,m} t + d_{ij}^{k,m} \quad (1.23)$$

$$\varepsilon_{ij}^{k,m}(t) = e_{ij}^{k,m} t^3 + f_{ij}^{k,m} t^2 + g_{ij}^{k,m} t + h_{ij}^{k,m} \quad (1.24)$$

where i (or j) = r, θ, z ; t is time in a cycle; $a_{ij}^{k,m}, b_{ij}^{k,m}, c_{ij}^{k,m}, d_{ij}^{k,m}, e_{ij}^{k,m}, f_{ij}^{k,m}, g_{ij}^{k,m}, h_{ij}^{k,m}$ are coefficients; $k=1,2,\dots,K$ is the number of sections in the tire model and $m=1,2,\dots,M$ is the number of elements in the section in a tire model. For a VE material, the stress in Equation (1.23) can be written as

$$\sigma_{ij}^{k,m}(t) = a_{ij}^{k,m} (t + \delta)^3 + b_{ij}^{k,m} (t + \delta)^2 + c_{ij}^{k,m} (t + \delta) + d_{ij}^{k,m} \quad (1.25)$$

In general, the energy loss ΔW per unit volume per cycle and the rate of heat generation \dot{Q} per unit volume as follows:

$$\Delta W = \int_0^T \sigma_{ij}(\tau) \frac{d\varepsilon_{ij}(\tau)}{d\tau} d\tau \quad (1.26)$$

$$\dot{Q} = \frac{\Delta W}{T_r} = \frac{1}{T_r} \int_0^T \sigma_{ij}(\tau) \frac{d\varepsilon_{ij}(\tau)}{d\tau} d\tau \quad (1.27)$$

where T_r is the elapsed time for one revolution, σ and ε are the stress and strain components with respect to time in a cycle extracted from the deformation of tire against pavement surface.

By substituting Equations (1.24) and (1.25) respectively into Equations (1.26) and (1.27) to get dissipated energy and rate of heat generation:

$$\Delta W = \sum_{m=1}^M \sum_{k=1}^K \int_{t_{k-1}}^{t_k} \sigma_{ij}^{km}(\tau) \frac{d\varepsilon_{ij}^{km}(\tau)}{d\tau} d\tau \quad (1.28)$$

$$\dot{Q} = \frac{\Delta W}{T} = \frac{1}{T} \sum_{m=1}^M \sum_{k=1}^K \int_{t_{k-1}}^{t_k} \sigma_{ij}^{km}(\tau) \frac{d\varepsilon_{ij}^{km}(\tau)}{d\tau} d\tau \quad (1.29)$$

All these studies provide a better understanding of tire hysteresis and its dependency on the temperature distribution in the tire.

1.5.2 Thermal State of a Tire

The thermal state of a tire can be described with a solution to the basic equation of heat conduction, subject to the appropriate set of boundary conditions (Browne and Arambages, 1981). For the case of an inflated, loaded, rolling tire, the most general form of this system of equations is:

$$\nabla \cdot k \nabla T = -\dot{Q} \quad (1.30)$$

where, k is the thermal conductivity ($\text{W}/\text{m} \cdot \text{K}$) and C is the specific heat ($\text{J}/\text{kg} \cdot \text{K}$).

subject to the boundary conditions:

a) Heat exchange by conduction at the tire-road interface

$$k \left. \frac{\partial T}{\partial n} \right|_0 = h_{T-R} (T_R - T)|_0 \quad (1.31)$$

b) Heat exchange by conduction at the tire-rim interface

$$k \left. \frac{\partial T}{\partial n} \right|_0 = h_{T-RI} (T_{RI} - T)|_0 \quad (1.32)$$

c) Heat exchange by convection and radiation at the exterior and interior, tire-air interfaces

$$k \left. \frac{\partial T}{\partial n} \right|_0 \cong h_{T-A} (T_A - T_0) + \sigma \varepsilon (T_E^4 - T_0^4) \quad (1.33)$$

where, T is the tire temperature (K); T_R is the road surface temperature (K); T_0 is the tire surface temperature (K); T_E is the temperature of environment (K); T_A is the air temperature (K); h_{T-A} is the heat transfer coefficient ($\text{W}/\text{m}^2 \cdot \text{K}$) between tire and air; h_{T-R} is the inverse of thermal contact resistance ($\text{W}/\text{m}^2 \cdot \text{K}$) between tire and road; and h_{T-RI} is the inverse of thermal contact resistance ($\text{W}/\text{m}^2 \cdot \text{K}$) between tire and rim.

1.6 Parameters influencing tire-pavement friction

Friction forces arise due to the interplay of complex mechanisms while there are several factors that affect the available pavement surface friction. These factors can be categorized as follows:

Tire factors:

- Speed
- cornering angle
- slip ratio
- tread wear
- tire groove depth and tread pattern
- tire inflation pressure and load

Pavement surface factors:

- surface texture (microtexture and macrotexture)

- type of surfacing
- age of the surface

Load factors:

- equivalent number of vehicle traffic loadings
- road geometry
- traffic flow conditions

Environmental factors:

- temperature
- water film
- seasonal variations

1.6.1 Tire factors

1.6.1.1 Speed

The friction resistance between the tire and road surface during emergency or locked-wheel braking is very much dependent on vehicle speed. The influence of vehicle speed on skid resistance is highly dependent upon the properties of the tire and the pavement surface. Past researchers found that instantaneous tire-pavement friction decreases non-linearly with increasing speed (Shah and Henry, 1978). Dijks (1974) conducted experimental investigations on various car and truck tires to determine the effect of speed on friction performance under wet pavement conditions. He observed that both peak and braking friction coefficients decrease with increase in speed. Meyer (1991) proposed the following relationship between skid resistance and vehicle speed,

$$SN_v = SN_0 e^{-(PNG/100)v}$$

$$\text{where, } PNG = \left(\frac{d(SN_v)/dv}{SN_v} \right) \times 100 \quad (1.34)$$

where SN_v is the skid number at vehicle speed v , SN_0 is a fictitious skid number at zero vehicle speed, and PNG is the percentage normalized gradient of the SN versus v curve. Kulakowski and Meyer (1990) proposed an alternative relationship for skid number SN at any speed v :

$$SN_v = SN_0 e^{-v/v_0}$$

$$\text{where, } v_0 = \frac{v_2 - v_1}{\ln \left(\frac{SN_{v_1}}{SN_{v_2}} \right)} \quad (1.35)$$

where v_0 is a speed constant that replaces PNG .

In 1995, the results of the International PIARC Experiment to compare and harmonize texture and skid resistance measurements were published (Wambold et al., 1995). This experiment was conducted to create a common scale for the reporting of pavement friction measurements. The result of the experiment was the development of the International Friction Index (IFI) which reports the frictional properties of a pavement with two terms: the speed constant, S_p , which is a function of the pavement macrotexture and the friction number F60, which depends on a measured friction value, the slip speed and the speed constant (Wambold et al., 1995). The speed constant is used to adjust the friction values measured at any slip speed to a friction value at 60 km/h. ASTM Standard Practice for Calculating International Friction Index of a Pavement Surface (E 1960-07) details the necessary equations for calculating and reporting the IFI.

The speed constant in km/h is determined from the macrotexture measurement as follows:

$$S_p = \alpha + b \cdot \text{MPD} \quad (1.36)$$

Where,

a, b = coefficients dependent on the device used for measuring macrotexture.

MPD = Mean Profile Depth

The next step uses the FRS at a given S to adjust the friction to a common slip speed of 60 km/h. This is accomplished using the speed number predicted by the texture measurement and using the following relationship:

$$\text{FR60} = \text{FRS} \cdot e^{\frac{S-60}{S_p}} \quad (1.37)$$

where,

FR60 = adjusted value of friction from a slip speed of S to 60 km/h for the equipment

FRS = measured friction value by the equipment at slip speed S

S = slip speed of the equipment, (km/h)

The final step in harmonization is the calibration of the equipment, by regression of the adjusted measurement FR60, with the calibrated Friction Number F60:

$$\text{FR60} = A + B \times \text{FR60} \quad (1.38)$$

where,

A, B = calibration constants for the selected friction measuring device.

F60 is the prediction of the calibrated Friction Number and S_p is the prediction of the calibrated Speed Number. The values of F60 and S_p are then reported as the International Friction Index, IFI (F60, S_p) (Wambold et al., 1995).

The use of IFI to estimate friction at any speed is illustrated in Figure 1.16. Having measured S_p and the friction value F60 at 60 km/hr, the friction value at any other speed can be estimated by choosing a value for S (Hall et al., 2009).

The Rado-IFI model (Rado, 1994), known also as the logarithmic friction model, was developed to complement the PIARC friction model by incorporating the first “leg” of the friction curve where the friction number increases to a maximum. This model has the following form (Henry, 2000):

$$\mu(S) = \mu_{\max} \times e^{-\left(\frac{\ln\left(\frac{S}{S_{\max}}\right)}{C}\right)^2} \tag{1.39}$$

where, $\mu(S)$ is the friction number at any slip speed (S), μ_{\max} is the maximum friction value (a function of surface and tire properties, measuring speed, and slip speed), S_{\max} is the slip speed at maximum friction value (also known as the critical slip speed, which is when the tire is slipping on the pavement with S_{\max} slip speed while it develops μ_{\max} friction); C is the shape factor which is closely related to the speed number S_p in the original IFI equation and determines the skewed shape of the friction curve. Figure 1.16 presents graphically friction computed using IFI ($F(60), S_p$) and the Rado-IFI models.

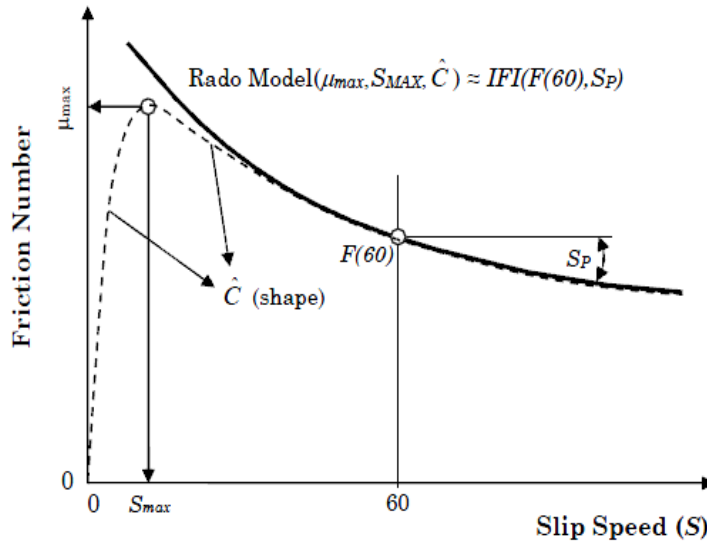


Figure 1.16 The IFI and Rado-IFI models (Rado, 1994)

The speed number, S_p , is the derivative of the friction curve at $F(60)$ point, when it is transformed to a logarithmic form:

$$S_p = \frac{60C^2}{2\ln\left(\frac{S}{S_{\max}}\right)} \tag{1.40}$$

The value of C controls the shape of the declining side of the friction curve.

Benedetto (2002) showed that an increase in vehicle speed causes a decrease in the dry skid resistance for dry pavement. This decrease is gradual as compared to the friction on wet pavement which decreases dramatically with increasing speed. The wet skid resistance is also related to other factors such as water depth, tire groove depth, tread pattern, inflation pressure and pavement surface properties. Heinrichs et al. (2003) conducted experimental investigations to determine the effect of vehicle speed on both pre-skid braking kinematics and average tire-pavement friction.

1.6.1.2 Cornering angle

Automobile tire variables such as cornering force and sideslip angle are the two essential factors which improves vehicle safety, handling, steerability, comfort and performance (Baffet et al., 2009). References (Clark, 1981), (Pacejka, 2006) and (Milliken & Milliken, 1995) found that lateral force increase with side-slip angle up to a certain value then decreases marginally for higher values. Dixon (1996) put forward an empirical relation between lateral force and normal load for different side-slip angles. Tönük and Ünlüsoy (2001) performed a FE simulation study on the prediction of tire cornering forces on a drum for up to side-slip angles of 5°.

Koishi et al. (1998) developed an explicit FE model to study the effects of the inflation pressure, rubber modulus, and effect of belt angle on cornering force characteristics. They concluded that, cornering force increases linearly as the slip angle increases up to 4°, and increasing inflation pressure leads to higher cornering forces. They found that lowering the belt angles decreases the cornering force and also increasing the rubber modulus to twice of the original value, increased the cornering force.

Recently, Baffet et al., (2006; 2008) conducted experimental investigations and simulation analysis to determine relations between tire-road forces, sideslip angle and wheel cornering stiffness. Rao et al. (2002), conducted a study on tire cornering behavior for different slip angles and vertical loads using explicit finite element code by ABAQUS.

1.6.1.3 Slip ratio

The difference between the peripheral velocity of the tire and the horizontal velocity of the wheel axle is defined as the relative skidding velocity occurring between the tire and the ground. The ratio of this relative skidding velocity to the horizontal velocity of the axle is defined as the slip ratio (Horne & Leland, 1962). Thus for a freely rolling wheel the slip ratio is effectively zero while for a completely braked wheel (full skid) the slip ratio equals 1. Tire slip condition has a major influence on the temperature development in the tire and resulting effect on friction (Grosch, 2005). In general, different testing devices, which operate at different slip ratios are used by road authorities to perform friction measurements. For example, a locked wheel skid trailer measures friction at 100% slip ratio (full skidding); fixed slip devices typically operate at 15% to 20% and variable slip devices operate at 15% to 85%. Grosch (2005) hypothesized that with increase in slip ratio, tire temperature increases which causes the peak longitudinal friction to decrease.

1.6.1.4 Wear

The wear of tires is the result of frictional work in the tire-pavement interface that is generated when tread surface elements go through a frictional force-slip cycle during each passage through the footprint (Grosch and Schallamach, 1961). Tread wear has only a small effect on average friction coefficient until the tread is about 80% worn, after which it drops rapidly (Leland and Taylor, 1965). The tread wear causes higher tread temperature and further aggravated tread wear.

This ultimately results in lower skid resistance (Veith, 1986). Staughton (1970) observed a sharp drop in skid resistance with the tread wears under his field experimental tests. Segel (1973) found that maximum cornering force is very sensitive to small amounts of wear in the shoulder region for tires that are produced with a sharp corner at the shoulder. He concluded that maximum cornering force increases as the shoulder becomes rounded. Cornering stiffness increases as the tread wears (Koessler, and Senger, 1964 cross referenced from Sinnamon, 1974). Braking stiffness (the initial slope of the braking force vs. wheel slip curve) is very sensitive to tread wear, and increases with decreasing tread depth (Sinnamon, 1974).

1.6.1.5 Tire groove depth & tread pattern

On dry surfaces, smooth tread tires provide somewhat better longitudinal traction than patterned tire treads (Forster, 1956 cross referenced from Sinnamon, 1974). Increase in tread causes the cornering stiffness to increase (Koessler and Senger, 1964 cross referenced from Sinnamon, 1974).

1.6.1.6 Tire construction

Tire construction has an appreciable effect on the tire-pavement friction. When compared to a bias ply tire of the same size, rubber compound, and tread pattern, the radial ply tire gives somewhat higher values of peak braking force coefficient, but no difference in locked wheel coefficient (Lander and Williams, 1968). However, compared to a typical production bias ply tire, much larger differences are observed because radial construction allows greater freedom in tread pattern design and tread rubber compounding (Meades, 1967). Radial ply tires have higher cornering stiffness than do bias ply tires (Koessler, and Senger, 1964 cross referenced from Sinnamon, 1974).

1.6.1.7 Tire load and inflation pressure

On a dry pavement surface an increase in inflation pressure causes a decrease in both peak and locked wheel brake force (Forster, 1956 cross referenced from Sinnamon, 1974). An increase in load usually causes a decrease in both braking and cornering traction (Close, 1961). With respect to tire/road friction, changes in load and inflation pressure in the range that can be used in automobile tires have a relatively small effect, but these variables are very important for aircraft tires which may be operated over a greater range of loads and inflation pressures. On a dry surface, peak cornering force coefficient is nearly independent of load (Forster, 1956 cross referenced from Sinnamon, 1974). Maximum cornering force and cornering stiffness increases with increase in inflation pressure and the increase is greater at high loads than at low loads (Koessler, and Senger, 1964 cross referenced from Sinnamon, 1974).

1.6.2 Pavement surface factors

1.6.2.1 Surface texture

The surface texture has a significant effect on the average braking friction of dry roads. Past researchers (Forster, 1956 cross referenced from Sinnamon, 1974) found that high microtextured surfaces have higher coefficients of average braking friction than worn and polished surface. For dry pavement conditions, higher pavement macrotexture increases the energy dissipation of the tire rubber which causes the hysteretic part of pavement friction to increase (Grosch, 1963; Grosch and Schallamach 1970). Correspondingly, higher microtexture increases the bonding (electrostatic attraction) between exposed rubber molecules and aggregate asperities which causes

the adhesion part of pavement friction to increase (Clapp, 1983).

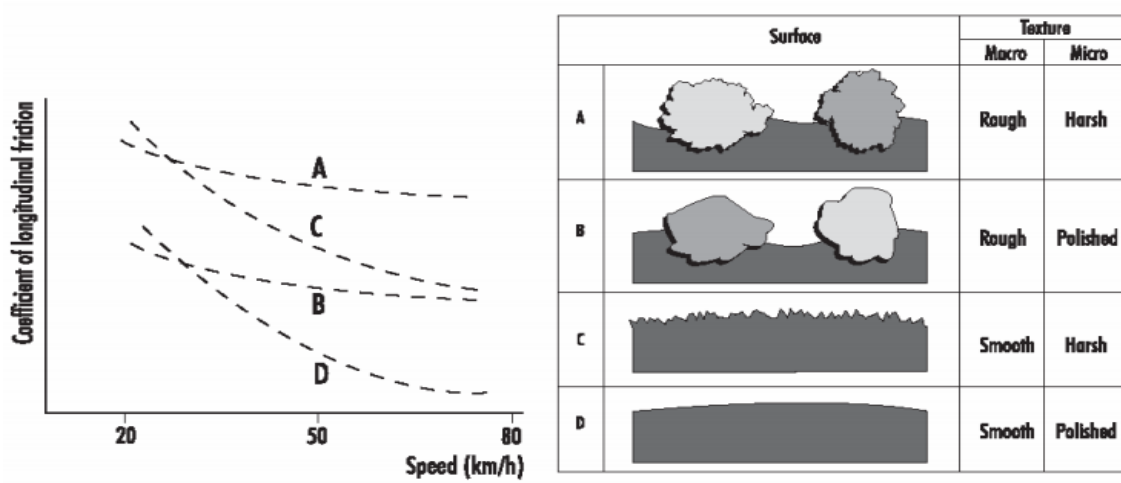


Figure 1.17 Relationship between microtexture, macrotecture, friction and speed
(PIARC World Road Association, 2003 cross referenced from Wilson, 2006)

Kennedy et al. (1990) pointed out that microtexture is predominant in determining the skid resistance at lower speeds (up to about 50 km/h) and macrotecture is predominant in determining the skid resistance at higher speeds. Microtexture is often described as the low-speed friction parameter. However, it affects the level of skid resistance at all speeds as shown in Figure 1.17. The macrotecture determines the rate at which skid resistance is lost as speed increases (PIARC World Road Association, 2003). It is often described as the friction-speed gradient parameter. Figure 1.17 also shows the extremes of pavement surface texture and demonstrates the relationship between microtexture, macrotecture, speed and friction. The diagram demonstrates that whilst good microtexture may be sufficient to provide adequate friction at low speeds, good micro and macrotectures are necessary at higher speeds. Whilst all four surfaces decrease in skid resistance as speed increases, the decrease is not as rapid when the pavement surface has a rough macrotecture (Wilson, 2006).

1.6.2.2 Age of pavement surface

Traffic has a cumulative effect on a pavement; it wears the pavement surface and polishes the aggregates over time. The protruding aggregates are worn off and polished and the surface microtexture and macrotecture reduce under these forces. In addition, under the compacting effect of traffic, the protruding aggregates may be embedded in the pavement layer, which leads to a reduction in the depth of macrotecture. Accordingly, up to a 40% reduction in skid resistance as a result of pavement wear has been reported (Kokkalis et al., 2002).

The general trend for pavement skid resistance is that pavement surfaces attain their peak skid resistance condition after a few weeks of traffic action because of the wearing of the pavement surface. After that, skid resistance declines at a rapid rate at first, as the exposed aggregates are worn, and some microtexture and macrotecture properties are lost as traffic loads polish the surface aggregates in the wheel paths. Then, it declines more slowly and reaches an equilibrium state in which small deviations in skid resistance are experienced as long as traffic levels are constant and no structural deterioration has taken place (Rezaei, 2010). Figure 1.18 shows the variation of pavement skid resistance versus pavement age.

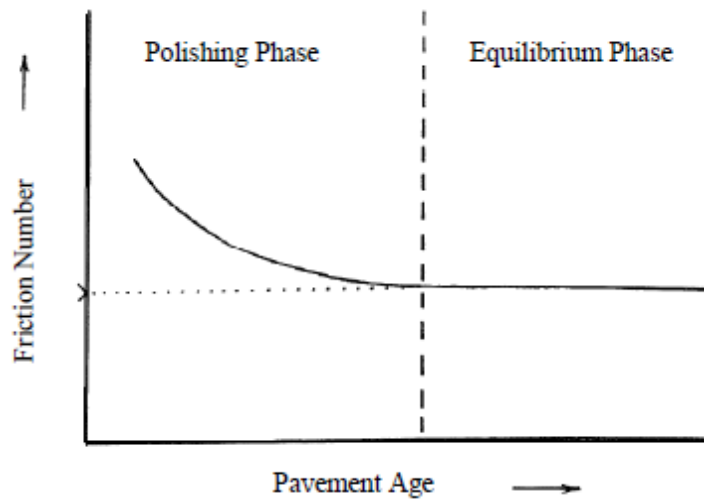


Figure 1.18 Schematic of skid resistance decrease due to polishing under traffic loading
(Skerritt, 1993)

1.6.3 Environmental factors

1.6.3.1 Temperature

As both tire rubber and bituminous materials are viscoelastic materials, it follows that these materials are sensitive to change in temperature due to the hysteretic component of surface friction, which will subsequently affect the skid resistance of the pavement surface (Wilson, 2006). As discussed by Jayawickrama and Thomas (1998), it is generally believed that, as the rubber temperature increases, the hysteresis losses in the rubber become less and the friction correspondingly reduces. There is some disagreement regarding the size of this effect over normal operating conditions. An Australian study by Oliver (1980) found that surfaces with high initial levels of skid resistance experienced the greatest decrease in the measured skid resistance with temperature. Furthermore, Oliver (1980) found that correction factors that had been developed in more temperate climates (such as in the cold countries) may not cover the range of normal operating temperatures experienced in more tropical and/or hot climates and therefore the correction factor applied to the raw test data may not be appropriate. A summary of the effect of temperature on the measured coefficient of surface friction primarily from Oliver (1980), Jayawickrama and Thomas (1981), Hill and Henry (1981) and Hosking (1992) is as follows:

- the measured coefficient of friction tends to decrease with increasing air temperature
- temperature change has more effect on the frictional properties of the tire, leading to an indirect effect on skid resistance as measured by testers and that is available to road users
- both air temperature and pavement surface temperature play a significant role in influencing the tire temperature and hence the skid resistance
- water temperature has negligible effect on measured coefficients of friction, and increased pavement temperatures lead to reduced coefficients of friction.

1.6.3.2 Water film

In dry conditions, clean surfaced roads have high skidding resistance because the vehicle tires can keep in good contact with the road surface. When a road surface transitions from dry to being slightly wet, there is a sharp reduction in the coefficient of friction due to the presence of the water film. This acts as a lubricant between the tire and road surface and furthermore reduces the contact area between the tire and the road, thereby reducing skid resistance (Wilson, 2006). As long ago as the 1930s, Bird and Scott (1936) proposed an idealized representation of the loss of skid resistance with time during a rain event from a dry surface to wet and then dry again (Figure 1.19).

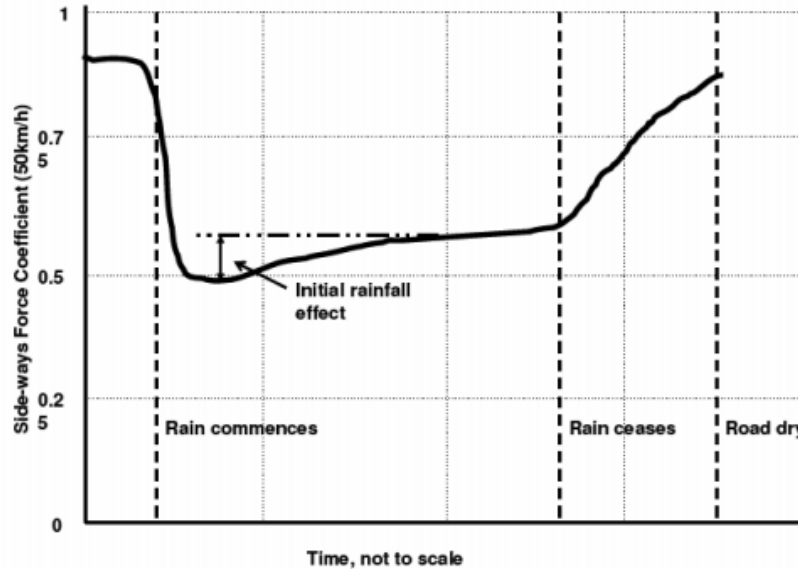


Figure 1.19 Skid Resistance variation during a rainfall event

(Bird and Scott, 1936 cross referenced from Wilson, 2006)

When rain intensity exceeds 0.1mm/hr, the water film formed may have a depth varying from microns to millimetres (Jellie, 2003). Harwood et al. (1989) reported that even as little as 0.025mm depth of water on the pavement can reduce the tire–pavement friction by as much as 75% on surfaces having poor skid resistance characteristics. Thin films of water have also been shown to be sufficient to produce hydroplaning. The micro drainage routes provided by the surface texture roughness (macrotexture) together with the tire tread help to eliminate the bulk of the water, an especially important requirement as speed increases. However, the penetration of the remaining water film can only be achieved if there are sufficient fine-scale sharp edges (microtexture) on which high pressures can build up as the tire passes. These high pressures are needed to break through the water film to establish dry contact between road and tire (Rogers & Gargett, 1991).

1.6.3.3 Seasonal variation effect on skid resistance

Weather-related factors (e.g. rainfall, air temperature, wind, etc.) can also be responsible for seasonal variations in the frictional properties of the tire-pavement interface. Past researchers (J.R. Hosking, 1976; R. Hosking, 1992; Rogers & Gargett, 1991; G F Salt, 1977; S.H. Dahir & Henry, 1979; Henry & Saito, 1983; Jayawickrama & Thomas, 1998; Rice, 1977) indicated that

the seasonal variation that is approximately sinusoidal with seasons of the year (see Figure 1.20). This variation has been found to be as high as 0.15 to 0.20 SFC between winter and summer months.

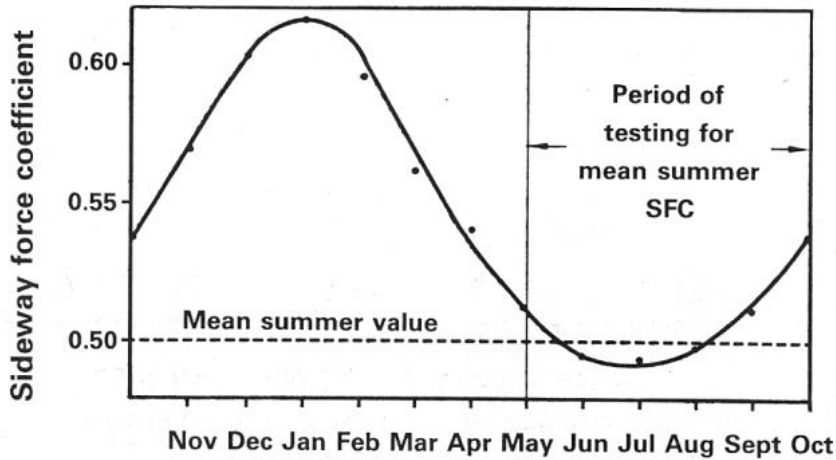


Figure 1.20 Measured seasonal variation of SFC with the reported Mean Summer SCRIM coefficient for the UK (Rogers and Gargett, 1991)

Friction measurements that were performed at the same pavement surface but in different seasons are depicted in Figure 1.21. It is obvious that summer months have the lowest levels of skid resistance.

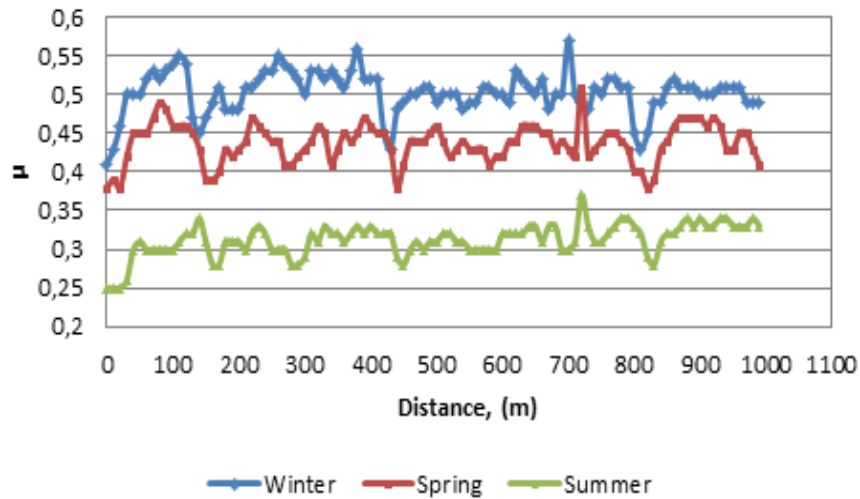


Figure 1.21 Comparison of friction measurements recorded in winter, spring and summer over the same surface (Skidsafe, 2011)

This can be attributed to the fact that during the summer months debris and rubber compounds are accumulated on the pavement surface blocking thus the pavement microtexture and clogging the drainage paths between the aggregates. In winter, rainwater rinses the accumulated debris and the

rubber compounds exposes the asperities of the aggregates and unclogs the drainage paths. As a result, the skid resistance increases.

1.7 Research objectives

From the above literature survey, it can be concluded that the tire rubber hysteresis plays an important role in counteracting the propensity for skidding for a vehicle travelling at high speed. Also, it was identified that the temperature development in the tire-pavement contact region results in a complex relationship between temperature and friction and renders unreliable the interpretation of friction data originating from friction measuring equipment.

The aim of this research is therefore the *development of a computational tool for the fundamental analysis of thermo-mechanical behaviour of a pneumatic tire over a real pavement textured surface*. Such a tool can greatly contribute to design guides for safe driving speed limits taking into account the in-time degradation of pavement skid resistance as a function of temperature, asphalt mix characteristics and tire operating characteristics. To achieve this aim, the mechanical, the energy dissipation and the heat flow phases contributing to the development of temperature in the tire body are identified and the controlling parameters are determined, an experimental framework to quantify these parameters is set-up and the numerical tools are developed and are demonstrated in this dissertation. The predictions of the developed FE model are validated by means of actual skid resistance tests.

Apart from the temperature, water is another important factor which decides the skid resistance for a given set of tire and pavement conditions. When large quantities of water accumulate on the pavement surface, due to an insufficient drainage of water and/or wear in the treads of the tire hydrodynamic forces are generated in front of the tire due to accumulation of water. These may cause loss of the contact between the two surfaces. This phenomenon is called hydroplaning. It is a particularly dangerous phenomenon as the tire is completely separated from the pavement by a continuous layer of water. The friction is then almost zero and the driver experiences severe difficulty with steering and braking.

The next objective of this research is to *further improvise the developed computational tool to simulate the skid resistance/hydroplaning phenomenon of a pneumatic tire traversing over a wet asphalt pavement surface*. Such a tool can provide valuable indicators to the highway agencies about the loss of friction or propensity to hydroplaning associated with in-service pavement surfaces under adverse weather conditions. In order to achieve this objective, the dry-contact algorithm developed in the previous stage is combined with a hydrodynamic algorithm capable of simulating the three-dimensional flow of water around the tyre-pavement finite element mesh. An efficient two-phase model was utilized for simulation of the free surface, the varying percentages of air to water in the flow domain. The computational model was calibrated against field wet skid resistance measurements, and then it was utilised for parametric analyses of the propensity to hydroplaning of several combinations of asphaltic materials and tire characteristics.

1.8 Thesis outline

The thesis consists of ten Chapters. In Chapter 1, after a general introduction to the tire-pavement friction phenomenon and its dependency on various parameters, an overview of the literature available on this subject was presented. Chapters 2 to 6 focus on various aspects of dry tire-asphalt pavement surface interaction aspects.

In Chapter 2, a three dimensional thermo-mechanical constitutive model for tread rubber is presented. The parameters of this model are calibrated via laboratory material tests conducted on tread rubber samples extracted from test tires. The material model is utilized in the three dimensional finite element simulations of the test tires.

Chapter 3 deals with the development of FE models of pneumatic tires which are capable to simulate the deformational characteristics of the tire under various inflation pressures and loading conditions. The tread rubber parameters obtained from the Chapter 2 were utilized. The calibration of the stiffness of all other materials was done on the basis of the results of static load-deflection tests. Next, the development of FE meshes of real asphalt pavement surfaces is described.

In Chapter 4, a staggered thermomechanical FE tire-pavement interaction algorithm is presented for the iterative determination of the effect of tire operating temperatures on hysteretic friction. Under this methodology, a pneumatic tire rolling at a specified slip ratio traverses over a textured pavement surface in a transient framework. By using the results of this step, energy dissipation rates are computed which serve as input to the subsequent heat flow analysis to determine the nodal temperatures in the various components of the tire. The rubber viscoelastic properties are changed according to the nodal temperatures obtained from the heat flow analysis. Pavement surface temperature, ambient air and contained air temperatures are input to the model. Finally, the mechanical module is invoked to calculate the hysteretic friction of the tire.

Chapter 5 presents the application of the developed algorithm for determination of the dependency of tire-pavement friction on various parameters like temperature of tire band, pavement surface temperature, ambient and contained air temperatures and operating conditions like slip ratio, speed, tire load and pavement surface texture characteristics. Results of analyses are shown, regarding the time required for a pneumatic tire traversing on an asphalt pavement surface to reach an effective equilibrated temperature state and, also, the time required to cool down after it is being stopped. The analyses provide insight into the thermal behavior of tires under different operating conditions and the resulting skid resistance behavior. Also this Chapter presents the application of the developed thermomechanical framework to analyze the influence of temperature on cornering friction. Under this analysis, the effect of tire load and inflation pressure, speed, sideslip angle and pavement surface macrotexture on the cornering hysteretic friction was determined. Such analyses give better insight into the inter-relationships between influencing factors and their combined effect on the lateral performance of a tire.

Availability of good braking traction and directional stability are two crucial factors for vehicles travelling in wet weather conditions. These issues become very critical when the pavement is highly flooded. Under such conditions, due to hydroplaning, there is no braking traction and steering control for the vehicle. Chapters 6 to 7 focus on various aspects of tire response under flooded pavement surface conditions.

Chapter 6 serves as a general introduction and a detailed literature survey on the ultimate loss of friction in terms of hydroplaning due to the presence of water in-between the tire-pavement contact area. This chapter also presents the numerical formulation of the hydrodynamic algorithm that was utilized in the subsequent finite element simulations of hydroplaning phenomena.

Chapter 7 the results of simulations performed on a standard smooth and a standard ribbed tire rolling/braking on a smooth-plane pavement surface under flooded pavement conditions. This scenario represents poor pavement surface texture conditions and is a conservative estimate of the hydroplaning for in-service pavements. The hydroplaning speed was simulated for full slip, no

slip and partial slip in the longitudinal direction. Furthermore, the hydroplaning speed was computed for different yaw angles of tire. This model serves as the basis for the next high scale modeling of a tire interacting with textured pavement surfaces in the presence of water. This Chapter also focuses on the simulation of tire-water-pavement interaction on various textured asphalt pavement surfaces to quantify the effects of macrotexture in the presence of thick water films and to demonstrate its contribution to reducing the risk of accidents. Parametric analyses of the developed numerical models results enabled the development of relations between asphalt mix design and safety against vehicle skidding.

Chapter 8 summarizes the main conclusions drawn in the current research and provides recommendations and directions for further research.

2 Determination of Rheological Properties of Rubber Materials

2.1 Introduction

When a tire rolls on a rough pavement surface, hysteretic deformations occur in the rubber body leading to energy dissipation in the form of heat. The energy loss is mainly due to the viscoelastic nature and the temperature dependency of the tire rubber material. Tire rubber exhibits aspects of both elastic and viscous behavior. Hence, it is necessary to model the tire rubber as a thermo-visco-elastic material. In this Chapter, a three dimensional thermo-mechanical constitutive model is presented for rubber. The parameters of this model were calibrated via laboratory material tests conducted on rubber samples extracted from test tires. The material model was utilized in three dimensional finite element simulations of test tires.

The rheological material characteristics are generally measured by frequency sweep tests (Karrabi et al. 2004). The test method that was adopted enables the quantification of rheological properties such as complex shear viscosity (η^*), elastic shear modulus (G') and viscous shear modulus (G'') of tire rubber on the basis of frequency sweep tests. The tests were carried out by using a Dynamic Shear Rheometer (DSR) apparatus. The complex modulus (G^*) was obtained at various temperatures and frequencies and from these results, using shift factors, the master curve was obtained. Details of the procedure will be discussed later in this Chapter.

2.2 Concepts of viscoelasticity

2.2.1 Terminology

Figure 2.1 indicates the common terminology used to describe the rheological parameters of viscoelastic materials (Dick 2003).

Elastic Torque (S'): It corresponds to the contribution of the elastic component of the rubber material and it is in-phase with the applied strain.

Viscous Torque (S''): It corresponds to the contribution of the viscous component of the rubber material and is out-of-phase with the applied strain. It represents the response of a dash pot.

Storage (Elastic) Modulus (G'): it is defined as

$$G' = \left[\left(S' / \text{Area} \right) / \text{Peak Strain} \right] \quad (2.1)$$

Loss (Viscous) Modulus (G''): it is defined as

$$G'' = \left[\left(S'' / \text{Area} \right) / \text{Peak Strain} \right] \quad (2.2)$$

Complex modulus (G^*): it is defined in complex space as

$$G^* = G' + iG'' \quad (2.3)$$

and its magnitude as

$$\|G^*\| = \sqrt{(G')^2 + (G'')^2} \quad (2.4)$$

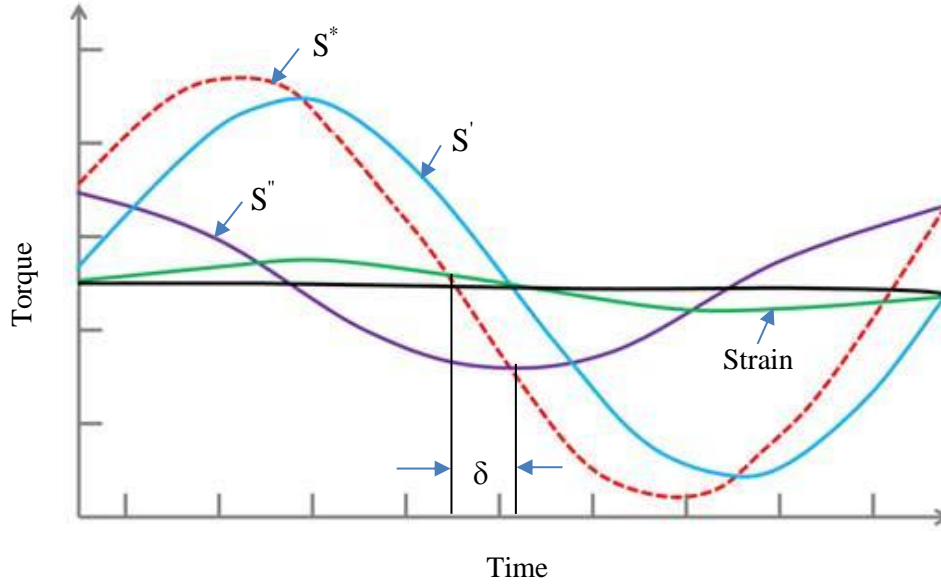


Figure 2.1 Application of sinusoidal torque: Splitting complex torque (S^*) into elastic (S') and viscous (S'') components

The complex modulus is a measure of the stiffness of the material in the frequency domain. The relative magnitude of the loss modulus (G'') versus that of the storage modulus (G') determines the material response. For instance, materials with higher storage moduli can recover from deformation, and materials with higher loss moduli have greater ability to dissipate energy.

The phase angle (δ) dictates the degree of elasticity and viscosity of the material under the test conditions. It can be interpreted, physically, as the time lag between the measured shear stresses and the applied strains and it can be expressed as

$$\delta = \tan^{-1}(G''/G') \quad (2.5)$$

It also holds that

$$\begin{aligned} G'(\omega) &= G^*(\omega) \cos(\delta(\omega)) \\ G''(\omega) &= G^*(\omega) \sin(\delta(\omega)) \end{aligned} \quad (2.6)$$

Dynamic Viscosities (η' , η'' , η^*): they are defined as

$$\text{Real Dynamic Viscosity} = \eta' = G''/\omega \quad (2.7)$$

$$\text{Imaginary Dynamic Viscosity} = \eta'' = G' / \omega \quad (2.8)$$

$$\text{Complex Dynamic Viscosity} = |\eta^*| = \sqrt{(\eta')^2 + (\eta'')^2} \quad (2.9)$$

where ω = frequency of sinusoidal oscillation in radians/second.

For a rubber material, at low frequencies, the dynamic modulus is low but as the frequency increases, the compound becomes increasingly stiff until it attains a glass like behaviour. This transition reflects the change from the unrestrained response of molecular segments when stresses are applied at low frequency, to their complete inability to move under high-frequency stresses.

Rubber response to excitation is mainly due to the Brownian movement of globular rubber particles. The rate (φ) of Brownian motion of globular rubber particles depends only on the internal viscosity and hence only on the temperature. As shown in Figure 2.2, below a certain temperature, known as the glass transition temperature T_g , the material is glassy, above T_g it is viscous. The dependence of φ upon temperature, or more precisely, upon the temperature difference $T - T_g$, follows from a characteristic law:

$$\log \left[\left(\frac{\varphi(T)}{\varphi(T_g)} \right) \right] = \frac{A(T - T_g)}{B + T - T_g} \quad (2.10)$$

in which A and B are constants.

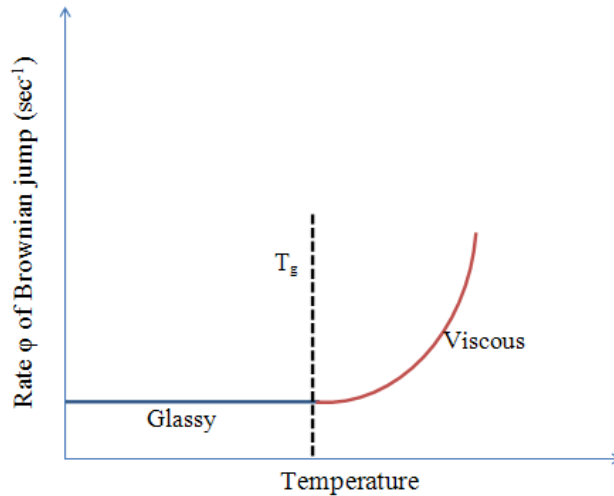


Figure 2.2 Rate φ of Brownian jump vs. temperature

2.2.2 DSR test

The rheological properties of a tire rubber can be determined by using the Dynamic Shear Rheometer (DSR). Under this test, a disk shaped sample of rubber is placed in the gap between the plates of DSR, Figure 2.3. The lower plate is fixed while the upper plate oscillates sinusoidally in torsion over a range of frequencies. The test can be conducted at temperatures

ranging from -20°C to +170°C. From these tests, the relation between critical stress and frequency can be obtained. G^* , G' , G'' and η^* can be measured as functions of the stress for each frequency.

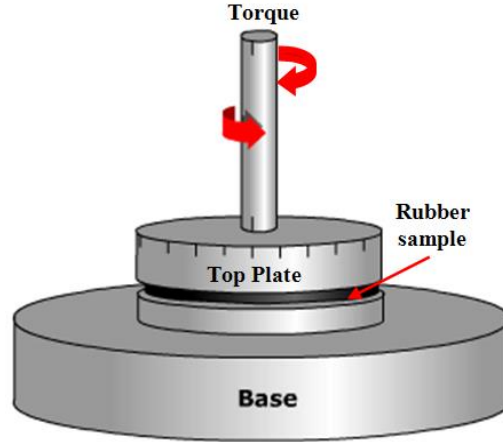


Figure 2.3 Schematic diagram of DSR test on a rubber sample

2.2.3 Master curve construction

For a full understanding of material response, availability of stiffness and phase angle values in a wide range of temperatures and frequencies is important. However, it is not practical to perform tests over the entire temperature and frequency ranges. Stiffness and phase angle values representing a broader range of temperatures and frequencies can be obtained by making use of the equivalency principle between frequency and temperature suggested by Williams-Landel-Ferry (WLF) and expressed as

$$\log[(a_t)] = \frac{A(T - T_0)}{(B + T - T_0)} \quad (2.11)$$

where A and B are constants, T is the measurement temperature (K), T_0 is the reference temperature to which the data is shifted (K) and a_t is the shift factor value.

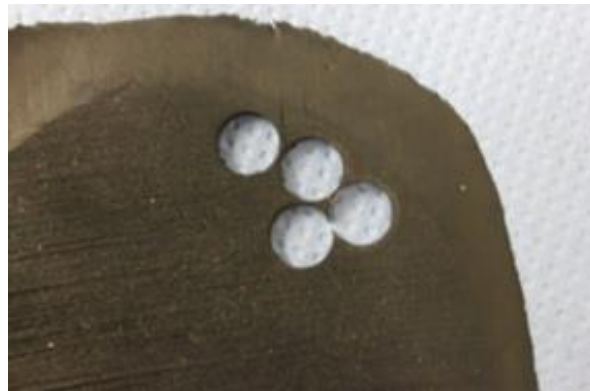
By means of the WLF equation, data at various temperatures can be shifted with respect to frequency until the curves merge into a single smooth function which is commonly known as master curve. The master curve as a function of frequency, formed in this manner, describes the frequency (time) dependency of the material. The amount of shifting at each temperature required to form the master curve describes the temperature dependency of the material.

2.3 Laboratory DSR test results

A rubber sample of uniform thickness from a PIARC 165 R15 (PIARC, 2004) test tire was sliced using a water jet as shown in Figure 2.4(a). From this sliced part, uniform cylindrical samples were chopped off as shown Figure 2.4(b). The thickness of the cylinder was 2.45 mm and the diameter of cylinder was 8.0 mm as shown in Figure 2.5(a) and Figure 2.5(b).

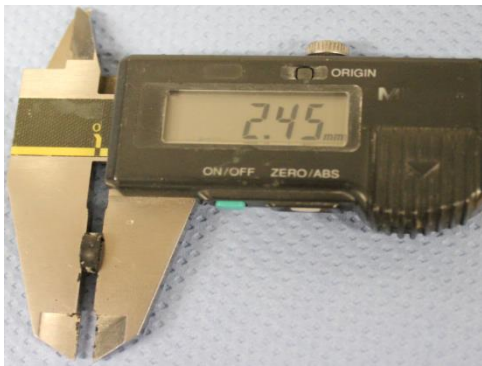


(a) Rubber sample sliced using water jet



(b) Cylindrical sample preparation for the test

Figure 2.4 SBR sample preparation for DSR test



(a) Thickness of sample (mm)



(b) Diameter of sample (mm)

Figure 2.5 Dimensions of SBR sample required for DSR test

The prepared sample was then placed between the two plates as shown in Figure 2.6.

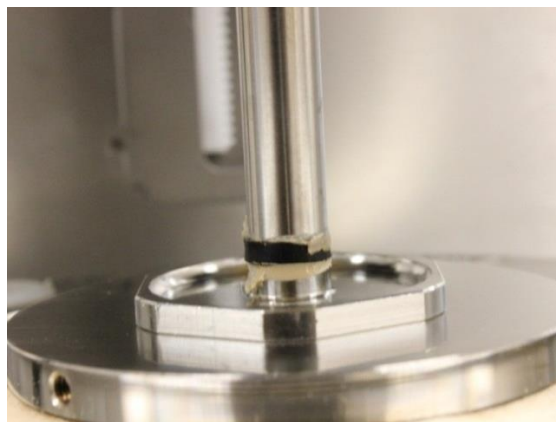


Figure 2.6 Rubber sample placed between two plates of DSR

The desired torque was applied at constant rate of rotation and up to a maximum angle of 25°. The torque response of the samples at frequencies of 0.01 to 50 Hz and at temperatures from -20°C to 170°C in 10°C increments was obtained. DSR test results i.e. complex modulus (G^*) and phase angle ($\tan\delta$) are plotted in Figure 2.7 and Figure 2.8 for various temperatures and frequencies.

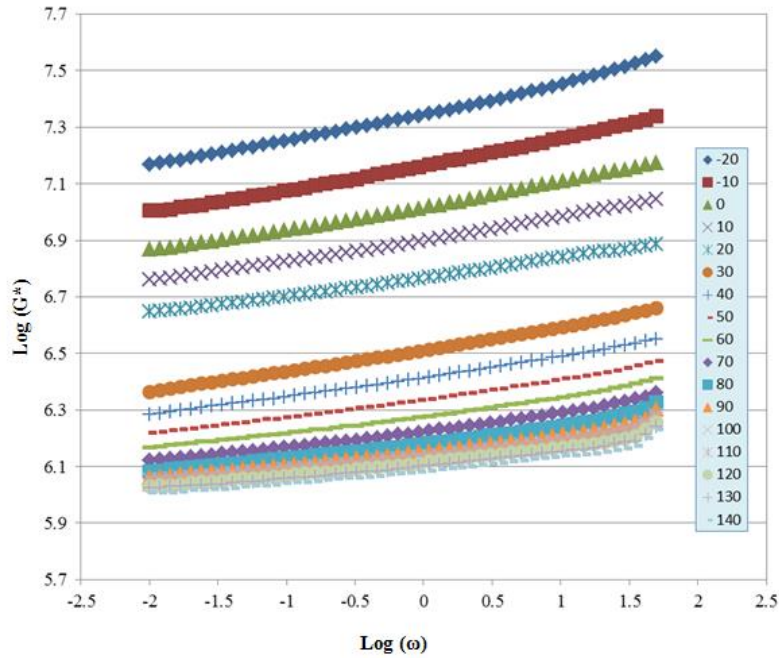


Figure 2.7 Complex modulus against frequencies at various temperatures

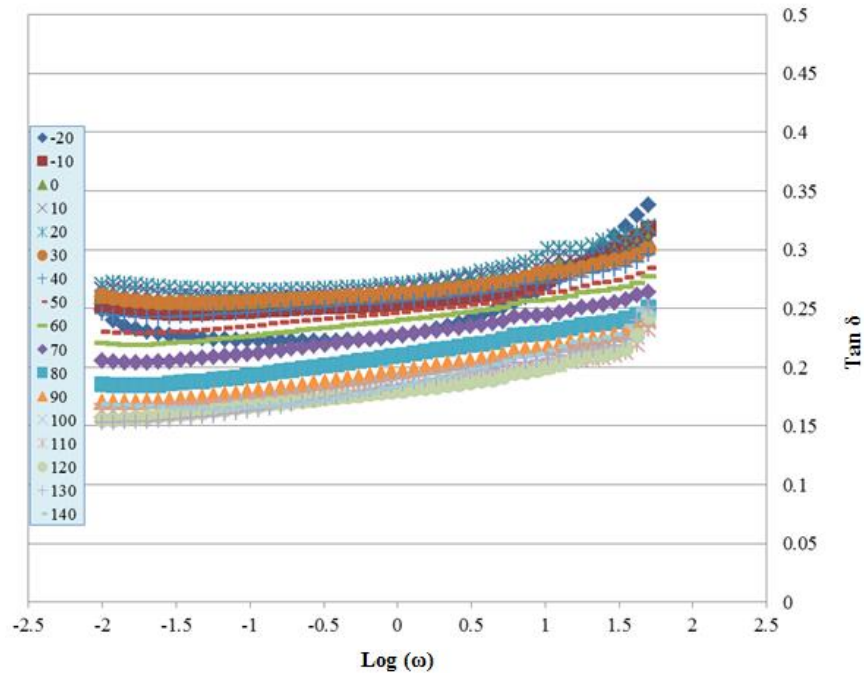


Figure 2.8 Phase angle against frequencies at various temperatures

It was observed that beyond the temperature of 140° C, the results are chaotic. Therefore, the test results are not acceptable beyond 140°C. The master curve and the $(\tan\delta)$ curve are obtained using Eq. (2.11) and are shown in Figure 2.9 for a reference temperature of 30° C. The corresponding shift factor is shown in Figure 2.10.

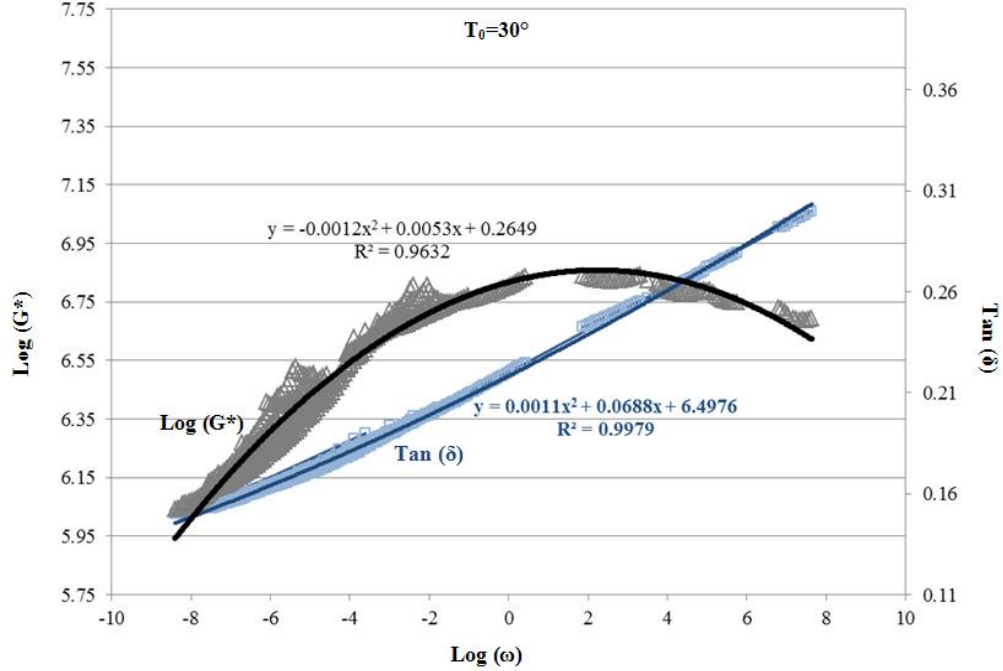


Figure 2.9 Master curve for G^* vs. frequency in a log-log scale for PIARC rubber

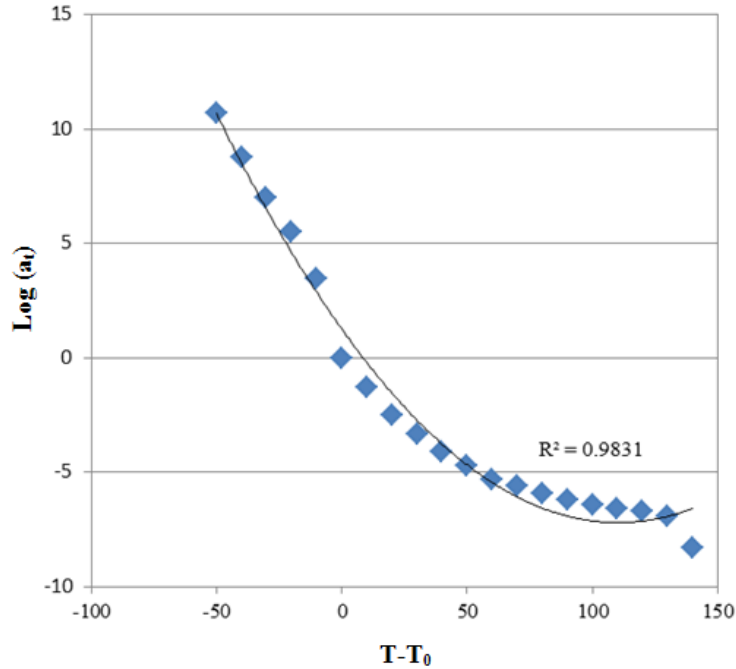


Figure 2.10 Shift curve at 30°C reference temperature for PIARC rubber

2.4 Visco-elastic parameter determination procedure

Creep and relaxation tests are most commonly used to determine the viscoelastic material properties. The stress in linear viscoelastic materials is given by the following constitutive equation which is based on the Boltzman's superposition principle:

$$\sigma(t) = \int_0^t G_{rel}(t - \tau) \frac{d\varepsilon(\tau)}{d\tau} d\tau \quad (2.12)$$

where ε is the strain tensor and $G_{rel}(t)$ is the linear relaxation (shear) modulus also known as the relaxation kernel (Schapery, 2000).

Figure 2.11 shows a schematic of the generalized Zener model which consists of a spring and 'm' Maxwell elements connected in parallel. The relaxation modulus of this model is given by

$$G_{rel} = G_{\infty} + \sum_{k=1}^m G_k \exp(-t / \rho_k) \quad (2.13)$$

where G_{∞} is the shear modulus of the single spring and G_k and ρ_k are respectively the moduli and relaxation times associated with the springs in the m viscoelastic components.

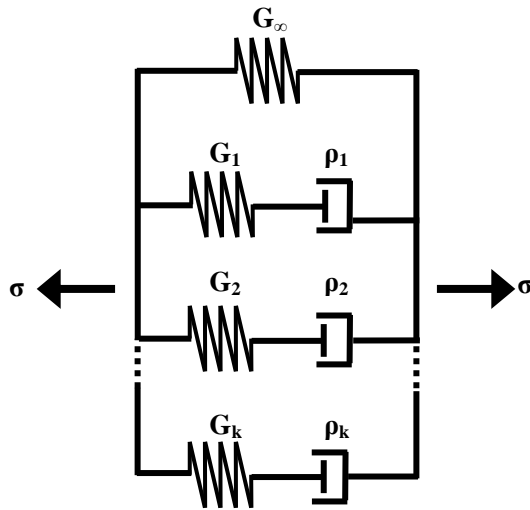


Figure 2.11. Generalized Maxwell model

The deformation history of a viscoelastic material, under an arbitrary loading, influences its stress-strain response. The load (stress) and displacement (strain) history, the loading rate (displacement rate) and time of load application on the specimen are all needed to determine the constants in the constitutive Eq. (2.13). Prony proposed a method for interpolating a sum of exponential functions through a series of data values at equally spaced points by solving a system of linear equations for the coefficients of a difference equation satisfied by the exponential functions.

The exponential expression in Equation (2.13) can be written in its complex form as:

$$\begin{aligned}\exp(-t/\rho_k) &= \exp(i^2 t/\rho_k) \\ &= \exp(i(it/\rho_k)) = \cos(it/\rho_k) + i\sin(it/\rho_k)\end{aligned}\quad (2.14)$$

This expression will be Carson transformed. The Carson's transform L_C is directly related to the Laplace transform L as:

$$L_C(f(t)) = s \cdot L(f(t)) \Big|_{s=i\omega} = s \cdot \int_0^{\infty} f(t) \exp(-st) dt \Big|_{s=i\omega} \quad (2.15)$$

The Carson's transform of the cosine component is computed as:

$$\begin{aligned}L_C(\cos(it/\rho_k)) &= s \cdot L(\cos(it/\rho_k)) \Big|_{s=i\omega} = s \cdot \left(\frac{s}{s^2 + (i/\rho_k)^2} \right) \Big|_{s=i\omega} \\ &= \frac{(i\omega)^2}{(i\omega)^2 + (i/\rho_k)^2} = \frac{-\omega^2}{-\omega^2 - (1/\rho_k)^2} = \frac{\omega^2 \rho_k^2}{\omega^2 \rho_k^2 + 1}\end{aligned}\quad (2.16)$$

Similarly the Carson's transform of the sine component can be calculated:

$$\begin{aligned}L_C(\sin(it/\rho_k)) &= s \cdot L(\sin(it/\rho_k)) \Big|_{s=i\omega} = s \cdot \left(\frac{i/\rho_k}{s^2 + (i/\rho_k)^2} \right) \Big|_{s=i\omega} \\ &= \frac{-(\omega/\rho_k)}{(i\omega)^2 + (i/\rho_k)^2} = \frac{-(\omega/\rho_k)}{-\omega^2 - (1/\rho_k)^2} = \frac{\omega \rho_k}{\omega^2 \rho_k^2 + 1}\end{aligned}\quad (2.17)$$

Therefore Carson's transform of the relaxation shear modulus G is defined as:

$$G = G_\infty + \sum_{k=1}^m G_k \exp(-t/\rho_k) = G_\infty + \sum_{k=1}^m \frac{\omega^2 \rho_k^2 G_k}{\omega^2 \rho_k^2 + 1} + i \sum_{k=1}^m \frac{\omega \rho_k G_k}{\omega^2 \rho_k^2 + 1} \quad (2.18)$$

A methodology was followed for back-calculation of parameters G_k and ρ_k of the generalized Zener model using a sequence of constraint optimization procedures. It is based on a nonlinear least squares approach that minimizes the difference between the predicted and the experimental parameter values. The coefficients G_k and relaxation times ρ_k were considered to be all positive.

It should be noticed that when a local optimization technique is applied to minimize the error, the problem may reach either to a wrong local minimum or to negative parameters. To overcome this problem, it has been suggested by past researchers (Bower and Gant, 1994) that the starting parameter set should be close to the global optimal set. However, in the present study, this would not be possible since the starting parameter set was not known beforehand. Thus a new methodology has been utilized to obtain the Prony constants as shown in Figure 2.12.

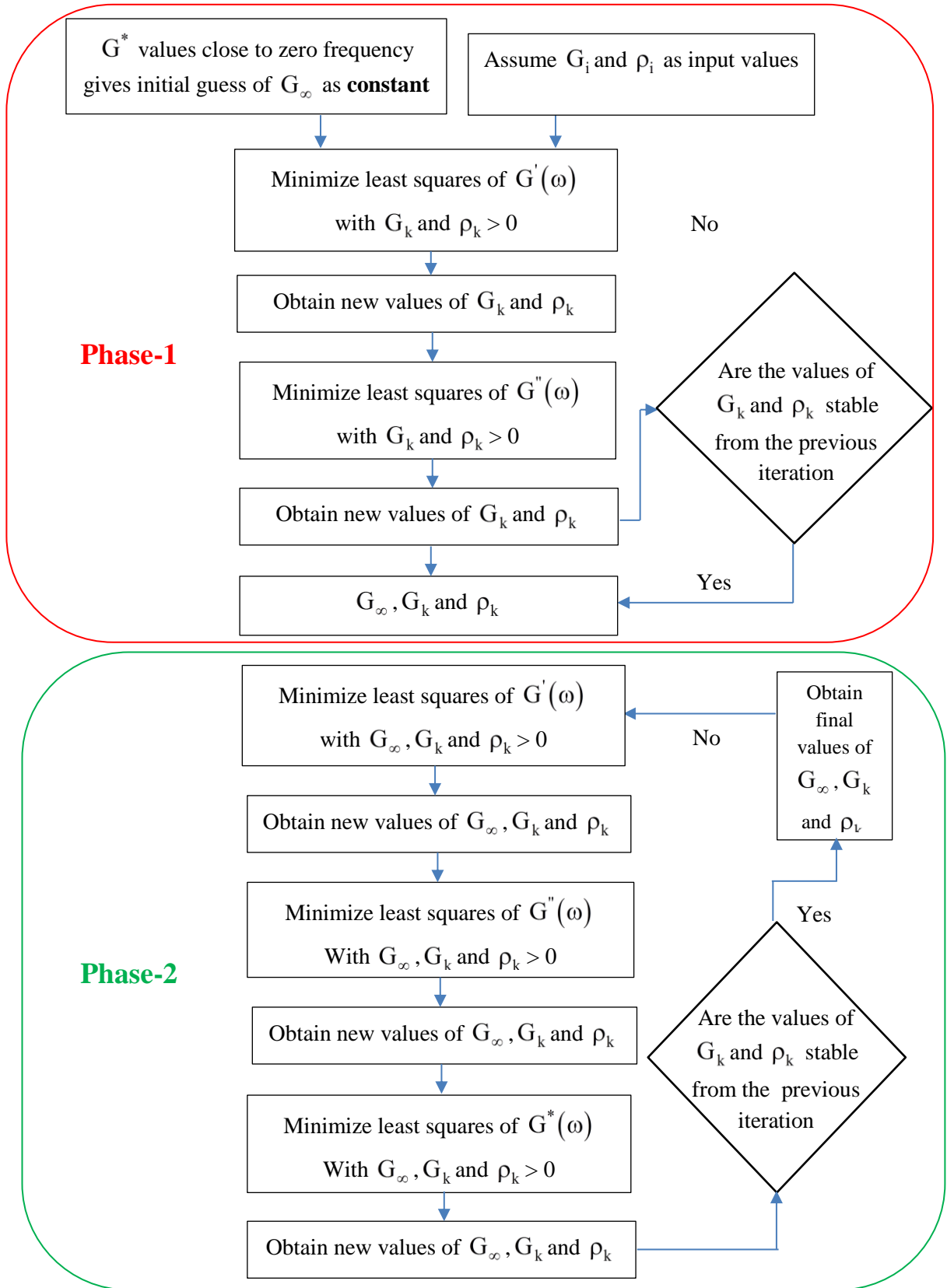


Figure 2.12 Developed algorithm to calculate Prony's constants

The proposed methodology was divided into two phases:

In the first phase, an initial guess of G_∞ was obtained using data set close to zero frequency. Approximately, 10% of the total experimental data of G^* data was utilized for the estimation of initial guess of G_∞ . The procedure to determine the value of G^* at zero angular frequency was demonstrated in Appendix-2.1.

The function in Eq. (2.19) was minimized on the variables G_∞, G_∞ and G^* according to the constraint optimization procedure demonstrated in Appendix-2.2.

$$\min_{g, \rho \in \mathbb{R}^N} F(G_k, \rho_k, G_\infty) \equiv \sum_{k=1}^M \left(\frac{(G'(\omega_k))}{G_k'} - 1 \right)^2 \quad (2.19)$$

With the new values of G_∞ and G^* , the minimization process was repeated for the following equation

$$\min_{g, \rho \in \mathbb{R}^N} K(G_k, \rho_k, G_\infty) \equiv \sum_{k=1}^M \left(\frac{(G''(\omega_k))}{G_k''} - 1 \right)^2 \quad (2.20)$$

This procedure using the equations (2.19) and (2.20) was repeated until a stable set of G_k and ρ_k was reached.

In the second phase, the same minimization procedure as described in the first phase was followed except that the value of G_∞ was also allowed to vary along with G_k and ρ_k . The first minimization step using the Eq. (2.19) produces the values of G_∞, G_k and ρ_k which approximately defines the shape of the G' vs. frequency curve shown in Figure 2.13.

The second minimization step using the Eq. (2.20) defines the shift of the G'' vs. frequency curve as shown in Figure 2.14 and also partially correcting the shape of the curve as shown in Figure 2.13.

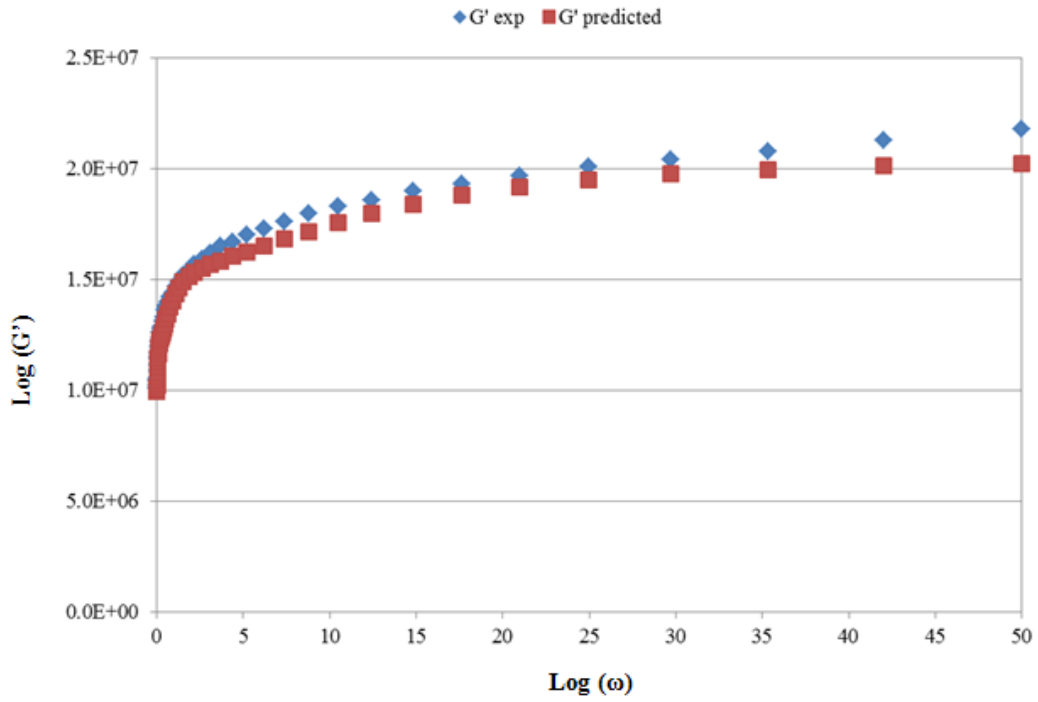


Figure 2.13 Typical comparison of experimental and estimated Storage modulus (G') vs. frequency in Log-Log scale

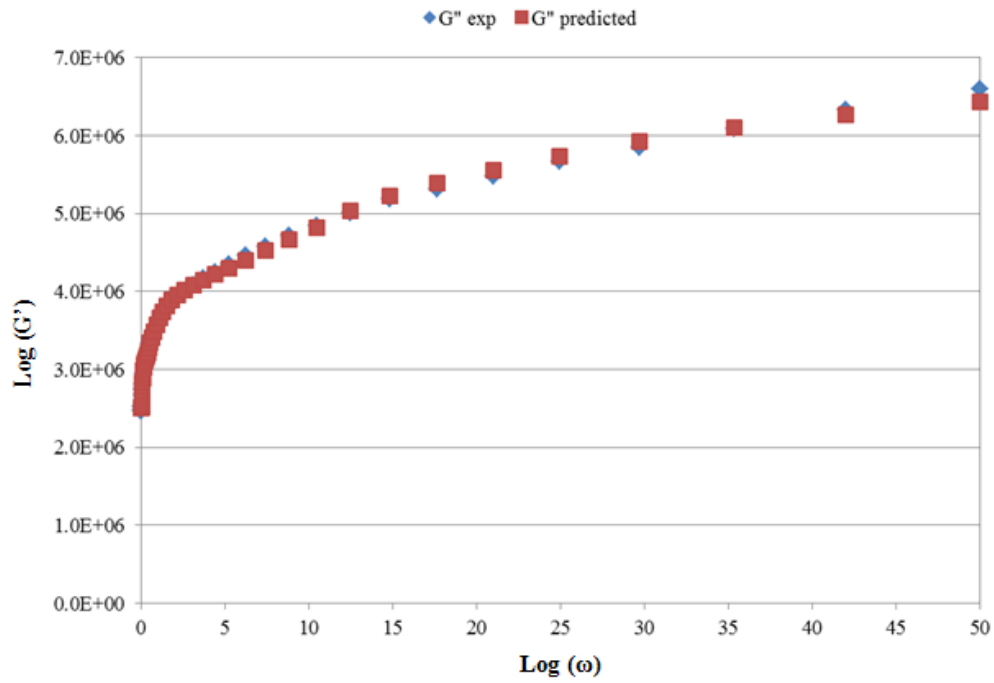


Figure 2.14 Typical comparison of experimental and estimated Loss modulus (G'') vs. frequency in Log-Log scale

Since, the lab test results are based on G^* values, the final minimization was carried out with G^* against G^* , G_k and ρ_k as variables using the following equation

$$\min_{g, \rho \in \mathbb{R}^N} L(G_k, \rho_k, G_\infty) \equiv \sum_{k=1}^M \left(\frac{G^*(\omega_k)}{G_k} - 1 \right)^2 \quad (2.21)$$

A typical comparison between the experimental and estimated G^* values against the frequency is shown in the Figure 2.15. Throughout this procedure, a balance between complex modulus and phase angle was maintained to fit the curve.

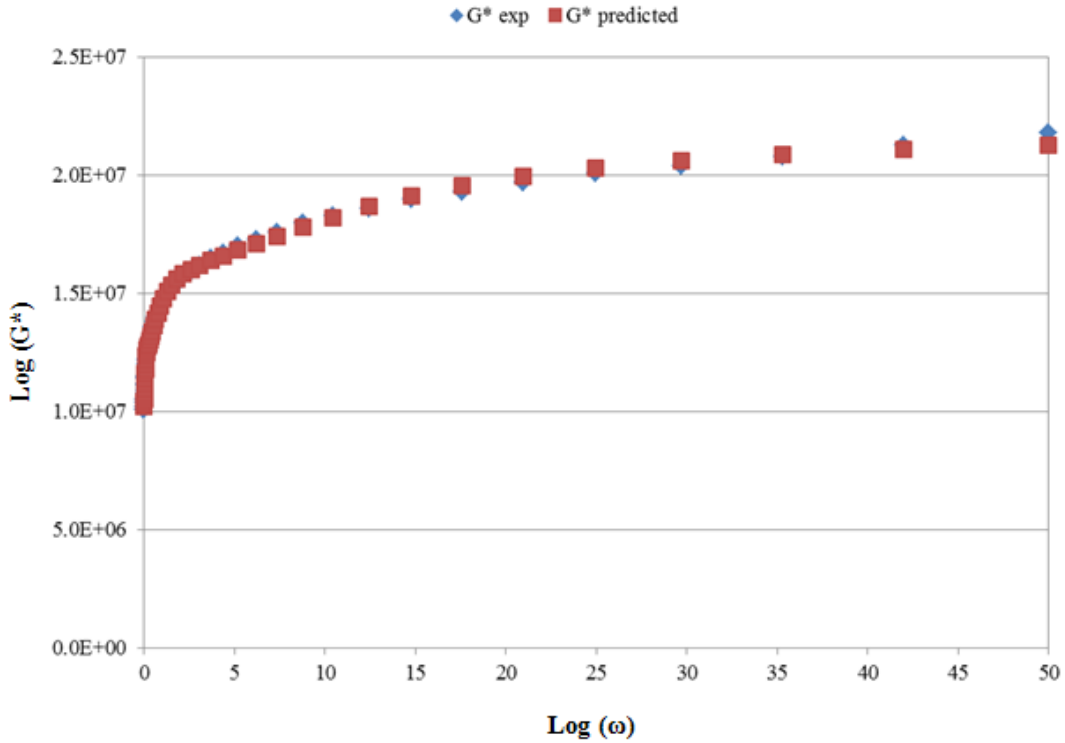
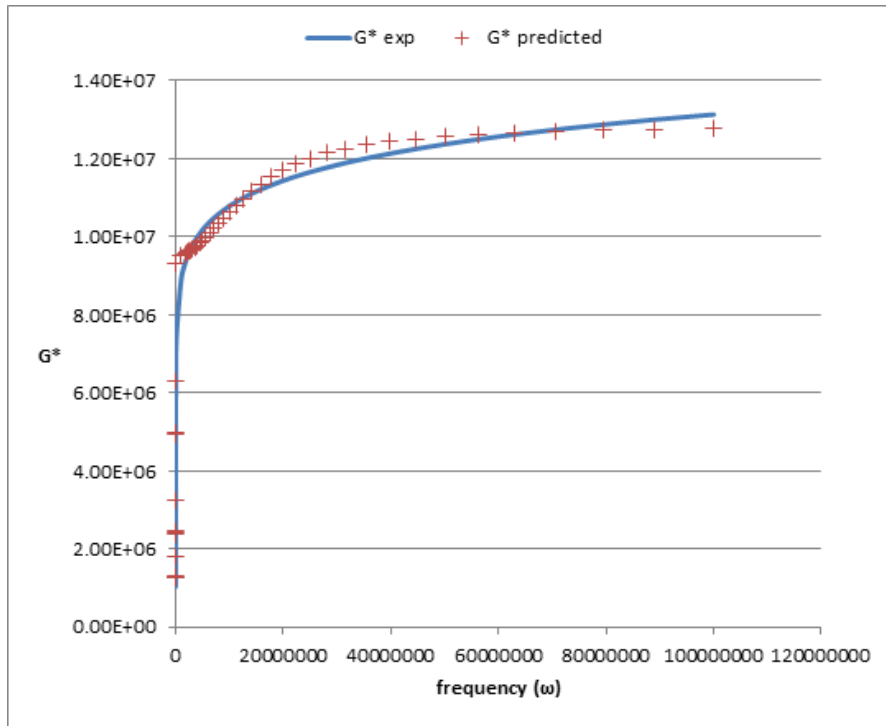


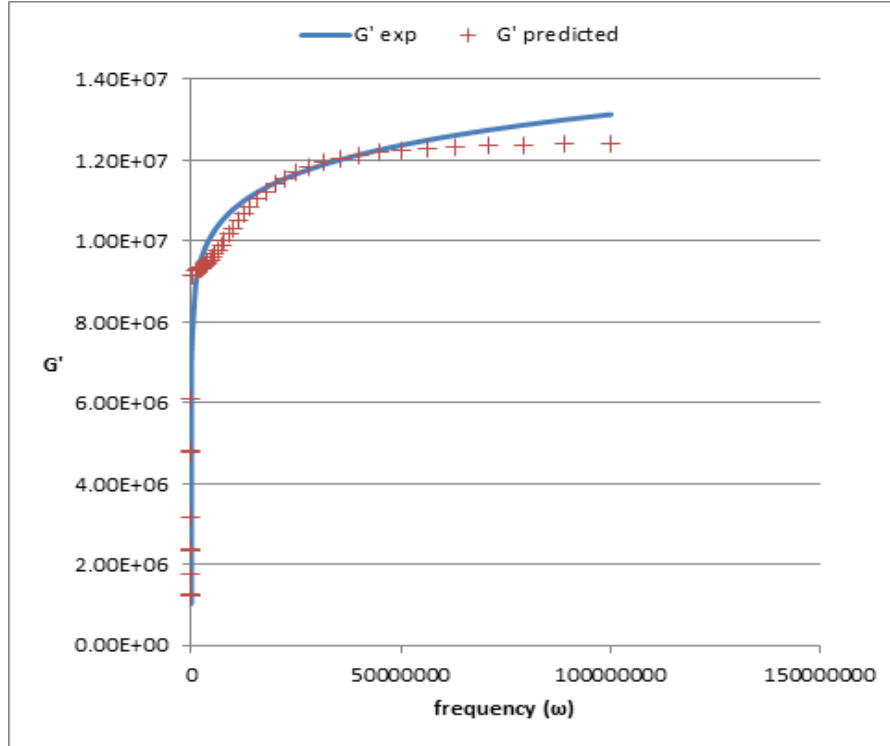
Figure 2.15 Typical comparison of experimental and estimated Complex shear modulus (G^*) vs. frequency in Log-Log scale

Also, a balance among G' , G'' and G^* was maintained (see Figure 2.16a to Figure 2.16c), as contrary to the previous methods where only one of these parameters are selected to fit the curve. The detailed minimization procedure can be found in Appendix-2.3.

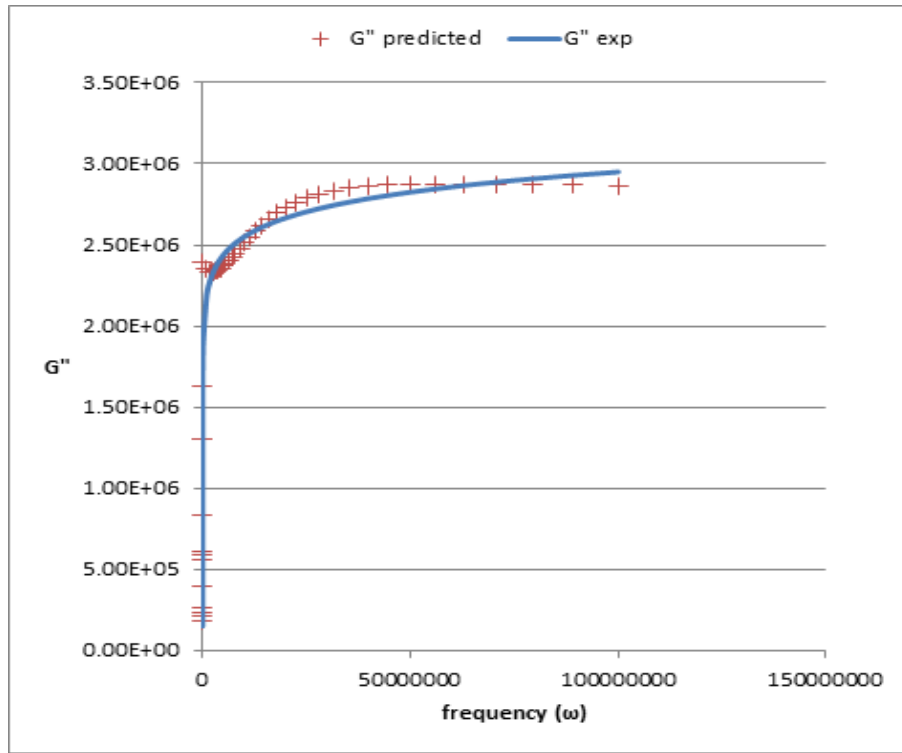
DETERMINATION OF RHEOLOGICAL PROPERTIES OF RUBBER MATERIALS



(a) Complex shear modulus (G^*) vs. frequency in Log-Log scale



(b) Elastic shear modulus (G') vs. frequency in Log-Log scale



(c) Loss shear modulus (G'') vs. frequency in Log-Log scale

Figure 2.16 Typical comparison of a set of G'' , G' and G^* with experimental data and estimated Prony's Constants of master curve

Figure 2.15a to Figure 2.15c shows the values of G^* , G' and G'' estimated from the experimental investigation and obtained by Prony's coefficients for a frequency range 0 Hz to 50 Hz C and Figure 2.16 (master curve) shows the values of G^* , G' and G'' for a frequency range of 0 Hz to 120000000 Hz respectively. Table 2.1 presents the Prony's coefficients obtained for the rubber material using the above mentioned approach.

Table 2.1 Prony's constants for PIARC tire by using DSR test

	G_k	τ_k
	4742623	1.74E-06
	2814458	0.005098
	1365902	17.55506
	105709	279605.4
G_{∞}	1.17E+06	

2.5 Summary

This Chapter discussed a procedure to obtain the rheological properties of a tire tread rubber. Under this procedure, first, laboratory material tests were performed on the rubber samples extracted from a test tire for a range of frequencies and temperatures. Subsequently, an iterative algorithm was developed and calibrated with the laboratory test results. The developed algorithm reproduces the viscoelastic properties of tire rubber in the form of Prony's coefficients. The resulting Prony's coefficients are incorporated into the tire part of thermo-mechanical tire-pavement interaction model.

In the next Chapter, laboratory loading tests are performed to ascertain the stiffness characteristics and foot print areas of a test tire which is used to calibrate the FE tire foot print of the simulation model. Results from Chapters 2 and 3 are used in the development of a 3-D numerical model to determine the hysteretic friction vs. temperature rise in a PIARC test tire under full/partial skidding conditions.

3 FE Modelling of Pneumatic Tires and Pavement Surfaces

3.1 Introduction

Modern passenger car tires are structurally complex, consisting of layers of belts, plies, and bead steel embedded in rubber. For simulation of tire-pavement interaction and in particular for computation of the effects of different factors, for example, temperature or water on frictional performance, such level of complexity is necessary to be included in the simulation.

In this Chapter, a procedure is presented for the three dimensional finite element (3D FE) simulation of tires. The FE models include all tire components like treads, carcass, plies, bead etc. Initially, a two dimensional (2D) mesh of the tire cross section is generated. Once available, it is constrained to the rim and inflation pressure is applied. Then, a three-dimensional tire FE mesh is generated by revolving the previously generated 2D mesh.

The calibration of FE tire models in terms of deflections, footprints and contact pressure distributions was conducted by static load-deflection tests under prescribed loading conditions. Under these tests, the tire was tested experimentally for a range of loads and inflation pressures and deflections were measured at various regions of tire. Also, tire footprints were obtained for various combinations of loads and inflation pressures.

The surface texture of the pavement plays a very important role in deriving the frictional properties at the tire-pavement interface. Particularly, the hysteretic friction due to viscoelastic deformations of tire rubber depends mainly on the pavement surface texture. In this study, the effect of micromechanical pavement surface morphology on tire-pavement friction was brought in by rolling the FE tire model on a FE mesh of an actual asphalt surface. The asphalt surface morphologies of these mixes were captured by using an X-ray tomographer. On the basis of the X-ray images, micromechanical FE meshes for SMA, UTS and PA pavements were developed by means of the SimpleWare software (2011).

These asphalt surface meshes and the calibrated FE tire model shall be integrated into a thermo-mechanical tire-pavement interaction model for determination of temperature development in the tire body and its influence on skid resistance.

3.2 Laboratory static load-deflection tests

The aim of these tests were to determine the stiffness characteristics of the PIARC smooth tire. The test set up was established at the research laboratory of Ooms Avenhorn Groep, in The Netherlands. The experiments were performed on the PIARC test tire under a wide range of inflation pressures and vertical loads to determine:

- normal and lateral stiffness properties of the side walls of the tire,
- deformation of tire
- length and width of tire footprint, and
- contact pressure distribution of tire footprint.

3.2.1 PIARC test tire

The PIARC test tires are made of SBR 1712 vulcanized rubber. The test tire was a PIARC 165R15 tubeless smooth tire as shown in Figure 3.1.



Figure 3.1 PIARC 165R15 smooth tire

The tire is of radial construction, constructed with cap (tread) over the sidewall with single-ply sidewall (polyester) and a three-ply tread (1 polyester and 2 steel belt). The tread width of the tire is 160 mm \pm 4 mm and the cross-sectional tread radius is 646 mm (\pm 1%). The tire has a nominal cross-section width of 167 mm and a nominal outside diameter of 646 mm (\pm 1%) when mounted on a 4 ½ x 15 rim. The cured cord angles are positioned at 90° \pm 2° for the carcass and 21° \pm 2° for the belts (PIARC, 2004). The cross section details of the tests tire are shown in Figure 3.2.

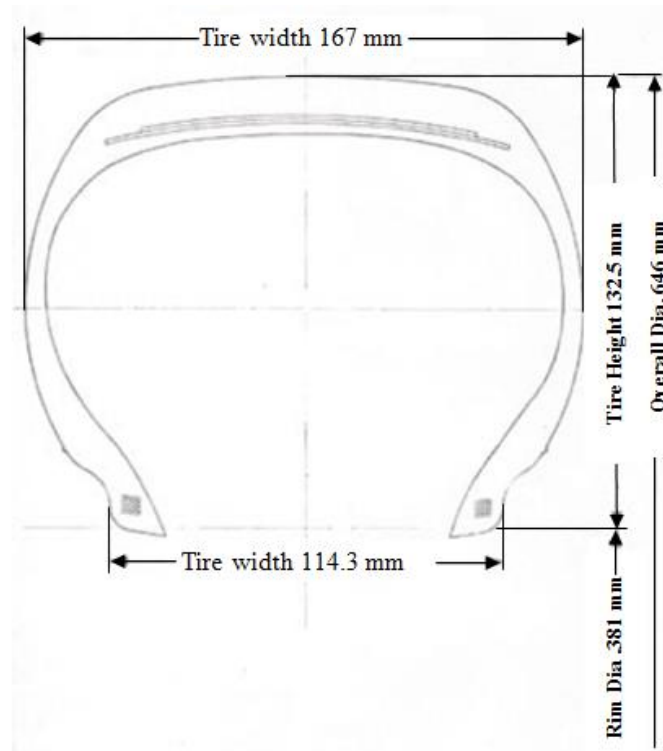


Figure 3.2. Cross section details of PIARC 165R15 smooth tire before inflation

3.2.2 Wheel load test facility

For all the tests an MTS servo-hydraulic test system was used. Figure 3.3 gives an illustration of the wheel load test set up. The test tire was mounted in between two smooth loading platens of the test machine and loaded along the vertical direction at various inflation pressures. Fuji pressure sensitive films were placed in between the tire surface and the smooth platens to acquire tread imprints and contact pressure distributions.

In Figure 3.3, the set-up of LVDTs and Extensometers of the measuring system is shown. LVDT 1 was mounted on the tread portion of the tire to measure the horizontal deformation of tread along its center line. LVDT 2 was mounted to measure the deformation of sidewalls. Extensometers 1 and 2 provide information about tread elongations along tread width and periphery directions.

The test tire was loaded by vertical load control under a desired vertical load level. The forces were measured by means of the MTS data acquisition system.

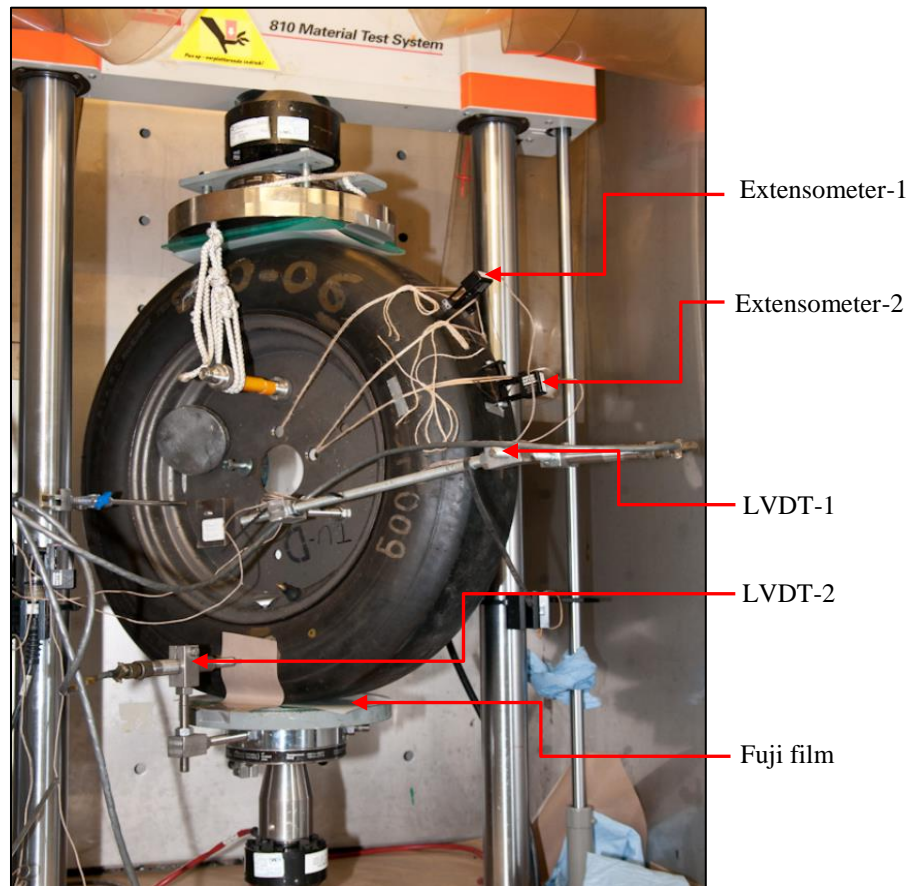


Figure 3.3. Tire load test

3.2.3 Load-deflection tests

Load-deflection data was measured at inflation pressures of 150, 180, 200 and 240 kPa. For inflation pressures of 200 kPa and 240 kPa, the applied load ranged from 1000 N to 4000 N at an increment of 1000 N. For inflation pressures of 150 and 180 kPa, the applied load ranged from

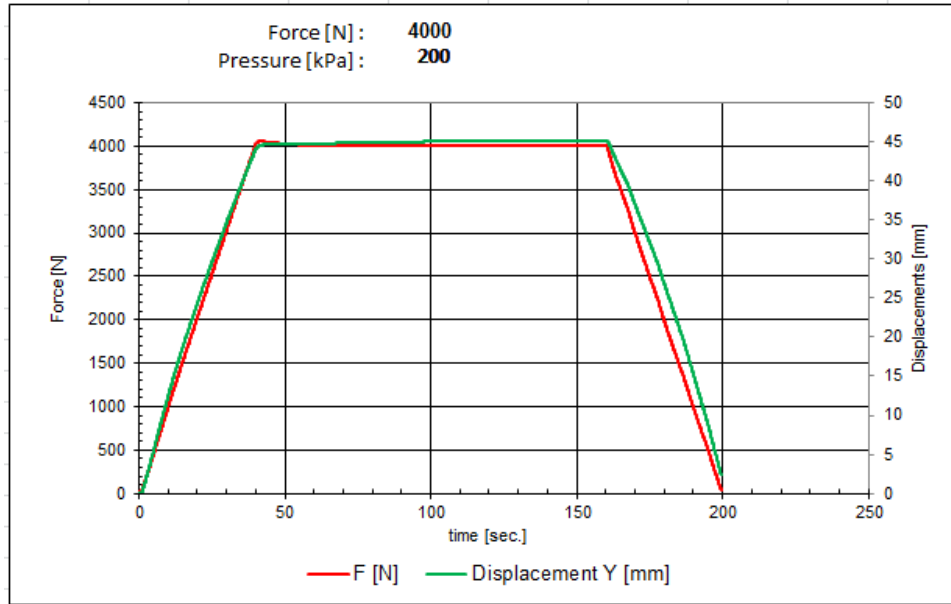
750 N to 3000 N at an increment of 750 N. This variation was due to the standards prescribed for PIARC (2004) smooth tires, which states that the allowable load should not be greater than 3600 N for inflation pressures less than 200 kPa.

The unloaded radius (UR) of the tire was determined from the circumference of the tire. As load was applied to the tire, the deflection δ was measured and the static load radius was calculated as the difference between the UR and δ . The axle height corresponding to a given load level was measured as well. This process was repeated for each test load under a particular inflation pressure. Figure 3.4 shows the deflection of the loaded tire.

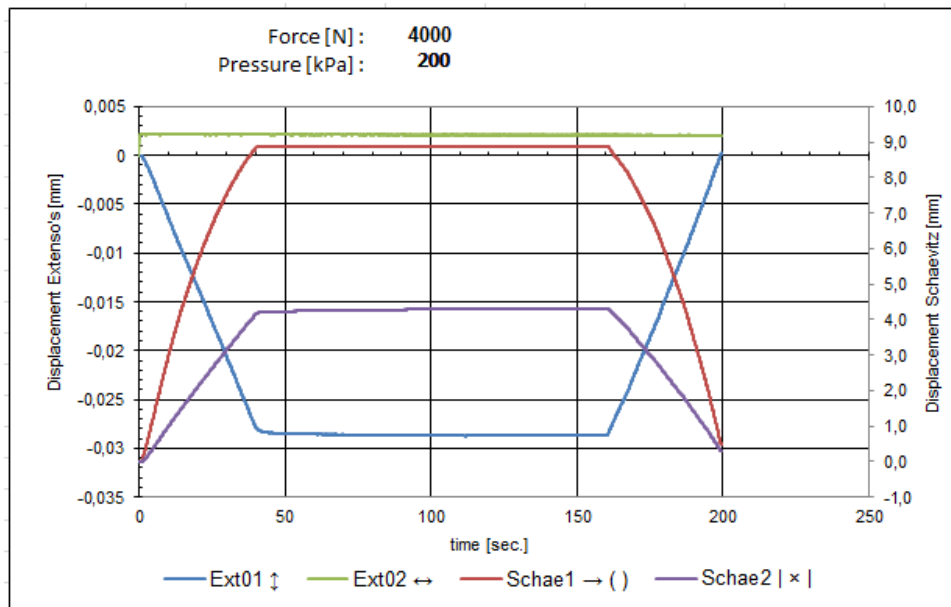


Figure 3.4. Deflection of tire under load

The typical load-deflection curve for a load of 4000 N and an inflation pressure of 200 kPa is shown in Figure 3.5. The load (F) and the vertical deflection (Y) of the tire are shown in Figure 3.5(a). In Figure 3.5(b), Ext01 and Ext02 represent the measured tread deformations along the periphery and the width directions. Schae1 is the measured sidewall deformation and Schae2 is the measured deformation of the tread along its horizontal center line.



(a) Load vs. vertical displacement of tire



(b) Load vs. sidewall and tread deformations of tire

Figure 3.5. Load deflection curves

The contact footprint was obtained by increasing the load of the tire to a prescribed value, and keeping it constant on Fuji film for 2 min in order to accurately capture the footprint. Fuji film uses an encapsulated dye on a Mylar film. When this material is used to produce a static footprint image, the image density is proportional to the normal stress applied between the tire and the pavement. The measured footprints for an inflation pressure of 200 kPa and its respective load classes (1000N-4000N) are shown in Figure 3.6.

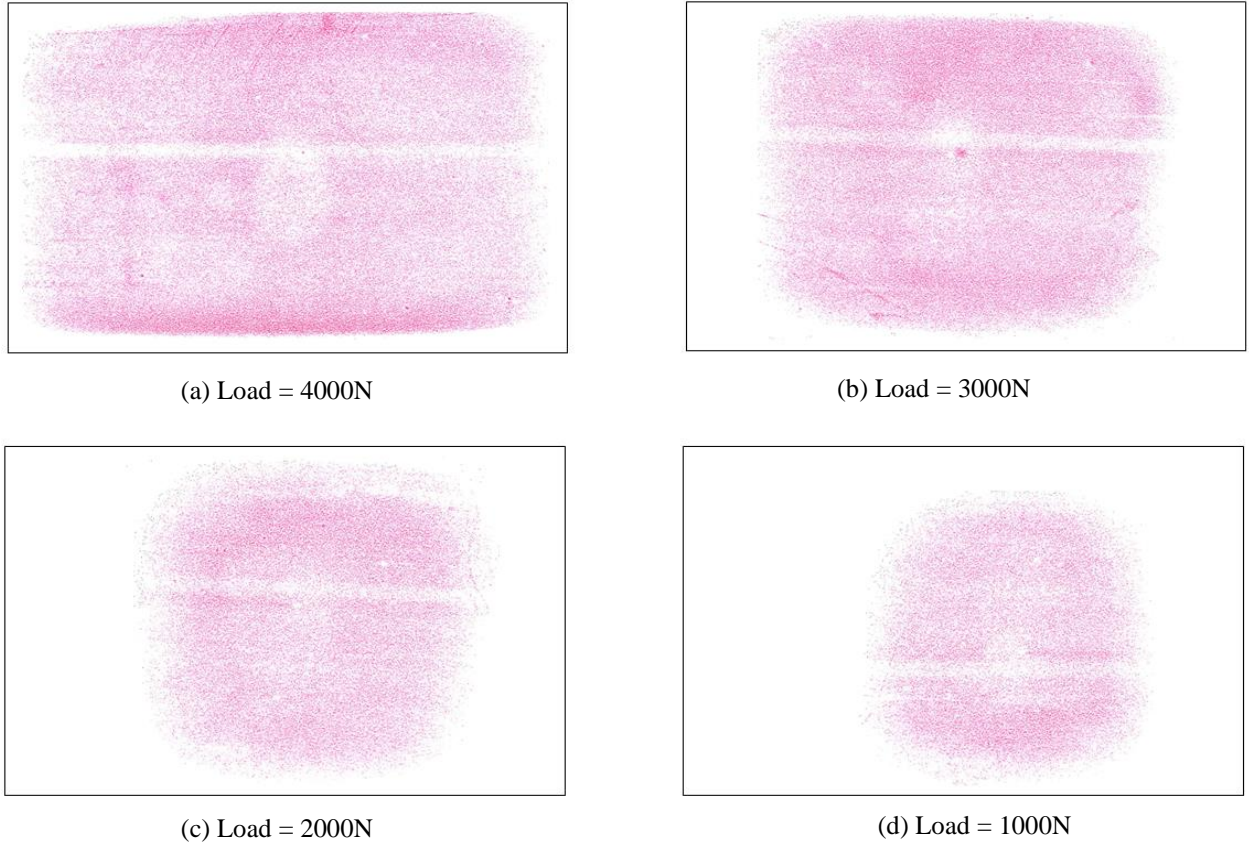


Figure 3.6. Tire imprints on Fuji film

3.3 FE modeling of a PIARC test tire

In this section, a procedure is described for the development of a PIARC FE tire model. The tread rubber properties of the tire model were obtained through laboratory material tests and all other material properties were obtained on the basis of calibration with the laboratory static load-deflection test measurements of Section 3.2. The successive steps necessary for FE tire modelling and calibration are described in the following.

3.3.1 Step 1: two dimensional cross section generation

The FE model of a tire consists of various components such as treads, sidewalls, inner-liners, ply, belts and the rim, Figure 3.7. The rubber components of the cross section are the tread, the sidewalls and the inner liner. They are also known as the carcass. The ply and the belts of the tire are the predominant load carrying components and are made of fiber-reinforced rubber composites. Development of the 3D PIARC tire model starts with the 2D cross sectional outline of all components, Figure 3.7. The 2D model is discretized with 4-noded axisymmetric quadrilateral and 3-noded axisymmetric triangular elements, Figure 3.7. The rim is assumed to be rigid. This assumption is justified because of the high elastic modulus of the rim in comparison to the other tire rubber components.

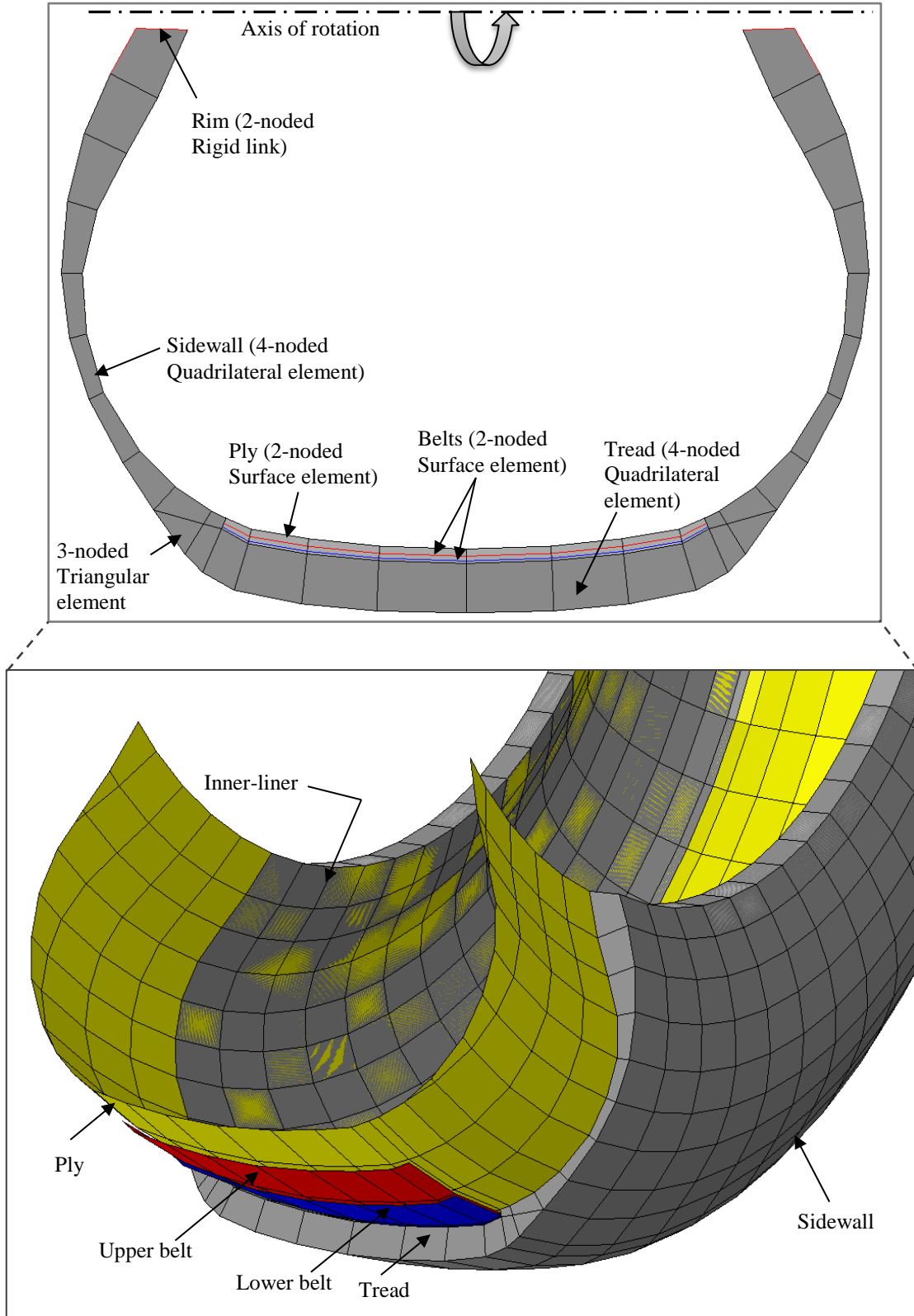


Figure 3.7 Cross sectional details of PIARC FE tire model

This assumption is justified because of the high elastic modulus of the rim in comparison to the other tire rubber components. The ply and the belts were placed inside the carcass using the embedded constraint technique (Abaqus 6.10). In this technique, the surface elements of ply and belts are embedded in a host matrix, Figure 3.8. Strains and stresses in the embedded element are calculated on the basis of the degrees of freedom of the host element and its location within the host element. The cross-sectional area, spacing and orientation of rebars are allocated to the embedded layers.

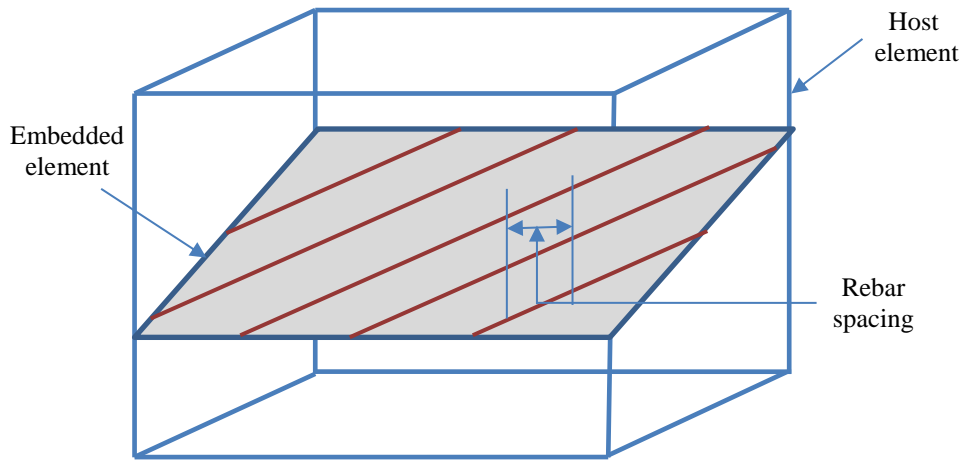


Figure 3.8 Embedded element technique

In the upper and lower belt layers, the rebars were placed in two opposite orientations in such a way that they make an equal angle (θ) with the direction of travel, Figure 3.9.

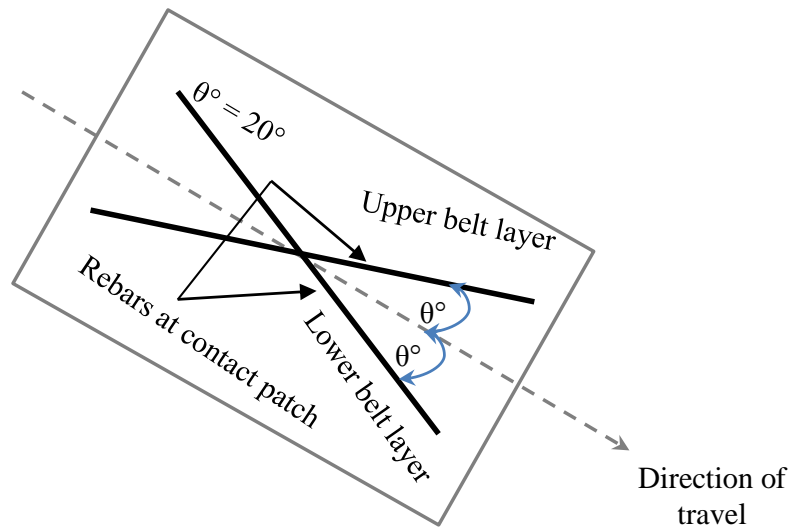


Figure 3.9 Plan view of the orientation of belt reinforcement with respect to the direction of travel

3.3.1.1 Material properties

Viscoelastic material properties obtained from laboratory DSR tests on tire rubber (Chapter 2) were assigned to the tread and the sidewall. The belt and ply reinforcement were assumed to be linear elastic materials, Table 3.1.

Table 3.1 Specified material properties of the various tire components (Abaqus 6.10)

Tire Section	Type of Material	Young's Modulus (MPa)	Poisson's Ratio	Density (kg/m ³)	Area per Bar (m ²)	Spacing (m)	Orientation Angle (°)	Remark
Rubber	Visco Elastic	From lab test	0.45	1200	-	-	-	Laboratory material tests
Belts	Elastic	172000	0.30	6500	0.20E-6	1.14E-3	±20	Specified
Ply	Elastic	9800	0.30	1500	0.41E-6	0.97E-3	90	Specified

3.3.1.2 Boundary and loading conditions

Appropriate boundary and loading conditions are specified for the 2D model, Figure 3.10.

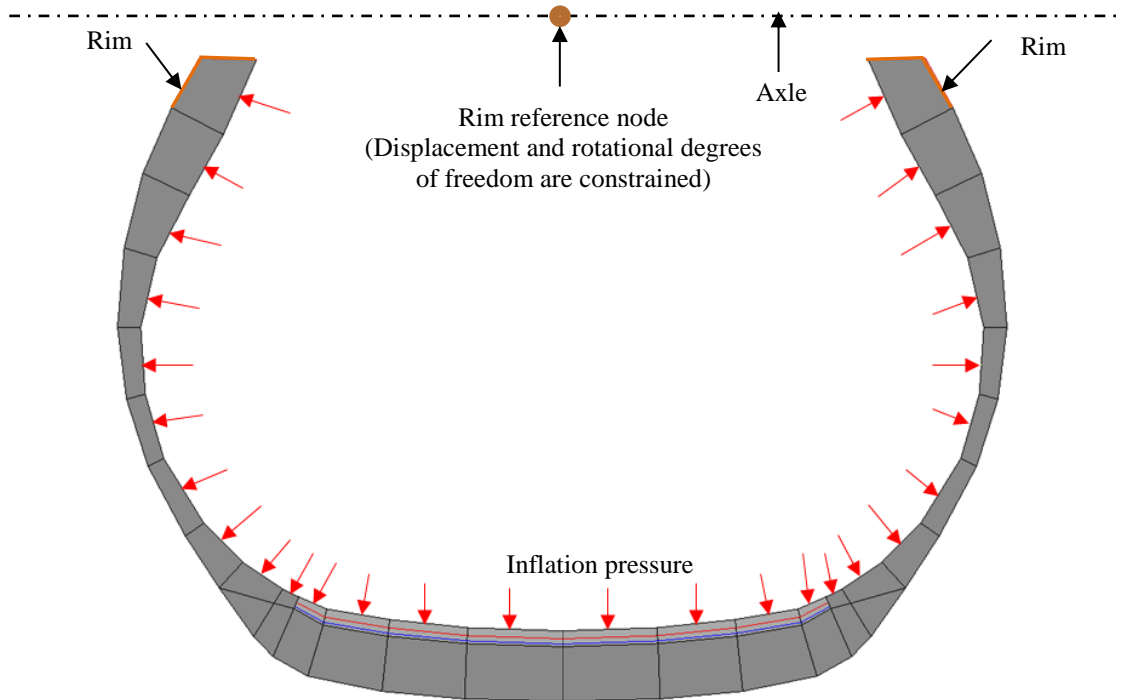


Figure 3.10 Boundary conditions and loads on the 2D tire cross section

The rim was rigidly connected to the tire carcass and axle, Figure 3.10. Rigid rim elements sharing the same nodes as the deformable carcass were used for this purpose. The rim reference node was placed on the axle position. The reference node is assumed fixed in space. The simulation is carried out at a prescribed tire inflation pressure. It should be noted that the pavement is not considered in this analysis yet. This analysis acts as a basis for the development of the 3D tire model.

3.3.2 Step 2: three dimensional tire model generation

The 3D model is generated by revolving the 2D tire mesh about an axis through the reference node. After revolution, 4-noded quadrilateral and 3-noded triangular elements are transformed to 8-node brick elements and 6-node triangular prism elements respectively, as shown in Figure 3.11. Similarly, 2-noded fiber reinforced surface elements are transformed to 4-noded quadrilateral elements. The discretization in the circumferential direction was specified by a constant segment angle.

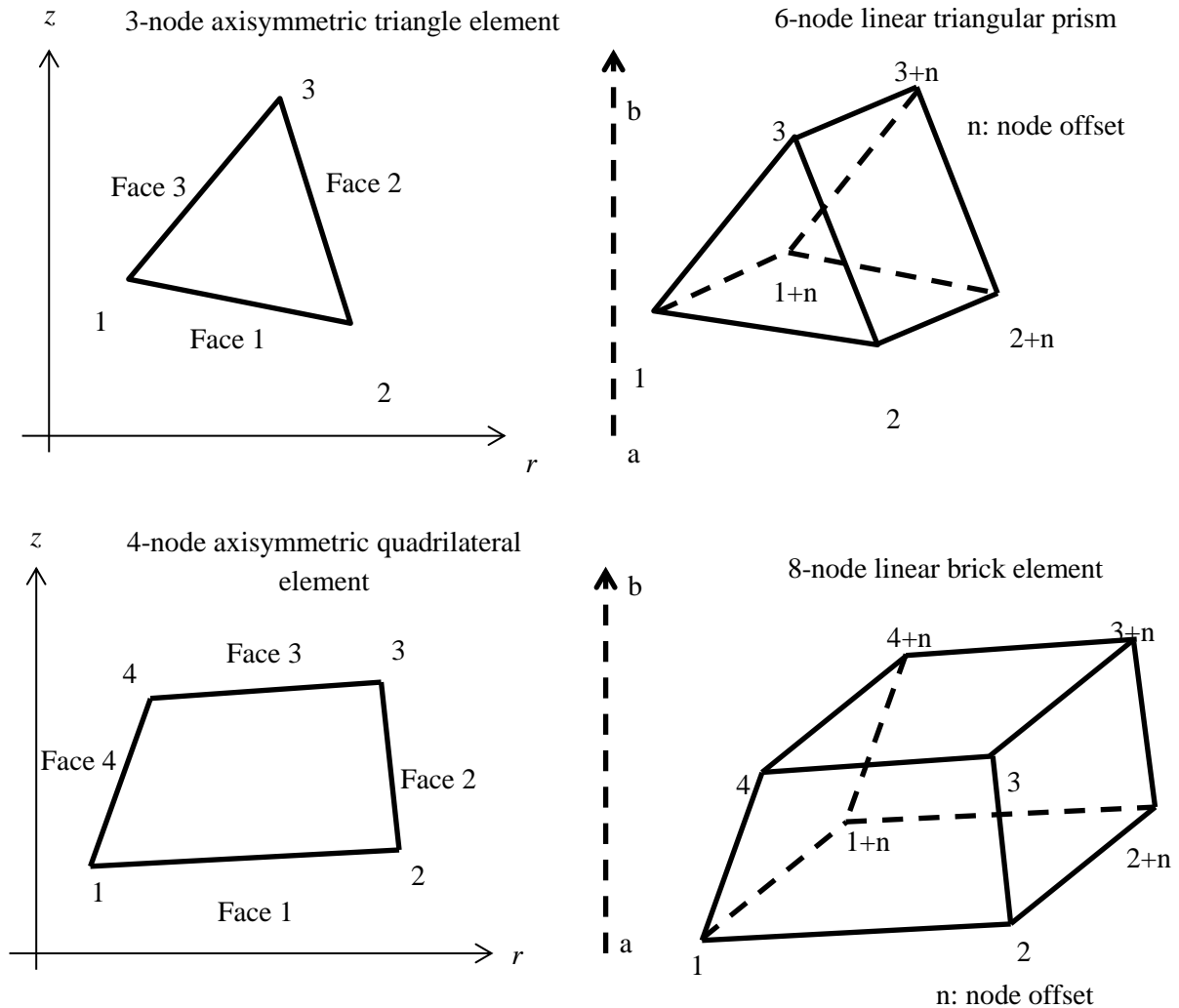


Figure 3.11 Correspondence between axisymmetric and three-dimensional elements
(Abaqus 6.10)

The rim-carcase definition, embedded element constraints and all material definitions and assignments were automatically carried over from 2D axisymmetric model to 3D model. However, all boundary conditions and loads must be redefined. The pavement is modeled as an analytical rigid surface which is a 3D infinite rectangular projection of a two-dimensional profile. The motion of analytical rigid surface is governed by a reference node which has six degrees of freedom (three translational and three rotational). Using analytical rigid surfaces instead of rigid surfaces formed by element faces may result in decreased computational cost incurred by the contact algorithm. An analytical rigid surface must always act as a master surface in a contact interaction.

In the simulation of 3D tire deformation, the stress strain history of 2D axisymmetric model that is transferred to the 3D model acts as an initial state. At first, the pavement is positioned at a small distance away from the tire tread surface such that the inflated tire does not touch the road. Subsequently, two steps were performed to deform the tire:

- a displacement control step in which the road was brought into contact with the tire tread surface,
- a load control step in which prescribed wheel load replaces the prescribed displacement. The undeformed and deformed profiles of 3D tire models are shown in Figure 3.12.

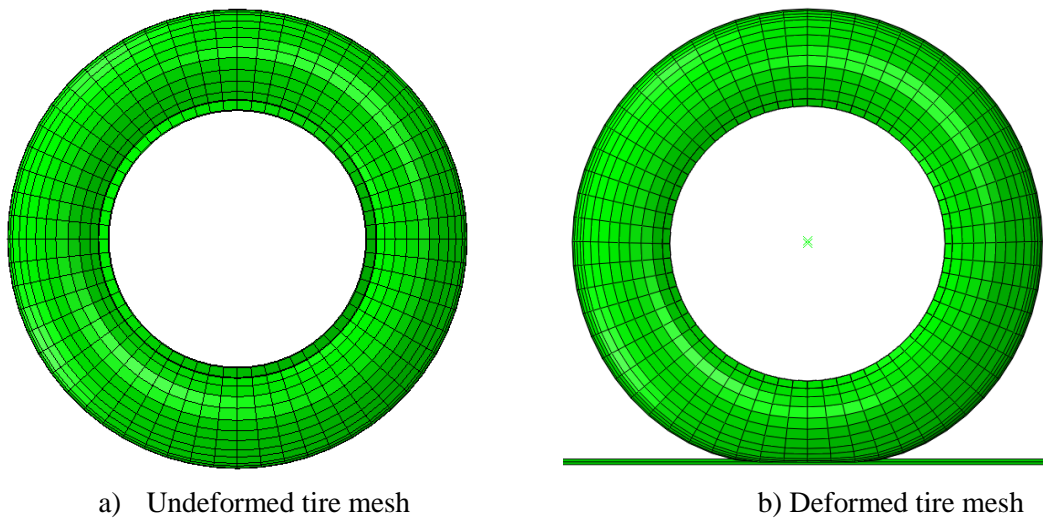


Figure 3.12 3D tire model

3.3.3 Step 3: 3D model calibration

For the precise modeling of the PIARC tire, precise details of reinforcement location, rubber and other material properties are necessary. The actual tire and rim radius, tire width, tread width and thickness, number of reinforcement layers and their orientation were obtained from the PIARC standards (PIARC, 2004). As mentioned earlier, the properties of tire tread rubber were obtained from laboratory material tests which provide the rheological behavior of the tread. No information was available for the ply and the belt materials. For this reason, the tire model had to be calibrated by varying the properties of the ply and the belts. The 3D model of the tire was utilized for simulation of the wheel load test as described in Section 3.2.

The FE model comprises of a smooth PIARC tire placed in between two analytical rigid smooth surfaces at top and bottom as shown in Figure 3.13a. The top rigid surface was constrained in all directions while the bottom rigid surface was allowed to translate in the vertical upward direction.

Subsequently, the bottom rigid surface was displaced upwards against the tire and until the resulting force equaled the one measured in the test. The corresponding deformed profile of the tire is shown in Figure 3.13b.

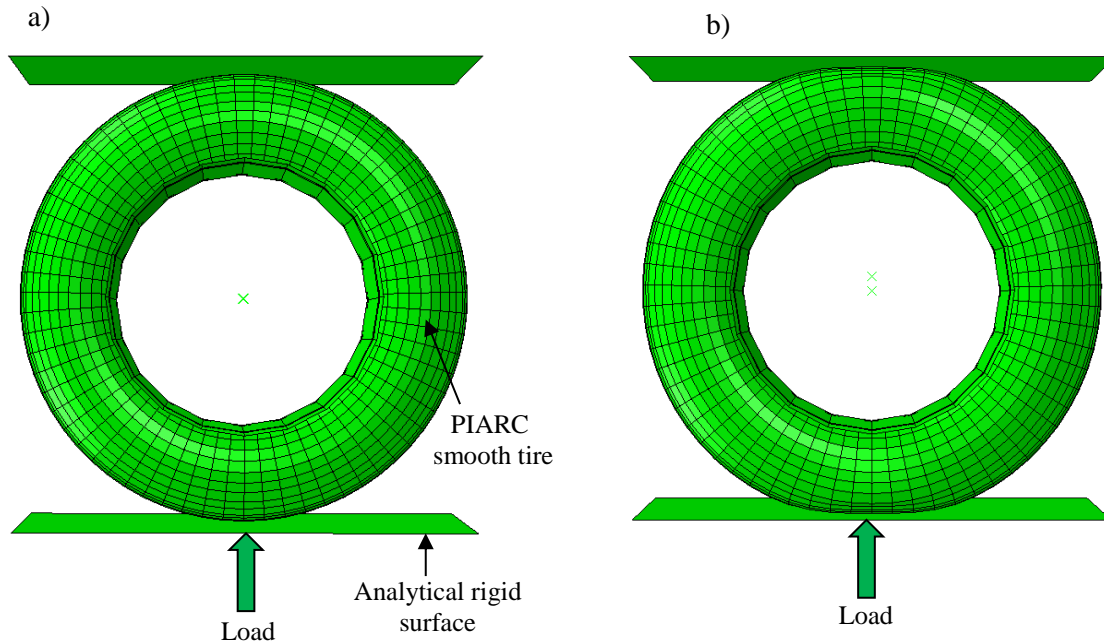


Figure 3.13. a) FE model simulation of wheel load test;

b) Deformed tread profile of PIARC tire under wheel load testing conditions

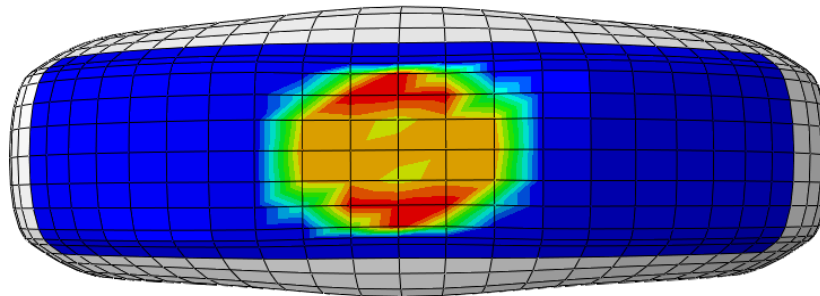


Figure 3.14 Deformed tread profile of PIARC tire under wheel load testing conditions and static contact pressure distribution at the footprint

The lateral deformations of the tire and its footprint are shown in Figure 3.14. At the beginning of the calibration effort, the properties of the tire ply and belts were specified in accordance to past literature on tire analysis and modeling (Abaqus 6.10). Based on the deviation of tire footprint dimensions with these properties, the moduli of elasticity of the carcass and the belts were modified in such a way that the simulated footprint would be as close as possible to the measured footprint of the stationary PIARC tire under the same load.

In the calibration process, the tire ply was tested for the values of elastic modulus from 2000 MPa to 13000 MPa. Similarly, the elastic modulus of tire belts were varied from 8620 MPa to 193400 MPa. For a wheel load of 4 kN and inflation pressure of 200 kPa, Table 3.2 shows the errors of different trial simulation results of the contact footprint dimensions against the measured tire contact footprint data. The analysis indicates that using the elastic modulus of 13000 MPa for the tire ply and 193400 MPa for belts would yield contact footprint dimensions with less than 6% error as compared to the experimental results.

Table 3.2 Contact footprint dimensions for different elastic moduli of tire carcass

E_{ply} (MPa)	E_{belt} (MPa)	Length of footprint (mm)	% error in length with experiment data	Width of footprint (mm)	% error in width with experiment data
2000	12930	213.0	33.1	76.7	-27.6
2000	17200	203.2	27.0	79.1	-25.4
2000	86200	196.3	22.7	82.7	-22.0
2000	129300	189.0	18.1	84.9	-19.9
2000	172400	186.2	16.4	86.7	-18.2
2000	193400	184.8	15.5	88.0	-17.0
9800	8620	206.7	29.2	81.1	-23.5
9800	12930	200.0	25.0	84.4	-20.4
9800	17200	191.5	19.7	88.8	-16.2
9800	86200	185.3	15.8	91.1	-14.1
9800	129300	179.5	12.2	95.2	-10.2
9800	172400	176.8	10.5	95.9	-9.5
9800	193400	174.9	9.3	97.1	-8.4
13000	8620	204.1	27.3	84.7	-20.1
13000	12930	192.2	19.9	86.5	-18.4
13000	17200	179.1	11.7	89.6	-15.5
13000	86200	175.3	9.4	93.9	-11.4
13000	129300	171.2	6.8	95.6	-9.8
13000	172400	168.8	5.3	97.8	-7.7
13000	193400	167.2	4.3	100.5	-5.2

Note: Footprint length and width of 160 mm and 106 mm respectively were obtained from the laboratory experiments of the PIARC test tire with a tire inflation pressure 200 kPa, under a wheel load of 4 kN reported in Section 3.2.

Figure 3.15 shows the comparison of footprints obtained for the wheel load test and the numerically predicted results for a load of 2 kN and 200 kPa inflation pressure.

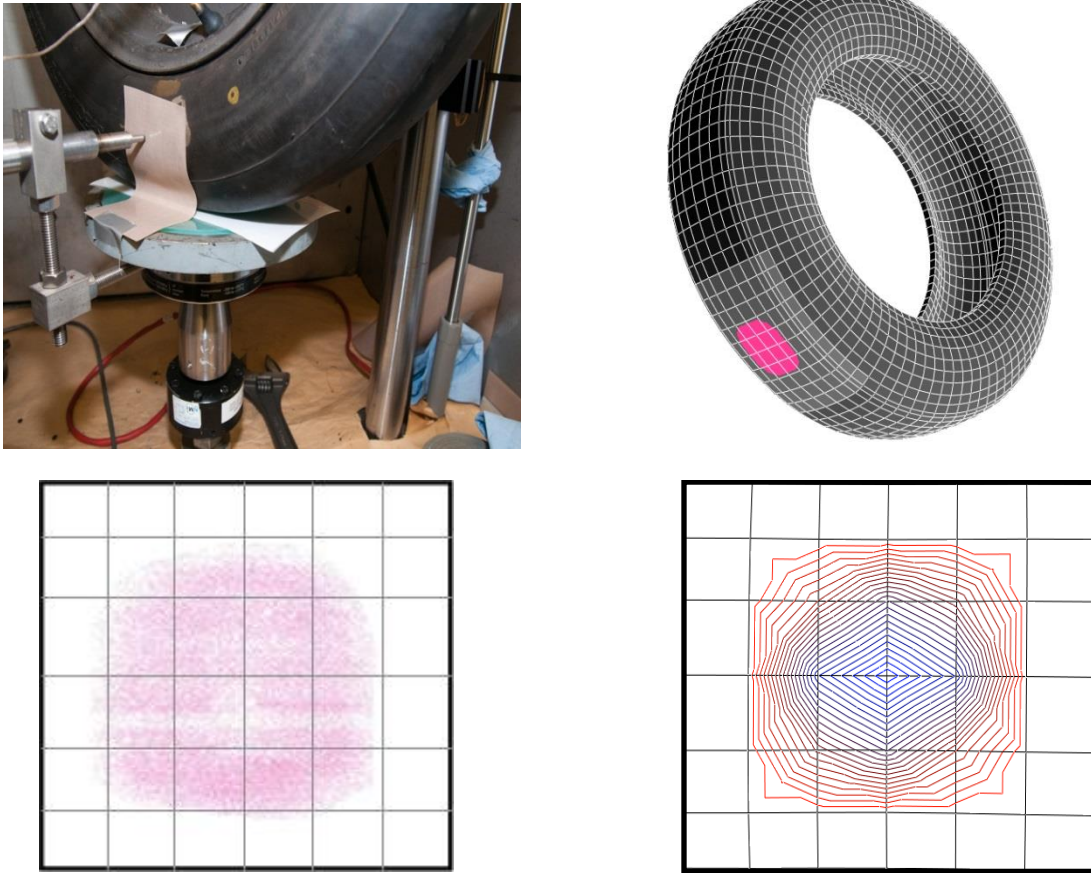


Figure 3.15. Comparison of footprints obtained from a wheel load test and the numerically predicted results

3.3.4 Fourth step: footprint analysis

Validation of the numerical model footprint results was made against the wheel load testing results as shown in Table 3.3. It can be observed that the simulation results using the elastic modulus of carcass of 13000 MPa and an elastic modulus of belts of 193400 MPa compare very well with those obtained experimentally, indicating that the calibrated model is appropriate for the analysis carried out in the present study.

The comparison of footprints was made for different inflation pressures (150, 180, 200 and 250 kPa) and their respective load classes (750N-4000N). Except in a few cases, the difference between experimental and computational results is under 8% which shows that the developed FE model simulates correctly the footprints of the tire under different loading conditions. This is a very important requirement in the simulations of the next level of tire-pavement interaction conditions such as rolling/braking/cornering wheel, tire traversing over an asphalt pavement surface, tire hydroplaning etc.

Table 3.3. A comparative analysis between numerically predicted results and experimental measurements of PIARC tire footprints

Tire Pressure (kPa)	Applied Load (N)	Experimentally Measured Results		Numerically Predicted Results	
		Length (mm)	Width (mm)	Length (mm)	Width (mm)
		70.8	79.2	76.4	82.3
	1200	101.3	97.1	107.5	93.5
	2250	139.5	103.6	130.2	107.8
	3000	160.4	106.5	142.4	110.2
180	750	68.2	78.4	72.0	83.2
	1200	90.1	93.0	93.8	88.2
	2250	120.3	101.1	114.4	95.0
	3000	150.2	105.4	136.4	96.4
200	1200	89.8	92.0	83.0	88.0
	2000	100.4	99.0	92.2	104.4
	3000	135.4	104.1	139.6	108.3
	4000	160.3	106.0	167.2	100.5
250	1500	80.0	88.0	84.1	84.9
	2000	97.1	95.2	101.3	91.6
	3000	124.2	101.3	130.3	97.1
	4000	149.5	104.8	158.2	101.4

3.4 Development of FE asphalt pavement mesh

A procedure to develop the FE meshes of three pavement mix designs, Stone Mastic Asphalt (SMA), Ultra-Thin Surfacing (UTS) and Porous Asphalt (PA) is presented in this section.

3.4.1 Asphalt mix compositions

Asphalt concrete slabs for the three different mixtures i.e. SMA, UTS and PA were prepared in the laboratory using a roller compactor and specimens of 60 mm in height and 150 mm in diameter were cored out of the slabs. These asphalt specimens were used for surface measurements and X-ray scanning. The composition, particle size distribution and the properties of each mix are shown in Table 3.4.

Table 3.4 SMA, UTS and PA Asphalt Pavement Mix Compositions

Composition (%)					
Components	4/10 mm aggregate	2/6.3 mm aggregate	0/4 mm aggregate	Limestone filler	Binder
SMA	55.2	13.8	15.9	8.4	6.4
UTS	52.0	13.7	21.7	7.1	5.5
PA	54.9	16.8	19.2	3.8	5.3

Particle size distribution								
Sieve size (mm)		14	10	6.3	4	2	1	0.063
Passing (%)	SMA	100	90	47	29	25	21	10.1
	UTS	100	91	51	33	28	22	8.8
	PA	100	99	47	27	19	14	5.6

Standard asphalt mix properties						
Property	Max. density (kg/m ³)	Voids at 10 gyrations (%)	Voids at 50 gyrations (%)	Texture depth (mm)	Bulk density (kg/m ³)	Voids (%)
SMA	2400	11.9	6.3	1.5	2294	4.4
UTS	2429	13.7	6.9	2.1	2104	13.4
PA	2582	22.7	18.8	NA	1975	23.7

3.4.2 FEM mesh generation

Having obtained the core samples, the internal structure of asphalt specimens in the form of 2D CT scans was obtained by utilizing the X-Ray Computed Tomography, Figure 3.16. For a given asphalt concrete mixture, the generated images were captured at every 0.1 mm. Each image consists of 256 levels of grey intensity.



Figure 3.16 Computed tomography 2D scans

In the CT scans, the three phases of asphalt concrete: aggregates, mastic and air voids can be distinguished. Since the intensity of each pixel is proportional to object density, air voids with the lowest density are black while the aggregates and mastic vary from dark to light gray depending on their relative densities. Subsequently, by using the specialized 3D-based image processing software Simpleware, the pixel-based 2D scans were assembled into 3D voxel-based meshes. By employing a reduction algorithm these meshes were then transformed into Finite Element meshes that were subsequently used for computational analyses in Abaqus (2010), Figure 3.17.



Figure 3.17 3D FE asphalt concrete mesh

A typical process for the creation of 3D voxel-based meshes out of a set of CT scans includes data preparation and filtering, segmentation, mask filtering and mesh generation, Figure 3.18.

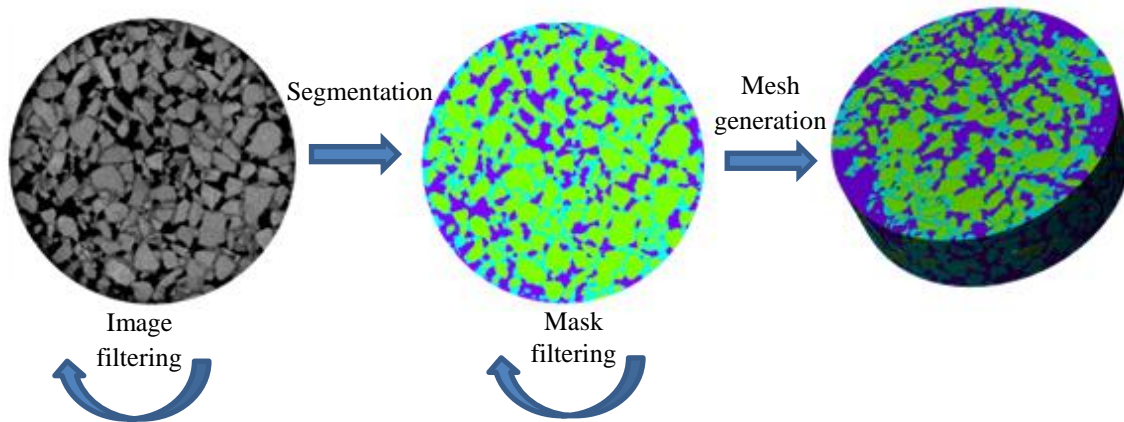


Figure 3.18 Process flow for FE meshes generation by means of the Simpleware software

In some cases, in a CT scan dataset, a number of undesirable discrepancies may exist. Common inconsistencies include artifacts created due to beam hardening effects while scanning the specimens, the sensitivity of the detector etc. In order to eliminate these artifacts, to reduce the noise and to smoothen the contours while preserving the features as much as possible, different varieties of filters are usually applied on the dataset obtained from Simpleware, Figure 3.19.

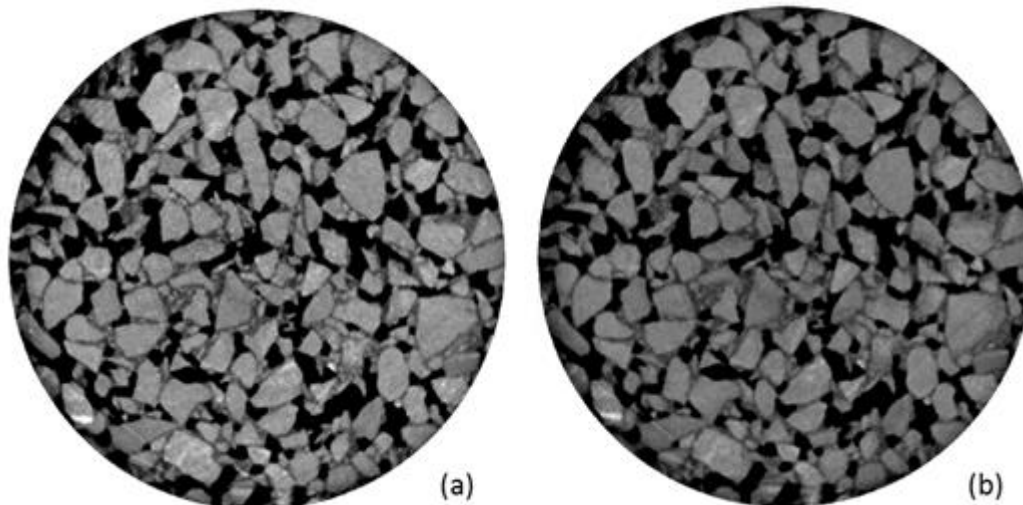


Figure 3.19: Image data before (a) and after (b) applying a smoothing filter

Next a threshold segmentation algorithm was utilized. By applying this algorithm, specific parts of the X-Ray scans were selected based on their grayscale values and binary volumes, called masks, were created. For example, in order to choose the voids, which are depicted in the scans in black color, the threshold segmentation algorithm was applied with a minimum and maximum grayscale value of 0 and 25, respectively. By choosing the right range of greyscale values, a mask was created for every asphalt constituent, Figure 3.20.

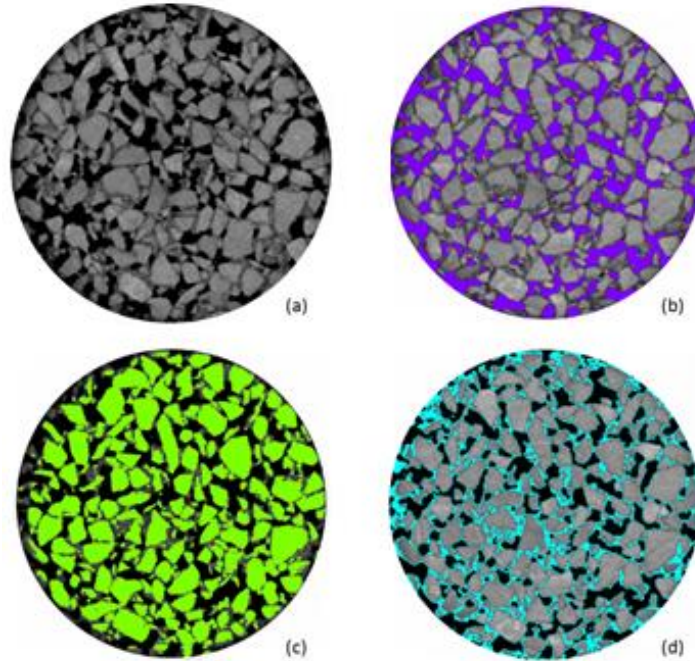


Figure 3.20: (a) Background data, (b) segmented masks for the air voids, (c) the aggregates and (d) the mastic

Then correction filters were applied to the segmented masks to clear up the segmentation e.g. filling holes, smoothing etc. The combination of the segmented masks for each slice, results in surfaces representing the geometry of the asphalt specimens. The Simpleware software allows a quick preview of the segmented masks using volume rendering techniques, Figure 3.21.

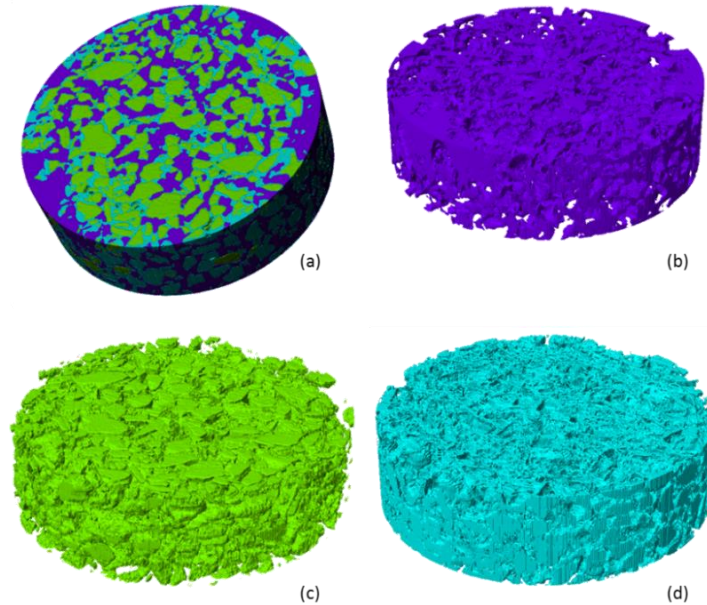


Figure 3.21: (a) Volume rendering of the asphalt specimen, (b) air void mask, (c) aggregates mask and (d) mastic mask

After cropping the segmented data to the desired dimensions for the analyses, a robust meshing algorithm was applied to enable the conversion of the 3D images into a FE mesh, Figure 3.22.

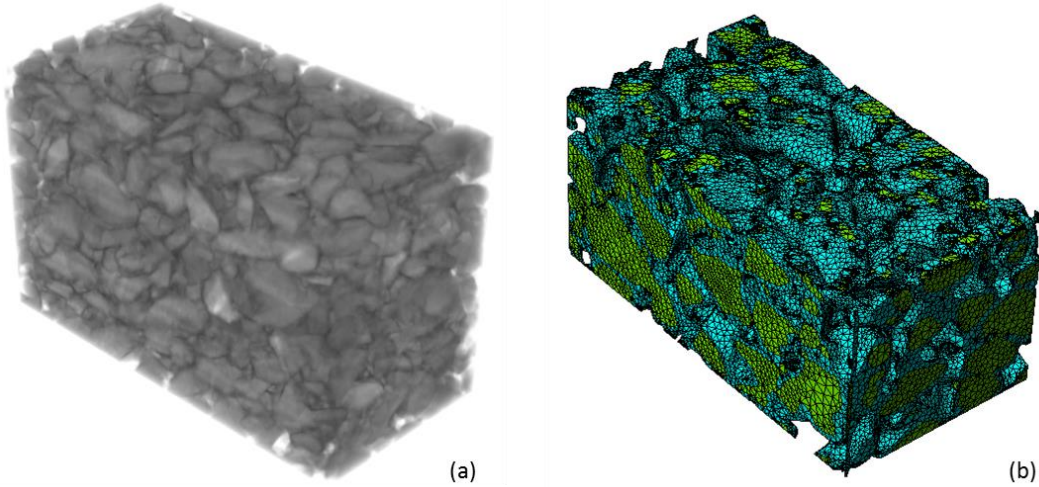


Figure 3.22: Volume rendering of (a) background data and (b) FE mesh

3.5 Summary

This Chapter presented a procedure for the simulation of a 3D FE pneumatic tire. In the first step, a 2D mesh of the tire cross section was generated. Once available, it is constrained to the rim and inflation pressure is applied. Then, a three-dimensional tire FE mesh was generated by revolving the previously generated 2D mesh. The calibration of developed FE tire was performed by static load-deflection tests under prescribed loading conditions. Under these tests, the tire was tested experimentally for a range of loads and inflation pressures and deflections were measured at various regions of tire. Also, tire footprints were obtained for various combinations of loads and inflation pressures. This Chapter also discussed a procedure to obtain the FE mesh of surface texture of any asphalt pavement. The developed asphalt mesh along with the calibrated FE tire model shall be integrated in Chapter 4 into a thermo-mechanical tire-pavement interaction model for the determination of the temperature development in the tire body and its eventual effect on its friction performance.

4 FE Modeling of Thermo-Mechanical Tire-Pavement Interaction

4.1 Introduction

A precise investigation of the micro-mechanical factors controlling the friction at the tire-pavement interface is of utmost importance in understanding the fundamental properties of friction. The temperature developed at the rubber-asphalt interface is one of such factors which have a crucial influence on the skid resistance. Evaluation of skid resistance without considering the temperature may lead to an overestimated pavement friction performance which might result to crashes and fatal accidents or underestimated friction performance which may hamper the flow of traffic due to erroneous speed limits.

As discussed in the Chapter 1, the hysteretic or bulk internal friction of a tire predominantly accounts for the friction at the interface. Hysteretic friction reflects the amount of energy dissipated within the tire rubber material when it is alternately compressed and expanded as it slides or rolls over the pavement surface texture. In the body of the tire energy is dissipated in the form of heat and an associated temperature increase in the tire rubber. Especially, during braking maneuvers, temperature increases continuously and at high rates in the body of the tire affecting the mechanical characteristics of the rubber materials and hence the area of the tire footprint and the developed friction at the interface.

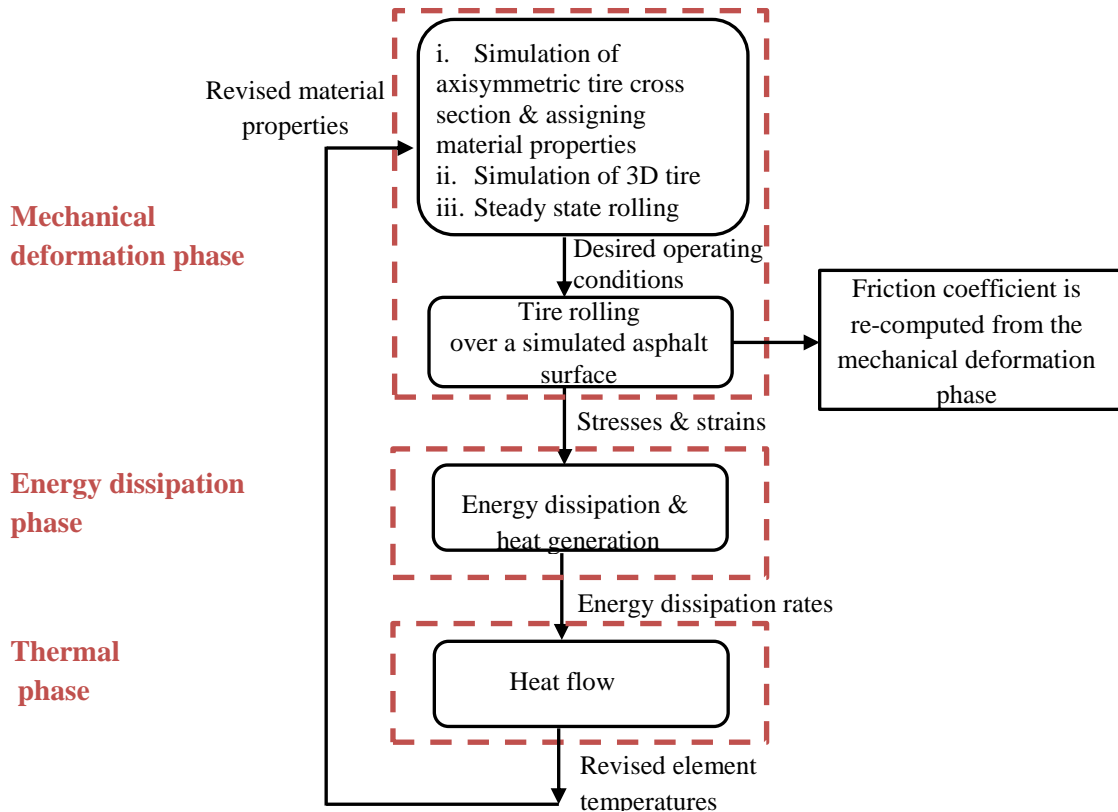


Figure 4.1 Schematic of thermo-mechanical coupling model

In the present chapter, a methodology is presented to develop a 3D thermo-mechanical tire-pavement interaction model in the FE framework which has the capability to capture the effect of tire operating temperatures on hysteretic friction, Figure 4.1. The procedure starts with a mechanical deformation phase in which a 3D FE tire is forced to traverse on an asphalt pavement mesh. The results of this phase are transported to a second phase known as energy dissipation phase. In this phase, the energy dissipation rates are computed from the stress-strain results of deformation phase. The results of the energy dissipation phase are transported to the next phase, known as thermal phase. In this phase, the nodal temperatures at various regions of tire cross section are computed. The results of this third phase are transported to the mechanical deformation phase in which the material properties of rubber are updated according to the revised temperatures. Validation of the methodology is made with past experimental results. Finally, parametric analyses are performed to determine :

- a) the time required to warm up and cool down the tire;
- b) the relationships between tire temperature (TT) and combined pavement temperature (PT) and ambient temperature (AT)
- c) the effect of the magnitude of friction between tire-pavement on the average temperature development in the tire body.

4.2 FE modeling of tire-asphalt surface interaction

A staggered thermo-mechanical coupling, Figure 4.1, is set up to ascertain the hysteretic friction and temperature distribution of a PIARC smooth tire partially or fully skidding on a micromechanical asphalt surface mesh. In this methodology, the mechanical deformation phase is divided in two different stages. In the first stage, 3D tire footprint analysis and steady state rolling analysis are carried out. In the next stage, the resulting stresses and strains are transferred from steady state rolling analysis to the transient rolling analysis, where the tire moves at a desired speed over an asphalt pavement surface mesh. This two-step procedure is known as Abaqus/Standard to Abaqus/Explicit analysis (Abaqus 6.10). The dissipated energy output at each Gauss point of every element from the explicit analysis, serves as input to the 2D thermal analysis. The following steps are discussed in detail in the subsequent subsections.

4.2.1 Deformation module

In Chapter 3, the procedures to develop a 3D FE tire model and the footprint calibration were discussed in detail. As a continuation, this section presents the rolling analysis of a PIARC 3D FE tire. The rolling analysis of tire is carried out in two steps:

- Steady state rolling;
- Transient rolling.

Because of computational limitations, it is not possible to develop a micromechanical FE mesh long enough for the tire to achieve the desired speed and other operating conditions. Instead, as a first step, a steady state rolling (SSR) at the desired operating conditions is achieved by means of a steady state solution of the tire rolling over a smooth pavement surface. The SSR uses an Eulerian analysis based on the steady state transport (SST) feature of Abaqus in which only the material moves at the specified velocity through the fixed FE mesh.

In the subsequent step, the results of the above steady state rolling deformation analysis are used as the starting values for a transient analysis of the tire rolling over the simulated asphalt surface.

This two-stage procedure drastically improves the computational time and is thus adopted in this study. Even then, the entire procedure required a LINUX cluster with at least 1 computing node, which consists of 16 CPU's running at 3 GHz which shares 64 GB of memory.

4.2.1.1 Steady state rolling

In Abaqus, the kinematics of steady state behavior of a tire rolling along a flat rigid surface can be described by using the Arbitrary Lagrangian-Eulerian method. This method allows the material to flow through the tire mesh, while the mesh itself is stationary. This method accounts for frictional and inertial effects in the material due to which the tire mesh can deform (Abaqus 6.10). As the FE mesh remains stationary in the analysis, only the part of the body in the contact zone requires fine meshing. This is an effective method to obtain the global force and moment characteristics of a tire under different driving conditions, such as rolling, braking and side slip angles, Figure 4.2, which otherwise would take large computational times to reach equilibrium conditions by using the transient approach. This entire procedure is termed as “steady state transport” (SST) in Abaqus (Abaqus, 6.10).

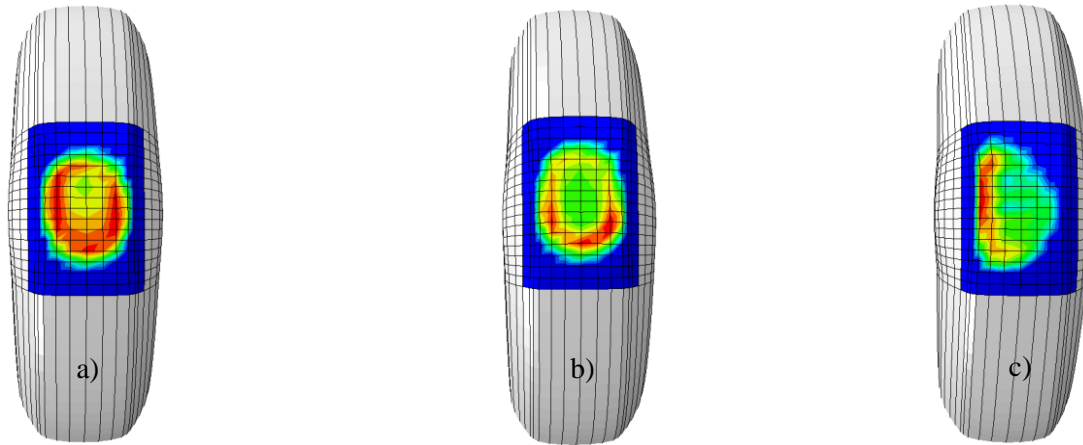


Figure 4.2. Steady state analysis of a PIARC smooth tire (a) rolling tire contact pressure, (b) braking tire contact pressure, (c) cornering tire contact pressure distribution

The SST analysis requires the stress-strain history of a 3D tire footprint analysis (Chapter 3) as a base step. The angular velocity (ω) of a free rolling tire can be computed from the horizontal velocity as follows:

$$\omega = \frac{V}{R_e} \tag{4.1}$$

where R_e is the effective rolling radius at zero torque (Pacejka, 2006).

R_e is an important parameter in the SST analysis of a tire. For a pneumatic tire, the value of R_e varies from a value close to the unloaded radius (R_u) to the same value as the loaded radius (R_l) at the projection point of the wheel center on the contact area, Figure 4.3. At R_e , the peripheral velocity of the tread (relative to the wheel center) coincides with the horizontal

velocity of the wheel center as shown in the Equation (4.1). The value of R_e increases with increasing speed and increasing inflation pressure.

R_e = Effective rolling radius

R_u = Unloaded radius

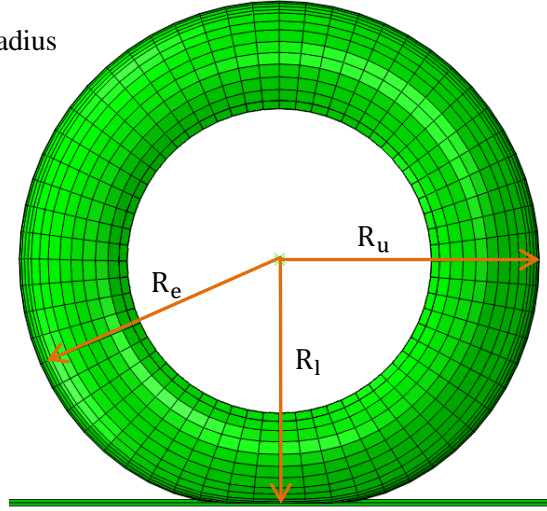


Figure 4.3 Schematic of tire radius

An equilibrium solution for a rolling tire that has a zero torque, T , applied around the axle, is referred to as a free rolling solution (Abaqus 6.10). An equilibrium solution with a nonzero torque is referred to as either a traction or a braking solution depending upon the sense of T . A wheel in free rolling, traction or braking will spin at different angular velocities ω for the same horizontal velocity V . In the present analysis, the forward velocity is kept constant during a steady-state rolling step and the rotational velocity is incrementally updated based on previous values of the torque. The angular velocity at which the torque at the rim is zero is taken as the rotational velocity of a free rolling tire. At this rotational velocity, the effective of radius of tire can be calculated from the Equation (4.1).

4.2.1.2 Transient rolling

Results from the steady state rolling phase are imported to the transient rolling step and are brought to equilibrium against the stationary asphalt micromechanical pavement mesh. Once equilibrium is established, the tire is forced to travel over the surface of the pavement mesh at prescribed operating conditions (velocity, slip ratio, inflation pressure and normal load), Figure 4.4.

Let Ω be the deformed configuration of a rolling tire, at current time t , with boundary $\partial\Omega = \partial\Omega_\delta \cup \partial\Omega_\eta \cup \partial\Omega_\zeta$ with $\partial\Omega_\delta$, $\partial\Omega_\eta$ and $\partial\Omega_\zeta$ the boundaries where displacement, surface traction and contact conditions are prescribed.

For the displacement field \mathbf{u} of the deformed tire it holds

$$\nabla\sigma(\mathbf{u}) + \mathbf{b} = \rho\ddot{\mathbf{u}} \quad \text{in } \Omega \times \langle 0, t \rangle \tag{4.2}$$

with the initial conditions

$$\mathbf{u} = \mathbf{u}^0; \dot{\mathbf{u}} = \dot{\mathbf{u}}^0 \quad \text{at } t=0 \quad (4.3)$$

and the boundary conditions

$$\begin{aligned} \mathbf{u} &= \hat{\mathbf{u}} \quad \text{in } \partial\Omega_e \\ \boldsymbol{\sigma} \cdot \hat{\mathbf{n}} &= \hat{\mathbf{t}} \quad \text{in } \partial\Omega_n \end{aligned} \quad (4.4)$$

with ρ the mass density, \mathbf{b} the body force, $\boldsymbol{\sigma}$ the Cauchy stress, \mathbf{n} the outward unit vector normal to the boundary and $\hat{\mathbf{t}}$ the external traction.

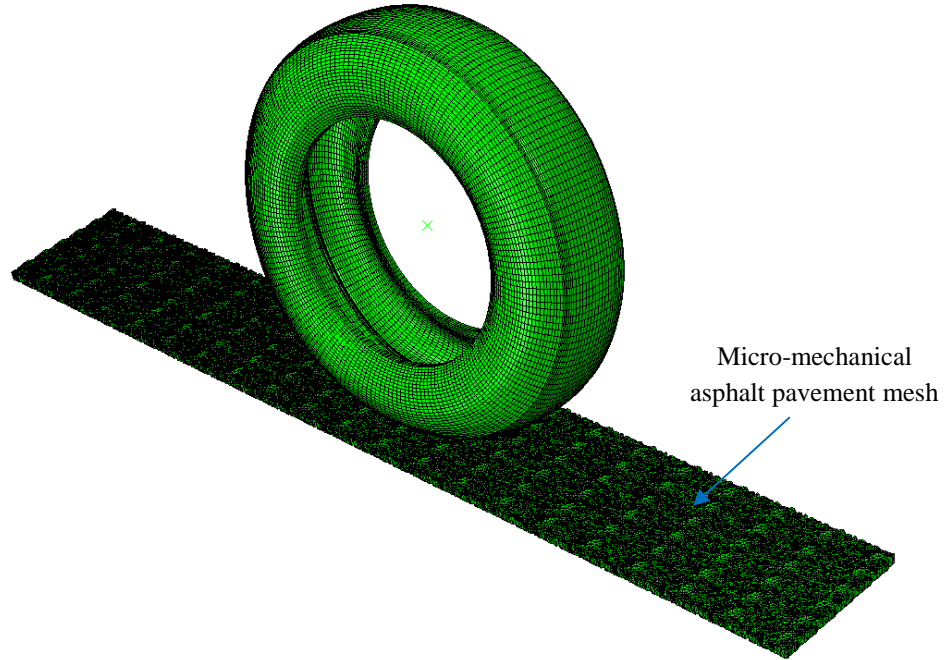


Figure 4.4 FE model simulation of tire rolling on asphalt surface

Eq. (4.2) expresses the dynamic equilibrium of the tire in its current configuration. For numerical computation efficiency and stability, it is preferable to express the same in the reference configuration Ω^0 . Therefore, $\boldsymbol{\sigma}$ can be expressed as

$$\boldsymbol{\sigma} = \mathbf{J}^{-1} \mathbf{F} \mathbf{S} \mathbf{F}^T \quad (4.5)$$

where, where, \mathbf{F} is the deformation gradient, \mathbf{J} is the Jacobian determinant ($\mathbf{J} = \det(\mathbf{F})$) and \mathbf{S} is the second Piola-Kirchhoff stress.

For every admissible displacement \mathfrak{U} , the first part of Equation (4.2) can be re-written as

$$\begin{aligned}
 \mathfrak{G}(\nabla \boldsymbol{\sigma}(\mathbf{u})) &= \mathfrak{G}_i \frac{\partial \mathfrak{G}}{\partial X_j} \sigma_{ij}(\mathbf{u}_k) \\
 &= \mathfrak{G}_i \frac{\partial}{\partial X_j} \sigma_{ij} + \mathfrak{G}_i \frac{\partial \sigma_{ij}}{\partial \mathbf{u}_k} \frac{\partial \mathbf{u}_k}{\partial X_j} = \mathfrak{G}_i \frac{\partial}{\partial X_j} \sigma_{ij} + \mathfrak{G}_i \frac{\partial \sigma_{ij}}{\partial X_p} \frac{\partial X_p}{\partial \mathbf{u}_k} \frac{\partial \mathbf{u}_k}{\partial X_j} \\
 &= \frac{\partial \mathfrak{G}_i}{\partial X_j} \sigma_{ij} + \mathfrak{G}_i \frac{\partial \sigma_{ij}}{\partial X_p} \frac{\partial X_p}{\partial \mathbf{u}_k} \frac{\partial \mathbf{u}_k}{\partial X_j} \quad (\because \mathfrak{G} \cdot (\nabla \cdot \boldsymbol{\sigma}) = \nabla \mathfrak{G} : \boldsymbol{\sigma})
 \end{aligned} \tag{4.6}$$

The first part of the right hand side of Equation (4.6) i.e. $\frac{\partial \mathfrak{G}_i}{\partial X_j} \sigma_{ij}$ can be expressed as

$$\frac{\partial \mathfrak{G}_i}{\partial X_j} \sigma_{ij} d\Omega = \frac{\partial \mathfrak{G}_i}{\partial X_j} J^{-1} F_{ik} F_{jl} S_{kl} J d\Omega^0 = \frac{\partial \mathfrak{G}_i}{\partial X_1} F_{ik} S_{kl} d\Omega^0 \tag{4.7}$$

In the second part of the Equation (4.6), $\frac{\partial \mathbf{u}_k}{\partial X_j}$ can be expressed as

$$\frac{\partial \mathbf{u}_k}{\partial X_j} = \frac{\partial \mathbf{u}_k}{\partial X_1} \frac{\partial X_1}{\partial X_j} = (\mathbf{F} - \mathbf{I})_{kl} F_{lj}^{-1} \quad \left(\because F_{kl} = \frac{\partial X_k}{\partial X_l} = \frac{\partial (X + \mathbf{u})_k}{\partial X_l} = \mathbf{I} + \frac{\partial \mathbf{u}_k}{\partial X_l} \right)$$

similarly $\frac{\partial X_p}{\partial \mathbf{u}_k} = (\mathbf{F} - \mathbf{I})_{pk}^{-1}$

Therefore, the second part of Equation (4.6) becomes

$$\begin{aligned}
 \mathfrak{G}_i \frac{\partial \sigma_{ij}}{\partial X_p} \frac{\partial X_p}{\partial \mathbf{u}_k} \frac{\partial \mathbf{u}_k}{\partial X_j} &= \mathfrak{G}_i \frac{\partial \sigma_{ij}}{\partial X_p} (\mathbf{F} - \mathbf{I})_{pk}^{-1} (\mathbf{F} - \mathbf{I})_{kl} F_{lj}^{-1} \\
 &= \mathfrak{G}_i \frac{\partial \sigma_{ij}}{\partial X_p} \delta_{pl} F_{lj}^{-1} = \mathfrak{G}_i \frac{\partial \sigma_{ij}}{\partial X_p} F_{pj}^{-1}
 \end{aligned} \tag{4.8}$$

By applying Divergence theorem to Equation (4.8),

$$\begin{aligned}
 \int_{\Omega} \mathfrak{G} \cdot (\nabla_0 \cdot \boldsymbol{\sigma}) \cdot \mathbf{F}^{-1} d\Omega &= \int_{\Omega^0} \mathfrak{G} \cdot (\nabla_0 \cdot \boldsymbol{\sigma}) \cdot \mathbf{F}^{-1} J d\Omega^0 \\
 &= \int_{\partial \mathcal{S}^0} \mathfrak{G} \cdot (\boldsymbol{\sigma} \cdot \mathbf{n}^0) \cdot \mathbf{F}^{-1} J dS^0
 \end{aligned} \tag{4.9}$$

in which the relation $d\Omega = J d\Omega^0$ has been used.

$$\hat{\mathbf{t}} = \boldsymbol{\sigma} \cdot \hat{\mathbf{n}} \tag{4.10}$$

where $\hat{\mathbf{n}} = \frac{\mathbf{n}^0 \cdot \mathbf{F}^{-1}}{\|\mathbf{n}^0 \cdot \mathbf{F}^{-1}\|}$

Therefore,

$$\hat{\mathbf{t}} = \boldsymbol{\sigma} \cdot \frac{\mathbf{n}^0 \cdot \mathbf{F}^{-1}}{\|\mathbf{n}^0 \cdot \mathbf{F}^{-1}\|} \quad (4.11)$$

$$\hat{\mathbf{t}} \cdot \|\mathbf{n}^0 \cdot \mathbf{F}^{-1}\| = \boldsymbol{\sigma} \cdot \mathbf{n}^0 \cdot \mathbf{F}^{-1}$$

$$\hat{\mathbf{t}} \cdot \|\mathbf{n}^0 \cdot \mathbf{F}^{-1}\| = \mathbf{J}^{-1} \cdot \hat{\mathbf{t}}^0 \quad (4.12)$$

$$\hat{\mathbf{t}}^0 = \mathbf{J} \cdot \boldsymbol{\sigma} \cdot \mathbf{n}^0 \cdot \mathbf{F}^{-1} \quad (4.13)$$

By using Equation (4.13) and the mass conservation equation $\rho = \mathbf{J}^{-1} \rho^0$, Equation (4.2) can be expressed as

$$\int_{\Omega^0} \left[\rho^0 \ddot{\mathbf{u}} \cdot \boldsymbol{\vartheta} + (\mathbf{F}\mathbf{S}) : \frac{\partial \boldsymbol{\vartheta}}{\partial \mathbf{X}} \right] d\Omega^0 = \int_{\Omega^0} \mathbf{b} \cdot \boldsymbol{\vartheta} d\Omega^0 + \int_{\partial\Omega_n^0} \hat{\mathbf{t}}^0 \cdot \boldsymbol{\vartheta} dS^0 \quad (4.14)$$

Figure 4.5 shows a pneumatic tire Ω in contact with an asphalt pavement on the surface $d\Omega_c$, where \mathbf{n} denotes the inward unit vector normal to the asphalt surface.

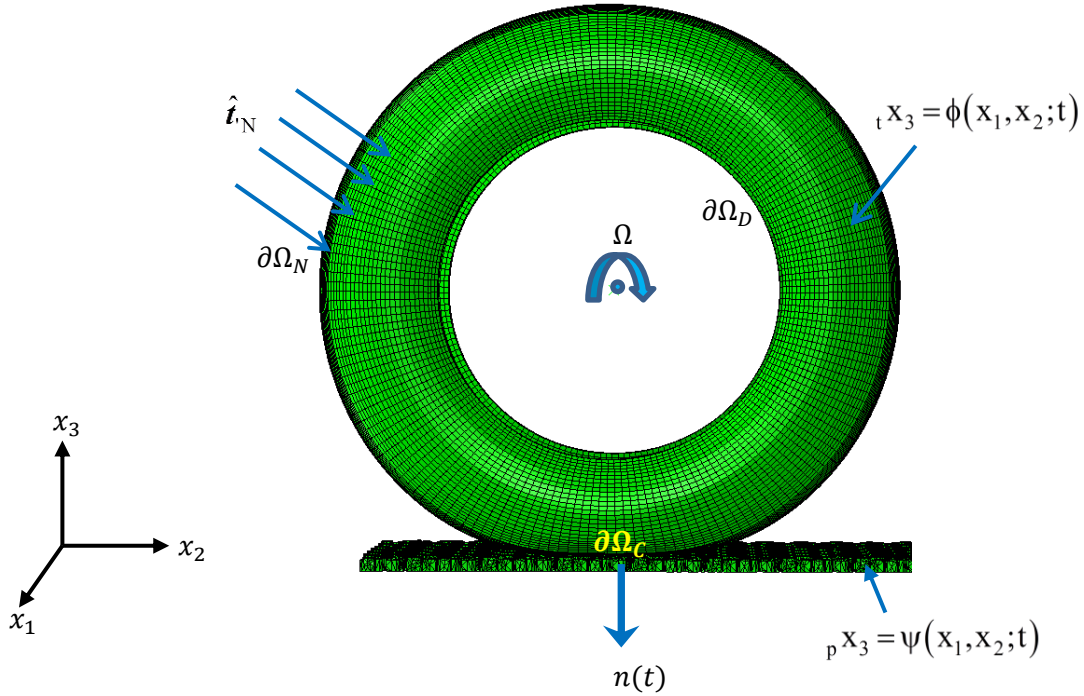


Figure 4.5 Schematic of tire-asphalt surface contact

The surfaces of the tire and the asphalt pavement at time t are described by

$${}_t x_3(t) = \phi(x_1, x_2; t), \quad {}_p x_3(t) = \psi(x_1, x_2; t) \quad (4.15)$$

Non-penetration of the tire into the asphalt surface requires (Cho et al., 2005)

$${}_{t}x_3 + u_3 \geq \psi(x_1 + u_1, x_2 + u_2) \quad (4.16)$$

Linearizing Eq.(4.16) with respect to \mathbf{u} leads to the linearized kinematic contact condition (Oden & Carey, 1984; Cho et al., 2005)

$$u_n - g \leq 0 \quad \text{in} \quad \partial\Omega_c \quad (4.17)$$

where $u_n = \mathbf{u} \cdot \mathbf{n}$ and $g(x_1, x_2; t) = \phi(x_1, x_2; t) - \psi(x_1, x_2; t)$ is a gap function between two bodies.

In Equation (4.17), $u_n = g$ indicates contact and $u_n < g$ indicates a gap between tire and asphalt surface. Thus Equation (4.17) is a non-penetration condition.

The normal traction σ_n at a point on the contact boundary should satisfy the static contact condition:

$$\sigma_n \leq 0 \quad \text{in} \quad \partial\Omega_c \quad (4.18)$$

$$\sigma_n (u_n - g) = 0 \quad \text{in} \quad \partial\Omega_c \quad (4.19)$$

Equation (4.18) means that the normal traction is purely compressive and Equation (4.19) signifies that the pressure can only be non-zero when there is contact.

Tangential contact stress (\mathbf{t}_T) can be written as

$$\mathbf{t}_T = c_T \mathbf{u}_T^e \quad (4.20)$$

where, c_T is the elastic tangential stiffness modulus and \mathbf{u}_T^e is the elastic stick portion of the total tangential slip \mathbf{u}_T between two contacting bodies. $\mathbf{u}_T^e = \mathbf{u}_T - \mathbf{u}_T^s$, where \mathbf{u}_T^s is the plastic slip portion (Wriggers, 2006).

Introducing a plastic slip criterion function

$$f_s(\mathbf{t}_T, \sigma_n) = \|\mathbf{t}_T\| - \mu \sigma_n \leq 0 \quad (4.21)$$

where μ is the Coulomb friction coefficient, the constitutive equation of the tangential plastic slip $\dot{\mathbf{u}}_T^s$ is defined by

$$\dot{\mathbf{u}}_T^s = \dot{\lambda} \frac{\partial f_s(\mathbf{t}_T, \sigma_n)}{\partial \mathbf{t}_T} = \dot{\lambda} \mathbf{n}_T \quad (4.22)$$

where $\mathbf{n}_T = \frac{\mathbf{t}_T}{\|\mathbf{t}_T\|}$ and λ is the magnitude of the tangential slip.

The loading-unloading conditions in Kuhn–Tucker form can be written as

$$\dot{\lambda} \geq 0, \quad f_s(\mathbf{t}_T, \sigma_n) \leq 0, \quad \dot{\lambda} f_s(\mathbf{t}_T, \sigma_n) = 0 \quad (4.23)$$

and, together with Equations (4.20) to (4.22), establish the constitutive relation for the frictional contact.

Finally, Equation (4.14) can be written as

$$\begin{aligned} \int_{\Omega^0} \left(\rho^0 \ddot{\mathbf{u}} \cdot \mathfrak{G} + (\text{FS}) : \frac{\partial \mathfrak{G}}{\partial \mathbf{X}} \right) d\Omega^0 + \int_{\partial S_c^0} k_p (x_n - g) \mathfrak{G}_n dS^0 \\ = \int_{\Omega^0} \rho^0 \mathbf{b} \cdot \mathfrak{G} d\Omega^0 + \int_{\partial S_n^0} \hat{\mathbf{t}}^0 \cdot \mathfrak{G} dS^0 + \int_{\partial S_c^0} \mathfrak{G}_T^T \mathbf{t}_T^0 dS^0 \end{aligned} \quad (4.24)$$

where k_p is the penalty parameter.

4.2.2 Dissipation module

From the results (total strains and stresses) of the mechanical deformation analysis, the dissipation losses are computed at each Gauss point of every element. The energy loss is summed for all elements to give a total energy loss for the tire in one revolution.

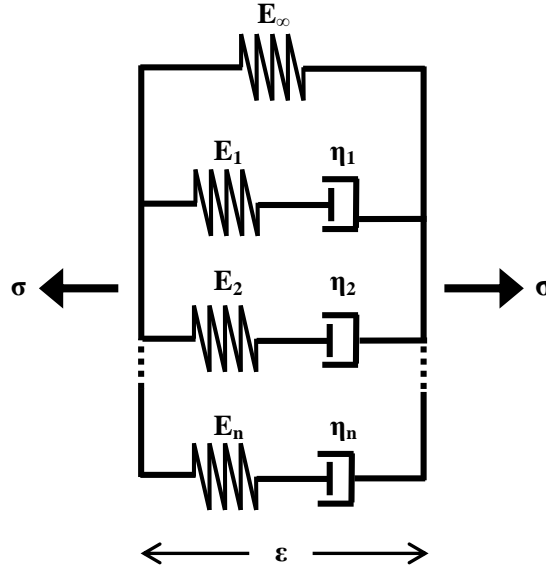


Figure 4.6 Generalized Maxwell model

A generalized linear viscoelastic model, Figure 4.6, is used to characterize the rubber material. The total stress (σ) can be expressed as

$$\sigma = E_\infty \epsilon + \sum_{i=1}^m E_i (\epsilon - \epsilon_{vi}) \quad (4.25)$$

where i indicates the Maxwell component index, $i=1..m$, ε is the total strain, ε_v inelastic strain, E_∞ and E_i are stiffness moduli of infinite spring and Maxwell springs respectively.

The stress in the dashpot of the Maxwell element (σ_M) is defined proportional to the inelastic strain rate $\dot{\varepsilon}_v$

$$\sigma_M = \eta_i \dot{\varepsilon}_{vi} \quad (4.26)$$

Also, the stress in the spring of the Maxwell element can be computed as

$$\sigma_M = E_i (\varepsilon - \varepsilon_{vi})$$

On the basis of Equations (4.26) and (4.27),

$$E_i (\varepsilon - \varepsilon_{vi}) = \eta_i \dot{\varepsilon}_{vi} \quad (4.27)$$

Also, the response of each one of the viscous components can be expressed as

$$\dot{\varepsilon}_{vi} + \frac{E_i}{\eta_i} \varepsilon_{vi} = \frac{E_i}{\eta_i} \varepsilon \quad (4.28)$$

By employing the technique of variable separable form to solve the Equation (4.28), the following expression can be obtained

$$\varepsilon_{vi} = c_i e^{-\frac{E_i}{\eta_i} t} + \int_0^t \frac{E_i}{\eta_i} \varepsilon(s) e^{-\frac{E_i}{\eta_i}(t-s)} ds \quad (4.29)$$

The second part of the right hand side of Equation (4.29) can be expressed as

$$\begin{aligned} \int_0^t \frac{E_i}{\eta_i} \varepsilon(s) e^{-\frac{E_i}{\eta_i}(t-s)} ds &= \frac{E_i}{\eta_i} e^{-\frac{E_i}{\eta_i} t} \int_0^t \varepsilon(s) e^{\frac{E_i}{\eta_i} s} ds \\ &= \frac{E_i}{\eta_i} e^{-\frac{E_i}{\eta_i} t} \left[\frac{\eta_i}{E_i} \varepsilon(s) e^{\frac{E_i}{\eta_i} s} \right]_0^t - \int_0^t \frac{\eta_i}{E_i} \dot{\varepsilon}(s) e^{\frac{E_i}{\eta_i} s} ds \\ &= e^{-\frac{E_i}{\eta_i} t} \left[\varepsilon(t) e^{\frac{E_i}{\eta_i} t} - \varepsilon(0) - \int_0^t \dot{\varepsilon}(s) e^{\frac{E_i}{\eta_i} s} ds \right] \\ &= \varepsilon(t) - \varepsilon(0) e^{-\frac{E_i}{\eta_i} t} - \int_0^t \dot{\varepsilon}(s) e^{-\frac{E_i}{\eta_i}(t-s)} ds \\ &= \varepsilon(t) - \int_0^t \dot{\varepsilon}(s) e^{-\frac{E_i}{\eta_i}(t-s)} ds \quad (\because \varepsilon(0) = 0) \end{aligned} \quad (4.30)$$

By substituting Equation (4.30) into Equation (4.29)

$$\varepsilon_{vi} = c_1 e^{-\frac{E_i t}{\eta_i}} + \varepsilon - \int_0^t \dot{\varepsilon}(s) e^{-\frac{E_i(t-s)}{\eta_i}} ds \quad (4.31)$$

at time $t=0$,

$$\left. \begin{array}{l} \varepsilon_v(0) = 0 \\ \varepsilon(0) = 0 \end{array} \right\} \rightarrow c_1 = 0 \quad (4.32)$$

$$\begin{aligned} \varepsilon_{vi} &= \varepsilon - \varepsilon_{ei} \\ &= \varepsilon - \int_0^t \dot{\varepsilon}(s) e^{-\frac{E_i(t-s)}{\eta_i}} ds \end{aligned} \quad (4.33)$$

$$\begin{aligned} \dot{\varepsilon}_{vi} &= \dot{\varepsilon} - \frac{\partial}{\partial t} \int_0^t e^{-\frac{E_i(t-s)}{\eta_i}} \left(\dot{\varepsilon}(s) e^{\frac{E_i s}{\eta_i}} \right) ds \\ &= \dot{\varepsilon} + \frac{E_i}{\eta_i} e^{-\frac{E_i t}{\eta_i}} \int_0^t \left(\dot{\varepsilon}(s) e^{\frac{E_i s}{\eta_i}} \right) ds - e^{-\frac{E_i t}{\eta_i}} \left(e^{\frac{E_i t}{\eta_i}} \dot{\varepsilon} \right) \end{aligned} \quad (4.34)$$

$$= \frac{E_i}{\eta_i} \int_0^t \left(\dot{\varepsilon}(s) e^{-\frac{E_i(t-s)}{\eta_i}} \right) ds$$

$$\sigma = E_\infty \varepsilon + \sum_{i=1}^m E_i \int_0^t \dot{\varepsilon}(s) e^{-\frac{E_i(t-s)}{\eta_i}} ds \quad (4.35)$$

Total energy dissipation can be expressed as

$$W = \sum_{i=1}^m \int_0^T \sigma_i \dot{\varepsilon}_{vi} dt \quad (4.36)$$

$$\sigma_i = E_i \varepsilon_{ei} = E_i \int_0^t e^{-\frac{E_i(t-s)}{\eta_i}} \dot{\varepsilon}(s) ds \quad (4.37)$$

$$\dot{\varepsilon}_{vi} = \frac{1}{\tau_i} \varepsilon_{ei} = \frac{1}{\tau_i} \int_0^t e^{-\frac{1}{\tau_i}(t-s)} \dot{\varepsilon}(s) ds \quad (4.38)$$

(The proof is described in Appendix 4.1)

$$\begin{aligned}
 {}^{T-\Delta T}\mathbf{W} &= \sum_{i=1}^m \int_0^{T-\Delta T} \sigma_i \dot{\epsilon}_{vi} dt, \quad {}^0\mathbf{W} = 0 \\
 {}^T\mathbf{W} &= {}^{T-\Delta T}\mathbf{W} + \sum_{i=1}^m \int_{T-\Delta T}^T \sigma_i \dot{\epsilon}_{vi} dt = {}^{T-\Delta T}\mathbf{W} + \sum_{i=1}^m \sigma_i \Delta \epsilon_{vi} \\
 &= {}^{T-\Delta T}\mathbf{W} + {}^T\Delta\mathbf{W} \quad \left(\because {}^{T-\Delta T/2}\sigma_i \approx \frac{{}^{T-\Delta T}\sigma_i + {}^T\sigma_i}{2} \right)
 \end{aligned} \tag{4.39}$$

$$\dot{Q} = \frac{{}^T\Delta\mathbf{W}}{T} \tag{4.40}$$

where \dot{Q} is the rate of heat generation and T is the elapsed time for one revolution.

4.2.3 Thermal module

The temperature distribution in the body of the tire is predicted using an axisymmetric heat transfer model by assigning heat generation rates obtained from the dissipation module. The 2-D cross section, Figure 4.7, with elements of equal FE mesh density as that of the deformation analysis is considered for the prediction of nodal temperatures. However, the elements of heat transfer analysis (4-node axisymmetric thermally coupled quadrilateral elements) are different from those of the mechanical deformation analysis (standard 4-node axisymmetric quadrilateral elements). On the basis of the heat generated at the tire-pavement contact region and the imposed heat boundary conditions, Figure 4.7, the heat flow module determines the distribution of temperature within the tire cross section. The representative element temperature is computed from the average of its nodal temperatures.

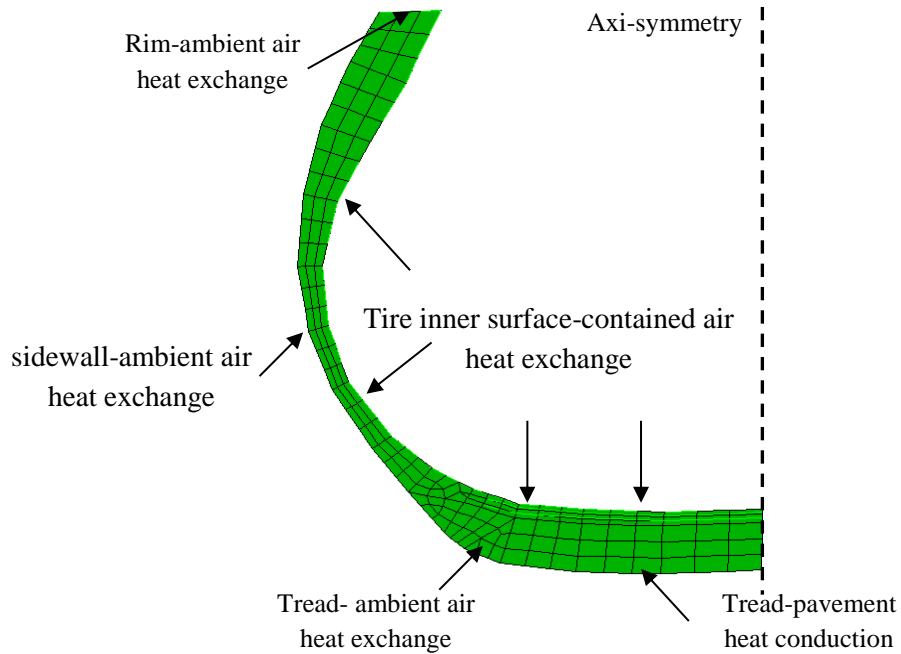


Figure 4.7 Thermal boundary conditions for the heat transfer analysis

The non-linear steady-state heat transfer of the pneumatic tire is governed by

$$-\nabla \cdot (\mathbf{k}\nabla T) = \dot{Q}(T) \tag{4.41}$$

with the boundary conditions

- i. $q = h(T - T_0)$ for rim-tire surface
- ii. $q = h_c(T - T_0)$ for tire inner surface
- iii. $q = h_c(T - T_0) + v\xi(T^4 - T_0^4)$ for tread and sidewall surfaces.

where q is the heat flux per unit area of the body flowing into the body; \mathbf{k} is the thermal conductivity; T_0 is the reference temperature, v is the Stefan-Boltzmann constant; ξ is the emissivity; h is the conduction coefficient and h_c is the convection coefficient.

Simulation conditions considered in the steady-state 2D heat transfer analysis are as follows:

- the initial temperature of all the nodes of ambient boundaries are defined to be equal to the ambient temperature.
- the contained air temperature (CAT) at steady-state conditions is 14°C to 16°C more than the outside ambient temperature (Rao et al., 2006).
- the pavement temperature is also considered as a variable, which in a standard case is assumed to be 25 °C.
- heat convection coefficients play a very important role in determining the temperature distribution across the cross section of the tire. Heat convection between the tread/road contact; tire/rim contact and liner/cavity air are assumed to be constant and the heat convection coefficients for tread/air; sidewall/air are assumed to increase linearly with the tire speed. The heat convection coefficients applied in this analysis are taken from the studies of Browne et al. (1980), Table 4.1.

Table 4.1. Heat Convection Coefficients used in this Study at Various Regions of Tire

(after Brown et al., 1980)

Region	Heat Transfer Coefficient (W/m ² °C)
Tread/Road Contact	12000
Tread/Air	5.9+3.7v
Sidewall/Air	5.9+3.7v
Tire/Rim Contact	88000
Linear/Cavity Air	5.9

As soon as the new temperature distribution in the tire cross section is computed, the material properties of each finite element are updated. A schematic layout of the whole iterative procedure is shown in Figure 4.8.

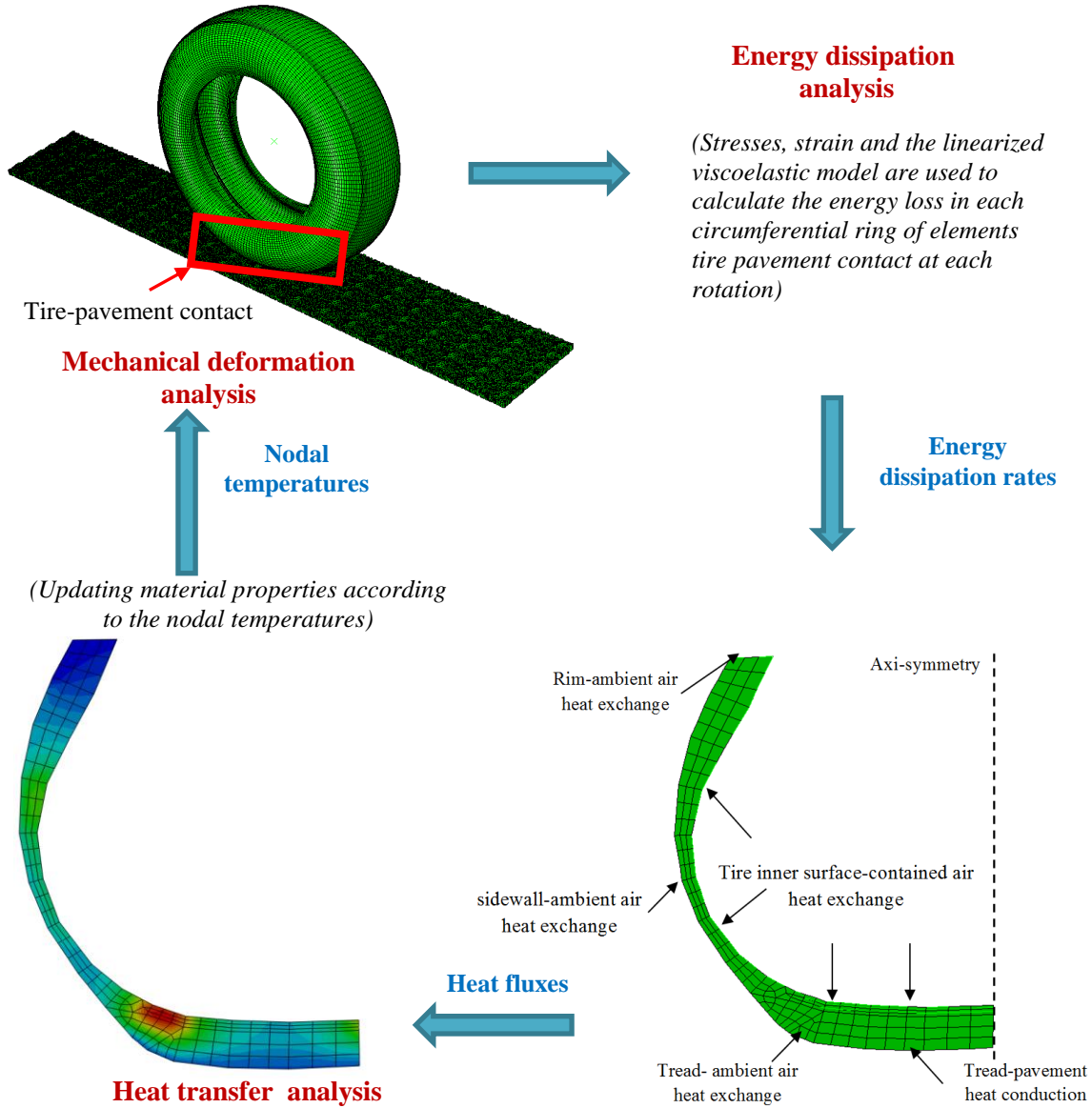


Figure 4.8. Proposed FE thermo-mechanical interaction model

4.3 Validation of temperature distribution

The experimental and FE simulation results of Ebbott et al. (1999) are utilized to validate the FE simulations of temperature development in the tire cross section. Ebbott et al. measured temperature in the tire cross section using a combination of infrared imaging and thermocouples. They also performed FE simulations of temperature development in different tires on the basis of experimental results.

In this study, the comparisons of FE simulations with the results of Ebbott et al. (1999) are made for a smoothly treaded P195/75R14 radial passenger car tire rolling on a smooth pavement

surface. An initial temperature of 30°C is considered. The procedure described in the Section 4.2 is then followed to generate temperature in the tire. A steady state heat transfer analysis is performed for approximately for 1000 sec beyond which there is no appreciable increase in the nodal temperatures at different regions of the tire cross section is observed, Figure 4.9. It is observed that the temperature distribution is not uniform throughout the tire cross section and the maximum temperature is developed in the shoulder area.

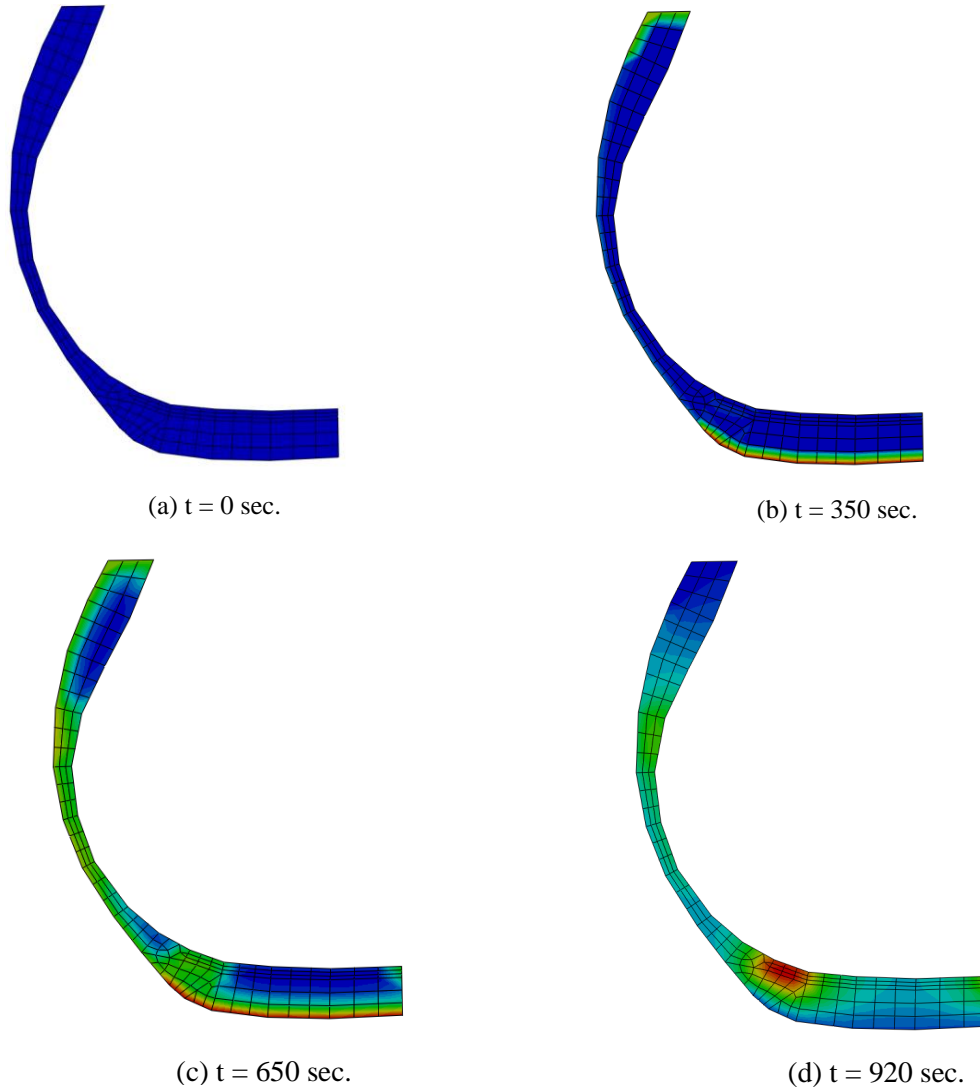


Figure 4.9. Development of temperature over time period in different time steps

An average temperature development in the tire shoulder is taken as the reference value for the comparison of temperature development in the shoulder region between predicted and experimental test data by Ebbott et al., Figure 4.10a. The results of the simulation are comparable with the experimental findings with a maximum difference of 5.2%. Figure 4.10b shows the comparison of temperatures in the different regions of tire cross section between the results of FE simulations and the experimental studies of Ebbott et al. A maximum of 8% difference is observed between the results of FE simulations and Ebbott et al. experimental studies.

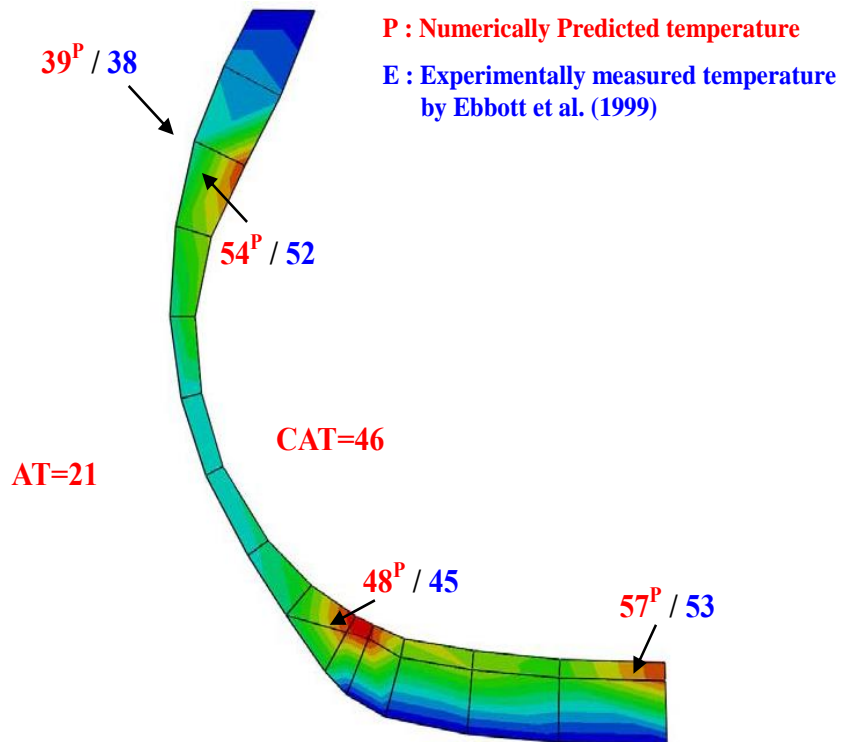
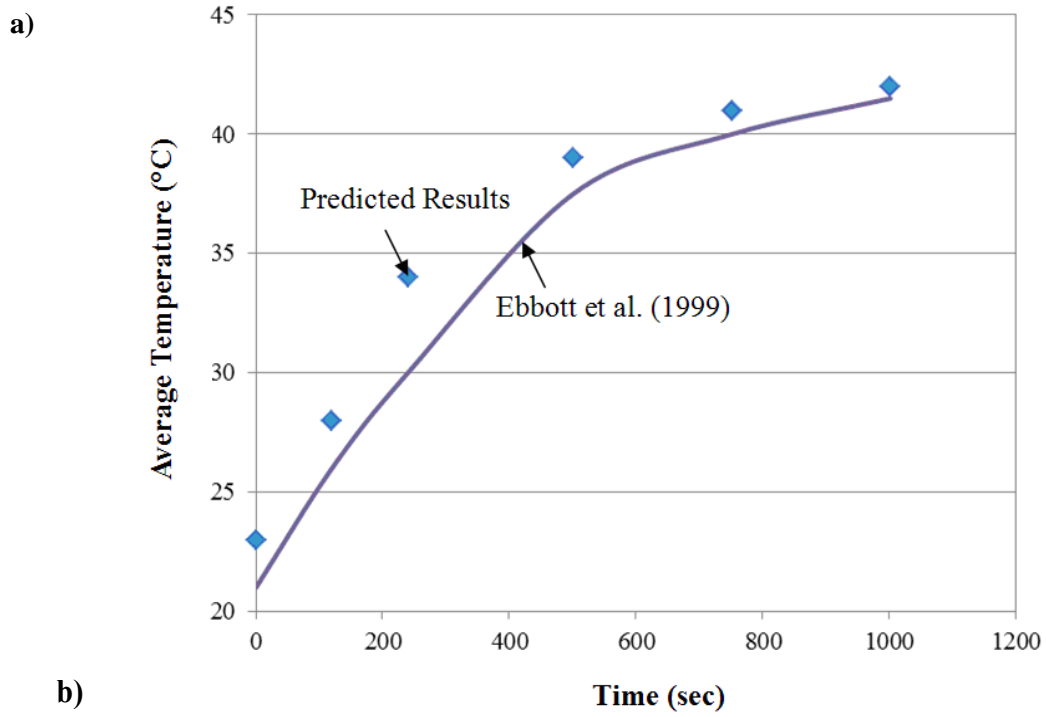


Figure 4.10. Comparison of temperature measurements in the tire shoulder measured by Ebbott et al. (1999) and numerical model

4.4 FE Model Tests

In general, friction measuring equipment are used to measure the pavement friction. However, the accuracy of friction measurements is very much dependent on the tire temperature of such equipment. Therefore, it is necessary to determine how much time it takes to warm up the tire and thus finding out the pretest run of the test tire required, before the actual friction measurements are taken. For this purpose, heat transfer techniques are used to determine the temperature development in a full rolling tire under steady state conditions and the time required to warm up and cool down of a partially skidding tire. Transient, heat transfer technique is used for the later part. Also, the time required for different regions of a full rolling tire to reach an effective temperature equilibrated state while a traversing on an asphalt pavement surface is ascertained. Such kind of analysis gives insight into the effect thermal behavior of tire on the tire hysteresis which ultimately decides its friction performance. Subsequently, relationships are found out between tire temperature (TT) and combined temperatures of pavement (PT) and ambient air (AT). Finally, the effect of friction between tire-pavement on the average temperature development in the tire body is analysed.

4.4.1 Temperature development in a test tire

It is important to determine, “*how much distance should the test tire traverse before the measurement of friction under given test conditions?*”. The developed FE model can be utilized to answer this question on the basis of the comparison of temperature development in the cross section of test tire moving at specified speed and test condition. For example, if the FE model simulates the condition of tire rolling at 0% slip (full rolling tire) and a speed of 70 km/h on a mesh of asphalt pavement, the output of the temperature distribution, Figure 4.11, which represents the actual field condition of test tire just before the brakes are being applied and at this stage, the tire is in steady state thermal condition.

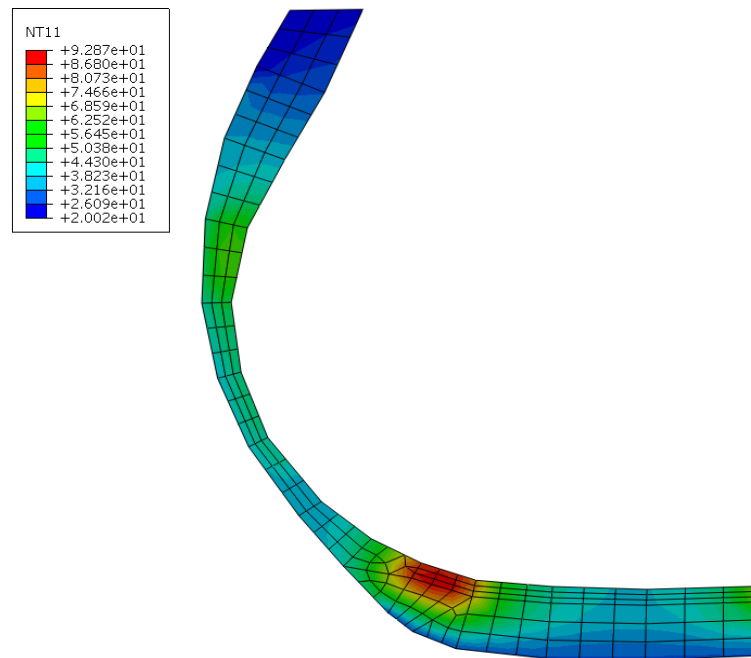


Figure 4.11. Development of temperature in the tire cross section at 70 km/h in pure rolling condition

However, if the same test tire is traversing at 70 km/h speed and 86 % slip ratio, it is observed that after 128 sec, the tire nearly develops the same temperature distribution, Figure 4.11. Based on this FE test, a recommendation can be made that at 21°C pavement temperature, 21°C ambient temperature, 36°C contained air temperature the test tire must be run for at least 2.6 km approximately before actual friction measurements are taken.

4.4.2 Temperature rise and cool down in the tire body

In order to predict temperature rise, the tire is assumed to slip (86%) instantaneously at 70 km/h over an asphalt surface. From this, the heat fluxes are computed and applied to the corresponding components of axisymmetric tire model and held constant. Besides, thermal convection coefficients for the various regions of the tire cross section as described in the previous section are applied. The initial temperature distribution is uniform and equals the ambient temperature. During the heat transfer analysis, temperature rises with time. The tire is assumed to come to halt at an assumed stop time to predict temperature cool down. At this stop time, the heat sources (dissipation energy rates) are released to zero in all components of the tire and let the tire to cool down.

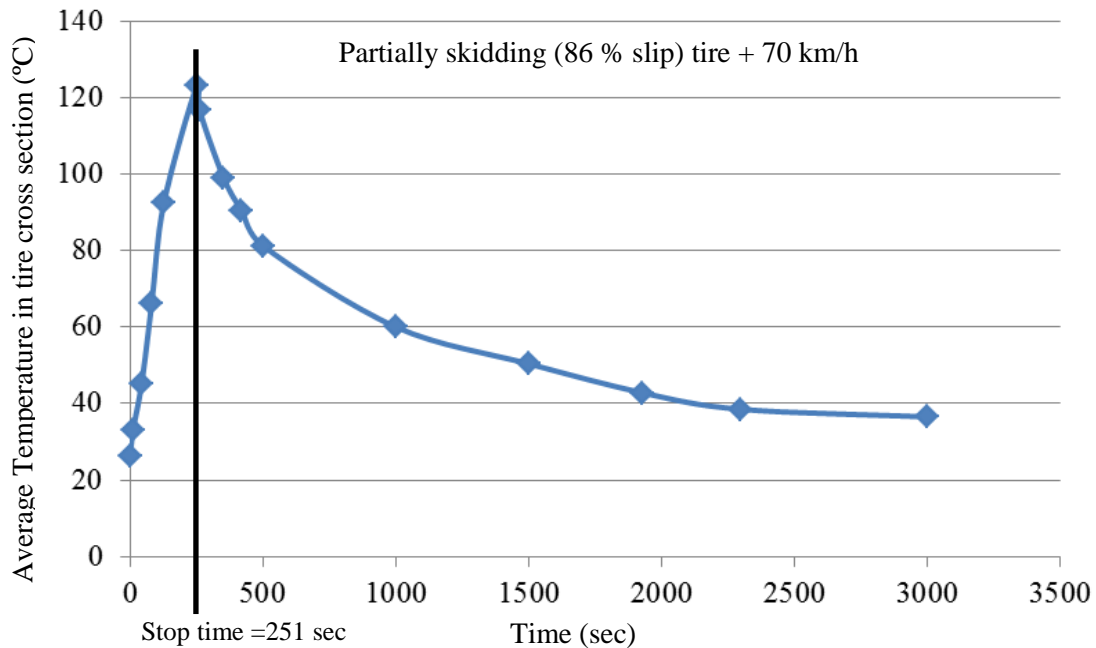


Figure 4.12. Prediction of average temperature rise and cool down in tire cross section over an asphalt surface

The prediction of temperature distribution in the tire body, from temperature rise and then temperature cool down, Figure 4.12. The simulation of temperature rise in the partially skidding tire is performed for 251 sec. Subsequently, the simulation of temperature cool down in the tire is performed by releasing the heat sources to zero in all components of the tire. It can be observed that the partially skidding tire takes approximately 2300 sec to come back to the steady state temperature condition.

4.4.3 Temperature development in different regions of a fully rolling tire

For this analysis, thermal coefficients of various regions of the tire cross section as given in the Table 4.1 are applied to the FE model. The heat transfer coefficients of tread-road contact, tread-rim contact and linear/cavity air are assumed to be constant while the coefficients corresponding to tread-air and sidewall-air are assumed to increase linearly with the tire speed. The heat generation rates, which are obtained for a tire rolling at a specific speed of 70 km/h and slip ratio of 0%, are used to compute nodal temperatures of various regions of tire cross section.

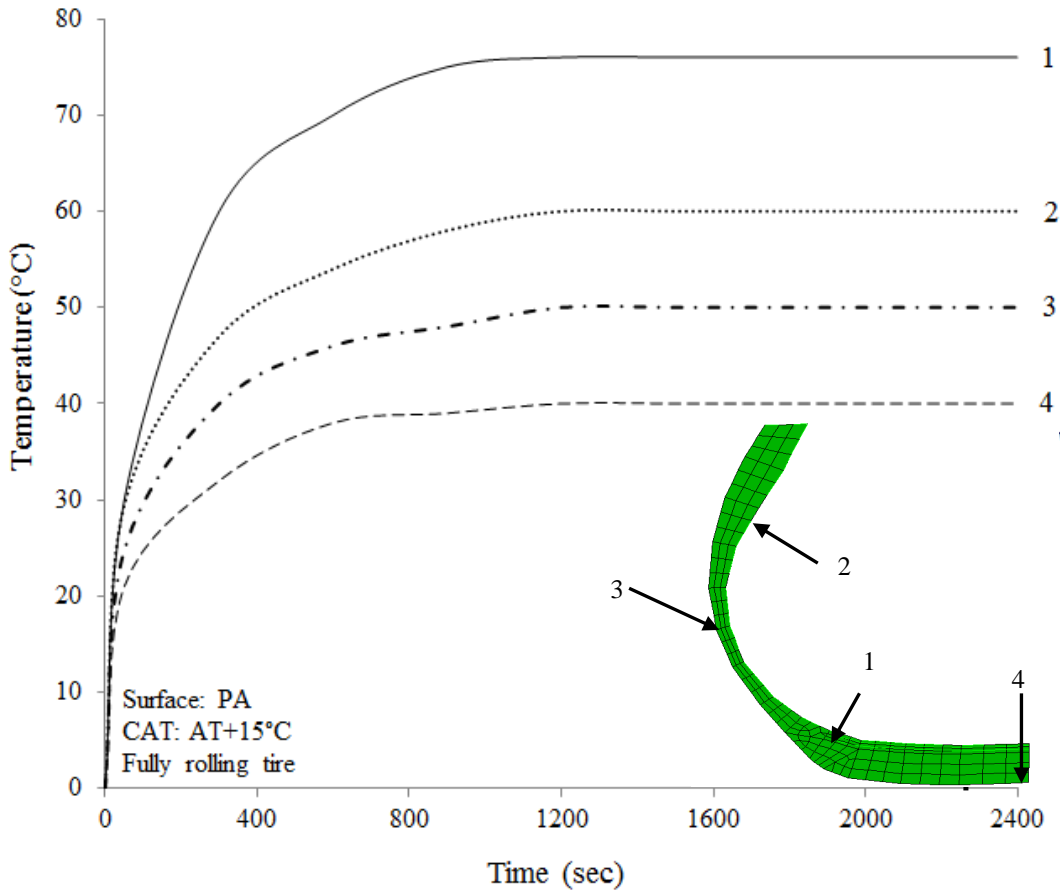


Figure 4.13 Temperature development in different regions of a fully rolling tire

In order to predict the temperature rise, four regions of the tire cross section are considered, Figure 4.13. Region-1 is a portion near the inner boundary around belt edge, approximately in between the tread and the sidewall regions. Region-2 is an inner boundary portion near apex of the tire cross section. Region-3 is an outer boundary of the side wall and Region-4 is an outer tread surface in contact with the pavement. At time zero, the tire is assumed to roll instantaneously at a given speed over a PA pavement surface. The heat fluxes are applied to the corresponding components of the axisymmetric tire model and held constant.

It can be observed that temperature rises in all the four components of the tire with time and at one point in time, the entire tire behaves in steady state thermal conditions. The maximum temperature distribution with time was observed in the Region-1 followed by Region-2, Region-3

and Region-4. This trend gives information about the magnitude of heat generation associated with the respective regions and also the lower heat losses associated with the inner tire surfaces than outer surfaces.

4.4.4 Relation between tire band temperature and combined pavement and ambient temperatures

In this section, the combined effect of pavement and ambient temperatures on tire band temperature is presented. A total of 100 data points (10 PT × 10 AT) are analysed for a given pavement surface. A high coefficient of determination exists for TT vs. sum of PT and AT, Figure 4.14. It can be observed that higher values of the sum of PT and AT result in a higher TT. The TT can be effectively predicted by using a single parametric Sigmoidal function (see Equation (4.42)) as opposed to the linear relationship proposed by the past researchers (Oliver 1989).

$$TT = (-0.413T + 10.057)e^{-0.05T} + (0.118T + 26.249)(1 - e^{-0.05T}) \tag{4.42}$$

where T is the sum of pavement and ambient temperatures.
The procedure to obtain the Sigmoidal function is described in Appendix-1.

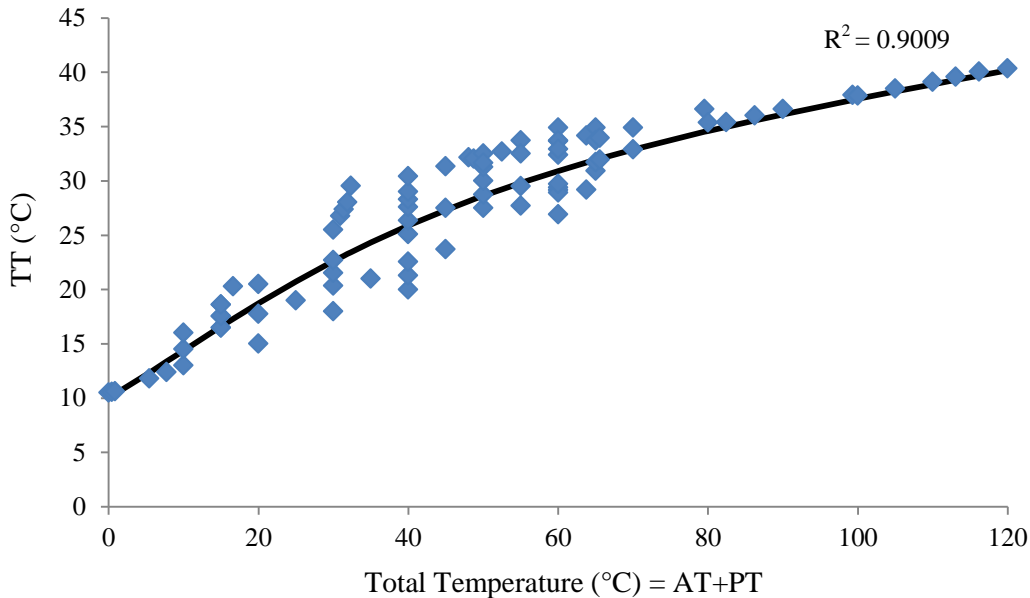


Figure 4.14. Tire band temperature vs. combined pavement and ambient temperatures

4.4.5 Effect of friction coefficient on the temperature development

Another application of the developed FE model is to find out the effect of tire-pavement friction coefficients on the rise of temperature in the tire body. The proper way to perform this analysis is to perform simulations with FE meshes of different asphalt pavement surfaces and relate the friction output with the temperature development which will be discussed in the next chapter. However, such analysis would require a huge simulation time and computational resources.

Thus an easier way to tackle this problem is given as below:

The pavement surface is considered to be smooth and friction is given as input. It should be noted that the input value of friction is the total effect of adhesion and hysteretic components of friction. Here it must be noted that the procedure described in Section 4.2 is capable to deliver friction as an output from the model.

Thermal boundary conditions are kept constant throughout the analysis, (a) 20°C pavement temperature, (b) 20°C ambient temperature, (c) 32°C contained air temperature with tire rolling at 70 km/h and 86% slip condition, (d) the time allowed for the temperature development was kept constant at 0.5 sec.

The variation of average temperature with different pavement friction values are studied until steady state thermal condition is achieved, Figure 4.15. Even though there is no macrotexture on the pavement, some temperature at zero friction coefficients is observed due to the difference between CAT and temperature due to the deformation of tire.

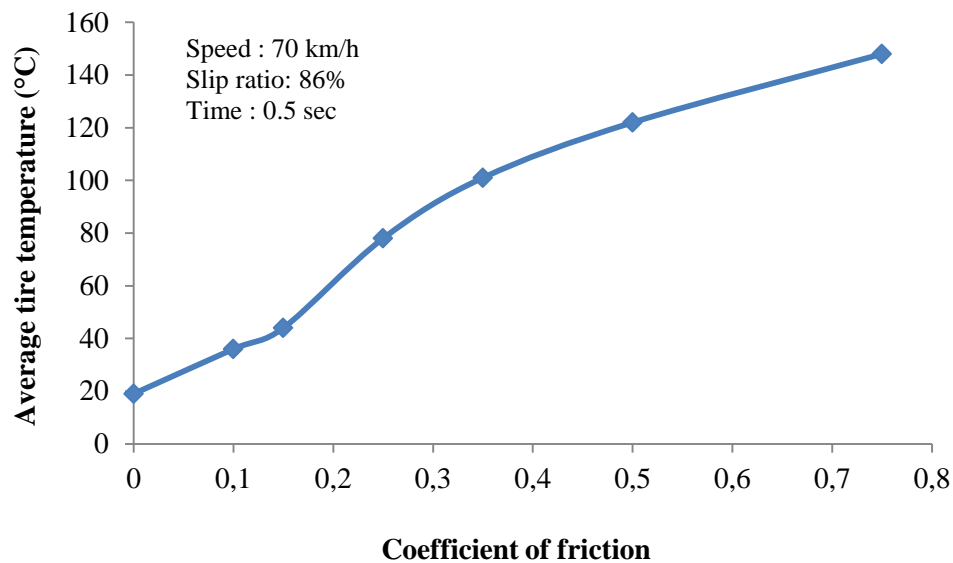


Figure 4.15 Average temperature development in tire pavement cross section with varying friction

4.5 Summary

This chapter is devoted to the development of a thermo-mechanical model to address the complex relationship between tire-pavement friction and tire temperature in the FE framework. In order to develop thermo-mechanical model, the tire rubber material is treated as time and temperature dependent VE material and the rheological properties of rubber are obtained from the results of chapter 2. Also, the micro-mechanical FE asphalt pavement surface and the three dimensional FE PIARC tire model which were developed in Chapter 3 are utilized in the analysis.

A computationally efficient approach of sequential static-transient deformation analyses is proposed. In this, the tire is made to travel over a micro-mechanical FE asphalt surface mesh. By using the stresses and strains from these simulations and by using the viscoelastic model of tire rubber, the energy dissipation is computed. Heat transfer analysis is carried out by using the results from energy dissipation analysis to compute the nodal temperatures and to obtain the temperature distribution in the various regions of tire cross section.

The results from the proposed FE analyses are in good agreement with the past experimental findings. It is observed from the analyses that the temperature develops in different components at different rates as the energy dissipation rates associated with the respective component. Pavement temperature and ambient temperature are the two important factors which influence the tire temperature. A statistical relationship between TT and AT/PT has been determined. It is observed that a strong correlation exists between TT and total temperature (i.e. AT+PT). In contrast to earlier studies, it was found that a Sigmoidal curve provides the best fit. The practical application of the developed tool will be discussed further in the next Chapter.

5 Tire-Pavement Interaction Under Different Operating Conditions

5.1 Introduction

Design speeds and other recommendations proposed by highway agencies for the safety against skidding are typically based on either past experience or they are derived from friction measurements which has a very limited scope in terms of transferability. It is also correct to say that not much attention has been paid to analyze the effect of temperature on the tire-pavement friction measurements. However, past research studies show that the skid resistance is usually influenced by the conditions such as pavement temperature, ambient temperature, contained air temperature and surface characteristic of pavement. Similarly, the knowledge of cornering force and sideslip angle is essential in order to improve vehicle safety, handling, steering ability, comfort and performance Baffet et al. (2009). Apart from the sideslip angle and the developed cornering forces, the overall anti-skidding performance of a pneumatic tire is also affected by the vehicle operating conditions such as the tire load, inflation pressure, speed, road texture and temperatures of ambience and pavement. Mutual interactions of these operating conditions create a complex relationship between these parameters and the tire's ability to combat against skidding during straight line braking and cornering actions. The developed forces and torques under such complex operating conditions require state-of-art dynamometers, sensors and expertise in order to arrive at the precise friction values. On the other hand, analytical modeling techniques require precise tire and pavement texture analytical models. This makes it extremely difficult for the tire industries and the road agencies to evaluate the tire's anti-skidding performance either experimentally or analytically, on different sets of test conditions.

This Chapter investigates the frictional behavior of a test tire under different surrounding temperature conditions using the thermo-mechanical finite element model as developed in Chapter 4. Under this investigation, the influence of critical combination of pavement temperature (PT), ambient temperature (AT) and contained air temperature (CAT) on the frictional measurements is ascertained. Finite Element models of fully and partially skidding tires over different asphalt pavement surfaces, namely, Porous Asphalt (PA), Ultra-Thin Surface (UTS) and Stone Mastic Asphalt (SMA) are analyzed. FE simulations are also performed to predict the effect of tire band temperature on the hysteretic friction. An attempt is also made to determine the cornering performance of a rolling tire running on aforementioned asphalt pavement surfaces under different operating conditions.

5.2 FE Model parameters

This Chapter deals with the sensitivity analysis of various factors associated with hysteretic friction of a pneumatic tire traversing over simulated asphalt pavement surfaces. For ease of presentation, a PIARC 165R15 (PIARC, 2004) tire traversing at a constant velocity of 70 km/h with a constant load of 4 kN and a constant inflation pressure of 200 kPa is considered. Tire rolling at 20%, 86% and 100% slip ratios were simulated to analyze the effect of different friction equipment which typically operate at these slip conditions. X-ray CT Scan of three different surfaces, namely, PA, UTS and SMA were considered. The tire stiffness and tire rubber material properties were obtained via laboratory tests. Pavement surface morphology, applied boundary conditions and other factors considered in the model are described in the Chapter 4.

Past experimental (Oliver, 1989) works show that, for a given set of tests conditions, AT and PT are interdependent and they are correlated to the tire temperature. However, AT and PT are dependent on several other factors such as humidity, wind and other local environmental factors. Hence, a universal relationship between AT and PT is difficult to establish. For this reason, in this study, AT and PT are considered as independent parameters with each other. A wide range of AT and PT is covered in the analysis. Some of the combinations, such as AT of 40°C and PT of 0°C, might be trivial in practice, but they are considered solely for research purposes. As a result, for any given pavement surface texture type and tire slip ratio, the model is analyzed for different AT values in a range from 0°C to 40°C and PT in a range from 0°C to 60°C. In general, CAT is 14°C to 16°C more than the outside ambient temperature (Bridgestone, 2012), if correct inflation pressure is maintained for the given normal load. Accordingly, a wide practical range of CAT from AT+10°C to AT+20°C is considered.

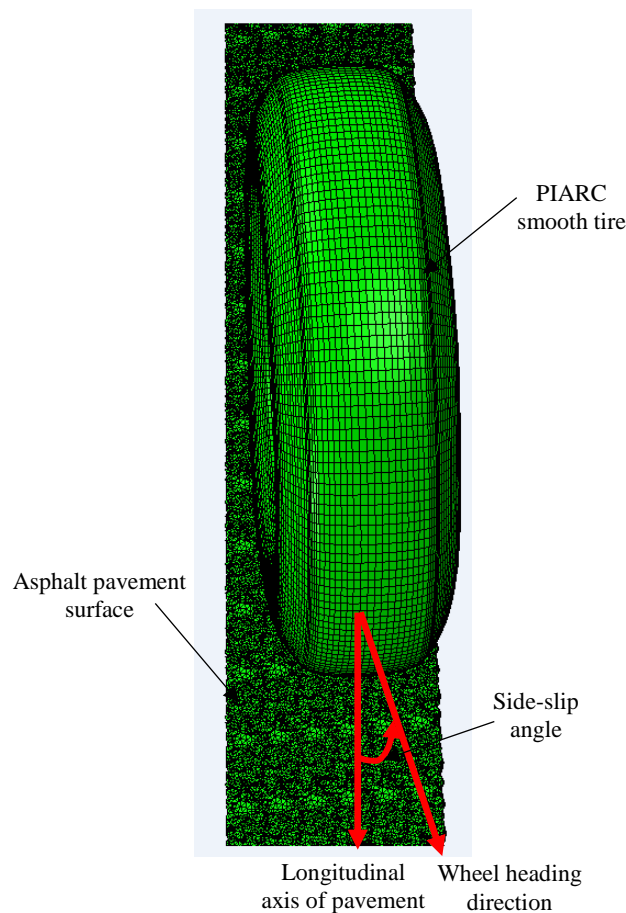


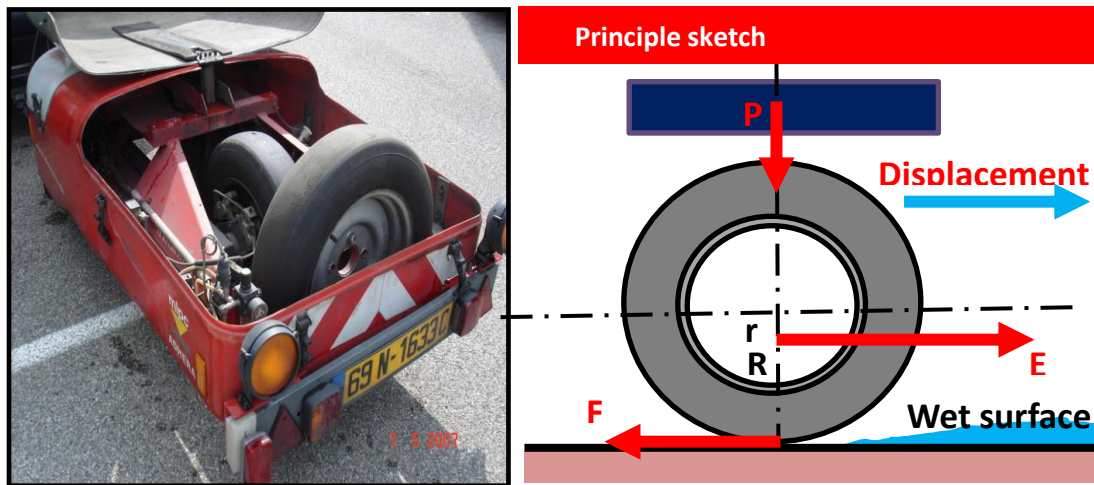
Figure 5.1 Three-dimensional FE model of a PIARC smooth tire rolling with sideslip angle on an asphalt pavement mesh

For the cornering analysis, the same PIARC 165R15 tire rolling at sideslip angles of 0° to 10° at 1° interval is simulated to analyze the effect of various slip conditions on the cornering frictional force. A wide range of loads, tire inflation pressures and vehicle speed of 1500 N to 4500 N, 110 kPa to 350 kPa and 25 km/h to 75 km/h respectively is considered in the simulations. The cornering simulations are performed on the same simulated pavement surfaces of PA, UTS and SMA. In this study, the cornering angle, also called the sideslip angle of a tire is defined as an

angle that is formed between the wheel's actual direction of travel and the longitudinal axis of the pavement, Figure 5.1, and the resulting lateral force is called cornering force. The phenomenon of side slip is mainly due to the lateral elasticity of the tire (Clark, 1981). The sideslip angle is introduced in the structure module at mechanical deformation analysis stage, and the resulting cornering friction is calculated. In order to model the cornering maneuvers, the tire is prescribed with a velocity boundary condition in both in the longitudinal and the lateral directions.

5.3 Validation

In order to validate the capability of the FE model to predict the tire-pavement friction coefficient on asphalt surfaces, data measured by a French friction testing device called Adhera is used, Figure 5.2. The field experiments were performed at the IFSTTAR research organisation on different asphalt pavement test tracks at various speeds.



(a) Adhera trailer with smooth PIARC test wheel

(b) Principle of measurement



(c) Friction measurements by Adhera device

Figure 5.2 Field friction measurements on IFSTTAR test tracks

The X-ray tomography technique was utilized to obtain the scans of the same asphalt pavement surfaces. The procedure to obtain discretised FE meshes from these scans was discussed in detail in Chapter 3.

The following are the summary of testing conditions of the field measurements:

- Adhera longitudinal friction testing device
- Tire type : PIARC 185/60 R15 smooth tire
- Slip ratio : 100%
- Velocity : 40, 60 ; 80 and 90 km/h
- Tire inflation pressure and weight : 200 kPa and 2.5 kN
- Pavement surface texture : Porous Asphalt Concrete 0/6; Dense Asphalt Concrete 0/10
- Water thickness : 0.5; 1.0 mm

The Adhera testing device is composed of a tractor and a trailer where the test wheel is located, Figure 5.2a. The structure of the trailer is very similar in its dynamics to a quarter of an average light vehicle. The wheel supporting arm and the bar, which measures the frictional force, form a parallelogram with the linkage to the towing vehicle, Figure 5.2b. The principle of measurement consists of determining the effort which, when applied to a lever of precise dimensions, balances the frictional torque exercised by the previously wetted roadway on the average tire of a loaded vehicle.

The test consists of running the equipment at a required speed, a water depth on a given asphalt surface, locking the measurement wheel and recording the effort required to drag it along. This drag effort divided by the load on the wheel gives the braking force coefficient. The running speed ranges between 40 and 120 km/h. By repeating the basic test at different speeds with a smooth tire under wetting conditions of the pavement enables the macrotexture of the road surface to be evaluated. The value of Longitudinal Friction Coefficient (LFC) is calculated by averaging the frictional force over a distance of 10 m out of total displacement of 20 m at 40, 60, and 80 km/h. The total displacement is increased to 25 m at a speed of 90 km/h, Figure 5.2c.

The comparison of the results from finite element friction model is made against the field measurements under the similar set of test conditions of:

- a PIARC smooth tire rolling at 100% slip ratio (full skidding) on a PA pavement surface,
- a PIARC smooth tire rolling at 100% slip ratio on an AC-10 pavement surface.

Figure 5.3a shows a comparison between experimentally measured and model predicted LFC values at three different speeds, 40 km/h, 60 km/h and 90 km/h for a locked PIARC tire on a PA surface. Similarly,

Figure 5.3b shows a comparison between measured and predicted LFC on an AC-10 surface at four different speeds, 40, 60, 80 and 90 km/h. From the figures, it can be observed that the LFC friction is highly dependent on the speed and it decreases with increase in the speed. The numerical differences between the predicted and measured LFC values are less than 0.07. In terms of percentage error, except for one case with 17% error, all the remaining cases have errors of 10% or less. For all the examined cases, the comparison between the measured and predicted results show a good agreement, considering the unavoidable variations of field conditions and

possible measurement errors.

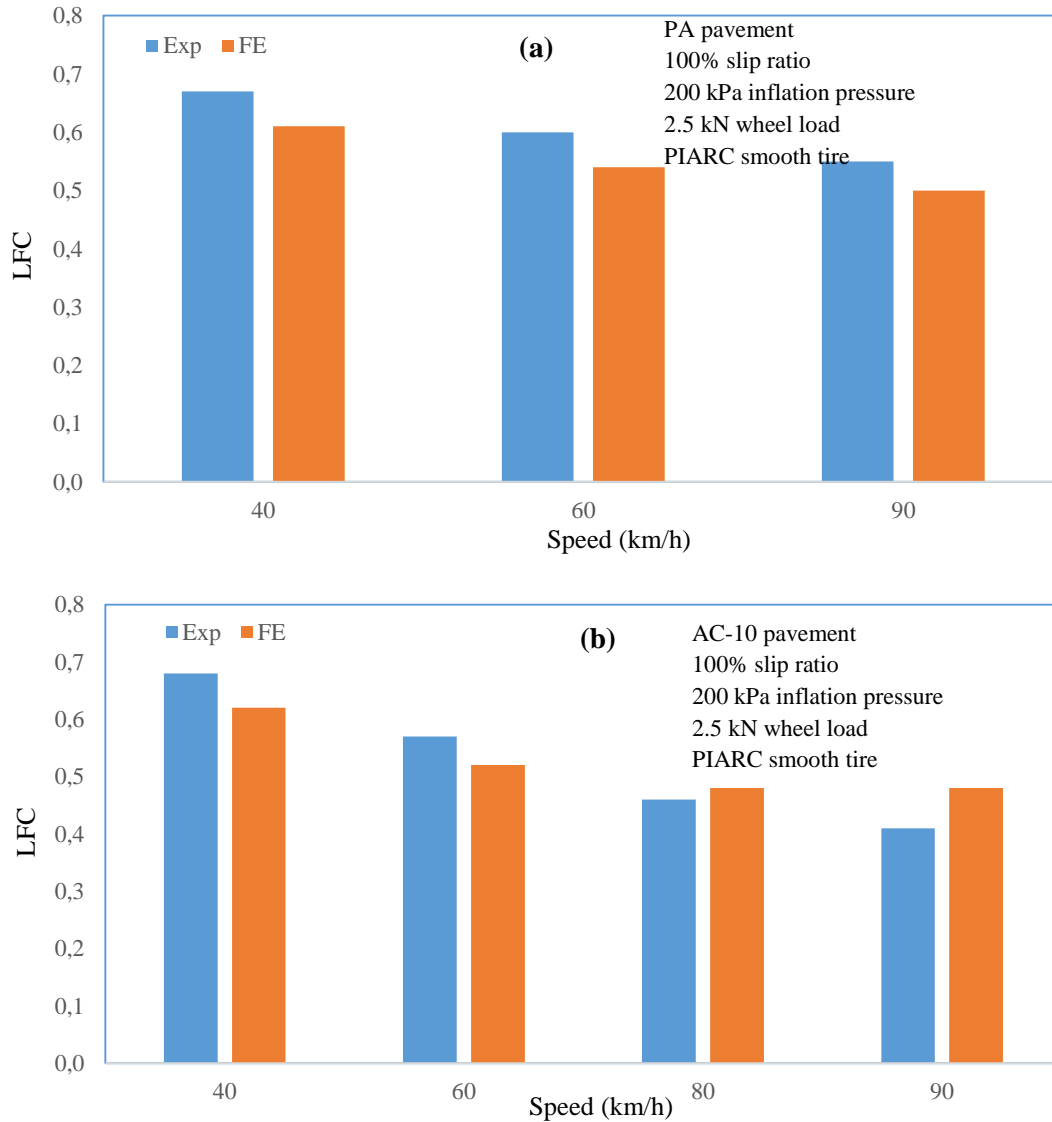


Figure 5.3 Verification of simulation model against experimentally measured data

5.4 Analysis of Straight-line Braking Tire

5.4.1 Effect of tire band temperature on the hysteretic friction

This subsection discusses the effect of the tire band temperature on the hysteretic friction of a PIARC tire rolling at different slip ratios over PA, UTS and SMA pavement surfaces, Figure 5.4 to Figure 5.6. Each plot shows the resulting hysteretic friction against the TT due to possible combinations AT and PT which give rise to the same TT. A nonlinear polynomial curve fit was employed to bring about the relationship between the hysteretic friction and TT.

TIRE-PAVEMENT INTERACTION UNDER DIFFERENT OPERATING CONDITIONS

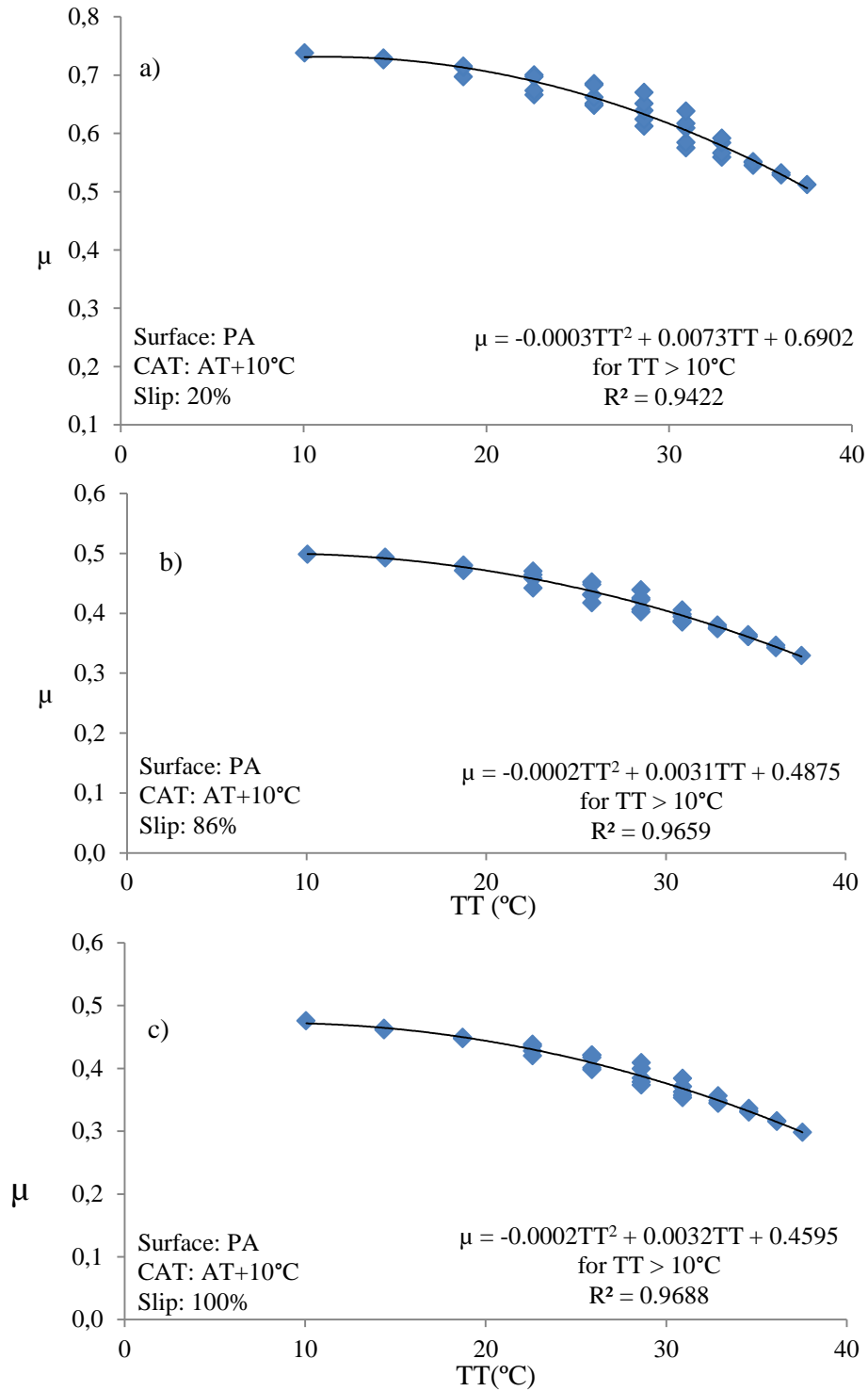


Figure 5.4. Hysteretic friction vs. tire band temperature for a PA surface under different slip conditions

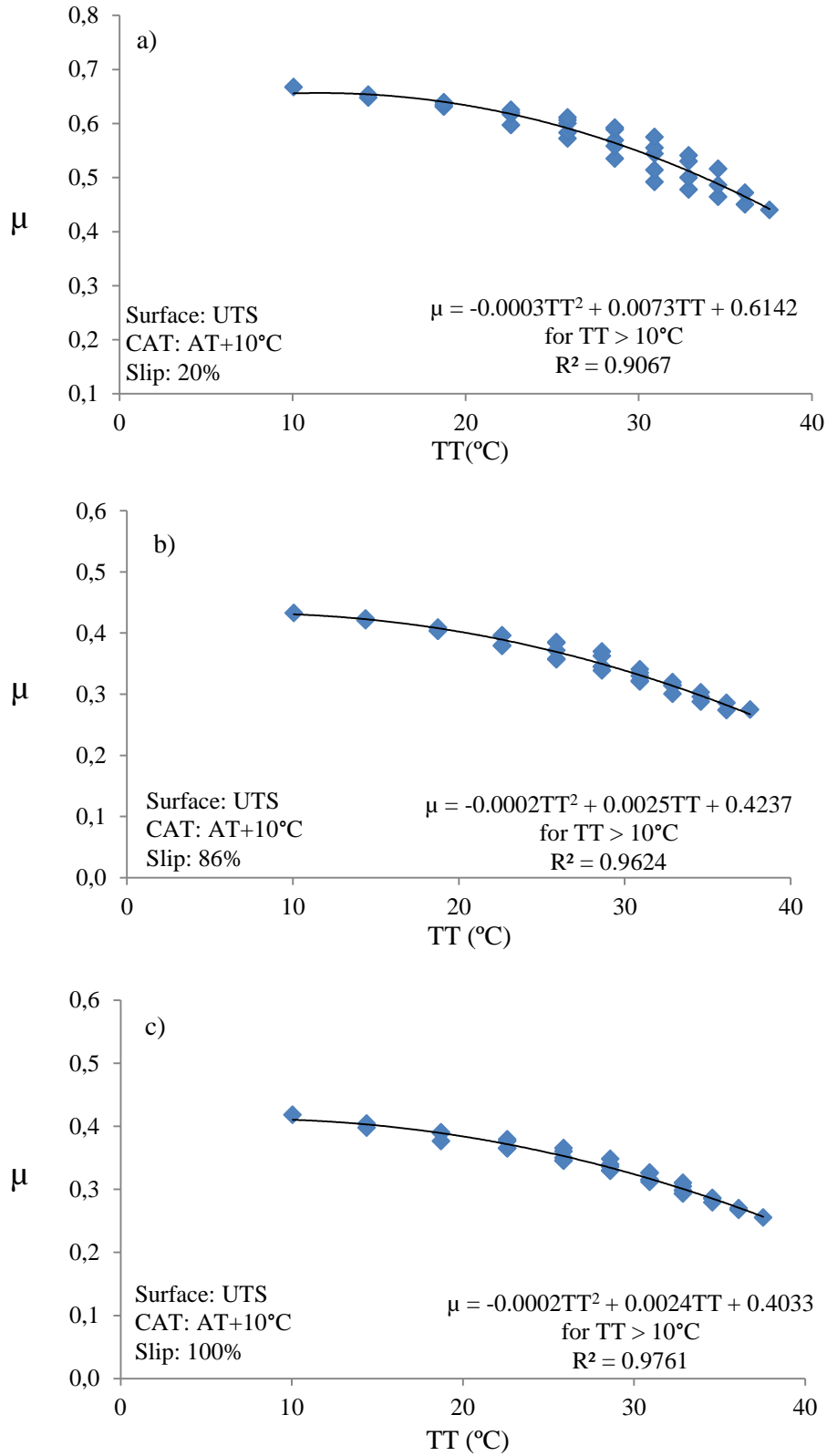


Figure 5.5. Hysteretic friction vs. tire band temperature for UTS surface under different slip conditions

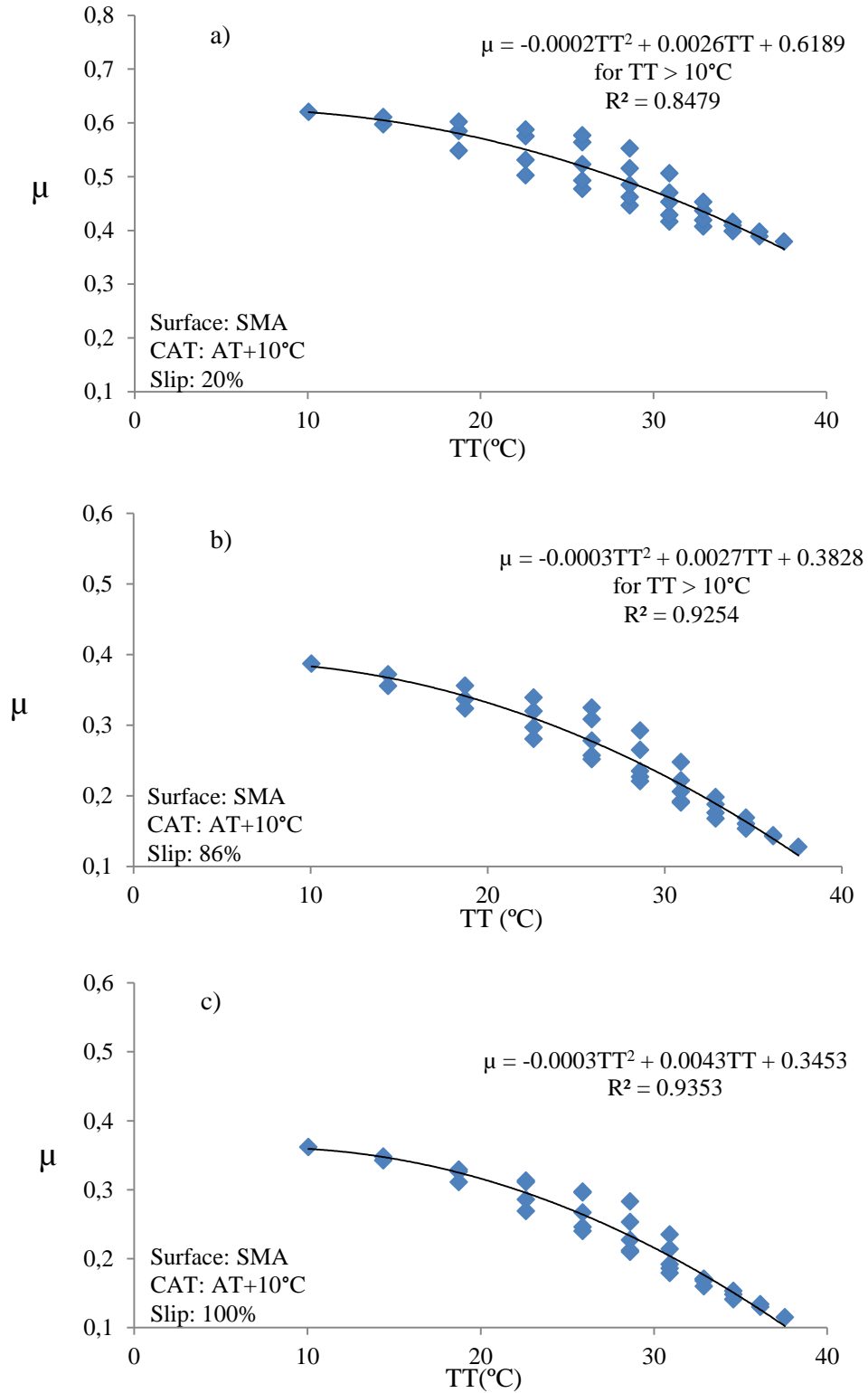


Figure 5.6. Hysteretic friction vs. tire band temperature for SMA surface under different slip conditions

It can be observed from the plots that the hysteretic friction decreases with increase in TT, for all cases analysed. For example, as shown in Figure 5.4a, for the case of a tire rolling with 20% slip ratio over a PA pavement surface, an increase in TT from 10°C to 38°C results in the decrease of hysteretic friction from 0.74 to 0.51 i.e. the friction value drops by a percentage of 31% for an increase in TT of 28°C. A similar trend can be observed for the same tire traversing with other slip ratios over other pavement surfaces. This implies that the risk associated with the loss of braking friction is more for tires with higher tire band temperatures.

Different friction measuring equipment operate at different slip conditions which may result in different tire band temperatures. For this comparison to be made, the same analysis was carried out at different slip ratios of 20%, 86% and 100% on the PA pavement surface as shown in Figure 5.4a to Figure 5.4c. The plots on the corresponding figures show that the hysteretic friction decreases with an increase in the TT for all slip ratios. However, the magnitude of decrement is in the order of increasing slip ratio. Similar trend can be observed for other pavement surfaces like UTS and SMA as shown in Figure 5.5 and Figure 5.6 which shows that the temperature vulnerability of the hysteretic friction for a blocked wheel condition is higher than for a wheel rolling at lower slip ratios.

Figure 5.4 to Figure 5.6 analyse the relationship between the hysteretic friction and the TT for different pavement surfaces at different slip ratios. The average percentage decrease in the hysteretic friction from PA pavement to UTS and SMA pavement were observed to be 11% and 22% respectively, which confirms the fact that the pavement surface with higher macrotexture produces higher hysteretic friction. The average percentage decrease in the hysteretic friction for a total increase in TT of 28°C was observed to be 58% for SMA, 37% for UTS and 34% for PA pavements. This implies that with surrounding tire band temperature, the hysteretic friction decreases at a faster rate for an SMA pavement surface followed by an UTS and a PA respectively.

5.4.2 Effect of Pavement Temperature on the Hysteretic Friction

This sub-section discusses the effect of PT on the hysteretic friction, and the computed results are shown in Figure 5.7. For a constant AT and CAT, the hysteretic friction decreases with an increase in PT, for all the cases analyzed. For example, as shown in Figure 5.7a, 60°C increase in PT decreases the friction from 0.74 to 0.58, for a constant AT of 0°C. This implies that the risk associated with the loss of braking traction is slightly more on pavements with higher temperatures. The friction values drops by 0.11 for an increase in PT from 0°C to 60°C as shown in Figure 5.7a to Figure 5.7c.

Figure 5.7 also shows the relationship between the hysteretic friction and the PT for different pavement surfaces, at a constant slip ratio of 20%. For the same increase in PT by 60°C, the average decrease in friction is observed to be 0.19 and 0.13 for SMA and UTS pavement surfaces respectively. This implies that with surrounding temperatures, the hysteretic friction decreases at a faster rate for an SMA pavement surface followed by an UTS and a PA respectively. The same analysis was carried out at different slip ratios as shown in Figure 5.7 to Figure 5.9. The plots on the corresponding figures show that the hysteretic friction decreases with an increase in PT for all slip ratios. However, the magnitude of decrement is in the order of increasing slip ratio. It should also be noted that the change in hysteretic friction between 86% and 100% slip ratios is marginal.

TIRE-PAVEMENT INTERACTION UNDER DIFFERENT OPERATING CONDITIONS

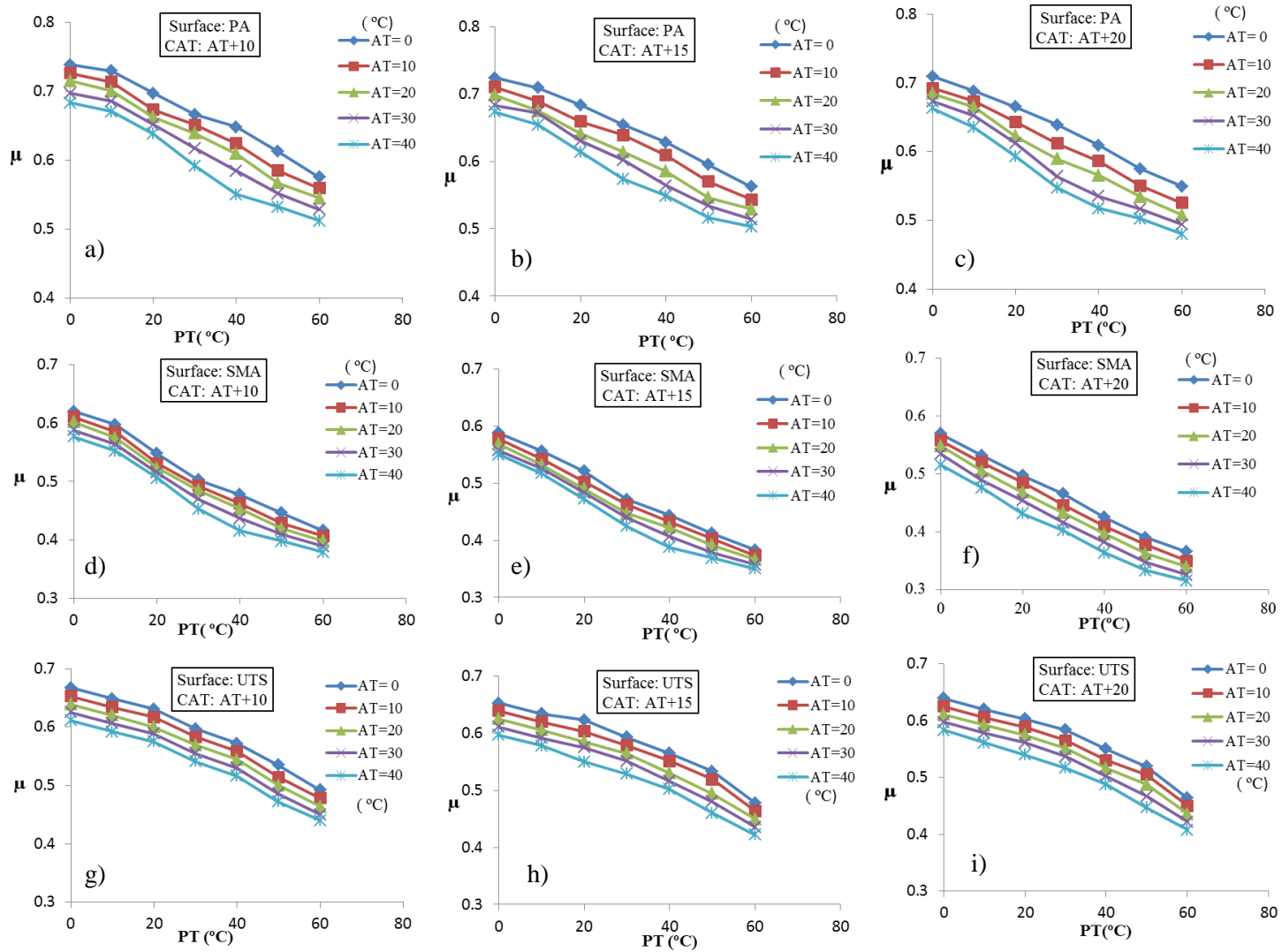


Figure 5.7 Friction vs. pavement temperature for a PIARC tire rolling at 20% slip ratio

TIRE-PAVEMENT INTERACTION UNDER DIFFERENT OPERATING CONDITIONS

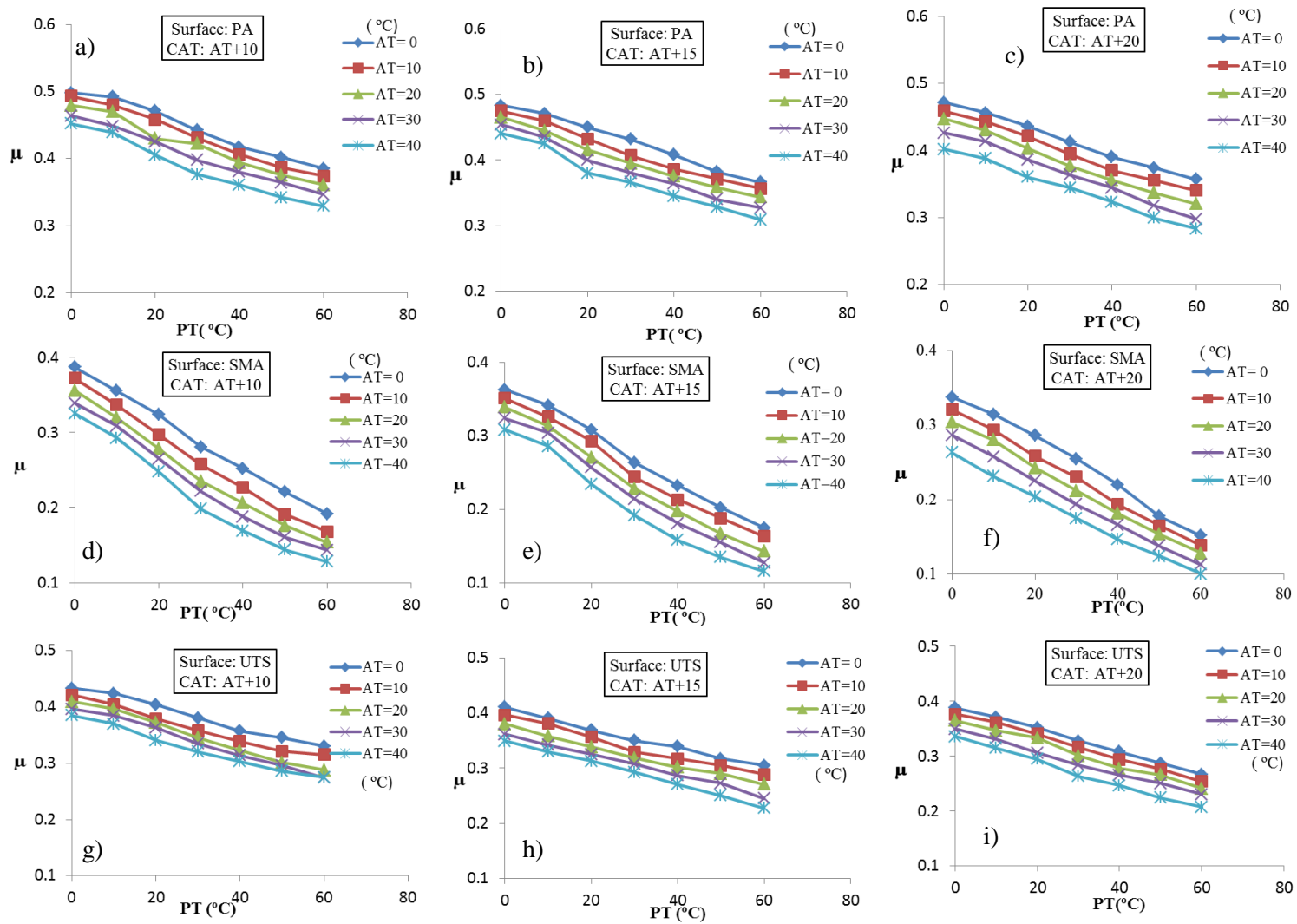


Figure 5.8 Friction vs. pavement temperature for PIARC tire rolling at 86% slip ratio

TIRE-PAVEMENT INTERACTION UNDER DIFFERENT OPERATING CONDITIONS

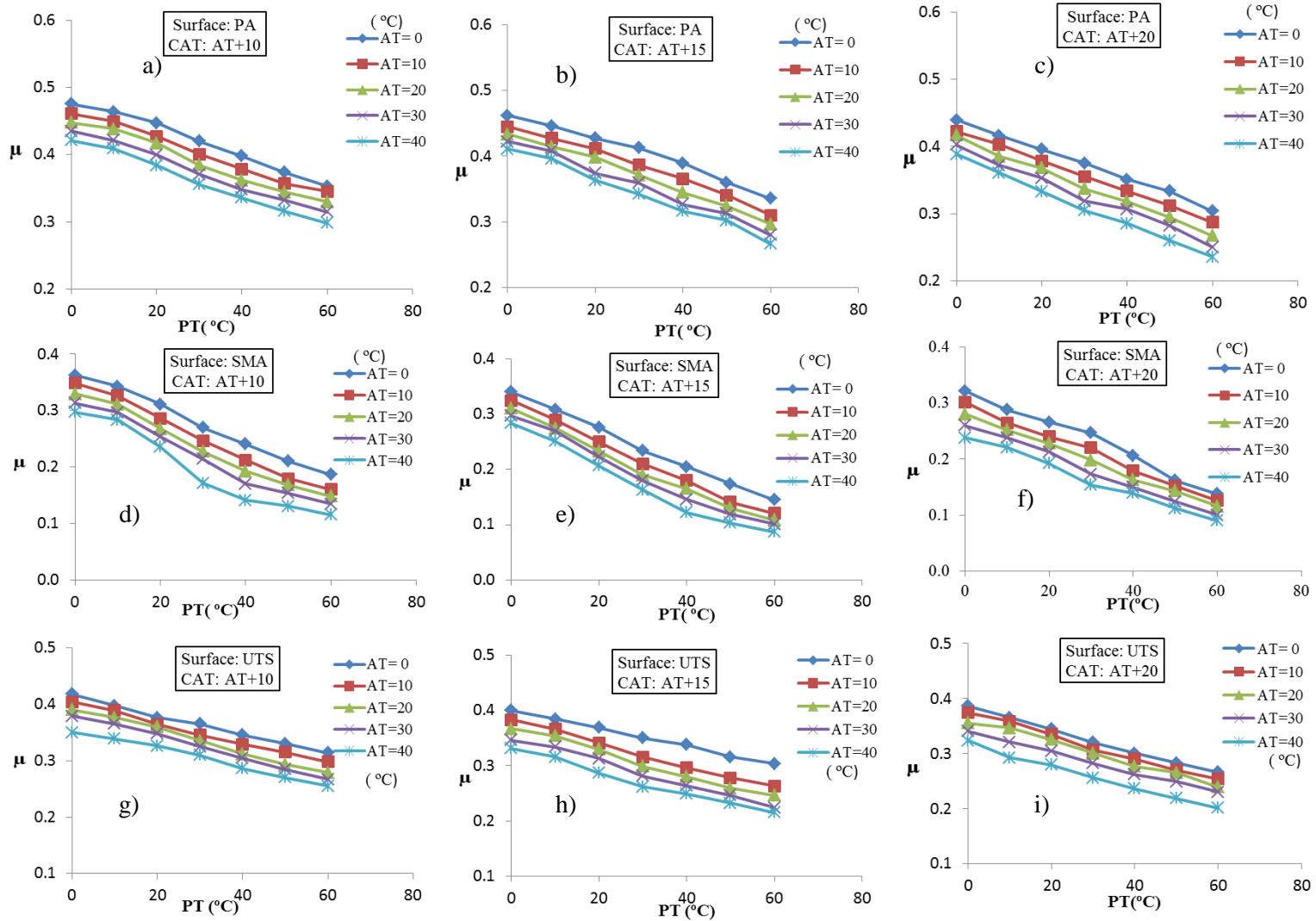


Figure 5.9 Friction vs. pavement temperature for PIARC tire rolling at 100% slip ratio

5.4.3 Effect of Ambient Temperature on the Hysteretic Friction

This sub-section discusses the effect of AT on the hysteretic friction, and the computed results are shown in Figure 5.10. The plots on the figure show that at a constant PT and CAT, the hysteretic friction decreases with increase in AT. For example, considering the plot of Figure 5.10a, at a constant PT of 0°C, the predicted hysteretic friction drops from 0.74 to 0.64 for an increase in AT by 40°C. Similar trends of hysteretic friction against AT was observed for all other PT. The average friction value for a PA surface at a tire slip of 20% drops by 0.08 for an increase in AT from 0°C to 40°C as shown in Figure 5.10a to Figure 5.10c.

Similar analysis for SMA and UTS pavement surfaces result in a drop of 0.06 and 0.07 respectively. Approximately the same drop in the hysteretic friction indicate that the variation of hysteretic friction with AT is marginally dependent on the type of pavement surface. Figure 5.10 to Figure 5.12 also show the plots of hysteretic friction with AT for different slip ratios. It was observed that irrespective of slip ratios, the hysteretic friction was always found to decrease with AT. Despite the fact that the friction values with AT are different at different slip ratios, the rate of drop is almost constant. Thus, it can be concluded that the variation of friction with AT is independent of slip ratio.

TIRE-PAVEMENT INTERACTION UNDER DIFFERENT OPERATING CONDITIONS

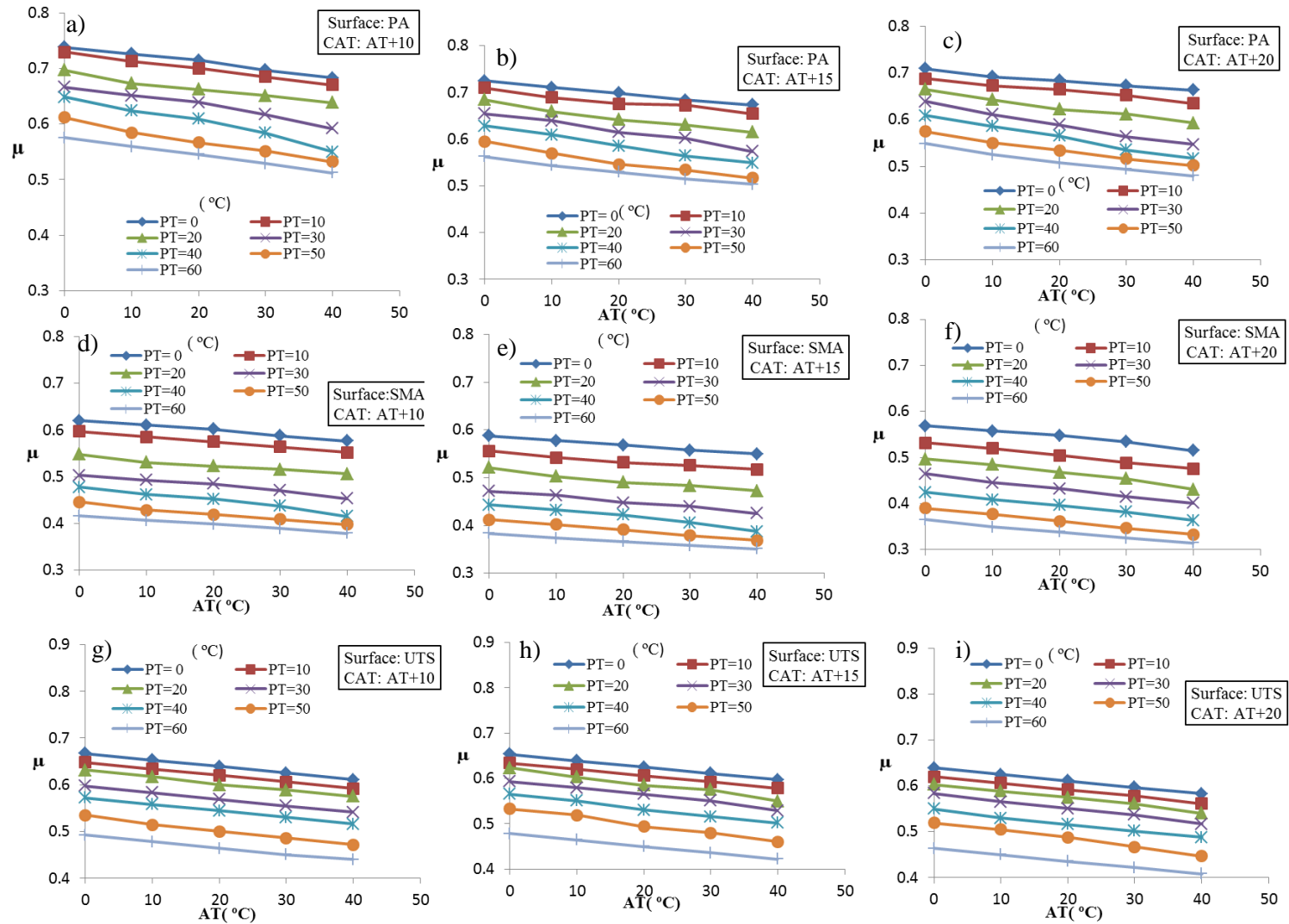


Figure 5.10 Friction vs. ambient temperature for PIARC tire rolling at 20% slip ratio

TIRE-PAVEMENT INTERACTION UNDER DIFFERENT OPERATING CONDITIONS

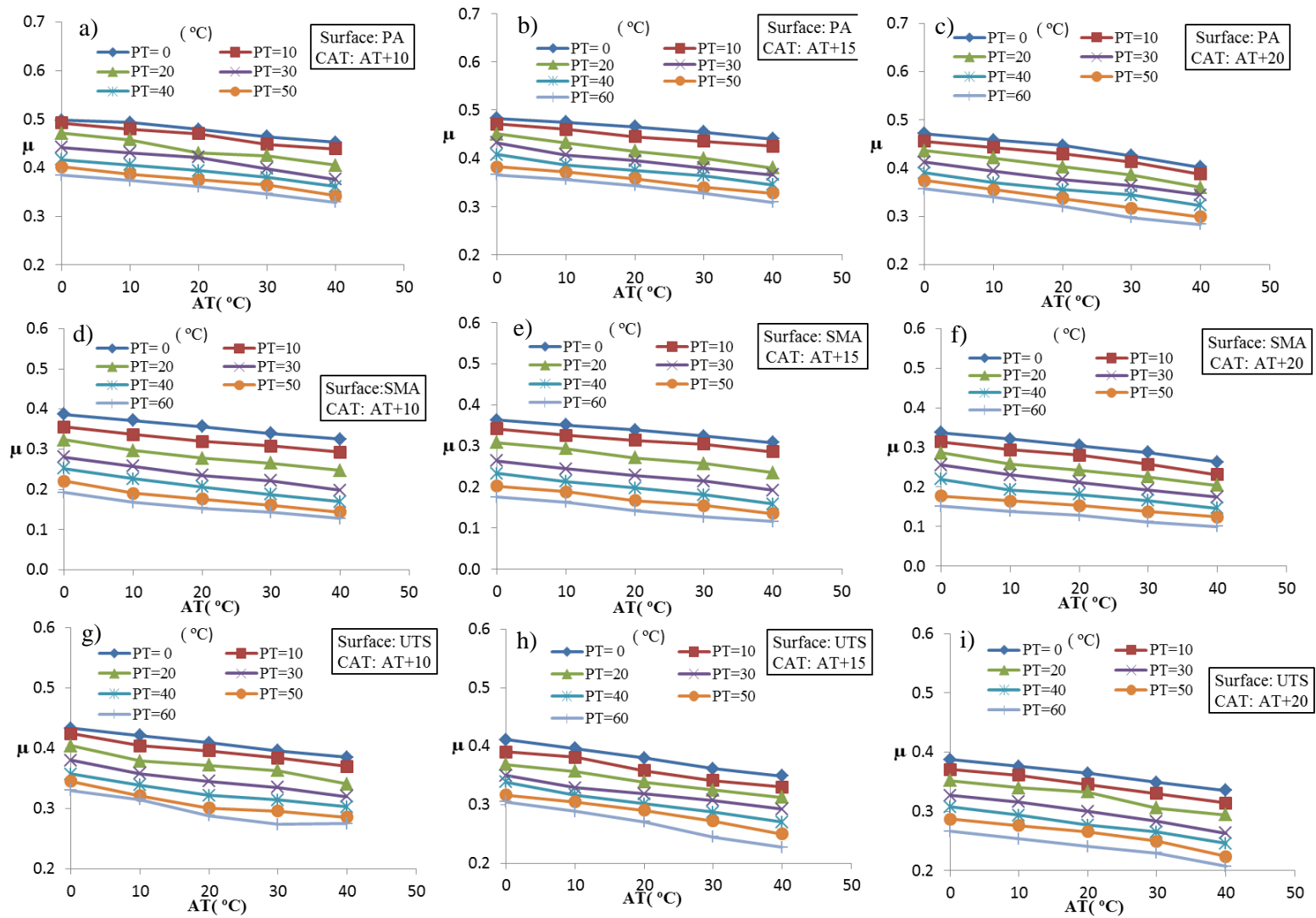


Figure 5.11 Friction vs. ambient temperature for PIARC tire rolling at 86% slip ratio

TIRE-PAVEMENT INTERACTION UNDER DIFFERENT OPERATING CONDITIONS

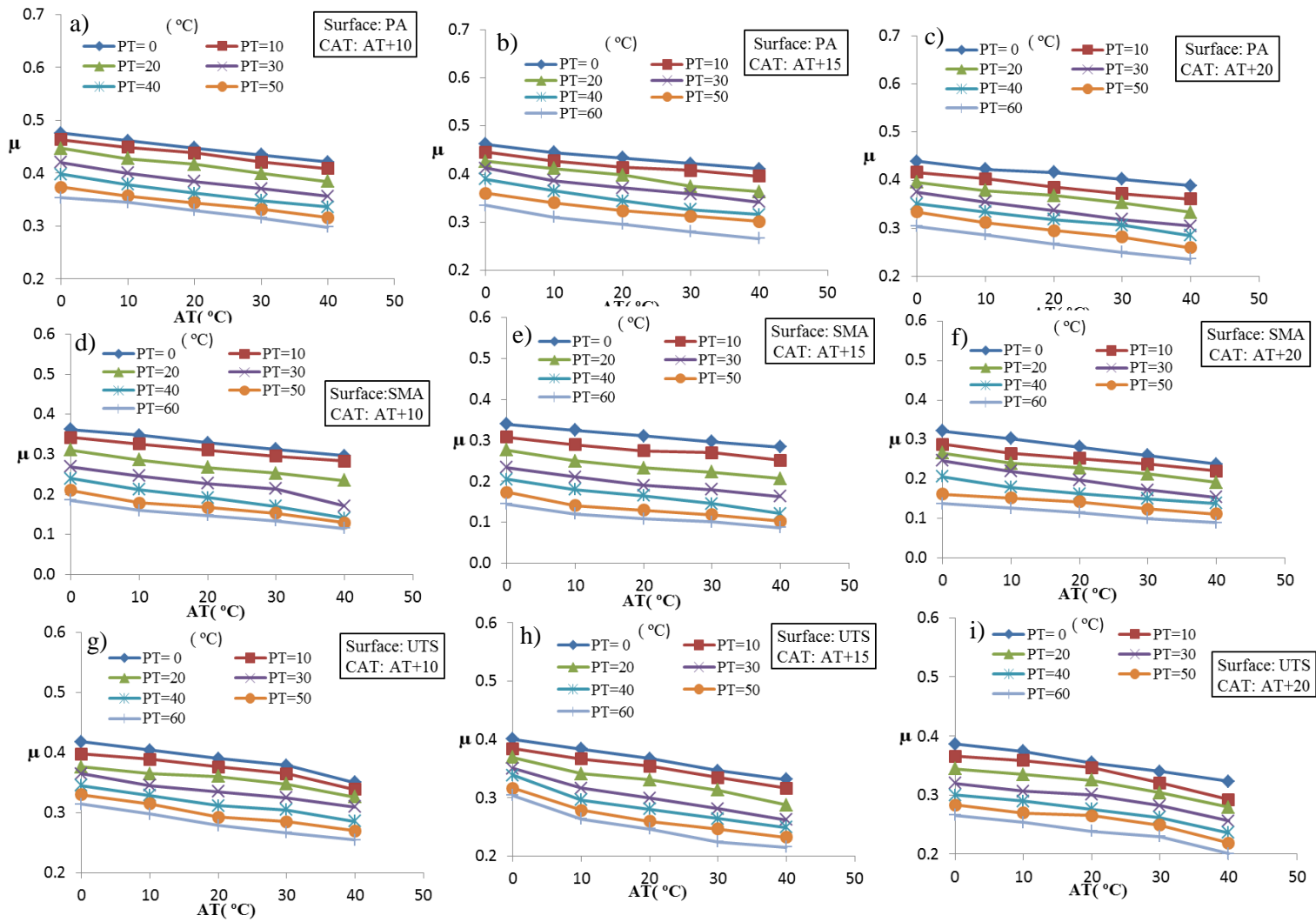


Figure 5.12 Friction vs. ambient temperature for PIARC tire rolling at 100% slip ratio

5.4.4 Effect of Contained Air Temperature on the Hysteretic Friction

This sub-section discusses the effect of CAT on the hysteretic friction. The computed results for hysteretic friction against different values of CATs are shown in Figure 5.13. At 20% tire slip, the hysteretic friction for a PA surface decreases from 0.64 to 0.59 for a 10°C increase in CAT, Figure 5.13a, the decrease in hysteretic friction for UTS and SMA surfaces are observed to be 0.02 and 0.05 respectively. Figure 5.13b shows a similar plot of results obtained at 86% tire slip.

The hysteretic friction over PA surface decreases from 0.42 to 0.38 for a 10°C increase in CAT at 86% tire slip. For the same figure, the decrease in hysteretic friction for UTS and SMA surfaces are observed to be 0.045 and 0.023 respectively. The intercept of the curves on these plots for different pavement surfaces are different but the slope of the curve remains comparable. This implies that irrespective of pavement surface type and slip ratios the increase in CAT reduces the hysteretic friction by the same magnitude.

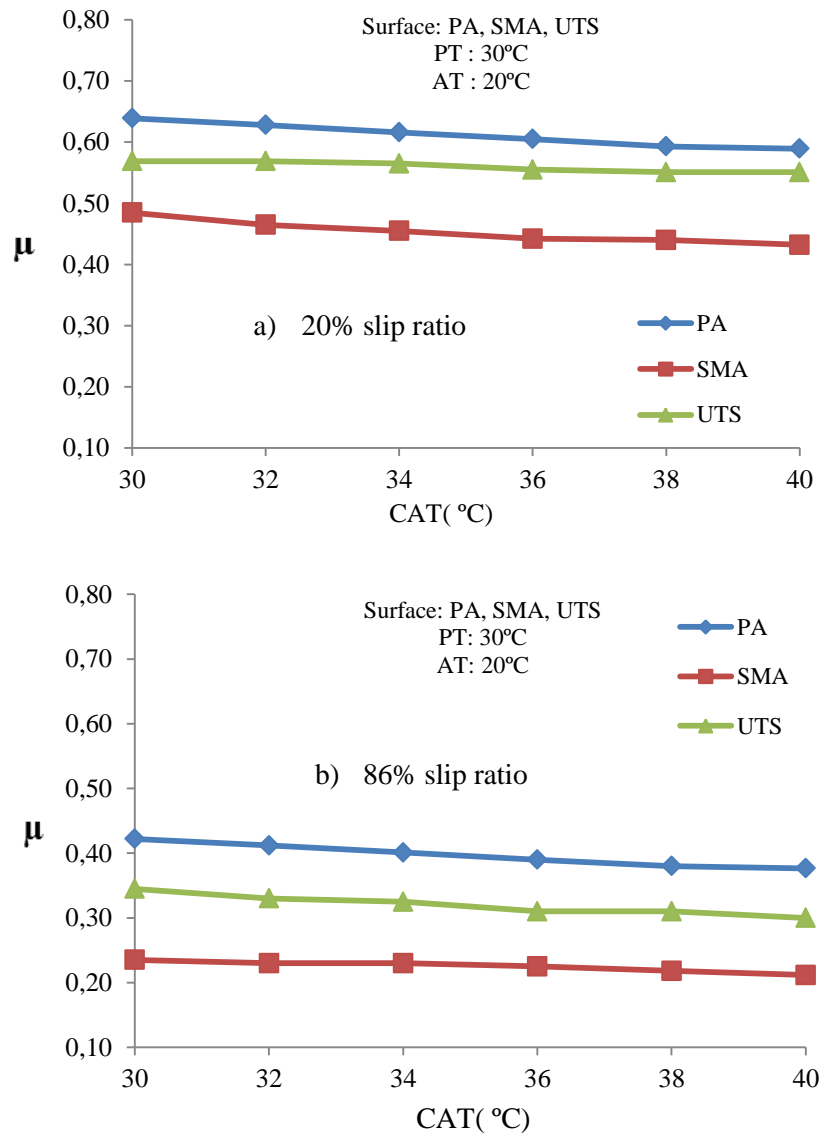


Figure 5.13 Friction vs. contained air temperature for PIARC tire

5.4.5 Effect of Pavement Surface Texture on the Hysteretic Friction

The surface macrotexture of an asphalt pavement varies with mix design. For better demonstration, a 3D surface plot of hysteretic friction against AT and PT is presented in Figure 5.14a to Figure 5.14c.

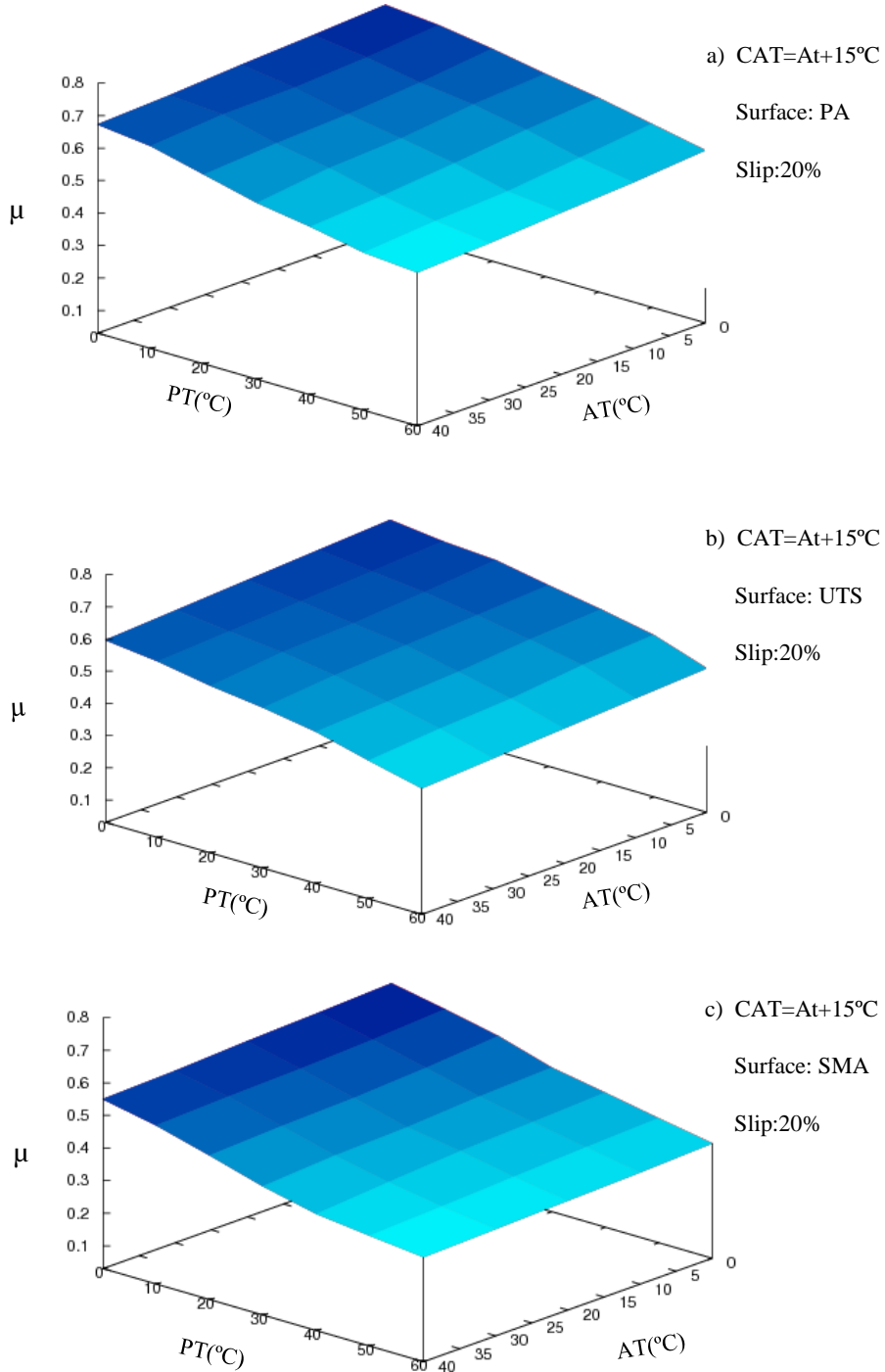


Figure 5.14 Variation of hysteretic friction coefficient with pavement surface morphology at a tire slip ratio of 20%

TIRE-PAVEMENT INTERACTION UNDER DIFFERENT OPERATING CONDITIONS

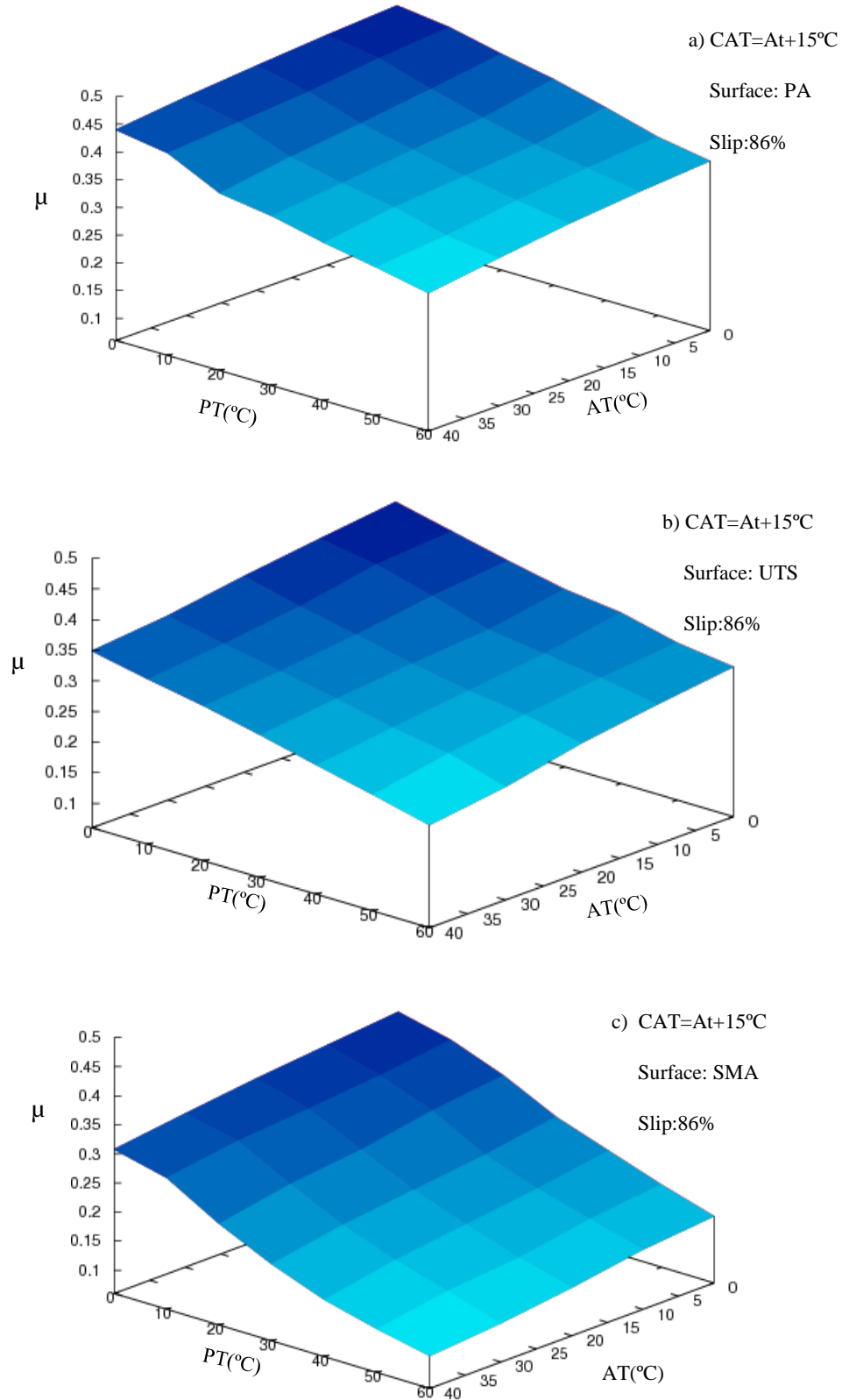


Figure 5.15 Variation of hysteric friction coefficient with pavement surface morphology a tire slip ratio of 86%

A closer examination of the results show that the PA surface offers more hysteretic friction followed by UTS and SMA surfaces. This trend might be due to the asphalt mix characteristics of PA, which possesses more macrotexture compared to other two surfaces. This also highlights the importance of maintaining good pavement macrotexture.

The results for PA, UTS and SMA surfaces are computed at a constant tire slip ratio of 20% and a constant CAT of AT+15°C. For a PA surface, the hysteretic friction varies from 0.72 to 0.50 in the analysed range of PT and AT. Under the same test conditions, UTS and SMA pavement surfaces produce the hysteretic friction in a range of 0.65 to 0.42 and 0.59 to 0.35 respectively.

5.4.6 Effect of Tire Slip Conditions on the Hysteretic Friction

The simulation model provides a useful tool to evaluate the effect of slip ratios on hysteretic friction. Discussion from the previous sections show that there is only a marginal variation in the hysteretic friction values between 86% and 100% slip ratios. Figure 5.14 and Figure 5.15 show that 86% slip ratio provides a lower hysteretic friction compared to 20% slip. Lower friction values are observed at near locked wheel condition which increase the probability of accidents. The results support the classical relationship between friction and slip ratio, which states that there is a continuous decrease in the values of friction above 20% slip ratio. A wide range of hysteretic friction coefficients observed from the corresponding figures show the need for the harmonization of different friction measuring equipment, which operate at different slip ratios.

5.4.7 Relative Effects of PT, AT, CAT, Pavement Texture and Slip Ratios

The sensitivity analysis of this Chapter shows that a higher PT, AT and CAT would result in a lower hysteretic friction for a given pavement surface and a given tire slip ratio. On the other hand, a lower tire slip ratio and a pavement with higher macrotexture results in a higher friction for a given AT, PT and CAT. A large variation in hysteretic friction shows that a critical combination of the factors may decrease the friction values significantly. For example, the value of friction coefficient for a tire slipping at 20% over a PA surface with PT and AT of 0°C, CAT of 10°C is 0.74 and for a tire slipping at 100% over a SMA surface with PT of 60°C, AT of 40°C and CAT of 60°C would result in a friction coefficient of 0.1.

For an easier interpretation of data, Table 5.1 shows the regression relationships between hysteretic friction vs. PT and AT for different pavement surfaces and tire slip ratios. A total of 105 data points (7 PT × 5 AT × 3 CAT) were analyzed for a given pavement surface at a given slip ratio which accumulates to a total of 730 (105 × 3 pavements × 2 slip ratios) data points. A high coefficient of determination exists among hysteretic friction, PT and AT as shown in the corresponding Table 5.1. The intercept values are driven by the type of pavement surface and the slip condition, which varies in a range of 0.74 to 0.34. It is observed that statistically the rate of decrease of hysteretic friction (μ) with PT i.e. $d\mu/dPT$ is observed to be in a range of 0.0019 per °C to 0.0035 per °C depending upon pavement type and slip condition. In other words, every 1°C increase in the PT would decrease the hysteretic friction by 0.0019 to 0.0035 and this rate of decrement is statistically valid for a given AT and CAT. This shows that the friction value at 0°C AT and 0°C PT depends on the type of pavement texture and slip ratio. On the other hand, the rate of decrement in friction depends mainly upon PT. Similarly, the rate of change of friction with respect to AT ($d\mu/dAT$) varies from 0.0012 per °C to 0.0017 per °C. It is worth noting that the rate of decrement in friction with AT is almost independent of type of pavement surface and slip ratio.

Table 5.1 Regression equations developed for hysteretic friction as a function of pavement and ambient temperatures

Pavement Surface	Slip Ratio (%)	Relationship	Adjusted R ² value
PA	20	$\mu = 0.7373 - 0.0017AT - 0.0029PT$	0.9369
	86	$\mu = 0.4924 - 0.0015AT - 0.0020PT$	0.8944
	100	$\mu = 0.4651 - 0.0015AT - 0.0019PT$	0.8564
SMA	20	$\mu = 0.5917 - 0.0012AT - 0.0035PT$	0.8922
	86	$\mu = 0.3653 - 0.0017AT - 0.0033PT$	0.9437
	100	$\mu = 0.3418 - 0.0017AT - 0.0032PT$	0.9248
UTS	20	$\mu = 0.6669 - 0.0015AT - 0.0030PT$	0.9473
	86	$\mu = 0.4138 - 0.0014AT - 0.0023PT$	0.8154
	100	$\mu = 0.4037 - 0.0017AT - 0.0021PT$	0.8596

5.5 Analysis of Cornering Tire

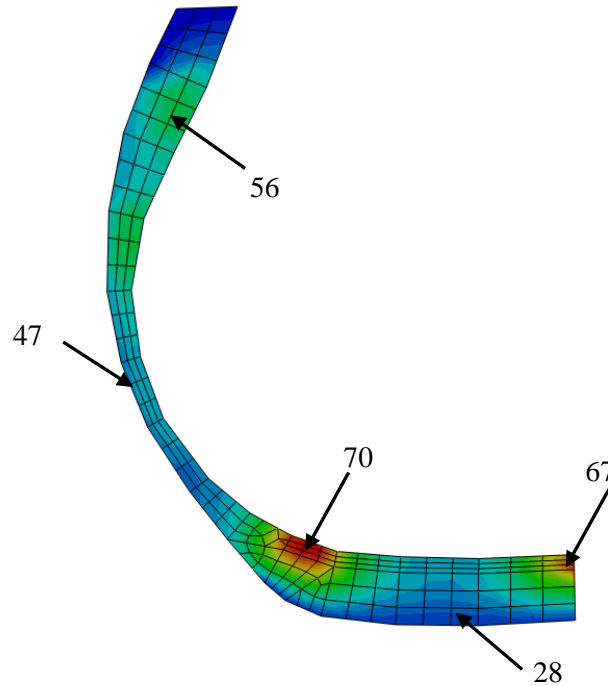
As the tire starts making cornering maneuvers, the available friction between the tire and road surface confines the lateral movement of the tire and results in lateral deformation. Therefore, a slip angle develops between a rolling tire's actual direction of motion and the pointing direction. When the slip angle becomes nonzero, the footprint shifts on one side and thus a change in value of the coefficient of friction is observed. As the tire experiences loading and unloading cycles, the deformation occurs in a non-linear fashion due to the mechanical behavior of polymer chains. Due to this viscoelastic nature of the tire rubber, the coefficient of friction is observed to be load dependent, speed dependent and temperature dependent. On the other hand, change in tire pressure can also affect the tire's characteristics as the pressure variation will change the overall stiffness of the tire and thus it will affect the friction coefficient. The effects of these tire characteristics on cornering friction performance can give researchers and practitioners more insight into the safety aspect of cornering performance. In this section, the effect of tire operating conditions (inflation pressure, speed and sideslip angle) and pavement types (PA, SMA and UTS) on cornering friction coefficient are investigated on the basis of the results obtained from the developed finite element model.

5.5.1 Applied Load on Tire vs. Cornering Friction Coefficient

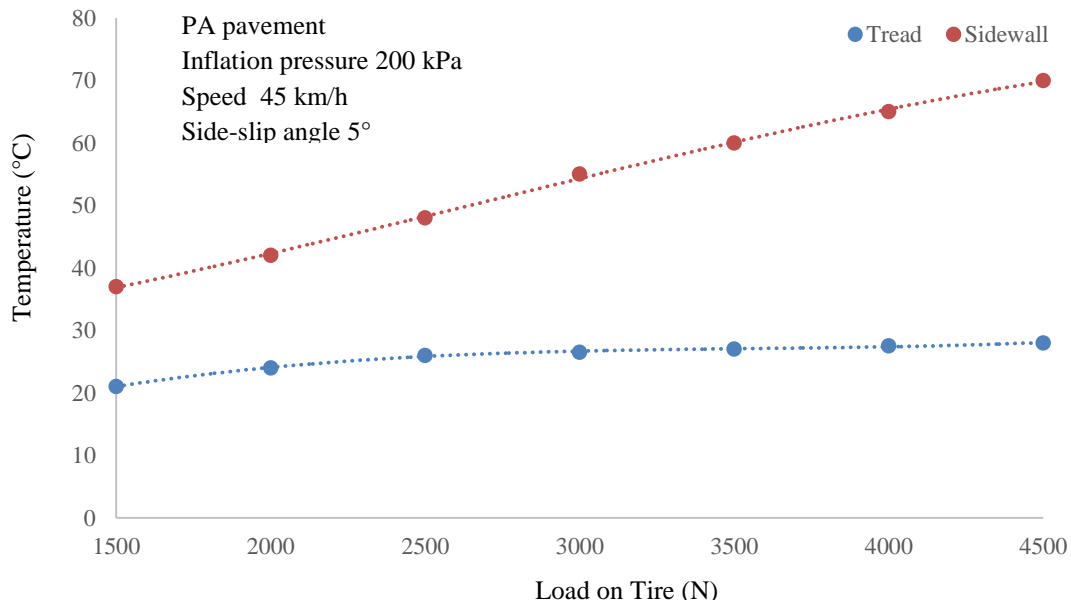
This sub-section discusses the effect of load on the tire cornering friction and temperature development, and the computed results are presented in Figure 5.16 and Figure 5.17 respectively.

TIRE-PAVEMENT INTERACTION UNDER DIFFERENT OPERATING CONDITIONS

A wide range of passenger car loads varying from 1500 N to 4500 N are considered for this purpose. A total of 210 cases (7 loads \times 10 sideslip angles \times 3 pavement surfaces) were analyzed to demonstrate the relationship between the cornering friction and the applied load. For the ease of examination, a constant sideslip angle of 5° , a constant speed of 45 km/h and a constant inflation pressure of 200 kPa on a PA pavement surface were considered, while the loading condition was gradually increased from 1500 N to 4500 N in a 500 N interval.



(a) Temperature distribution in the cornering tire cross section



(b) Load vs. Temperature

Figure 5.16 Effect of load on temperature increase in different regions of cornering tire

TIRE-PAVEMENT INTERACTION UNDER DIFFERENT OPERATING CONDITIONS

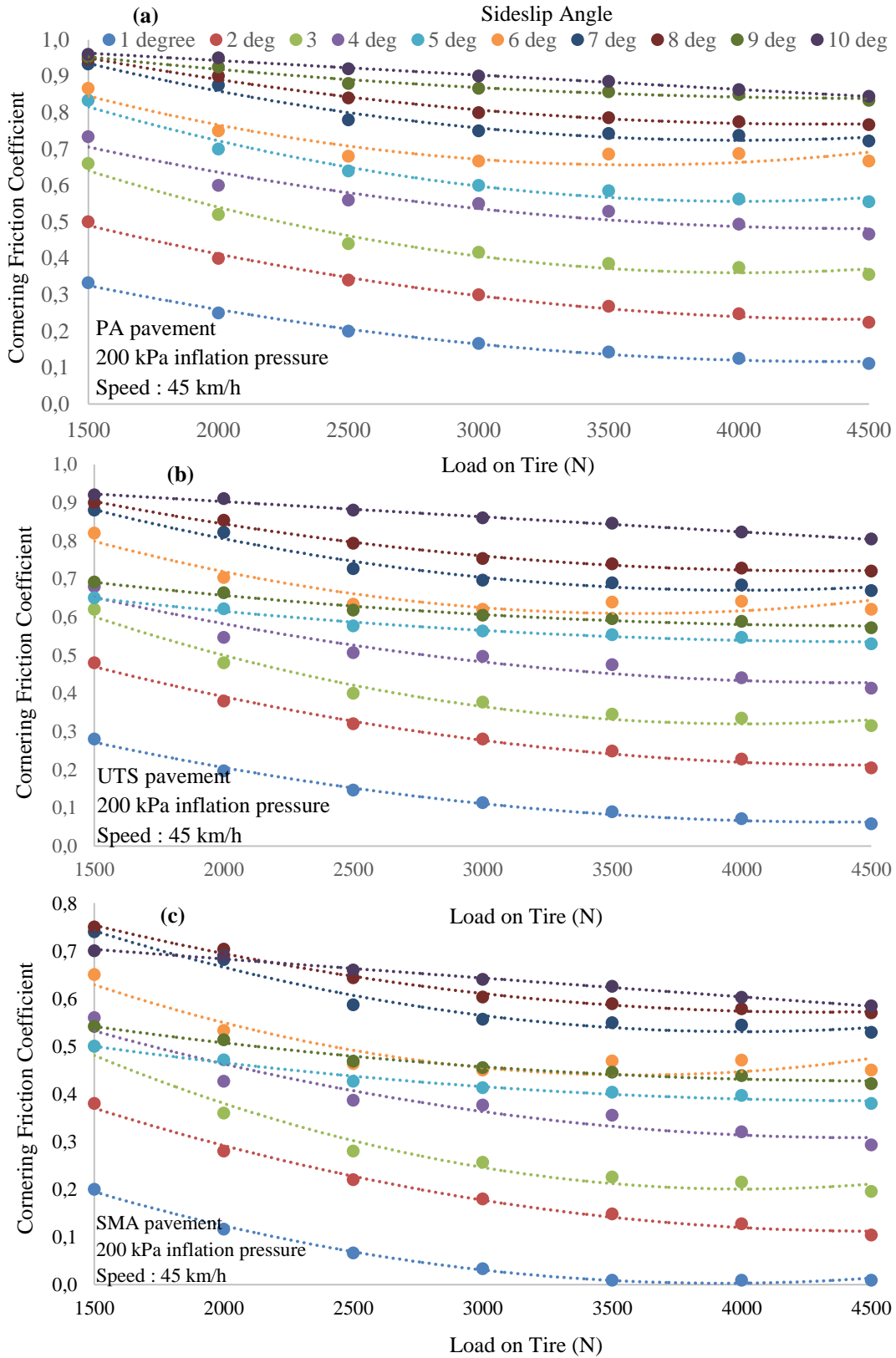


Figure 5.17 Cornering friction coefficient vs. load on tire

For a given set of operating conditions, when a tire rolls over a pavement surface, energy dissipation in the rubber takes place. This energy dissipation causes a rise in the temperature in different regions of the tire as shown in Figure 5.16a. It can be seen that the temperature rise takes place in the tread, the side walls and other regions of the tire when the load on the tire increases. However, the temperature increase with load is not same for all regions of the tire. Figure 5.16b shows a comparison between the temperature development in the tread portion and the sidewall of the tire. Plots of the figure show that the temperature development in the tire tread region is found to be less than the side walls. A load increase of 3000N, from 1500 to 4500 N shows a temperature increase of 7°C in the tread region and 33°C in the sidewall region. The observed trend is similar to the findings by the investigations of (Wilburn, 1972).

The change in the tire temperature changes the material and rheological tire properties and in turn changes the tire pavement friction. It can be observed from the Figure 5.17 that an increase in the tire load decreases the cornering friction. For example, as shown in Figure 5.17 a, when the tire rolls at 5° sideslip angle on a PA surface, the cornering friction decreases from 0.83 to 0.56 when the load increases from 1500 N to 4500 N, i.e. the friction value drops by a percentage of 33%.

Figure 5.17a, Figure 5.17b and Figure 5.17c shows the variation in the cornering friction coefficient with respect to the load for the three different surfaces i.e. PA, UTS and SMA respectively. It can be concluded that irrespective of sideslip angle and the type of pavement surface used, the cornering friction decreases with the increase in the tire load.

5.5.2 Inflation Pressure vs. Cornering Friction Coefficient

This sub-section discusses the effect of tire inflation pressure on the temperature development and the cornering friction as shown in Figure 5.18 and Figure 5.19 respectively. A range of tire inflation pressures varying from 110 kPa to 350 kPa are considered for this purpose. A constant load of 4000 N was maintained. The remaining operating conditions are the same as in the previous section. A total of 300 cases (10 inflation pressures \times 10 sideslip angles \times 3 pavement surfaces) are analyzed in this section.

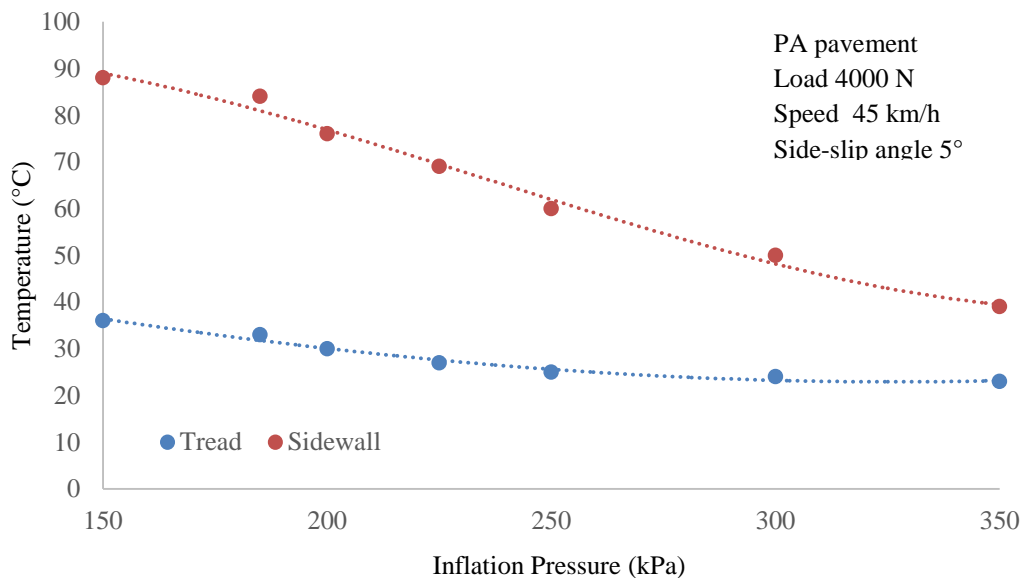


Figure 5.18 Effect of inflation pressure on temperature increase in different regions of tire

TIRE-PAVEMENT INTERACTION UNDER DIFFERENT OPERATING CONDITIONS

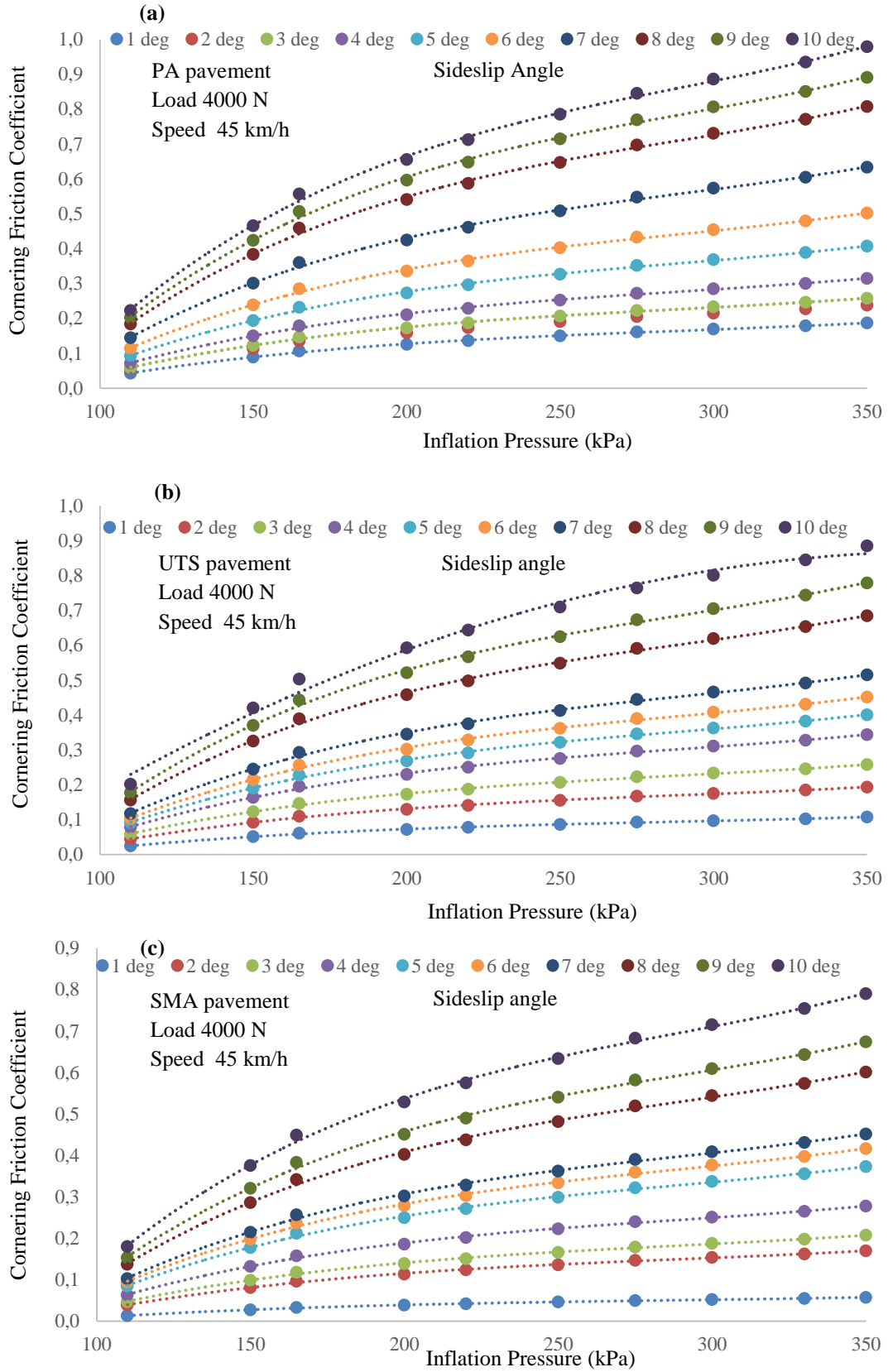


Figure 5.19 Cornering friction coefficient vs. inflation pressure of tire

It can be seen that the temperature drop takes place in the tread, the side walls and other regions of the tire when the tire inflation pressure on the tire is gradually increased. However, the temperature drop with the pressure is also non-uniform in the tire cross section. Figure 5.18 shows a comparison between the temperature drop in the tread portion and the sidewall of the tire. Plots of the figure show that the temperature decrease in the tire tread region is less than the side walls. A load increase of 3000N, from 1500 to 4500 N shows a temperature increase of 7°C in the tread region and 33°C in the sidewall region.

As shown in Figure 5.19, as the inflation pressure increases the cornering friction coefficient decreases. The reason can be attributed to the fact that a drop in average tire temperature results in positive effect on the cornering frictional performance of a pneumatic tire. For example, as shown in Figure 5.19a, an increase in the inflation pressure from 110 kPa to 350 kPa, increases the cornering friction from 0.14 to 0.63 i.e. an overall 77% increase in the cornering friction coefficient is observed for an increase in the inflation pressure of 240 kPa for a tire rolling at 7° sideslip angle. Similar trends were observed for other pavement surfaces considered in the analysis. That means, irrespective of tire operating and pavement surface conditions, proper tire inflation pressure always enhances the friction performance of a vehicle. However, increase in the frictional forces relies upon the sideslip angles at which the cornering maneuvers are taking place.

5.5.3 Speed vs. Cornering Friction Coefficient

This sub-section discusses the effect of speed on the cornering friction and the computed results shown in Figure 5.20. A total of 60 cases (6 speeds × 10 yaw angles) are analyzed. Each plot in Figure 5.20 shows the change in cornering friction with speed at a constant load of 4000 N and a constant inflation pressure of 200 kPa. Results show that the cornering friction decreases with speed. For example, at a constant sideslip angle of 5°, an increase in speed of 50 km/h decreases the value of cornering friction by 0.24. In terms of percentages, about 25% to 54% decrease in cornering friction values are observed with an increase in speed of 50 km/h within 1° to 10° sideslip angle.

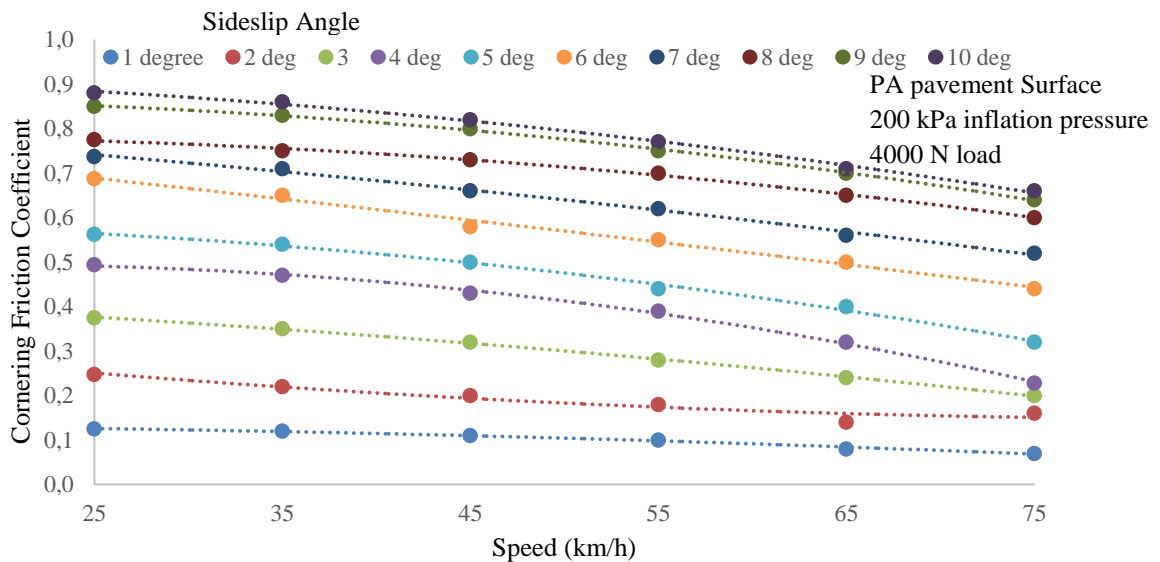


Figure 5.20 Cornering friction coefficient vs. speed

5.5.4 Side-slip Angle vs. Cornering Friction Coefficient

Figure 5.21 shows the effect of sideslip angle on the cornering friction coefficient within a load range of 2200N to 4500 N. A constant tire inflation pressure of 200 kPa and a speed of 45 km/h are considered for the analysis. It can be observed that an increase in sideslip angle increases the cornering friction and this trend is true for all loading analysed cases. For example, an increase in cornering friction value of 0.63 is observed when the sideslip angle increases from 0° to 10°, at a constant load of 1500N. However, it must be noted here that the rate of increase of cornering friction with sideslip angle is more pronounced for higher loads. A similar trend was observed by Clark (1971).

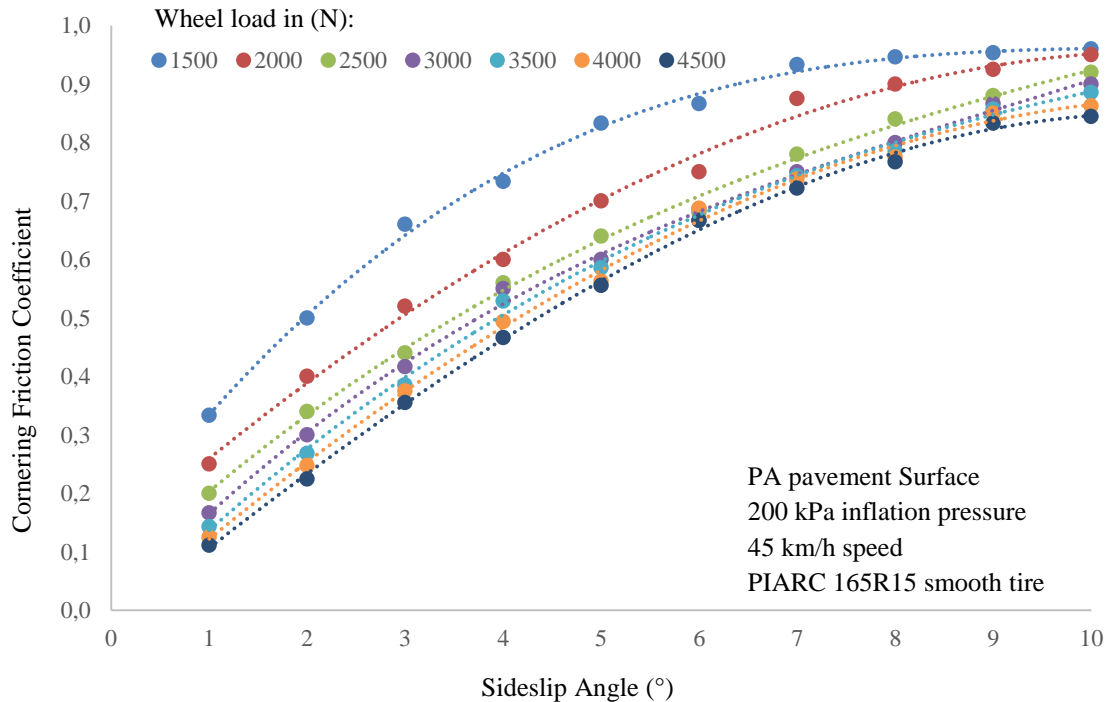


Figure 5.21 Cornering friction coefficient vs. sideslip angle

5.5.5 Pavement Surface Texture vs. Cornering Friction Coefficient

The surface macrotexture of asphalt pavements varies with their respective mix designs. As shown in the previous chapter, the pavement surface macrotexture has an influence on the tire-pavement frictional properties. From Figure 5.17 and Figure 5.19 the effect of pavement macrotexture on cornering friction coefficients can also be studied. It can be observed that values of cornering friction coefficients are higher in PA surface followed by UTS and SMA surfaces, under given loading and sideslip angle. For example, Figure 5.17 shows the cornering friction coefficients on PA, UTS and SMA surfaces, at a constant speed of 45 km/h, inflation pressure 200 kPa and load of 4000 N, varies in range of 0.13-0.90, 0.06-0.82 and 0.01-0.60 respectively. The observed trend might be due to the asphalt mix characteristics of PA, which possesses more macrotexture compared to other two surfaces. This highlights the importance of maintaining good pavement macrotexture on pavement surfaces for safe cornering maneuvers.

5.6 Summary

This Chapter demonstrated the capability of the developed FE thermo-mechanical tire-asphalt pavement interaction model to evaluate the effects of tire band temperature, pavement temperature, ambient temperature, contained air temperature, pavement surface texture and tire slip ratio on the hysteretic friction. Tire rolling with 20-100% slip conditions are analysed over three different asphalt pavement surfaces, namely, PA, UTS and SMA. The analyses of results show that higher TT, PT and AT result in a lower hysteretic friction for a given pavement surface and a given tire slip ratio. The analysis also shows that the CAT has a marginal effect on the variability of hysteretic friction. It is also observed that the full skidding tire results in lower hysteretic friction values followed by 86% and 20% slipping tires. The study also highlights the importance of maintaining proper macrotexture on pavement surfaces which in turn provides better hysteretic friction. Overall, this sensitivity analysis shows the effect of important components of tire-pavement interaction on the friction performance and such a study would give better insight into the tire-pavement friction mechanism.

The developed thermo-mechanical framework was also utilized to analyze the influence of temperature on cornering friction which is another important manoeuvres of pneumatic tires and greater level of complexity in the simulation of tire-pavement interaction. The analysis of the cornering performance of vehicles on real asphalt pavement surfaces is performed under different vehicle operating conditions. In general, it was observed that the change in the load and the inflation pressure changes the temperature in the tire cross section. The tire temperature was found to increase with increase in load and to decrease with the inflation pressure. It was also noted that the rate of increase in the tire temperature is not uniform throughout the tire cross section. The study showed that because of the change in the temperature, material properties of tire rubber also changes and thus the anti-skidding forces developed beneath the tire also vary. The cornering friction coefficients were found to decrease with the increase in the loads and the speeds. On the other hand, the cornering friction coefficients were found to increase with the increase in inflation pressures, sideslip angles and pavement surface texture depths.

The next Chapter presents the greater complexity in the tire-pavement interaction i.e. the estimation of friction on a given asphalt pavement surface in the presence of water.

6 Hydroplaning

6.1 Introduction

The dynamic hydroplaning phenomenon can be envisaged as the progressive infringement of a water wedge into the tire-pavement contact area which results in the build-up of hydrodynamic lift forces on the tire tread portion and, at some point in time, may force the tire to lift off the pavement and literally glide on a thick film of water. If only a portion of the tire-pavement contact region is separated by water, the contact shear force is considerably reduced but not totally lost and the tire is said to be partially hydroplaning (Sinnamon and Tielking, 1974). In hydroplaning, the density, the viscosity and the inertial properties of the fluid predominate (Horne and Dreher, 1963).

The hydroplaning phenomenon is a multifaceted problem, involving the interaction of fluid dynamics with the contact mechanics of a load-carrying, pressurized, complex pneumatic tire structure with rough macrotexture of the pavement surface. Although a number of useful empirical relationships have been derived from the extensive field experimental programs, the variability in the field conditions render the usage of these relationships to minimal. Similarly, far less breakthrough of analytical formulations of this complex problem forced the researchers to look for numerical techniques like finite element (FE) analysis. In recent years, development of powerful FE tools made it possible to simulate complex wet tire-pavement interaction as close as possible to the actual field conditions. However, to the best of the author's knowledge, none of the past analytical/numerical studies were able to include the actual pavement surface texture in the tire-wet pavement analysis. An attempt has been made in this contribution to include real macro texture of the asphalt pavements to ascertain its effect on the hydroplaning speed and wet friction coefficients. This part of the thesis start with the literature review of hydroplaning, followed by the numerical formulation of tire-fluid-pavement interaction and concludes with the analysis of hydroplaning/wet friction of tire on asphalt pavement surfaces.

6.2 Three Zone Concept

Hydroplaning phenomenon can be well explained by the well-known three-zone concept, first put forwarded by Gough (1959) for locked wheels and then further developed by Moore (1966) for rolling tires. This concept suggests that the tire contact area can be divided along the driving direction into three regions, Figure 6.1.

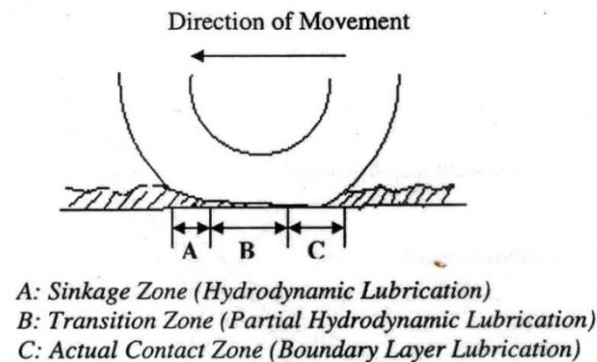


Figure 6.1 Three zone concept of hydroplaning (Moore 1966)

- a) *Sinkage zone*: In this zone, the tire floats on a thick water film, and the water wedge penetrates into the contact patch so that the tire is fully separated from the road and hence the elasto-hydrodynamic lubrication governs. It is also called the squeeze zone, because some of the water is gradually squeezed out from the sides of the tire, but some is trapped to form a water wedge under the tire. The area of this water wedge gradually expands backward into the contact patch as the speed of the tire or the water depth increases. This zone is formed mainly due to the displacement inertia of the entrapped fluid. The frictional forces developed in this zone are strongly dependent on the bulk properties of the entrapped fluid, namely viscosity and the velocity gradient in the lubricant film.
- b) *Transition zone*: In this zone, the tire is on a thin water film and this is the transition region from floating to contact. The transition zone arises when the tire tread penetrated through the entrapped fluid film, commence to drape dynamically about the asperities of the pavement surface, and make contact with the lesser asperities. Throughout this zone, a progressive breakdown of the water film occurs down to thickness and hence, a mixed-lubrication regime exists which is partially hydrodynamic and partially boundary. The effective friction coefficient ranges between a very low value due to viscous hydroplaning at the leading edge of the transition zone to the friction of boundary layer lubrication at the end edge of this zone, which is more or less equal to dry friction. This zone occurs at normal speeds.
- c) *Actual contact zone*: In this zone, the tire can make a complete contact with the pavement. The entrapped fluid film has been totally or substantially removed, and vertical equilibrium of the tread elements with the pavement surface can be attained. In this zone, boundary lubrication is dominant and full skid resistance or traction capability can be achieved.

On the basis of above discussion, the friction coefficient can be determined by the following equation:

$$\mu_{\text{wet}} = (1 - F_{\text{EHL}})\mu_{\text{BL}} \quad (6.43)$$

μ_{wet} is the friction coefficient, μ_{BL} is the boundary-layer wet friction, F_{EHL} is the fraction of footprint in elasto-hydrodynamic lubrication mode (EHL). The total hydroplaning occurs at very high speeds when $F_{\text{EHL}} \equiv 1$ and $\mu_{\text{wet}} \equiv 0$. At low speeds, where $F_{\text{EHL}} \equiv 0$, the boundary-layer lubrication prevails.

6.2 Manifestations of Hydroplaning

The hydroplaning phenomenon was first demonstrated by NACA in 1957 and since eight manifestations of tire hydroplaning have been observed. Horne and Dreher (1963) listed and described these manifestations as follows

6.2.3 Detachment of tire footprint

As ground speed increased, a wedge of fluid progressively infringes into the tire-pavement contact patch and a hydrodynamic pressure is developed between the tire and the pavement. The resulting hydrodynamic lift tends to detach the tire footprint from the pavement surface.

6.2.4 Hydrodynamic ground pressure

The tire hydroplaning speed is the ground speed required for the average hydrodynamic pressure acting in the tire footprint region to equal the average tire-ground bearing pressure or, in approximation, to equal the tire inflation pressure. It should be noted from the field experimental results that (1) the ground hydrodynamic pressure develops ahead of the initial tire-pavement contact point due to action of the tire bow wave, (2) the peak ground hydrodynamic pressure is considerably in excess of the tire inflation pressure, and (3) negligible hydrodynamic ground pressures are developed at the rear of the tire-ground footprint at the higher ground speeds.

6.2.5 Spin-down of unbraked wheel

The most striking manifestation of tire hydroplaning is the condition in which unbraked free rolling wheels slow down or stop completely on wet pavement surfaces. Unbraked-wheel spin-down arises from the following two hydrodynamic lift effects which combine to produce a total wheel spin-down moment in excess of the wheel spin-up moment due to tire drag sources, (1) as ground speed increases, the hydrodynamic lift progressively detaches the tire footprint from the pavement surface and makes the tire ground frictional spin-up moment tend towards zero values, and (2) the center of pressure of the hydrodynamic pressure and resulting lift developed between the tire footprint and ground surface shifts increasingly forward of the axle as the ground speed increases and produces the wheel spin-down moment. At high speeds comparable to the total hydroplaning speed of the tire, this wheel spin-down moment overcomes the wheel spin-up moment from all the drag sources and wheel spin-down commences.

6.2.6 Suppression of tire bow wave

Tires under wet or flooded conditions indicate that a large bow wave forms in front of the tire for all ground speeds below the hydroplaning speed. As the ground speed increases, the angle of the bow wave with respect to the pavement surface tends to reduce progressively until at some high ground speed in the total hydroplaning region, the bow wave disappears completely.

6.2.7 Scouring action of escaping fluid in tire-ground footprint region

The wheels tend to deposit rubber in the pavement surfaces during high-speed braking on dry pavement surfaces. However, during total hydroplaning conditions, the escaping fluid under the influence of high hydrodynamic pressures tends to clean the runway surface in the tire path with the result that white streaks instead of black streaks are formed by the tires on the pavement surface. It should be noted that this scouring action may also develop when smooth tires are braked on wet smooth pavement surfaces at ground speeds below the tire hydroplaning speed because of viscous effects which also produce high hydrodynamic pressures in the tire-ground contact region.

6.2.8 Peaking of fluid displacement drag

It was observed that the fluid displacement drag reaches a maximum value at a ground speed near the tire hydroplaning speed during field hydroplaning tests at the Langley test tracks. It was also observed that increasing the ground speed above the critical hydroplaning speed results in appreciable reductions in fluid drag. This result is attributed to the tires lifting off the runway surface at the higher ground speeds and consequently displacing less runway fluid from the tire-pavement contact patch.

6.2.9 Loss in braking traction

Whenever a pavement surface is flooded with fluids such as slush or water to depths large enough to the onset of tire hydroplaning, the loss in braking traction is more catastrophic. At this point, applying brakes to wheels that have either completely or nearly stopped rotating from hydroplaning effects cannot be expected to improve the existing tire retardation forces and friction coefficient at all.

6.2.10 Loss in directional stability and control

Another significant manifestation of tire hydroplaning is a loss of directional stability, as jointly demonstrated by the FAA and NASA on a four-engine jet transport. During their tests, it was observed that the aircraft tend to yaw and drift laterally on the runway while in the slush bed at speeds in excess of the predicted hydroplaning speed. The loss of tire directional stability at and above tire hydroplaning speeds could be extremely serious to the aircrafts especially during take-off and landing operations.

6.3 Factors Influencing Hydroplaning Speed

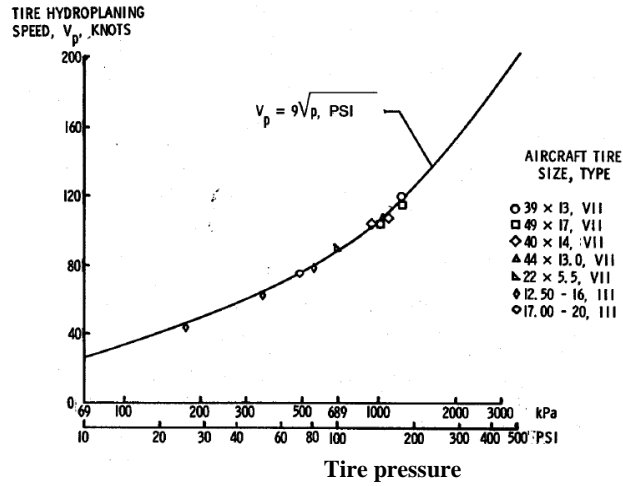
The safety of vehicles against hydroplaning is strongly dependent on the factors related to, 1) tire, for example, tread pattern, tire size, tire construction, tire shape, tire load, inflation pressure, tire slip ratio etc., 2) pavement, for example, microtexture, macrotexture, mix design etc. 3) fluid, for example, depth of the water film, density etc., but the main influence is the driving speed, because the hydrodynamic lift increases with the velocity squared (Grogger and Weiss, 1997).

6.3.3 Tire parameters

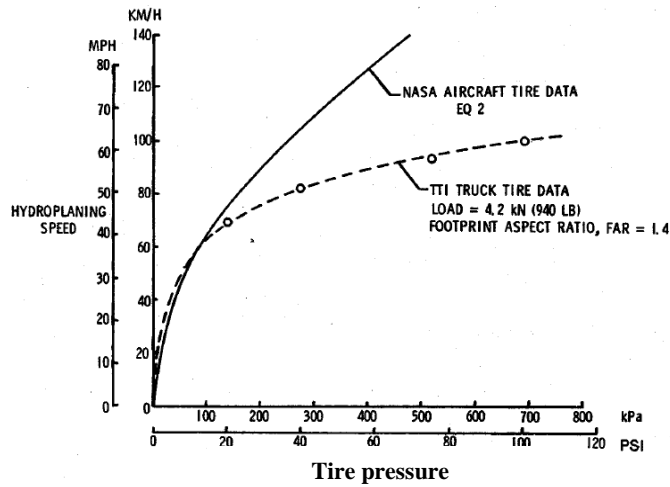
6.3.3.1 Tire Inflation Pressure

When the critical water depth is exceeded for any tire-pavement surface combination, the critical speed required to detach the tire from the pavement surface and hence the total hydroplaning condition to occur was found to be almost entirely dependent upon tire inflation pressure. NASA expressed the critical hydroplaning speed of aircrafts and ground vehicles as a function of the inflation pressure, Figure 6.2. From the figures, it can be observed that the critical hydroplaning speed increases with the tire inflation pressure.

Similarly, Staughton and Williams (1970) expressed the critical spin-down speed of a tire on a flooded pavement as a function of the tire pressure and wheel load as shown in Figure 6.3. Staughton and Williams also found from their field experiments that the tire load did not have a significant influence on hydroplaning speed. This outcome can be explained by the knowledge that dynamic hydroplaning occurs when the average hydrodynamic pressure beneath the tire approximately equals the ratio of tire load to gross contact area, and this ratio depends primarily upon inflation pressure.



(a) Hydroplaning speed vs. aircraft tire inflation pressure (Horne, 1974)



(b) Comparison of hydroplaning speeds of aircraft tire and truck tire against tire inflation pressure (Horne et al., 1986)

Figure 6.2 NASA Experiments to determine the effect of tire inflation pressure on the dynamic hydroplaning speed for aircraft and truck tires

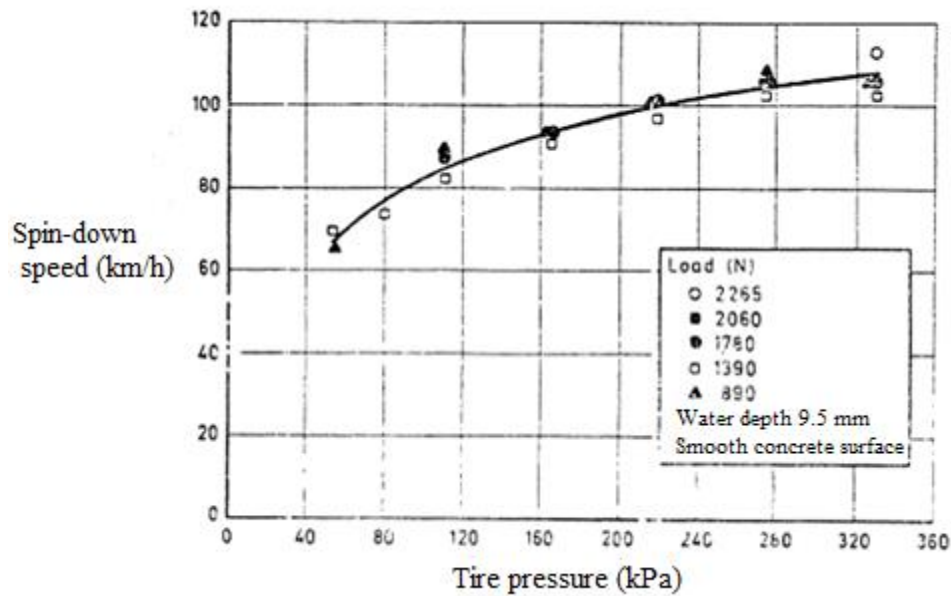


Figure 6.3 Prediction of hydroplaning speed against tire inflation pressure from the experimental results of Staughton and Williams (1970)

As discussed earlier, higher tire inflation pressures lead to lower hydroplaning risk due to the following reasons:

- (a) Brown (1975) found that the higher the inflation pressure leads to the greater the stiffness of the tire and the greater the resistance of its tread region against the inward bending of tire under the action of fluid inertial forces. It is this inward bending which allows the penetration of fluid film into the tire contact patch resulting in the dynamic hydroplaning.
- (b) Yeager and Tuttle (1972) found that higher tire inflation pressures lead to greater groove openings which act as channels to expel the water from tire-pavement contact area and thus delay the onset of hydroplaning. A tire with low inflation pressure will allow the center of the tread to collapse and become very concave, trapping water rather than flowing it through the tread design.

6.3.3.2 Speed

Horne and Dreher (1963) conducted an extensive experimental program to determine the effect of ground speed on the average friction coefficient on flooded runway surfaces at Langley research centre. Their results indicated that the wet runway friction coefficients varies inversely with aircraft ground speed for all the operating conditions and at higher ground speeds hydroplaning conditions prevail, Figure 6.4. The reason can be attributed to the greater hydrodynamic uplift forces acting on the tire because of the higher ground speeds of an aircraft on a wet runway surface. This causes the net wheel load to be lower, as a result, lower runway friction coefficients with higher speeds. Figure 6.4 also shows that even for the large aggregate asphalt surface, the flooded surface resulted in a large loss in traction at the higher ground speeds. Their field experimental results indicate that a total traction loss at about 106 knots which corresponds to the predicted hydroplaning speed from dynamic hydroplaning theory (Horne et al., 1963).

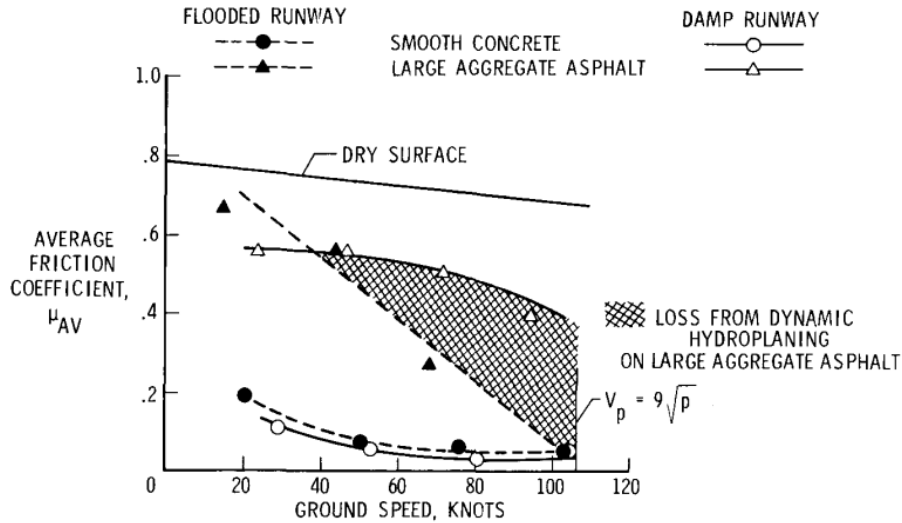


Figure 6.4 Effect of ground speed on average friction coefficient
(Horne et al., 1962; Horne and Dreher, 1963)

6.3.3.3 Tire tread grooves

The primary effect of tread pattern is to reduce the size of squeeze film by providing low pressure squeeze boundary to the water entrapped beneath the tread ribs. In case of deep water films, the groove pressure increases in order to motivate the flow of water. A number of researchers performed experiments to determine the effect of groove geometry on the wet traction performance. Horne and Joyner (1965) measured the hydrodynamic pressures in the grooves and beneath the tread ribs of an aircraft tire comprised of straight and circumferential grooves and measured the pressure in the center groove and beneath an adjacent rib as a function of speed, Figure 6.5.

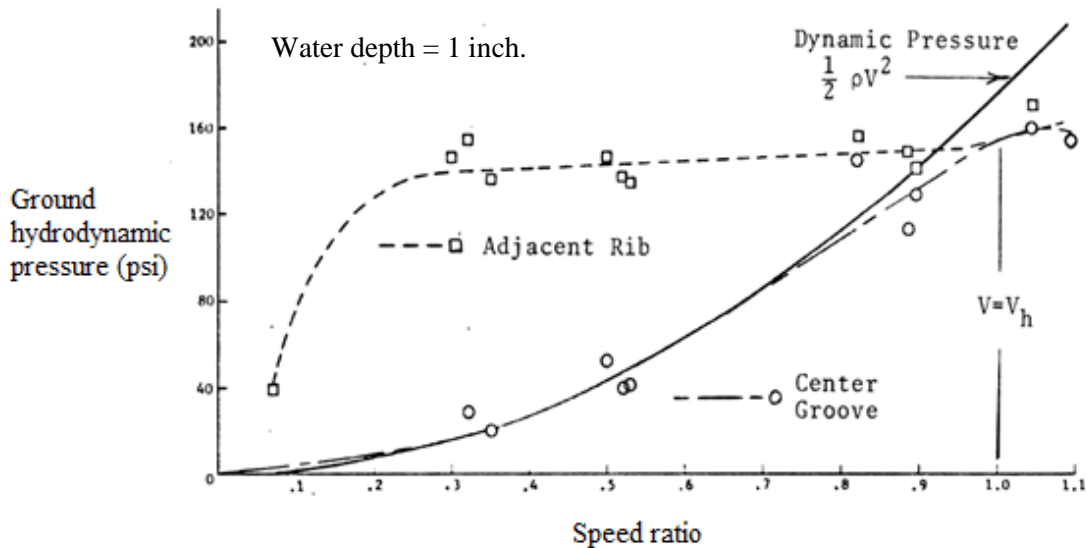


Figure 6.5 Hydrodynamic pressure in the centre groove and beneath an adjacent rib against speed ratio (Horne and Joyner, 1965)

Figure 6.5 shows that as speed ratio increases, pressure inside the groove increases and the difference in the pressure between groove and rib decreases. As the rate of expulsion of squeeze water film from beneath the rib depends on the groove-rib pressure difference, it follows that the increase in groove hydrodynamic pressure constrain the expulsion of squeeze water film and result in more of the contact region being supported by a water film than would be the case at the same speed in the shallow water films. At a certain speed, the groove pressure becomes equal to the pressure on the squeeze film beneath the ribs. At this speed, the grooves are said to be "choked" and no longer provide a low-pressure boundary for the squeeze film beneath a rib. A further increase in speed cannot increase the groove flow rate so the water entering the contact region is accommodated by separation of the tire from the road surface. The groove choke speed is also the speed of total dynamic hydroplaning.

6.3.3.4 Tread design

Suitable and adequate tread design increases the critical ground speed required for hydroplaning and thus reduces the risk of accidents in flooded pavement conditions. Also proper tread design tends to increase the minimum fluid depth required for a tire to hydroplane. Tire tread provides escaping channels for entrapped water to discharge it away from the tire-pavement contact area, and helps to retard the development of hydrodynamic pressure, thereby delaying the occurrence of hydroplaning. Tires with proper tread design also helps to increase the wet braking traction than for smooth treaded tires (Horne and Dreher, 1963).

Staughton and Williams (1970) conducted field experiments to measure the effect of transverse grooves of tire on the hydroplaning speed at various water depths. Federal Aviation Administration (FAA) and Federal Highway Administration (FHWA) conducted field experiment programs to study the hydroplaning behaviors of longitudinal grooved tires (Hays et al., 1981; Balmer and Gallaway, 1981).

Apart from the tread design, geometric properties of the tire tread have influence on the hydroplaning speed. The deeper grooves of tire offers more effective channels for water flow and hence hydroplaning takes place at a higher speed due to a lower rate of development of the hydrodynamic uplift force. Maycock (1967) and Gengenbach (1968) conducted field experimental studies to determine the effects of width, depth and spacing of a tire tread groove on skid resistance. They showed that width, depth and spacing of the tire tread grooves have tremendous effect on wet skid resistance. Tire tread pattern also affects the other operating characteristics of a tire such as noise, wet skid resistance, riding comfort and steering stability (Horne and Leland, 1962).

6.3.3.5 Tire footprint aspect ratio

Horne (1984) experimentally proved that tire footprint aspect ratio has a significant influence on the hydroplaning speed. The Footprint Aspect Ratio (FAR) of pneumatic tires is defined as the ratio of the tire foot print width to its length. The following equation put forwarded by Horne et al. (1986) shows the hydroplaning speed is dependent on the tire FAR as described by the and is shown in Figure 6.6.

$$v_p = 51.8 - 17.15\text{FAR} + 0.72p \quad (6.44)$$

where v_p is the hydroplaning speed in mph, FAR is the tire foot print aspect ratio and p is the tire inflation pressure in psi.

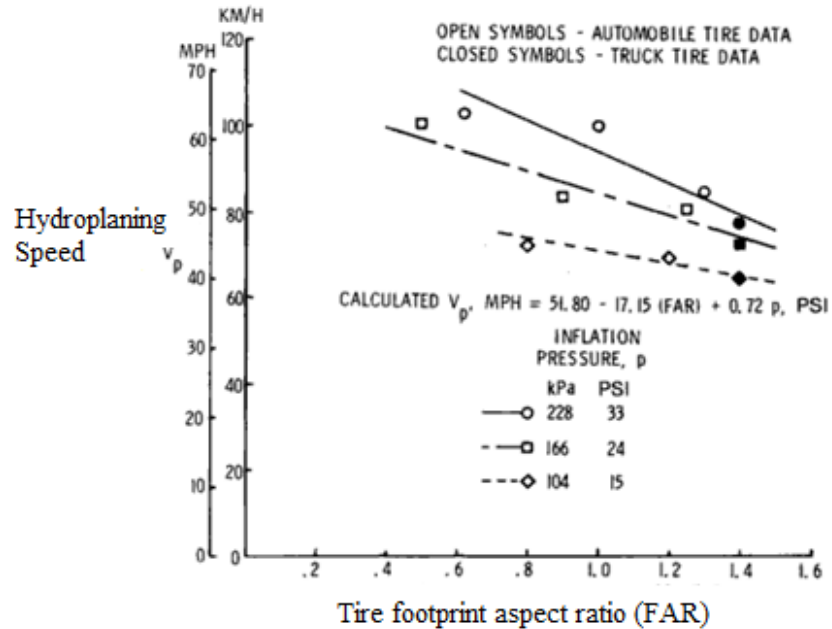


Figure 6.6 Variation of dynamic hydroplaning speed with tire foot print aspect ratio
(Horne et al., 1986)

6.3.3.6 Sipes

Automobile tire manufacturers demonstrated that the addition of closely spaced sipes or small knife cuts in the rib areas of circumferentially grooved tires increases traction on wet smooth surfaces to a much greater extent than simple grooving (Horne et al., 1968). Sipes, or knife cuts, do appear on tire surfaces to give a significant improvement on smooth, polished, surfaces. The mechanism by which sipes improve wet friction is still a matter of speculation. The following four mechanisms can be attributed to the functionality of sipes in the wet pavement conditions (Horne and Dreher, 1963; Sinnamon and Tielking, 1974):

- The sharp edges of a sipe act like squeegees in wiping away the water film so that the following tread can make contact with the road surface.
- The sharp edges of a sipe provide points of high contact pressure which permits penetration of the water film.
- The sipes provide temporary low-pressure storage cavities for squeeze film water trapped beneath the tread ribs, thereby reducing the size of the squeeze film.
- The sipes that have at least one end opening into a groove will provide additional drainage in much the same manner as surface macrotexture. This mechanism has been confirmed by glass plate observations

6.3.3.7 Vertical load

Past researchers (Horne and Joyner, 1965; Staughton and Williams, 1970) proved under their field experimental studies that an increase in the vertical load on a pneumatic tire has a minor effect on the tire's hydroplaning speed, Figure 6.7.

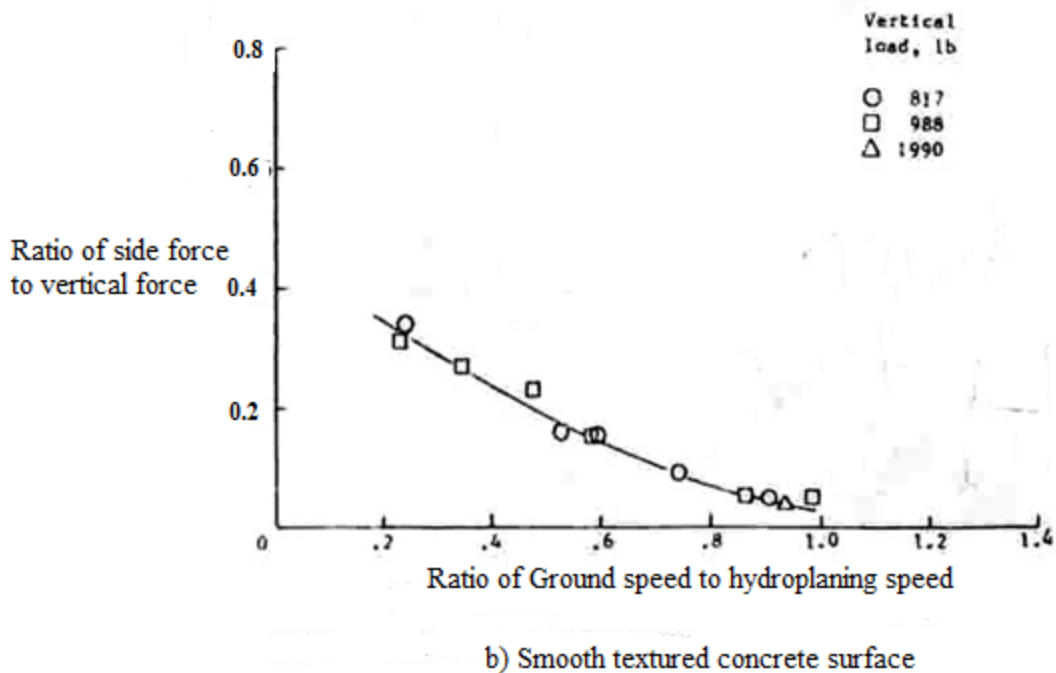
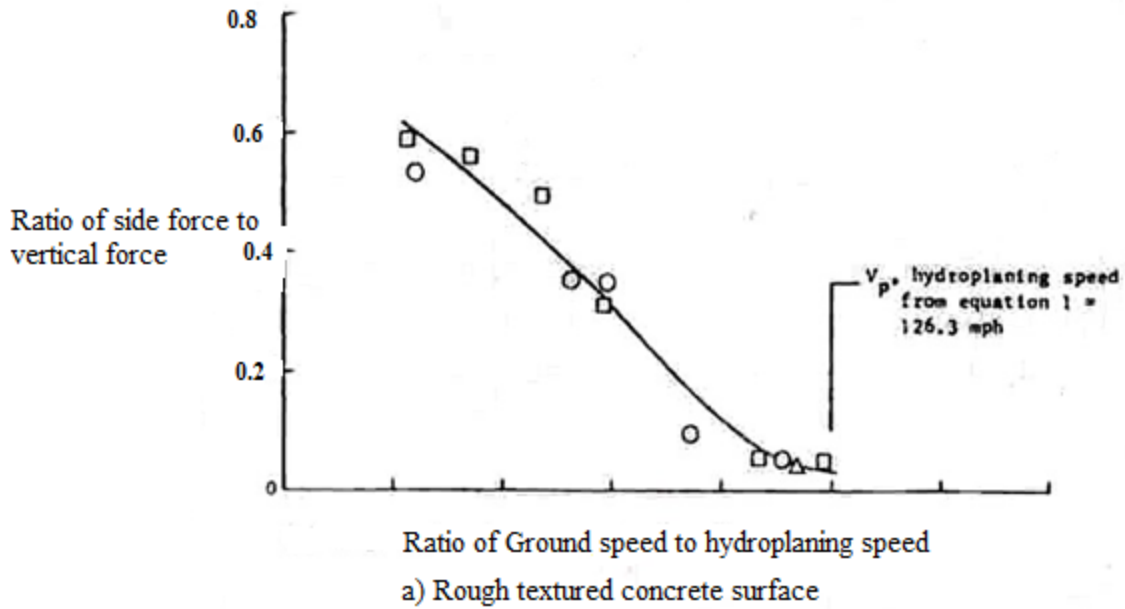


Figure 6.7 Effect of vertical load on hydroplaning for flooded smooth and rough textured concrete surfaces. Water depth = 0.3 in; 20x4.4 rib tread aircraft tire; tire pressure = 155 psi (Horne and Joyner, 1965)

This due to the fact that the tire acts as an elastic body and any change in the vertical load on the tire produces corresponding changes in the tire-ground footprint area such that the ratio of vertical load to footprint area remains constant for a given tire inflation pressure (Horne and Joyner, 1965).

6.3.3.8 Tread Wear

Tire wear is an important factor in wet-runway stopping performance of tires of automobiles and aircrafts. Tests conducted by Horne et al. (1968) at the NASA Langley Research Center showed that on a wet runway surface, with tire tread wear greater than 80 percent, braking effectiveness dropped noticeably and hydroplaning conditions prevail, Figure 6.8.

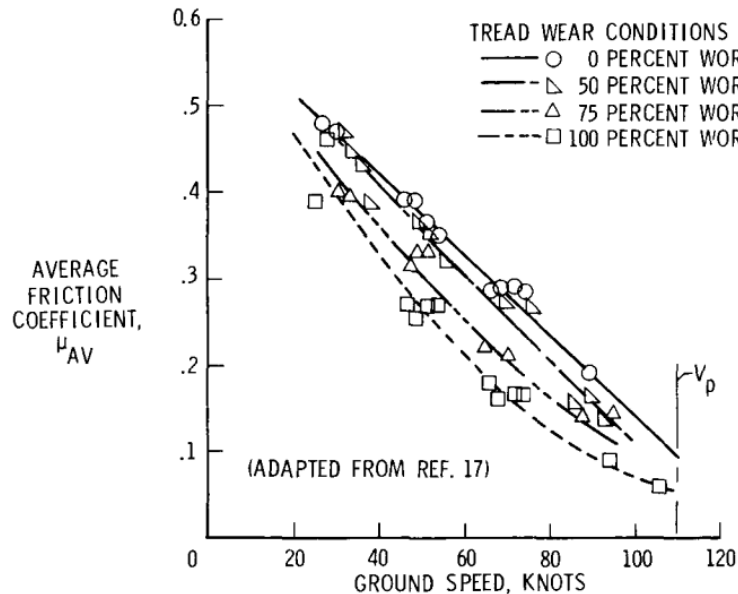


Figure 6.8 Effect of tread wear on the average friction coefficient on the flooded runway surface (Horne et al., 1968)

As discussed in the previous Sections 6.3.3.3 and 6.3.3.4, tire grooves are necessary to dissipate water from under the footprint. Figure 6.8 shows that this benefit is lost as the tire tread wears. Moreover, badly worn tire tread likely to flatten the remaining grooves as vertical load increases. This in turn causes the tire to hydroplane even at lower speeds, at which hydroplaning occurs. In effect, a worn tire "behaves very much like a smooth tire during braking" (Trafford et al., 1965).

6.3.4 Fluid parameters

6.3.4.1 Depth of fluid

Higher surface water depths combined with even practical ground speed of aircraft could result in hydroplaning by developing hydrodynamic uplift force on the tire contact patch at a faster rate. Such a situation demands proper drainage of surface water by either constructing asphalt runways with open graded mix designs or providing runway surface grooving. Dynamic hydroplaning occurs only under a certain minimum fluid depth on pavement surfaces (Horne, 1974) as shown in Table 6.1.

Rib tread tires operating on open-textured and transverse-grooved pavement surfaces require the largest fluid depths. It was also found that hydroplaning speed decreases rapidly for water film thicknesses between 0.1 mm and 2 mm and tends to level-off for larger water film thicknesses (Ong et al., 2005).

Table 6.1 Effect of water depth on hydroplaning phenomena (Horne, 1974)

RUNWAY WATER DEPTH RANGE, IN.	HYDROPLANING PHENOMENA EXPERIENCED
Greater than (0.05-0.10) Between (0.02-0.03) and (0.05-0.10) Less than (0.02-0.03)	(a), (b), (c), and (d) (b), (c), and (d) (c) and (d)
<p>(a) <u>DYNAMIC HYDROPLANING</u>.- Unbraked wheel spindown, zero tire braking and cornering friction coefficients (aircraft ground speeds must be greater than tire dynamic hydroplaning speed, $V_p = 9\sqrt{p}$).*</p> <p>(b) <u>COMBINED DYNAMIC AND VISCOUS HYDROPLANING</u>.- Reduced tire braking and cornering coefficients, slow recovery of wheel synchronous (ground speed) angular velocity from braking skid (from brake application).</p> <p>(c) <u>VISCOUS HYDROPLANING</u>.- Reduced tire braking and cornering coefficients, slow recovery of wheel synchronous (ground speed) angular velocity from braking skid (from brake application).</p> <p>(d) <u>REVERTED RUBBER HYDROPLANING</u>.- Very low tire braking friction coefficients at all ground speeds, tire cornering friction coefficient = 0 (only develops if prolonged locked wheel tire skid occurs due to pilot or antiskid failure to release wheel brake pressure after wheel skid from brake application).</p>	
<p>* Where V_p tire dynamic hydroplaning speed, knots p tire inflation, lb/in.²</p>	

Agarwal and Henry (1977) performed experiments on locked wheel on pavement with water depth less than 2.4 mm and the hydroplaning speed is expressed in terms of water film thickness as follows,

$$v_p = 37.5 + 5.28(t_w)^{-0.5} \quad (6.45)$$

where v_p is the hydroplaning speed in mph and t_w is the water film thickness in inch.

Equation (6.45) was modified by Huebner et al. (1986) who proposed the use of Equation (6.46) which is valid for the water film thickness above 2.4 mm.

$$v_p = 26.04(t_w)^{-0.259} \quad (6.46)$$

Staughton and Williams (1970) measured the spin-down speed for several production tires in various water depths on a smooth concrete surface. The results of the spin-down tests are shown in Figure 6.9. For all but one of these tires, an increase of water depth above about 5 mm (0.20 in.) has no effect on the hydroplaning speed. For high rainfall rates and poor drainage conditions, the available friction coefficient can drop drastically, especially at higher aircraft ground speeds close to hydroplaning speed. To help promote water drainage, most runways are constructed with a cross slope or crown and coarse, highly textured surface finishes are applied. In general, runway water buildup or surface flooding that occurs during periods of precipitation is directly related to the rainfall intensity, the surface macrotexture (coarse, large-scale, surface roughness), and the runway cross slope.

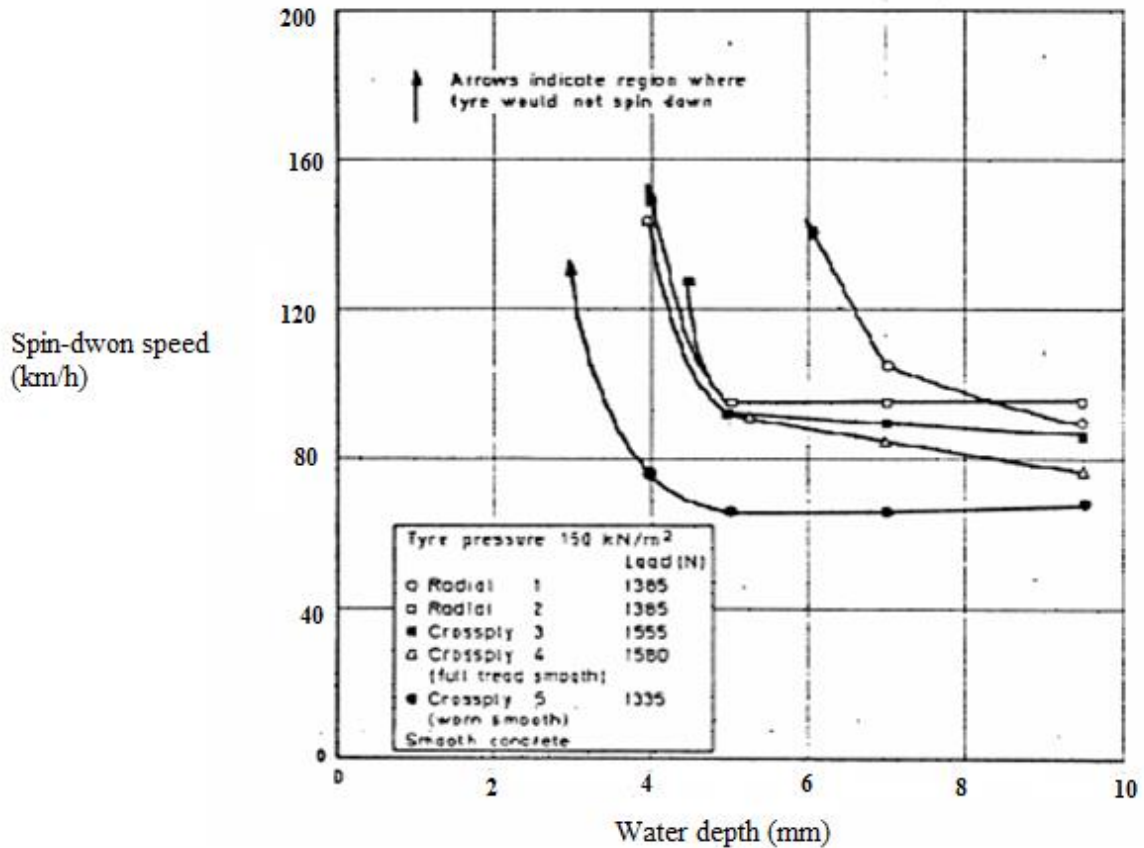


Figure 6.9 Hydroplaning speed predicted by experimental results of Staughton and Williams (1970) for different water depths

Gallaway et al. (1971) developed an equation based on tests at the Texas Transportation Institute (TTI) to predict the water depth on un-grooved pavements. It should be noted that the water depth predicted by the equation is the water film depth lying above the mean pavement texture depth.

$$d = 3.38 * 10^{-3} \left[(I/T)^{-0.11} * L^{0.43} * I^{0.59} * (1/S)^{0.42} \right] - T \quad (6.47)$$

where d is the water depth (in) ; T is the average pavement texture depth (in) ; L is the drainage path length (ft) ; I is the rainfall intensity (in/hr) ; and S is the pavement cross slope (ft/ft). The water depth given by Equation (6.47) is shown in Figure 6.10.

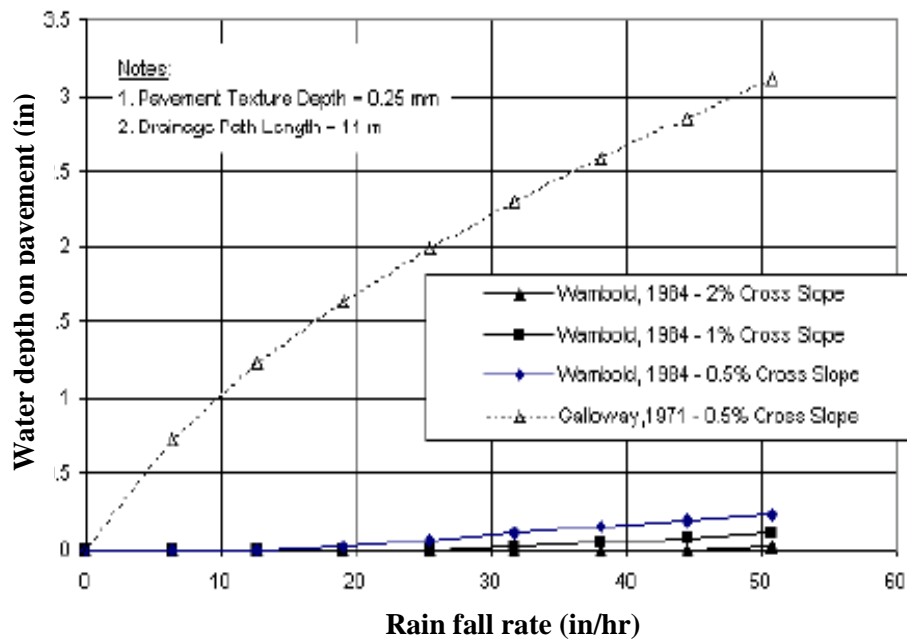


Figure 6.10 Water depth required to cause hydroplaning predicted by Galloway's equation (1971) for different rainfall intensities

6.3.4.2 Density of Fluid

The density of fluid is considered to be a significant fluid property in tire hydroplaning because of the severe curvature of the streamlines in the vicinity of the tire and the high speeds involved (Martin, 1966). The squeeze films which prevail under partial hydroplaning conditions are thinner than the maximum film thickness observed when total hydroplaning begins. Thus, in partial hydroplaning, tire deformation due to hydrodynamic pressure should be sufficiently small that the pressure available to squeeze a water film from beneath a tread element is essentially the dry surface contact pressure. It was observed that an improvement in wet traction performance should accompany an increase in tire-road surface contact pressure. This can be accomplished in two ways: a) the groove, or void, area can be increased, decreasing the actual area of tire - pavement contact. The contact pressure for a given tire load will thus be increased; b) the inflation pressure can be increased, reducing the contact area and increasing the tire-road contact pressure.

6.3.5 Pavement surface parameters

6.3.5.1 Microtexture

Pavement microtexture affects the actual contact between tire and pavement by penetrating the thin film of water that is not removed by the tire. A good microtexture on a pavement is a major means of combating viscous hydroplaning (Moore, 1967; Horne, 1975). Microtexture is a fine scale roughness contributed by the fine aggregates (ACPA, 2000) and technically it is the texture defined by the wavelengths of 0.001mm to 0.5 mm and vertical amplitude less than 0.2 mm (PIARC, 1987). It was found that the pavement microtexture in the 0.2- to 0.5-mm range delays hydroplaning by increasing the hydroplaning speed by up to 20% (Ong et al., 2005).

6.3.5.2 Macrotexture

The surface macrotexture of asphalt pavement varies with mix design. An effective pavement mix design brings about a better surface macrotexture which in turn serves as flow channels to facilitate the drainage of entrapped water trapped within the tire–pavement contact area and thus reducing the magnitude of hydrodynamic forces on the tire footprint which may otherwise cause the tire to float on the water (Horne and Joyner, 1965).

Pavement macrotexture is a function of aggregate size, shape, angularity, spacing and distribution of coarse aggregates (Kokkalis and Panagouli, 1998). Macrotexture refers to texture with wavelengths of 0.5 mm to 51 mm and vertical amplitudes ranging between 0.1 mm and 20 mm (PIARC, 1987). It is most commonly produced through small surface channels, grooves, or indentations that are intentionally formed to allow water to escape from beneath a vehicle's tires (FHWA, 2002). The hydroplaning risk associated with different types of surfaces and their macrotexture depths was found by Yager (1983), Table 6.2.

Table 6.2 Classification of pavement surfaces by hydroplaning potential and macro-texture depth
(Yager, 1983)

Class	Type of Surface	Hydroplaning potential	Macrotexture depth (mm)	
			Grease sample method	Sand patch method
I	Deep grooving Open texture Porous friction course	Low	>1	>1.8
II	Shallow grooving Scoring and wire combing Large aggregate asphalt	Poor	1 to 0.5	1.8 to 0.9
III	Heavily textured concrete Mixed gradation aggregate asphalt	Fair	0.5 to 0.3	0.9 to 0.6
IV	Lightly textured concrete Worn and trafficked Small gradation aggregate asphalt	Good	0.3 to 0.1	0.6 to 0.25
V	Very little texture Painted and rubber coated Heavily trafficked	High	<0.1	<0.25

Smiley and Horne (1960) demonstrated from their experimental investigations that for a given speed, increasing the surface texture increases braking traction up to some level after which no further increase in traction is obtained. The results indicate that a greater depth of texture is required to develop maximum tire friction coefficient at the higher speeds, Figure 6.11.

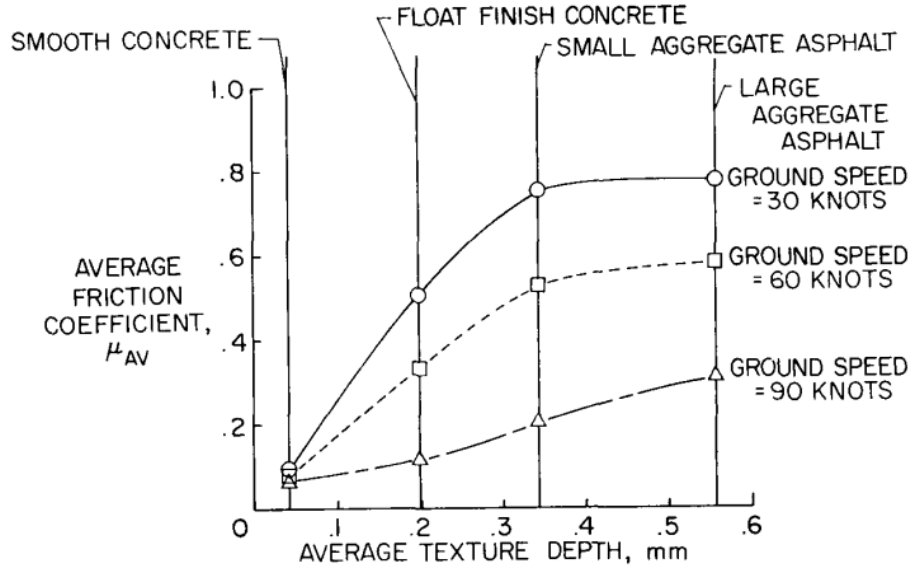


Figure 6.11 Correlation of braking friction coefficient with average texture depth (32 X 8.8 smooth tread aircraft tire; Load 53.4 kN; inflation pressure 96.5 N/cm²; flooded runway; Water depth = 0.2 to 0.5 cm)

A pavement with good macrotexture in the form of grooving can also delay the dynamic hydroplaning considerably (Horne, 1975). Gray (1962; 1963) found that transverse (to vehicle motion) pavement grooves can substantially increase the minimum water depth required for tire hydroplaning to occur, Figure 6.12.

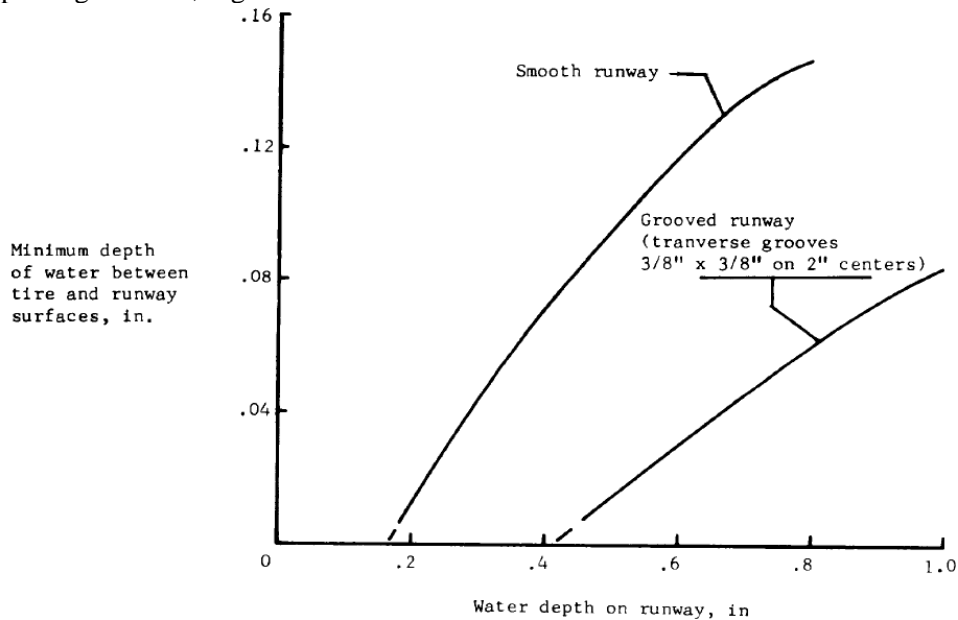


Figure 6.12 Effect of runway water depth on tire displacement from runway under hydroplaning conditions. British Meteor fighter; ground speed, 87 knots; tire pressure, 60 lb/sq in.; $v_g/v_g = 1.2$ (Gray, 1963)

6.4 Empirical Equations to Determine Critical Hydroplaning Speed

6.4.3 NASA equations

The hydrodynamic dynamic lift generated under a tire rolling and sliding along a water-covered surface is given by the following equation (Horne, 1963; 1975; 1976):

$$\text{Lift Force (LF)} = \frac{1}{2} C_{Lh} \rho v^2 S \quad (6.48)$$

where, ρ is the density of the fluid, S is the tire footprint area and C_{Lh} is the hydrodynamic lift coefficient. When total dynamic hydroplaning occurs, LF/S is equal to the tire bearing pressure that can be approximated by the tire inflation pressure p .

Hence, the total dynamic hydroplaning speed can be expressed as:

$$\text{Hydroplaning Speed (v}_h) = \sqrt{\frac{2p}{\rho C_{Lh}}} \quad (6.49)$$

On the basis of a large number of field tests, the value of C_{Lh} is considered as 0.7 for a rolling tire and 0.95 for a sliding tire.

Based on these values of hydrodynamic lift coefficients and the density for water, NASA proposed the following equations to determine the critical hydroplaning speed for rolling and locked wheels as a function of tire inflation pressure:

$$v_{h,\text{rolling}} = 6.36\sqrt{p} \quad (6.50)$$

$$v_{h,\text{locked}} = 5.43\sqrt{p} \quad (6.51)$$

where, $v_{h,\text{rolling}}$ is the hydroplaning speed for rolling tire in km/h, $v_{h,\text{locked}}$ is the hydroplaning speed for locked wheel in km/h and p is the tire inflation pressure in kPa.

NASA also proposed an empirical equation to determine the critical spindown speed for truck tires (Horne, 1984; Horne et al., 1986) as a function of the tire footprint aspect ratio and the tire inflation:

$$v_{\text{spindown}} = 23.3 * [p]^{0.21} (1.4 / \text{FAR})^{0.5} \quad (6.52)$$

where, FAR is the Footprint Aspect Ratio is defined as: Tire width/Tire length

6.4.4 Gallaway's hydroplaning equation

Gallaway et al. (1979) proposed an empirical equation to predict the critical hydroplaning speed as a function of tire inflation pressure, tread depth, water depth and mean texture depth:

$$v_p = (\text{SD})^{0.04} (p_t)^{0.3} (\text{TRD} + 1)^{0.06} A \quad (6.53)$$

where A is defined as follows,

$$A = \max \left\{ \left[\frac{10.409}{t_w^{0.06}} + 3.507 \right], \left[\frac{28.952}{t_w^{0.06}} - 7.819 \right] (MTD)^{0.04} \right\}$$

where v_p is the hydroplaning speed in mph, SD is the spin-down in percentage, t_w is the water-film thickness in inch, MTD is the mean texture depth in inch, p_t is the tire inflation pressure, in psi and TRD is the tire tread depth in 1/32 inch.

6.4.5 Wambold's hydroplaning equation

Wambold et al. (1984) proposed the following equation to predict the critical hydroplaning speed for tires rolling under low inflation pressure conditions:

$$v_p = k1 * [(TD / 25.4 + 1)^{k2} * MTD^{k3} * (k4 / WT^{k5} + 1)] [3.5] \quad (6.54)$$

where, WT is the estimated water film thickness (mm); MTD is the mean texture depth (mm); TD is the tire tread (mm); v_p is the critical hydroplaning speed (km/h) and k1, k2, k3, k4 and k5 are empirical coefficients and 0.05, 0.01, 1.8798 and 0.01 as typical values for these coefficients, respectively.

However, the above equation is applicable only for hydroplaning speed corresponds to 10% spin-down; and 165 kPa tire pressure.

6.4.6 PAVDRN hydroplaning equation

The predicted hydroplaning speed (v_p) computed by PAVDRN equation speed is expressed as follows:

a) for water film thickness (t) is less than 2.4 mm

$$v_p = 96.3 t^{-0.259} \quad (6.55)$$

b) for water film thickness (t) is equal to greater than 2.4 mm

$$v_p = 4.94 A \quad (6.56)$$

where A is the greater of following equations:

$$\left(\frac{12.64}{t^{0.06}} + 3.507 \right) \text{ or } \left[\frac{35.15}{t^{0.06}} - 7.817 \right] (0.0393 \text{ MTD})^{0.14}$$

MTD is the mean texture depth (mm).

6.5 Analytical/Numerical Modeling of Hydroplaning

Martin (1966) conducted an analytical study of total dynamic hydroplaning phenomenon from the standpoint of view of theoretical hydrodynamics and compared with the experimental results. The following are salient features of his study: (a) potential flow theory was applied and conformal mapping techniques were used to get the solution, (b) two-dimensional irrotational flow problem of rigid curved surfaces involving incompressible inviscid fluid, (c) the coefficient

of lift obtained was 0.8 compared to 0.644 for NASA and does not change appreciably for moderate water depths and grooved tires. The drawbacks his analytical model are that (a) the side flow and the viscosity were neglected completely and (b) the formation of bow wave was completely neglected.

Eshel (1967) conducted an analytical study on the total dynamic hydroplaning phenomenon. The major features of his study are as follows: (a) In the inlet region: no side flow was allowed, the effect of bow wave was considered and the fluid inertial effects were considered; (b) In the central region: two dimensional viscous flow was assumed and non-inertial side flow was considered; (c) In the exit region: the atmospheric pressure was considered at the trailing edge; (d) parabolic velocity profile across the water film thickness was considered. The major drawback of his study is that there is no definite side flow in the inlet region.

Moore (1967) presented an analytical model to explain both partial and total viscous hydroplaning phenomena. The following are the major contributions of his analytical study: (a) solving the problem of a sliding rubber block on a two-dimensional smooth sinusoidal asperity separated by a thin film of fluid, (b) one-dimensional Reynolds solution was proposed in which inlet, central and outlet regions for the film above the single asperity were treated separately. The major drawbacks of his study are that (a) limited to viscous hydroplaning problems with a two-dimensional sinusoidal asperity, and (b) the effect of side flow was neglected.

Tsakonas et al., (1968) conducted analytical work based on inviscid approach to solve the problem of the planning of a flat rigid surface of small aspect ratio in extremely shallow water. The salient features of their study : (a) employing the theory of hydrofoil, (b) solution was possible when the pressure distribution on the pavement was a step function equal in magnitude to the tire inflation pressure. The major disadvantages of their study are that, (a) their model does not represent practical conditions, in which tire surface is not planar and the actual flow is not inviscid for the whole tire foot-print region and (b) their lift coefficient was quite small compared to that of NASA' experimentally determined value.

Daughaday and Tung (1969) were the first to introduce a three-dimensional tire surface model to solve the total hydroplaning problem by using a two-region approach. The salient features of their model are: (a) In the inlet region, the fluid inertial effects are predominant while the flow in the foot-print region is non-inertial and viscous, (b) the foot print region was assumed to be planar. The major findings of their analytical study were that (a) the planar footprint region cannot produce the magnitude of the recovery factor that is necessary for the tires to hydroplane, thus, the tire deformation is necessary for an accurate prediction of hydroplaning speed, (b) the inward buckling of the tire which produces a more two-dimensional flow in the footprint region and which results in the right order of magnitude of recovery factor which is a crucial ingredient in the theory of hydroplaning. The major drawback of their study was that the flow in footprint region was viscous and noninertial. The hydrodynamic pressure distribution computed for a totally hydroplaning tire with flat-tread surface in the contact region is shown in Figure 6.13.

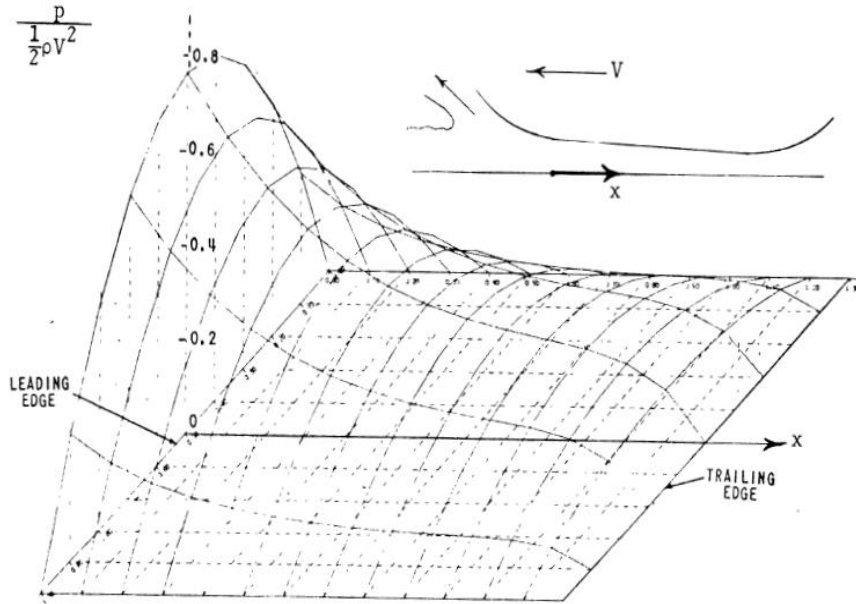


Figure 6.13 Hydrodynamic pressure distribution under total hydroplaning conditions for a tire with flat-tread surface in the contact region (Daughaday and Tung ,1969)

Browne (1971) proposed a two-dimensional treatment for a three-dimensional tire deformation model for hydroplaning, making use of Navier-Stokes equations, Figure 6.14. In his model, inviscid, laminar and turbulent models were explored, with the side flow component. Browne investigated the influence of deforming tire using the Moire Fringe technique to measure the fluid thickness distribution under the tire and predicted the hydroplaning well. Browne adopted steady-state analysis for the hydroplaning problem. Browne shows that tire hydroplaning must be accompanied by inward buckling of the tire tread in the central portion of the contact region.

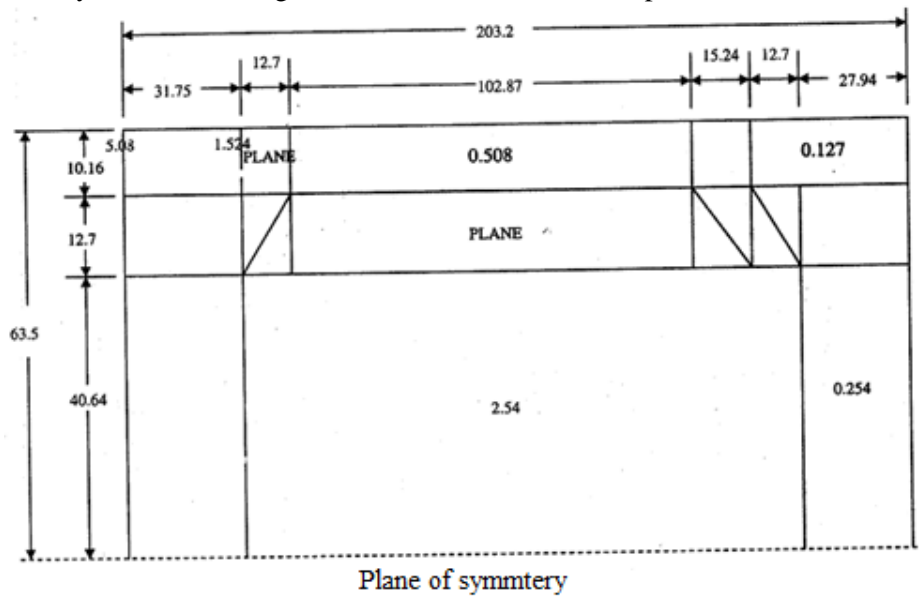


Figure 6.14 Tire deformation profile under hydroplaning conditions (Brown, 1971)

Browne's analysis shows that viscous effects are not important in hydroplaning where the amount of water encountered by the tire exceeds the combined drainage capacity of the tread pattern and the pavement macrotexture. Further Brown and Whicker (1983) adopted an interactive procedure to introduce the tire deformation by considering the interaction of a fluid flow model and the tire deformation profile. The major drawbacks in Browne's study were (a) the flow in the hydroplaning situation is not turbulent; (b) the recovery factors of 0.56 in his model is low compared to NASA's value of 0.644; and (c) the model verification made use of a plane of symmetry, a laminar flow and pavement surface was used in numerical verification.

Grogger and Weiss (1996) did the pioneering work and numerically solved the hydroplaning phenomenon, using a combination of general-purpose packages of fluid dynamics and in-house code of structural analysis. Fluid meshes were defined around contact area of a deformed tire and their velocity and pressure fields were obtained. Grogger and Weiss's investigation was limited to non-rotating and non-deforming tire to simplify the analysis. Their investigation closely matched the experimental results for lower vehicle speeds. They concluded neglecting tire deformations caused higher pressure distribution at increased speeds. In the following year, Grogger and Weiss (1997) investigated the influence of hydrodynamic pressures on smooth and grooved tires including deformation and rotation of a tire and compared with an undeformed tire. Their results show tremendous influence of deforming tires at higher vehicular speeds.

Seta et al. (2000) established a numerical procedure to predict the hydroplaning speed. They considered the following three important factors: (a) fluid-structure-interaction, (b) rolling tire, and (c) tire tread pattern. The tire and fluid were analyzed by the finite element method with Lagrangian formulation, and the finite volume method with Eulerian formulation respectively. Seta et al. focused on the simulation of dynamic hydroplaning with thick water films and hence they ignored the effect of fluid viscosity. They verified the predictability of the hydroplaning model by varying different parameters such as the water depth and velocity, tread pattern etc. However they could not predict the precise speed at which the onset of hydroplaning takes place.

Janajreh et al., (2001) used fluid dynamics theory to ascertain the drag force, which is an indication of the fluid evacuation around the tread pattern. The hydroplaning speed is considered to be low as the drag force increases. Okano and Koishi (2001) proposed a coupled Eulerian Lagrangian numerical method to predict the hydroplaning speed by computing its dependence on the contact force between tire and road, using MSC.Dytran for different tire tread patterns.

Ong et al. (2005) developed a numerical hydroplaning model based on finite volume framework. The hydroplaning simulations were performed by utilizing Brown (1971)'s work of smooth tire-plane pavement conditions. The results were found to be in good agreement with the well-known NASA hydroplaning equation. The model was further improvised to investigate the effectiveness of transverse and longitudinal grooving in reducing hydroplaning risk (Ong and Fwa, 2006a; 2006b) and different tread patterns of tires (Fwa et al., 2008; 2009, 2010). The drawback of their model was the use of a non-rotating tire with an artificial pavement. Cho et al. (2006) proposed a method to estimate the frictional energy loss of a passenger car tire rolling on a flooded smooth pavement, which is based on a numerical-analytical approach. The drawback of this model was the use of smooth pavement surface.

6.6 Computational Formulation of Hydroplaning

The problem of hydroplaning in which a rolling/skidding tire impacts a thick layer of water has been tackled by applying the Coupled Eulerian Lagrangian (CEL) technique, thereby avoiding numerical difficulties associated with extensive mesh distortion in the Lagrangian approach due to fast flow fields. This improvement in fluid-structure-interaction (FSI) modeling resulted in a more realistic behavior of the fluid material during impact. The Abaqus/Explicit transient dynamic analysis technique has been utilized to combine geometrical and material nonlinear response characteristics. The method consists of periodic surface reconstruction and solution of the coupled fluid - structure equations. The tire is discretized by the traditional Lagrangian finite element formulation. The water is represented by means of an Eulerian formulation in which the fluid flows through a stationary cube finite element (FE) mesh. The interaction forces between the fluid and the tire are transferred through Eulerian–Lagrangian penalty based contact.

The strategy for CEL calculations is to apply pressure boundary conditions on the Lagrangian mesh from the Eulerian mesh, and to treat the Lagrangian mesh boundaries as velocity boundary conditions in the Eulerian mesh. Since the Eulerian mesh is fixed and the fluid material flows through it, a larger Eulerian mesh than the actual physical fluid mesh is required to prevent the loss of fluid material after the impact, as this would lead to the artificial loss of kinetic energy and consequently decrease the level of accuracy of the obtained results.

In the following, details of the utilization of the CEL method for simulation the interaction of tires with a given speed and slip ratio with wet/flooded asphalt pavement surfaces.

6.6.3 CEL method

6.6.3.1 Governing Equations

The equations of the structure (tire and pavement), come from the conservation of momentum and material models (in this case viscoelasticity).

For the displacement field \mathbf{u} of the deformed structure it holds

$${}_s\rho \frac{D^2\mathbf{u}}{Dt^2} = \nabla \cdot {}_s\boldsymbol{\sigma} + {}_s\mathbf{b} \quad (6.57)$$

where ρ is the density, $\boldsymbol{\sigma}$ is the Cauchy stress, \mathbf{b} is the body force. The subscript ‘s’ denotes the structure.

From Figure 6.15, the displacement boundary conditions on the boundary $\partial_s\Omega_1$ and the traction boundary conditions on the boundary $\partial_s\Omega_2$ can be written as

$${}_s\mathbf{u} = {}_s\hat{\mathbf{u}} \text{ on } \partial_s\Omega_1 \quad (6.58)$$

$${}_s\boldsymbol{\sigma} \cdot {}_s\mathbf{n} = {}_s\hat{\mathbf{t}} \text{ on } \partial_s\Omega_2 \quad (6.59)$$

Where \mathbf{n} is the outward unit vector normal to the boundary and $\hat{\mathbf{t}}$ is the external traction including hydrodynamic pressure.

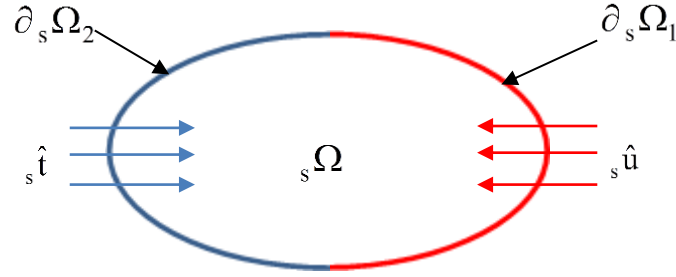


Figure 6.15 Structure domain

The system of fluid equations in non-conservation partial differential form,

$$\frac{D_f \rho}{Dt} + {}_f \rho \nabla \cdot \mathbf{v} = 0 \quad (6.60)$$

$${}_f \rho \frac{D\mathbf{v}}{Dt} - \nabla \cdot {}_f \boldsymbol{\sigma} - {}_f \mathbf{b} = 0 \quad (6.61)$$

$${}_f \rho \frac{DE}{Dt} - \nabla \cdot ({}_f \boldsymbol{\sigma} \cdot \mathbf{v}) - {}_f \mathbf{b} \cdot \mathbf{v} = 0 \quad (6.62)$$

where \mathbf{v} is the flow velocity and E is the total energy per unit volume. The subscript 'f' denotes the fluid.

In Equation (6.62), $\boldsymbol{\sigma} \cdot \mathbf{v}$ is a function of (p, μ, \mathbf{v}) , where, p is pressure and μ is viscous terms.

E can be expressed as the sum of the kinetic energy and the internal energy e ,

$$E = \frac{1}{2} {}_f \rho \mathbf{v} \cdot \mathbf{v} + e \quad (6.63)$$

$$e = E - \frac{1}{2} {}_f \rho \mathbf{v} \cdot \mathbf{v} \quad (6.64)$$

$$\begin{aligned} \frac{De}{Dt} &= \frac{DE}{Dt} - \frac{1}{2} \frac{D({}_f \rho \mathbf{v} \cdot \mathbf{v})}{Dt} \\ &= \frac{DE}{Dt} - \frac{1}{2} \frac{D_f \rho}{Dt} (\mathbf{v} \cdot \mathbf{v}) - \frac{1}{2} {}_f \rho \left(\frac{D\mathbf{v}}{Dt} \cdot \mathbf{v} + \mathbf{v} \cdot \frac{D\mathbf{v}}{Dt} \right) \\ &= \frac{DE}{Dt} - {}_f \rho \frac{D\mathbf{v}}{Dt} \cdot \mathbf{v} \quad \left(\because \frac{D_f \rho}{Dt} = {}_f \rho \nabla \cdot \mathbf{v} = 0 \right) \end{aligned} \quad (6.65)$$

$$\begin{aligned}
\frac{De}{Dt} &= \frac{DE}{Dt} - {}_f\rho \frac{D\mathbf{v}}{Dt} \cdot \mathbf{v} \\
&= \nabla \cdot ({}_f\boldsymbol{\sigma} \cdot \mathbf{v}) + {}_f\mathbf{b} \cdot \mathbf{v} - (\nabla \cdot {}_f\boldsymbol{\sigma} + {}_f\mathbf{b}) \cdot \mathbf{v} \\
&= \nabla \cdot ({}_f\boldsymbol{\sigma} \cdot \mathbf{v}) - (\nabla \cdot {}_f\boldsymbol{\sigma}) \cdot \mathbf{v} = (\nabla \cdot {}_f\boldsymbol{\sigma}) \cdot \mathbf{v} + {}_f\boldsymbol{\sigma} : \nabla \mathbf{v} - (\nabla \cdot {}_f\boldsymbol{\sigma}) \cdot \mathbf{v} \\
&= {}_f\boldsymbol{\sigma} : \nabla \mathbf{v}
\end{aligned} \tag{6.66}$$

$$\frac{De}{Dt} = {}_f\boldsymbol{\sigma} : {}_f\mathbf{D} \tag{6.67}$$

where D is the rate of deformation tensor.

The initial condition is

$$\mathbf{v}(\mathbf{x}; 0) = 0 \text{ in } {}_f\Omega \times (0, T] \tag{6.68}$$

From Figure 6.16, the inflow boundary condition is

$${}_f\mathbf{v} = {}_f\hat{\mathbf{v}} \text{ on } \partial {}_f\Omega_1 \tag{6.69}$$

the traction boundary conditions are assumed to be imposed on the remaining part of the boundary $\partial {}_f\Omega_2$

$${}_f\boldsymbol{\sigma} \cdot {}_f\mathbf{n} = {}_f\hat{\mathbf{t}} \text{ on } \partial {}_f\Omega_2 \tag{6.70}$$

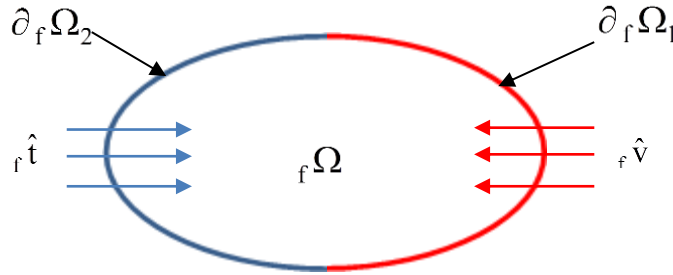


Figure 6.16 Fluid domain

6.6.3.2 Interface Conditions

In the current fluid–structure interaction problem, compatibility conditions are applied at the common displacement and traction boundaries and between the boundaries of the structure and the fluid.

For example, the imposed traction compatibility condition on $\partial\Omega_2^c$ is

$${}_s\boldsymbol{\sigma} \cdot {}_s\mathbf{n} = {}_f\boldsymbol{\sigma} \cdot {}_f\mathbf{n} \text{ on } \partial\Omega_2^c \tag{6.71}$$

while, since a frictionless model is considered between the fluid and the structure, the tangential tractions vanish.

Similarly, the imposed kinematic compatibility condition on $\partial\Omega_1^c$ is

$${}_f \mathbf{v} = \frac{\partial {}_s \mathbf{u}}{\partial t} \quad (6.72)$$

6.6.3.3 Fluid-structure interaction (FSI)

In the FSI, the interface boundary conditions as described in the Section 6.6.3.2 need to be imposed on both the Eulerian and Lagrangian grids. The position of the interface is determined on the basis of the velocity of Lagrangian grid nodes. However, both calculations (Lagrangian and Eulerian) use this interface normal velocity so that $\mathbf{v} \cdot \mathbf{n} = 0$ is enforced. The Lagrangian mesh simply uses the computed velocities of its boundary nodes, while the Eulerian calculation captures this interface velocity by assigning the interface velocity of the nearest point on the interface. Since the interface velocity is defined as the velocity of the nodes on the Lagrangian mesh boundary with no contribution from the Eulerian mesh, velocity boundary conditions cannot be enforced on the Lagrangian mesh at the interface. Instead, force boundary conditions are applied by interpolating the Eulerian grid pressure to this Lagrangian interface. However, both calculations (Lagrangian and Eulerian) use this interface pressure so that $p = 0$ is enforced. The interface pressure can be interpolated from the Eulerian grid to apply force boundary conditions to the Lagrangian calculation. In this way, the interface pressure is determined using only the Eulerian grid values, ignoring contributions from the Lagrangian mesh (Fedkiw, 2001).

6.6.3.3.1 FSI Partitioned Solver

In the CEL method, a partitioned solver is utilized to couple structure and fluid domains. As the name indicates, the partitioned solver consists of a structure solver and a fluid solver and a coupling algorithm that couples the solvers at the interface of fluid and structure domains both in time and space. The coupling algorithm contains an interpolation method to transfer data from one domain to the other and an iteration scheme to obtain a coupled solution that is within the desired accuracy. The most common way of realizing this approach is by selecting a master surface for a certain variable, and projecting the variable to the other domain at the beginning of the next time step. For fluid-structure problems, the most natural combination is to select the structure surface location and rate of deformation as the master-grid for displacements and the fluid grid as the master-grid for the loads (pressures, shear stresses etc.). The product of displacement times load yields work, making the combination physically appealing (Löhner et al., 1998).

6.6.3.3.2 Coupling of Eulerian-Lagrangian Meshes

Employing a proper coupling algorithm is the most important step of a CEL algorithm for the transfer of forces between the un-matched Eulerian and the Lagrangian mesh regions. The FSI problem domain consists of water and structure traction structural domains ${}_s \partial\Omega$ and ${}_f \partial\Omega$ both share a common interface $\partial\Omega_2^c$. If ${}_f \mathbf{u}$ denotes the displacement field of the fluid and p its pressure field, ${}_s \boldsymbol{\sigma}$ and ${}_f \boldsymbol{\sigma}$ the structure stress tensor and the fluid viscous stress tensor and \mathbf{n} the normal at a point to $\partial\Omega_2^c$, the fluid and structure equations are coupled by imposing that

$${}_s \boldsymbol{\sigma} \cdot \mathbf{n} = -p {}_f \mathbf{I} \cdot \mathbf{n} + {}_f \boldsymbol{\sigma} \cdot \mathbf{n} \quad \text{on } \partial\Omega_2^c \quad (6.73)$$

Equation (6.73) states that the tractions on the wet surface of the structure are in equilibrium with those on the fluid side of $\partial\Omega^c$.

Similarly, Equation (6.74) expresses the compatibility between the displacement fields of the structure and the fluid components at the fluid-structure interface.

$${}_s \mathbf{u} = {}_f \mathbf{u} \text{ on } \partial\Omega_1^c \quad (6.74)$$

Most of the times, the fluid and structure meshes are incompatible along the fluid/structure interface because the fluid and structure problems have different mesh refining requirements.

Due to the fact that the fluid mesh is mostly much finer than the structure mesh along the fluid-structure-interface, it is necessary to compute the surface forces and moments induced by the fluid on the structure using the discretization of the fluid and its boundary ${}_f \partial\Omega$.

A precise way of handling the data transfer between two non-matching FE meshes is by projection, Figure 6.17. In this method, in order to obtain information from the other mesh, a point can be orthogonally projected on that mesh and the information in that projection point can be used in the original point.

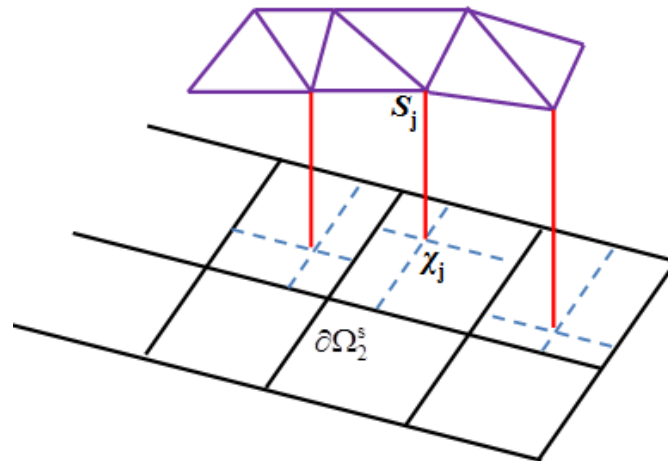


Figure 6.17 Fluid grid point-wet structural element pairing (Farhat et al., 1998)

Another method involves in the orthogonal projection of a whole element on the other mesh and the proportions of the area of intersection can then be utilized to define to what degree the values of that element have to be taken into account. The following are the two important criteria in which such a data exchange or coupling between two non-matching meshes ideally should satisfy:

- global conservation of energy over the interface,
- global conservation of loads over the interface.

In order to ensure that the energy balance of the interface loads on either side of the interface is zero at all time, the following computational algorithm for evaluating the forces induced by the fluid on the structure (Farhat et al., 1998) is utilized.

In terms of the finite element formulation, the structural displacement field ${}_s\mathbf{u}_e$ inside the wet region ${}_s\Omega_e \in {}_s\partial\Omega$ of an element e is given by

$${}_s\mathbf{u}_e = \sum_{i=1}^{i_e} N_i {}_s\mathbf{u}_i \quad (6.75)$$

where i_e denotes the total number of wet nodes belonging to structural element e , and N_i , is the finite element shape function associated with node i of element e .

In the case of fluid and structure meshes with non-matching discrete interfaces, equation (6.74) can be discretized by

- a) pairing each fluid grid point S_j on ${}_f\partial\Omega$ with the closest wet structural element ${}_s\Omega_e \in {}_s\partial\Omega$, Figure 6.17.
- b) determining the natural coordinates χ_j in ${}_s\Omega_e$ of fluid point S_j (or its projection onto ${}_s\Omega_e$).
- c) Interpolating ${}_f\mathbf{u}$ inside ${}_s\Omega_e$ to obtain

$${}_f\mathbf{u}_j = {}_f\mathbf{u}(S_j) = {}_s\mathbf{u}(\chi_j) = \sum_{i=1}^{i_e} N_i(\chi_j) {}_s\mathbf{u}_i \quad j \in {}_f\partial\Omega, i \in {}_s\partial\Omega \quad (6.76)$$

The virtual work of the fluid tractions acting on ${}_f\partial\Omega$ can be expressed as

$$\begin{aligned} {}_f\delta W &= \int_{{}_f\partial\Omega} (-p_f \mathbf{n} + {}_f\boldsymbol{\sigma} \cdot \mathbf{n}) \cdot {}_f\mathbf{u} \, ds \\ &= \sum_{j=1}^{j_f} \int_{{}_f\partial\Omega} (-p_f \mathbf{n} + {}_f\boldsymbol{\sigma} \cdot \mathbf{n}) D_j {}_f\mathbf{u}_j \, ds \\ &= \sum_{j=1}^{j_f} \Phi_j {}_f\mathbf{u}_j \end{aligned} \quad (6.77)$$

where D_j is an extrapolation function defined on ${}_f\partial\Omega$ and Φ_j is defined as the numerical flux.

By substituting Equation (6.76) into Equation (6.77), the following relation can be obtained:

$${}_f\delta W = \sum_{i=1}^{i_s} \left(\sum_{j=1}^{j_f} N_i(\chi_j) (-p(\chi_j) \mathbf{n} + {}_f\boldsymbol{\sigma}(\chi_j) \cdot \mathbf{n}) \right) {}_s\mathbf{u}_i \quad (6.78)$$

$${}_f\delta W = \sum_{i=1}^{i_s} \left(\sum_{j=1}^{j_f} \Phi_j N_i(\chi_j) \right) {}_s\mathbf{u}_i \quad (6.79)$$

The virtual work of the structural forces acting on ${}_s\partial\Omega$ can be expressed as

$${}_s\delta W = \sum_{i=1}^{i_s} f_i {}_s\mathbf{u}_i \quad (6.80)$$

and that the energy is conserved at the fluid/structure interface if ${}_f \delta W = {}_s \delta W$, from Equations (6.79) and (6.80)

$$f_i = \sum_{j=1}^{j=j_f} \Phi_j N_i(\chi_j) \quad (6.81)$$

given that the shape functions of a finite element satisfy $\sum_{i=1}^{i=i_e} N_i = 1$, it can be verified that the nodal loads expressed in Equation (6.81) satisfy

$$\sum_{i=1}^{i=i_s} f_i = \sum_{i=1}^{i=i_s} \sum_{j=1}^{j=j_f} \Phi_j N_i(\chi_j) = \sum_{j=1}^{j=j_f} \Phi_j \quad (6.82)$$

6.6.3.3.3 Interface tracking

In the CEL method, as explained before, the structure is embedded in an Eulerian fixed mesh. When fluid material leaves the Eulerian mesh through the element faces, it will occupy adjacent elements that are initially empty or air material elements. During material transport or advection, the volume fraction of all elements occupied by fluid is tracked by computing its Eulerian volume fraction (EVF) within each element. By definition, if fluid completely fills an element, its volume fraction is one; if no fluid is present in an element, its volume fraction is zero. The fluid boundary does not have to match element geometry at any time during the analysis and has to be recomputed in each time increment as the material flows through the mesh (Abaqus, 6.10).

The VOF utilized in this study was based on a concept of a fractional volume proposed by Hirt and Nichols (1981).

The volume of a fluid element k can be represented as (Rider and Kothe, 1997)

$$V^k = \int \alpha^k(V) dV \quad (6.83)$$

where $\alpha(V)$ is an indicator function of fluid presence,

$$\alpha(V) = \begin{cases} 1 & \text{if fluid } k \text{ is present;} \\ 0 & \text{otherwise} \end{cases} \quad (6.84)$$

Cells with values between zero and one must then contain a free surface.

Given V^k , the volume fraction f is defined as

$$f = \frac{V^k}{V} \quad (6.85)$$

where $V = \int dV$. When water volumes fill all space $\sum_k f^k = 1$.

It should be observed that the Net flow out ' f ' of an Eulerian cell through its surface is equal to the time rate of decrease of ' f ' inside the Eulerian cell. Apart from the evolution of ' f ', it is still

unknown where the fluid is in each cell. This information is necessary for the reconstruction of the interface.

$$\frac{\partial}{\partial t} \int_V f \, dV = - \int_S f \mathbf{v} \cdot \mathbf{n} \, dS \tag{6.86}$$

By applying divergence theorem on the right side of Equation (6.86)

$$\int_V \left(\frac{\partial f}{\partial t} + \nabla \cdot f\mathbf{v} \right) dV = 0 \tag{6.87}$$

In the Equation (6.87), the velocity \mathbf{v} stems from the fluid equations.

The evolution of an incompressible fluid field is governed by the following transport equation, given in a conservative form as,

$$\frac{\partial f}{\partial t} + \frac{\partial uf}{\partial x} + \frac{\partial vf}{\partial y} + \frac{\partial wf}{\partial z} = 0 \text{ in } \Omega \times (0, T] \tag{6.88}$$

where t is the physical time, (x, y, z) the Cartesian system, (u, v, w) Cartesian components of the velocity. The evolution of the function f in each cell is made from fluxes calculations of through all the faces of a cell.

However, it is still unknown where the fluid is in each cell. This information is needed for the reconstruction of the interface. There are several interface reconstruction methods, both first and second order accurate in space, such as simple line (SLIC) and piecewise linear interface construction (PLIC) methods, Figure 6.18.

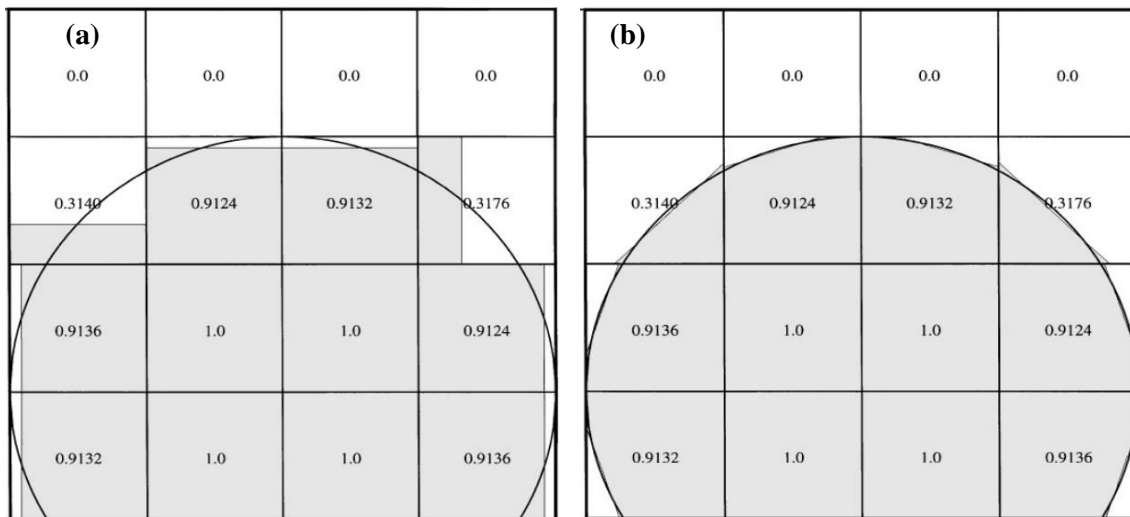


Figure 6.18 Reconstructed interfaces (shaded regions) for a circle (continuous line) using the (a) SLIC and (b) PLIC methods (Rider and Kothe, 1997)

The piecewise constant approximation in SLIC forces the reconstruction to align with selected

mesh logical coordinates, whereas the piecewise linear approximation in PLIC allows the reconstruction to align naturally with the interface. In the Figure 6.18, numbers in the cells denote volume fractions. Abaqus' CEL method utilizes PLIC interface construction technique.

6.7 Summary

This Chapter presented a general introduction of the hydroplaning phenomenon, the influencing factors and a literature review of experimental, analytical and numerical studies on hydroplaning. Also the numerical formulation of the hydrodynamic algorithm that will be utilized in the subsequent finite element simulations of hydroplaning was presented.

7 Finite Element Simulations of Tire-Wet Pavement Interaction

7.1 Introduction

As discussed in the previous Chapter, the risk of hydroplaning exists when the speed of the vehicle is high enough to develop upward hydrodynamic pressure which is equal to or higher than the tire inflation pressure. When the hydroplaning condition prevails, there is a significant loss in braking traction and steering control which may result in fatal accidents. Hydroplaning of vehicles is a very important safety concern particularly during wet-weather highway operations for highway authorities and road user. Hydroplaning speed is known to vary over a range of tire operating and pavement conditions. These two aspects are very important over which the degree of when the hydroplaning situation prevails.

For the past few decades, there are many experimental, analytical and numerical studies were conducted to quantify the effect of different factors on hydroplaning (Horne, 1962, 1964, 1968; Horne & Leland, 1962; Horne & Joyner, 1965). These studies showed that although, there are many factors which have definite influence in reducing the hydroplaning susceptibility of vehicle, the road macrotexture is the only other component to channel away the water entrapped in the tire contact patch other than tire tread (Ivey et al., 1989). Hence, it is generally agreed that pavement surface texture and tire groove depth are one of the most important factors in controlling the wet friction and hydroplaning propensity of a flooded pavement. Past experimental also showed that the slip ratio and the yaw angle conditions at which a particular tire is operating have a significant effect on hydroplaning susceptibility and hence its braking efficiency and steering ability. Under wet pavement conditions, despite the fact that vehicle is not subjected to the hydroplaning, accidents still can occur as a result of reduced skid resistance.

In the first part of this chapter, the procedure to simulate 3D hydroplaning model by using the commercial FE package, Abaqus (6.10) was described. Hydroplaning speed was computed for the full rolling and three slip conditions of a pneumatic tire. Hydroplaning speed was also computed for three cases of yaw angles for the rolling case only. Further analysis was carried out to study the loss of braking traction and steering ability in pavement puddles due to hydroplaning by computing the longitudinal friction force and the cornering force with respect to speed. All these simulations were performed on the smooth pavement surface. The smooth surface represents a poor texture condition of a pavement and is a conservative estimate of the hydroplaning for in-service pavements.

The second part of this Chapter devoted to the further development of FE 3-D hydroplaning model to incorporate the effect of pavement surface texture. For this purpose, the smooth pavement surface was replaced by the simulated asphalt mix design surfaces to examine their relative effectiveness against the wet skid resistance/hydroplaning under changeable water film and tire operating conditions. Such a study will provide valuable indicators to the highway agencies about the risk of hydroplaning associated with the in-service pavement surfaces.

7.2 FE Simulation of Tire Hydroplaning on Smooth Pavement Surface

7.2.1 Study parameters of proposed hydroplaning model

For hydroplaning analysis, 3-D FE models of ASTM standard smooth and rib tires are developed by following procedure as described in the Chapter 3. The ASTM standard test tires are made of SBR vulcanized rubber. The ASTM E 524 smooth tire (2006) is a size G78-15 tube-less tire of belted bias ply construction. It has a tread width of 148.6 mm and a 393.7 mm cross-sectional tread radius. In addition to the above mentioned features of smooth tire, the ASTM E 501 rib tires (2006) also have seven 16.8 mm wide plain ribs, separated by six straight grooves of 5.08 mm width each. Each groove is parallel to the tread-radius arc and has a uniform depth of 9.8 mm. The tires have a recommended cross-section width of 212.1 mm and a recommended section height of 161.0 mm when mounted on a rim. These tires should be operated with not less than 165 kPa inflation pressure. The recommended static test load on the tire is 4826 N, with loading to a maximum of 6138 N permissible.

A tire inflation pressure of 200 kPa and a wheel load of 4.826 kN is adopted for the present analysis. A smooth analytical rigid pavement surface is considered for all the cases presented. The analytical surface feature of the pavement does not require any meshing, which gives the feasibility to consider any length of the pavement under rolling wheel conditions and also makes the whole model computationally less expensive.

Four scenarios of slip ratios are considered namely, free rolling (0% slip) and three partial slips of 10%, 20 % and 40%. Four yaw angles of 0° , 5° , 10° and 15° were considered for the rolling case only. It is known from past studies that the hydroplaning behavior of tires is also affected by the groove depth of the tire, as well as the thickness of water film present on the pavement surface. To establish a trend of variation of the hydroplaning speed with tire groove depth, the following 3 groove depths were considered for the ASTM E 501 rib tire: 5, 7 and 9.8 mm. Likewise, the variation of hydroplaning speed with water depth was analyzed by considering two water-film thicknesses of 5 and 10 mm.

7.2.2 Salient features of proposed hydroplaning model

The hydroplaning model phenomenon is simulated by using the Coupled-Eulerian-Lagrangian (CEL) approach. Although, the CEL methodology is described in detail in the previous Chapter, the key features of the CEL methodology utilized to simulate hydroplaning are discussed here. The tire is modeled in the Lagrangian framework and the fluid part is modeled with Eulerian elements fixed in space. The tire and fluid grids are two non-matching discrete interfaces and the coupling between these two grids is enforced by using the general contact coupling algorithm (Abaqus 6.10) to transfer the forces between fluid and structures. The CEL algorithm considers the boundary of the tire to identify the interface between the two different frameworks. The CEL algorithm applies the velocity of the tire as a deformation constraint in the fluid calculations and the pressure calculated in the fluid is used to calculate the resulting surface stress on the tire body through contact stress constraints. The deformation and movement of the tire mesh causes the water to flow through the fixed fluid mesh elements. This results in the high velocity and pressure gradients within the fluid.

The Lagrangian and the Eulerian equations are solved independently in the iterative partitioned approach. The interface tracking is obtained by using the volume of fluid (VOF) method. As mentioned in the previous Chapter, Abaqus uses the piecewise linear interface construction (PLIC) technique to calculate volume fraction of fluid in each control volume. The Eulerian grid is divided into a water film layer over which another layer is defined as a voids layer. The fluid region comprises of a velocity inlet, velocity outlet and no side flow boundary conditions, Figure 7.1a. It should be noted that the tire has to be partly embedded in the Eulerian mesh.

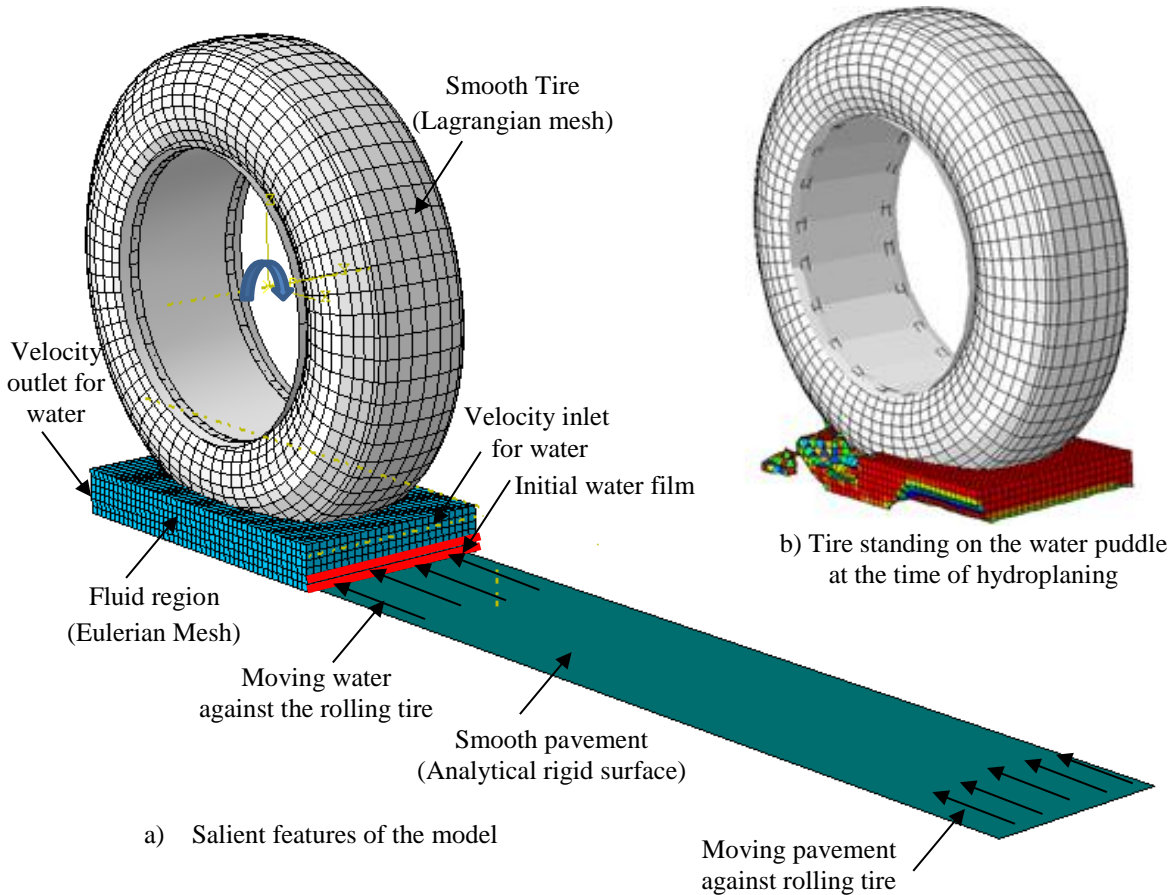


Figure 7.1 Proposed 3D hydroplaning model

Hydroplaning simulation was started with the tire deformation under presence of no fluid. In this approach, the tire is inflated to a pre-requisite pressure, being firmly fixed at a reference position. An upward load is applied on the analytical rigid pavement which results in moving the analytical rigid pavement towards the inflated tire due to which the deformation of tire takes place. The static footprint of the tire is matched against the experimental results of Horne et al. (1986). An accurate tire contact patch is the crucial parameter in determining accurate hydroplaning speed.

The analysis of a rolling tire with a specific slip ratio or yaw angle is performed by employing two steps:

- 1) a no-slip or non-yawed rolling analysis is performed to reach a steady rolling state with a given speed from rest, followed by
- 2) a slipping or a yawing analysis with a specific slip ratio and yaw angle.

For the slipping analysis, translational (v) and angular (ω) velocities of tire are specified in such a way that it produces a particular slip ratio according to the following Equation:

$$\text{Slip ratio (\%)} = \frac{v - r\omega}{v} \quad (7.89)$$

where r is the effective rolling radius of tire.

For yawing analysis, the analytical rigid pavement is uniformly translated in the horizontal direction. This forces the tire to rotate in the presence of friction until it attains a defined steady angular velocity. Then, the yaw angle is set by applying the pavement velocity in lateral direction. The same translational velocity of the pavement is applied to the water, Figure 7.1a. In the present analysis, the hydroplaning speed is considered as the striking velocity of water at which there is no or relatively very low horizontal contact force between the tire and the analytical rigid pavement surface, Figure 7.1b.

7.3 Validation of 3D Hydroplaning Model

The validation of the developed 3D hydroplaning model was made by means of the results of Horne (1963, 1975 & 1976) for fully rolling and locked ASTM smooth tire. A constant water depth of 7 mm, wheel load of 4800 N and tire inflation pressure in a range of 110 kPa to 260 kPa were considered to validate the simulation model as shown in Figure 7.2.

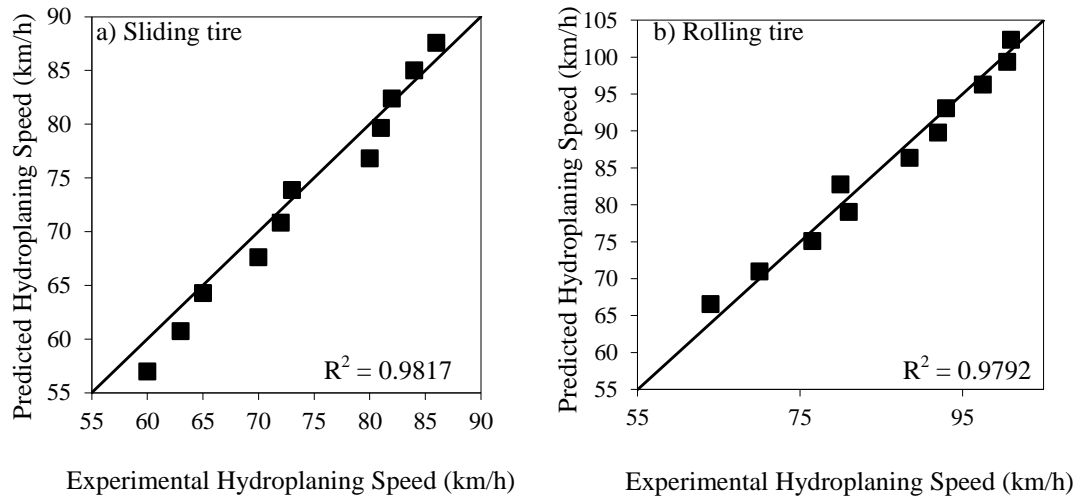


Figure 7.2 Verification of simulation model against experimentally measured data

The pavement surface tested is considered to be a plane surface with negligible surface asperities as the flooded pavement conditions prevail. The hydrodynamic dynamic lift generated under a tire rolling and sliding along a water-covered surface is given by the following equation (Horne, 1963; 1975; 1976):

$$\text{Lift Force (LF)} = \frac{1}{2} C_{Lh} \rho v^2 S \quad (7.90)$$

where, ρ is the density of the fluid, S is the tire footprint area and C_{Lh} is the hydrodynamic lift coefficient. When total dynamic hydroplaning occurs, LF/S is equal to the tire bearing

pressure that can be approximated by the tire inflation pressure p . Hence, the total dynamic hydroplaning speed is given as:

$$\text{Hydroplaning Speed } V_h = \sqrt{\frac{2p}{\rho C_{Lh}}} \quad (7.91)$$

The value of C_{Lh} is considered as 0.7 for a rolling tire and 0.95 for sliding tires. These values are based on a large number of tests conducted.

Using these hydrodynamic lift coefficients and the density for water, Equation (3) simplifies to:

$$V_{h,rolling} = 6.36\sqrt{p} \quad (7.92)$$

$$V_{h,locked} = 5.43\sqrt{p} \quad (7.93)$$

where, $V_{h,rolling}$ is the hydroplaning speed for rolling tire in km/h, $V_{h,locked}$ is the hydroplaning speed for a locked wheel in km/h and p is the tire inflation pressure in kPa. Figure 7.2 compares the measured values of hydroplaning speed based on the NASA hydroplaning Equations and predicted results from the simulation model. The figure shows a good agreement between the experimental and the simulation model with R^2 values of 0.9817 and 0.9792 for the sliding and rolling tires respectively.

7.4 Analysis of Hydroplaning

This section presents the results obtained by the developed FE hydroplaning model to analyze the influence of common tire operating conditions on hydroplaning speed.

7.4.1 Effect of tire groove depth and surface water depth on hydroplaning speed

In this section, the effect of tire groove depth and surface water depth on hydroplaning speed for the slipping and yawing tire is analysed and the results are presented in Figure 7.3. In general, for all slip and yaw conditions, hydroplaning speed rises as groove depth becomes deeper. This implies that the common practice of controlling tire groove depth to maintain sufficient skid resistance for wet-weather driving is also valid for hydroplaning control. The rate of increase in hydroplaning speed for each mm increase of groove depth generally varies from about 1.6 to 2.0 km/h and they do not change much among the different slip and yaw conditions.

Similarly, the general falling trend of hydroplaning speed with increasing water-film thickness is also observed for all slip and yaw conditions. The rate of decrease in hydroplaning speed for each mm increase of water depth varies from about 0.7 to 1.5 km/h. This is in agreement with observations made by past researchers that hydroplaning risk rises with increasing surface water depth.

7.4.2 Effect of slip ratio on hydroplaning speed

The computed hydroplaning speeds from simulation analyses of 32 cases of the standard ASTM smooth and rib tire are presented in Figure 7.3 for different slip ratios, for different tire groove

depths and surface water depths.

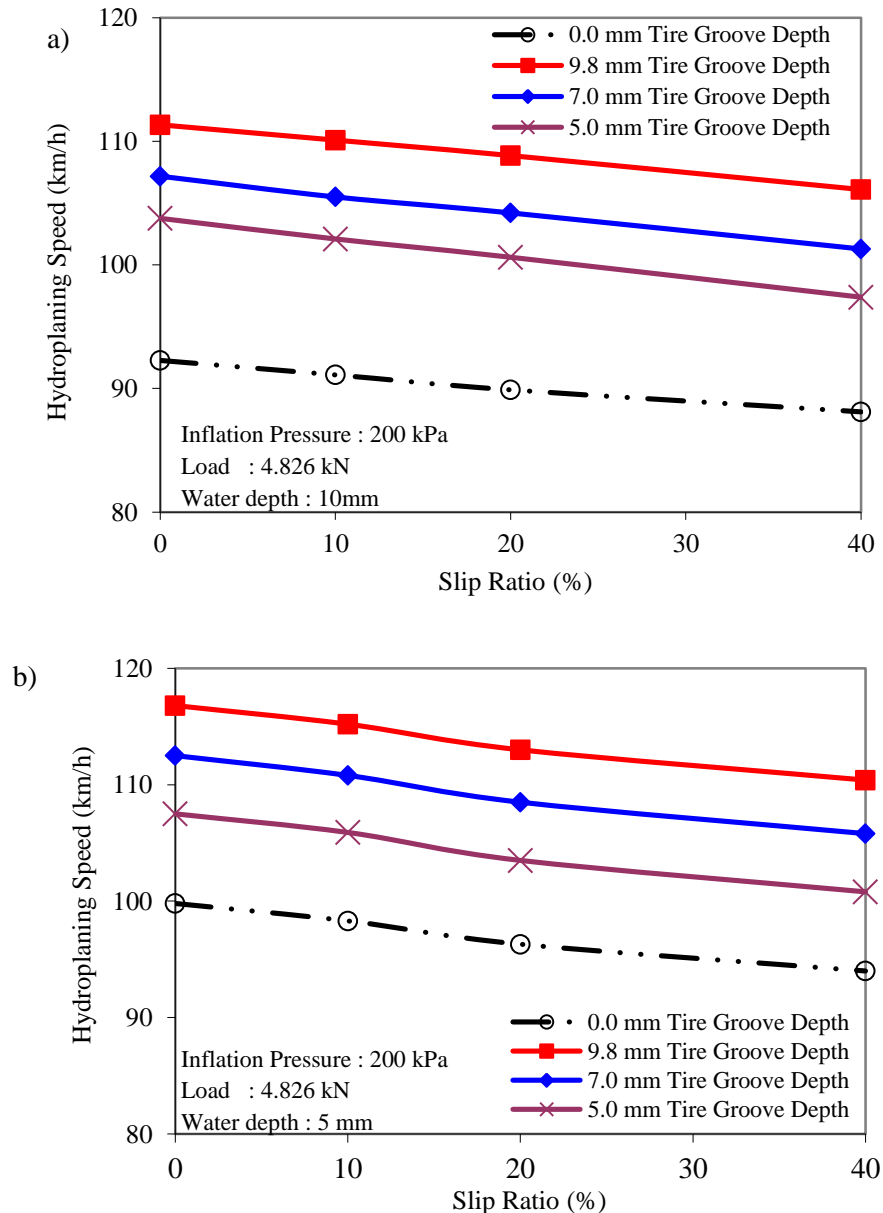


Figure 7.3 Hydroplaning speed vs. slip ratio for ASTM smooth and rib tires

Each curve in Figure 7.3 represents the change of hydroplaning speed as the slip ratio increases from 0% to 40%. It shows that at a constant groove depth and surface water depth, the hydroplaning speed decreases with increasing slip ratio. For both ASTM tires, the hydroplaning speed at the full rolling tire (0% slip) condition is higher than the value at 40% slip tire condition depending on the surface water depth.

By inspecting the simulation results, it is well understood that the rolling tire hydroplanes at higher speeds than the slipping tire. It might be due to the penetration of more water into the tire-pavement contact patch for a slipping tire than a non-slipping tire. From these analyses, it can also be presumed that under flooded pavement conditions, fully locking the wheel to stop the vehicle would increase the probability of the vehicle to hydroplane faster than operating the

brakes at some slip ratio.

7.4.3 Effect of yaw angle on hydroplaning speed

In this section, the results are presented by the utilization of the FE model for the simulation of a tire rotating continuously with a particular yaw angle and subjected to hydroplaning conditions. Here also the computed hydroplaning speeds for a total of 32 cases of simulation analyses of the standard ASTM smooth and rib tire are presented for yaw angles of 0° to 15° and their variation with tire groove depth and surface water depth, Figure 7.4.

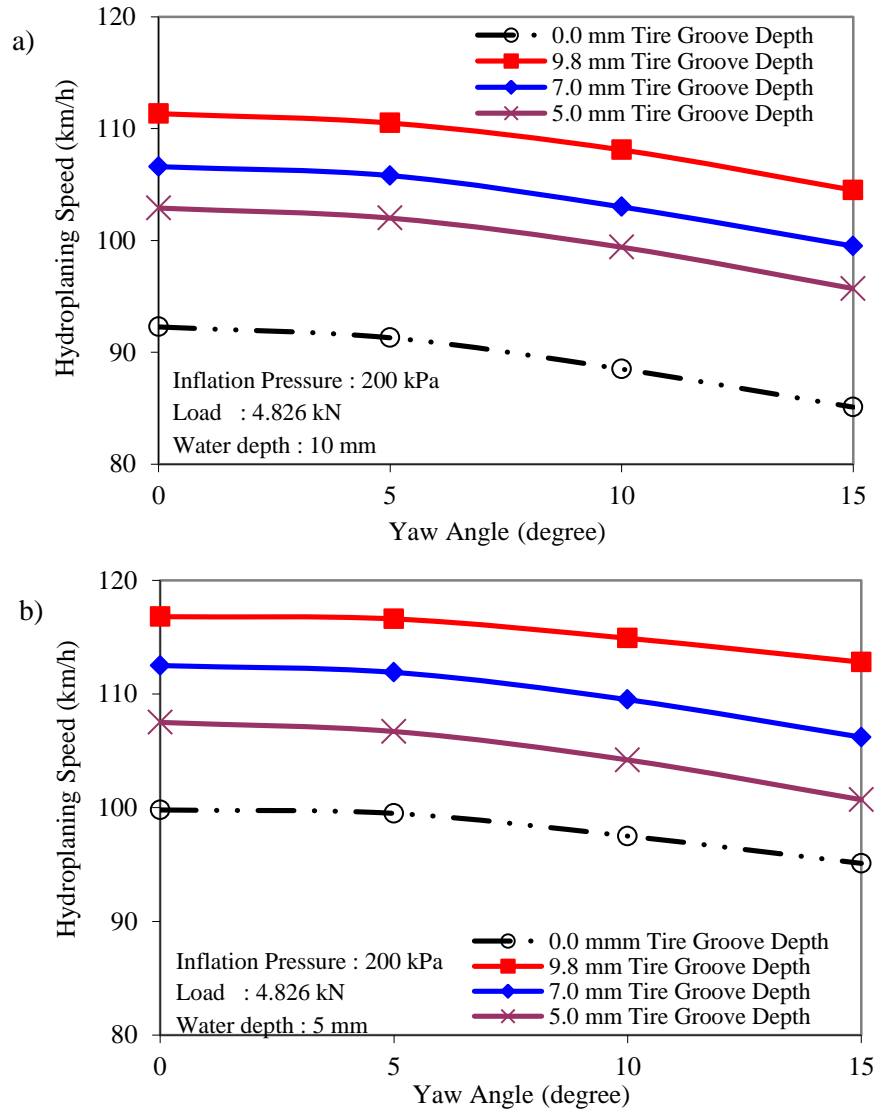


Figure 7.4 Hydroplaning speed vs. yaw angle for unbraked ASTM smooth and rib tires

As shown in Figure 7.4, hydroplaning speed inversely varies with increasing yaw angle. The decrease in hydroplaning speed is nominal for lower values of slip angle (5°) but as the yaw angle increases beyond 5° , the hydroplaning speed decreases at a higher rate. From these results, it can be deduced that if a tire is subjected to a yaw moment under incipient hydroplaning conditions, this will further aggravate the directional instability and lead to increased propensity for a vehicle

to hydroplaning.

7.4.4 Effect of slip ratio on longitudinal friction force

Figure 7.5 shows the variation of the longitudinal friction force with speed for different slip ratios that acts on the ASTM rib tire with 7 mm groove depth and 7 mm surface water depth.

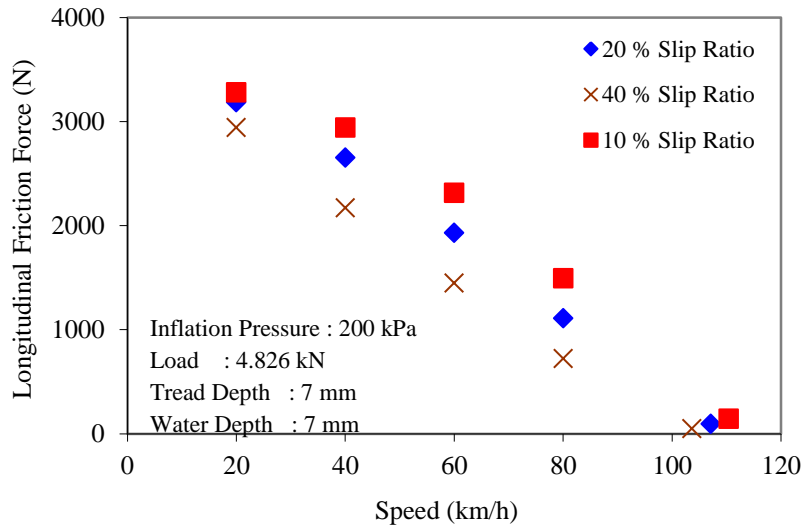


Figure 7.5 Loss of longitudinal friction force with increasing speed and slip ratio under flooded pavement conditions for an ASTM rib tire

It can be observed that the friction force decreases with increasing speed. Also the friction force decreases as the slip ratio increases. The decreasing rate of friction force is observed to be minimal for lower speeds irrespective of slip ratio. But, as the speed increases, there is an apparent drop of longitudinal friction force with increasing slip ratio. From these trends, a strong relationship can be observed between the slip ratio and the braking ability of a tire. A striking reduction in the braking force can be observed when velocity reaches hydroplaning speed and at that speed there is hardly any braking traction available for the tire.

7.4.5 Effect of yaw angle on cornering force

In this section, the effects of yaw angle on cornering force for different speeds under flooded pavement conditions are presented. Figure 7.6 shows the variation of the cornering force with speed under flooded pavement conditions. Each curve shows yaw angle of rolling tire for which the cornering force was obtained. A decreasing trend of cornering force can be observed with speed and yaw angle.

The percentage of decrease in cornering friction force for 15° yaw angled rolling tire with lateral friction force of 5° yaw angled rolling tire is observed to be 18 % to 48 % depending on speed. Since the cornering force dictates the lateral stability of the vehicle, it can be deduced that the yaw angle strongly affects the directional control and stability of the vehicle under flooded pavement conditions especially if there is a propensity for hydroplaning.

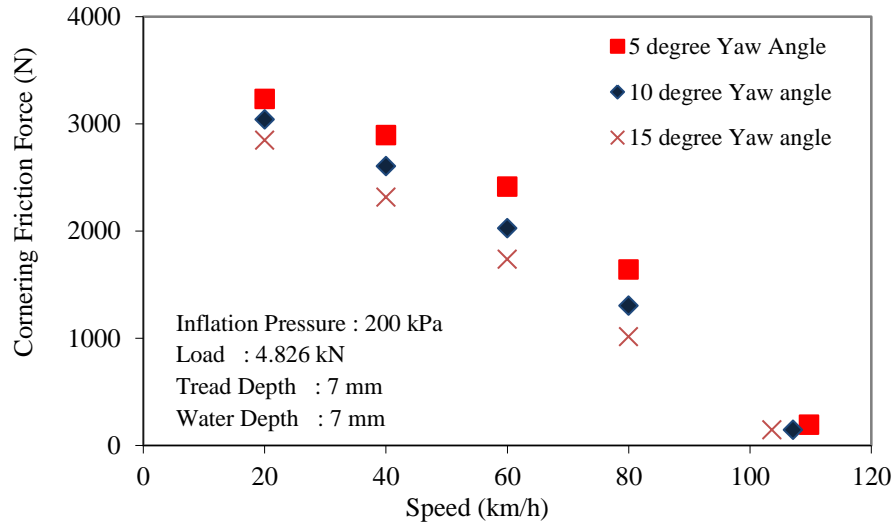


Figure 7.6 Loss of cornering friction force with increasing speed and yaw angle under flooded pavement conditions for ASTM rib tire

7.5 Relation Between Asphalt Mix Design and Wet Friction

The objective of this section is to quantify the effect of surface textures of different asphalt pavements on the wet friction by using the improvised 3D FE tire-wet pavement interaction model which can take into account the macrotexture of asphalt pavement. The developed FE model simulates the condition of a pneumatic tire rolling/sliding over a simulated asphalt pavement surface in the presence of water film. Parametric analyses of this model enable the development of relations between asphalt mix design and safety against vehicle skidding.

Within the scope of this study, the following parameters influencing the wet friction are studied;

- four types of asphalt pavement surfaces representing open graded asphalt mix design to dense graded asphalt mix design;
- two tire slip ratios representing full skidding and common ABS conditions;
- two different tires, one is standard PIARC smooth test tire and another one is GOODYEAR commercial passenger car tire with summer tread pattern;
- two water film thicknesses representing wet and flooded pavement conditions.

7.5.1 Study Parameters

In order to simulate wet friction/hydroplaning phenomena on simulated asphalt pavement surfaces, two types of tires, (1) PIARC 165R15 (2004) standard smooth tire which is widely used for skid resistance tests and (2) Goodyear 185/60 R15 DuraGrip summer tire which is widely used for commercial passenger cars were used in the analyses. By using these two different tires for the modeling, the effect of tread pattern on wet friction/hydroplaning can be captured.

A constant inflation pressure of 220 kPa and a constant normal load of 4.29 kN were considered. Tires rolling at 10%, and 100% slip ratios were adopted to quantify the effect of ABS in improving the wet friction and delaying the occurrence of hydroplaning. Different surface water depths (2.5 mm, 5mm, 7.5 mm and 10 mm) were adopted in the analysis to facilitate comparison.

The properties of water at 20°C were used in this study. The density and dynamic viscosity of water at 20°C were 1000 kg/m³ and 1.002 × 10⁻³ Ns/m³ respectively (Chemical Rubber Company, 1988).

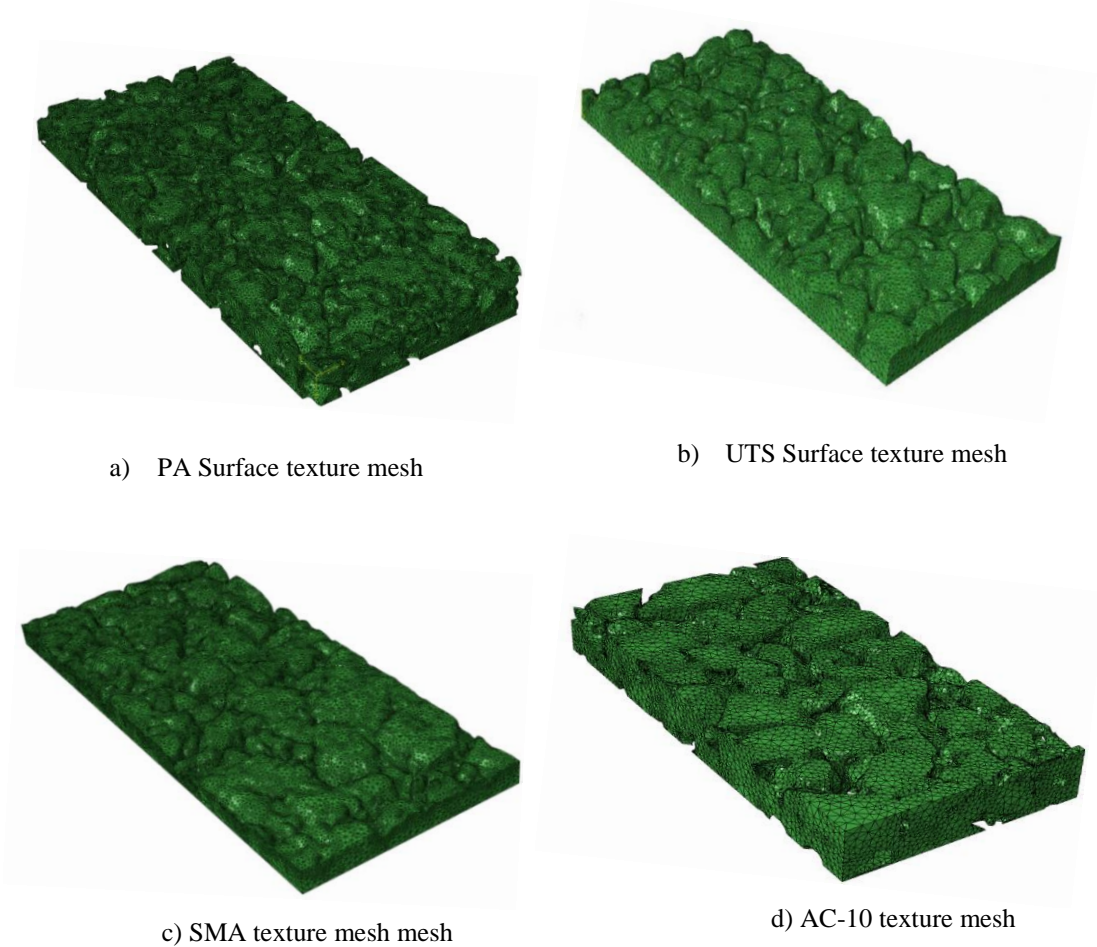


Figure 7.7 FE meshes of different asphalt pavement surfaces

Four types of asphalt pavement surface morphologies comprise of closed gradation to open graded, namely, Asphalt Concrete-10 (AC-10); Stone Mastic Asphalt (SMA); Ultra-Thin Surface (UTS) and Porous Asphalt (PA) were adopted in the present study. The procedure to obtain FE meshes of asphalt pavement surface was explained in previous chapters and the pavement meshes for PA, UTS, SMA and AC-10 are shown in Figure 7.7.

In general, two types of indicators available for the assessment of pavement surface macrotexture, (1) Mean Texture Depth (MTD) and (2) Mean Profile Depth (MPD). The MTD method consists of spreading a known volume of material like sand on the pavement surface and measure the area covered. Then the macrotexture depth is obtained by dividing the volume by the area. Devices like Circular Track Texture Meter (CTM) can measure macrotexture of pavement at traffic speeds and can be expressed as MPD. The MPD is calculated by dividing the measured profile into segments of small length. The slope of each segment is suppressed by subtracting a linear regression of the segment, providing a zero mean profile. According to ISO 13473-1, MPD is a more reliable indicator than the MTD if used in porous surfaces. Therefore, in the current study, MPD is considered as the indicator to quantify pavement macrotexture. The composition, particle

size distribution and the properties of each mix are shown in Table 7.1.

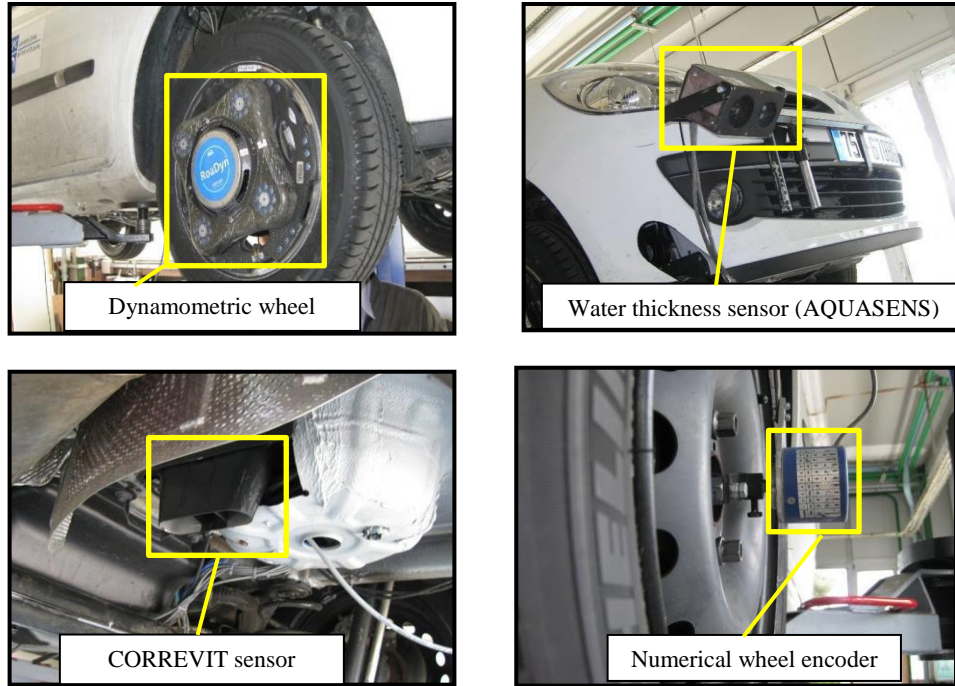
Table 7.1 AC-10, SMA, UTS and PA asphalt pavement mix compositions

Composition (%)								
Components	4/10 mm aggregate	2/6.3 mm aggregate	0/4 mm aggregate		Limestone filler		Binder	
SMA	55.2	13.8	15.9		8.4		6.4	
UTS	52.0	13.7	21.7		7.1		5.5	
PA	54.9	16.8	19.2		3.8		5.3	
AC-10	17.9	33.9	37.7		4.7		5.8	
Particle size distribution								
Sieve size (mm)		14	10	6.3	4	2	1	0.063
Passing (%)	SMA	100	90	47	29	25	21	10.1
	UTS	100	91	51	33	28	22	8.8
	PA	100	99	47	27	19	14	5.6
	AC-10	100	97	80	51	41	16	7.8
Standard asphalt mix properties								
Property	Max. density (kg/m ³)	Voids at 10 gyrations (%)	Voids at 50 gyrations (%)		Texture depth (mm)	Bulk density (kg/m ³)	Voids (%)	
SMA	2400	11.9	6.3		1.5	2294	4.4	
UTS	2429	13.7	6.9		2.1	2104	13.4	
PA	2582	22.7	18.8		NA	1975	23.7	
AC-10	AC	6.3	3.5		0.7	2348	3.7	

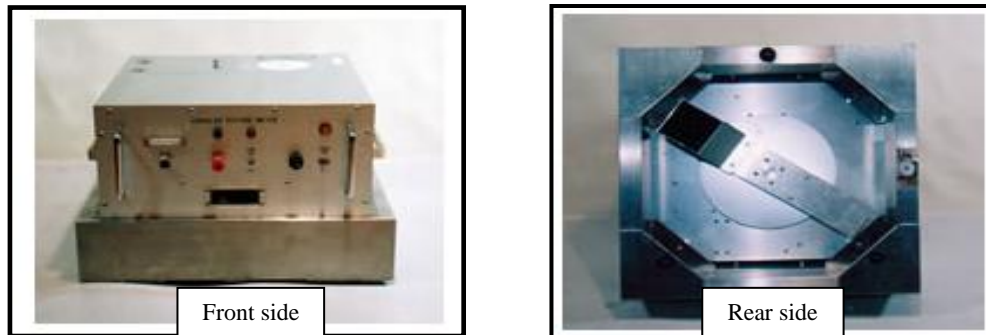
7.5.2 Field Measurements of Wet Friction and Hydroplaning

In this task, the effect of pavement surface texture on the wet friction and the propensity of hydroplaning were investigated through field tests. The following parameters were investigated in the field wet friction/hydroplaning tests:

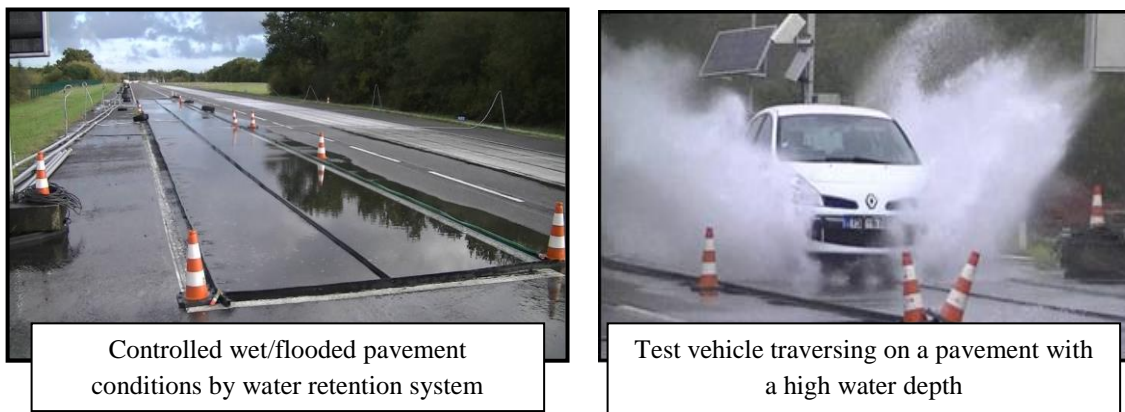
- Pavement surface texture (Porous Asphalt Concrete 0/6; Dense Asphalt Concrete 0/10)
- Tire type (185/60 R15 GoodYear DuraGrip summer tire)
- Water thickness (2.5 mm ; 5 mm)
- Slip ratio (10% ; 100%)
- Velocity (60 ; 90 ; 120 km/h) for wet friction analysis
- Tire inflation pressure and weight (220 kPa and 4.29 kN)



(a) Test wheel set-up



(b) CTM



(c) Field test set-up

Figure 7.8 Field testing of wet friction/hydroplaning

All the field experiments were performed on the IFSTTAR test tracks. Figure 7.8a shows the test vehicle with necessary components that was used in the field investigation studies of wet friction and hydroplaning. The test passenger car was equipped with specialized torque meters on the two transmission lines by means of a dynamometric wheel measure the forces and torques of the three directions of the test wheel. The wheel was equipped with the state-of-the art AQUASENSE sensors to measure precise water film thickness ahead the wheel. A CORREVIT sensor and a numerical wheel encoder were used to measure the longitudinal speed of vehicle and the wheel speed of the test vehicle. The MPD values of different asphalt pavement surfaces were measured experimentally by using Circular Track Texture Meter (CTM) as shown in Figure 7.8b.

The wet friction/hydroplaning measurements were performed when the test vehicle was traversing at a desired testing speed on the wetted/flooded pavement surface (Figure 7.8c). The test tire braking system was then actuated with or without ABS to lock the test tire. Instrumentation measures the horizontal drag force (force acting tangentially on the test wheel in line with the direction of travel) and vertical force (force applied by the wheel assembly i.e. static and dynamic force on the test tire, the test tire weight and the rim weight) on the contact area. The ratio between horizontal drag force and vertical force was reported as a longitudinal friction coefficient. A threshold longitudinal friction value of 0.1 or less is assumed to determine the onset of hydroplaning.

7.5.3 Description of Numerical Model

In the present study, the model was developed by using the commercial FE software ABAQUS (2010). The wet friction/hydroplaning model simulates the skidding/slipping or hydroplaning of a pneumatic tire rolling on a wet (or flooded) asphalt pavement surface morphology. There are two stages involved in this procedure as shown in Figure 7.9:

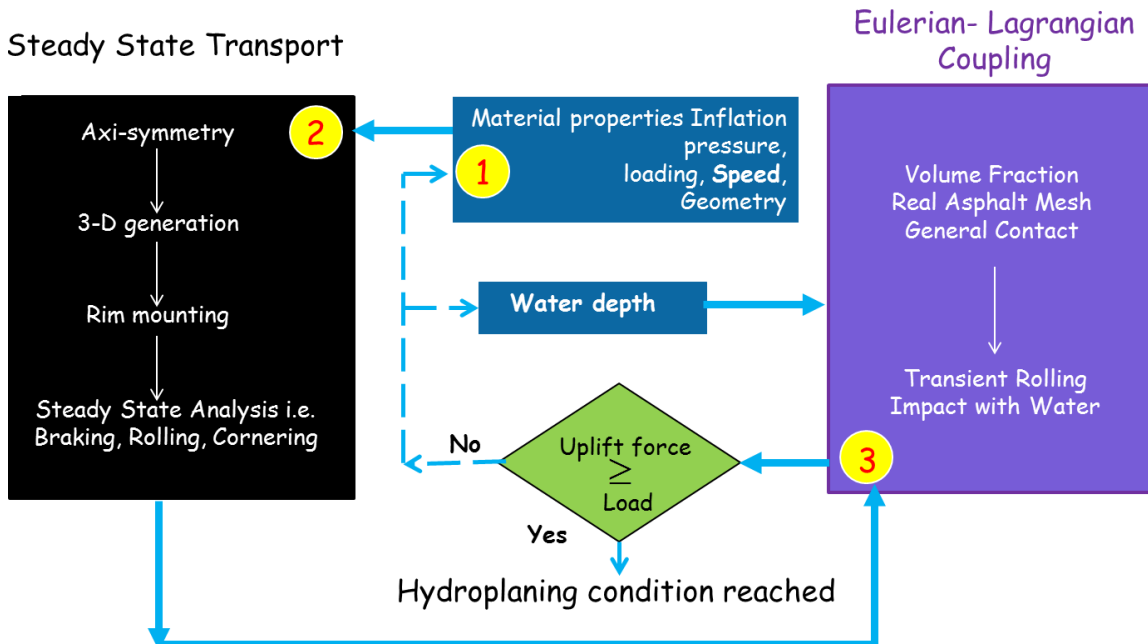
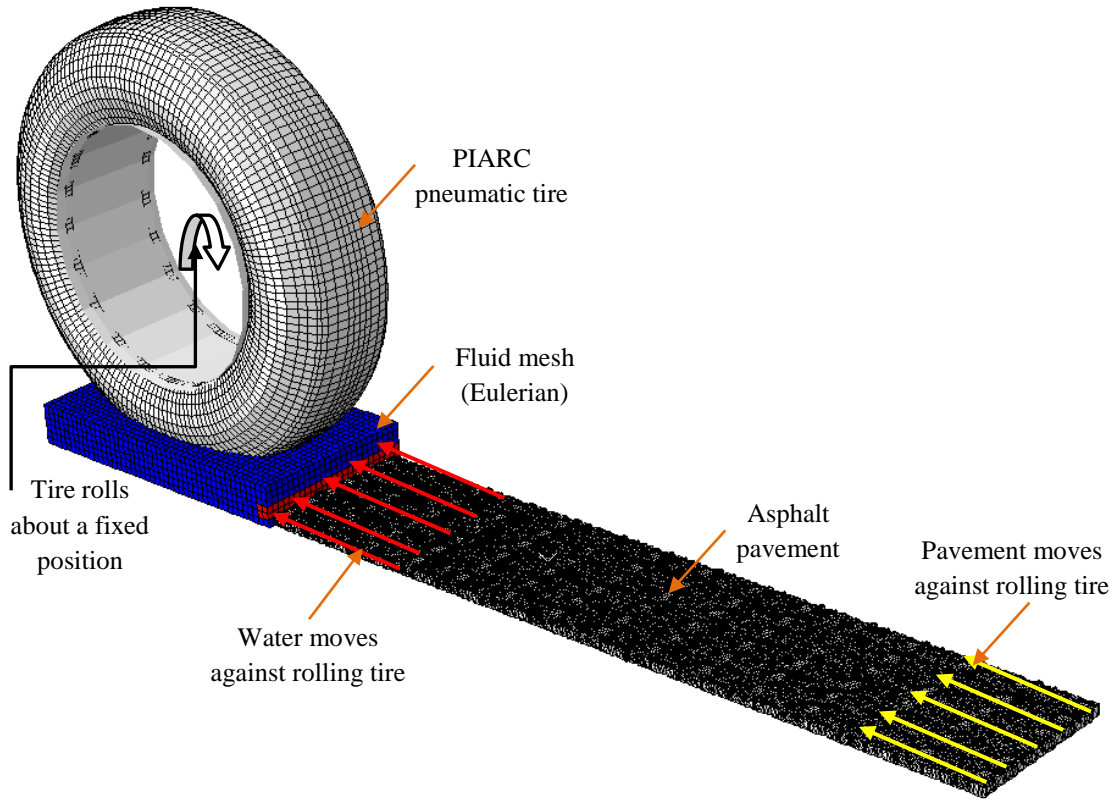


Figure 7.9 Procedure to obtain wet friction/hydroplaning model

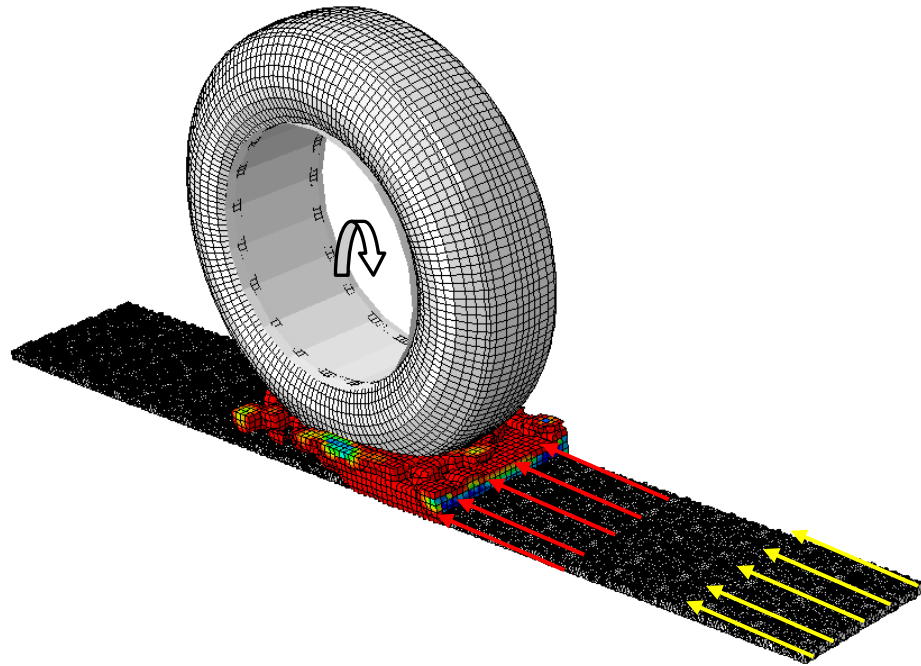
- A steady state implicit analysis of a 3D tire rolling over a smooth plane pavement surface was performed. In this stage tire deformation and footprint analysis, rolling radius analysis and steady state braking/rolling analyses were carried out. The history of stresses, strains and displacements obtained from this stage were transferred to the subsequent transient analysis step.
- In second stage, an equal translation velocity was applied to both water and asphalt pavement in the longitudinal direction. At the same time, an angular velocity of tire was specified as either zero or 90% corresponding to that of translation velocity prescribed for pavement and water such that it can simulate 100% skidding or 10% slip ratio respectively. That means, tire skids or rotates about a fixed axis under all the loading conditions with no forward motion, while pavement and water moves towards the skidding/slipping tire. Such a procedure would reduce the enormous fine Eulerian mesh required by the fluid region throughout the length of the pavement to a limited fluid mesh with fine Eulerian elements to capture the phenomena.

Depending on the pavement surface texture and (or) tread pattern capability to drain water, part of the water volume can flow into the tire grooves and pavement macrotexture; at the same time, due to the dynamic water pressure against the tire deformable structure, a lift force arises and increases; therefore water can also progressively penetrate under the tire footprint area, thus reducing the original contact area between tire and pavement surface. The horizontal force can be computed from energy principles through which wet friction can be obtained. On the other hand, the hydroplaning is assumed to occur at the striking velocity of water at which there is no or relatively very low contact force between the tire and asphalt pavement surface.

Figure 7.10 shows the developed finite element wet friction/hydroplaning simulation model.



(a) Components of the proposed wet friction/hydroplaning model



(b) Wet friction/hydroplaning phenomena of a PIARC tire

Figure 7.10 3-D numerical tire-asphalt pavement surface-water interaction model

7.5.4 Calibration of Numerical Model against Experiment Data

The validation of the developed three dimensional wet friction model was made against the field measurements under the same test conditions for the determination of wet friction of

- a GOODYEAR patterned tire rolling at 100% slip ratio (full skidding) on a PA pavement surface,
- a GOODYEAR patterned tire rolling at ABS slip ratio (10%) on a PA pavement surface,
- a GOODYEAR patterned tire rolling at 100% slip ratio on an AC-10 pavement surface
- a GOODYEAR patterned tire rolling at ABS slip ratio on an AC-10 pavement surface.

Four different speeds, 40, 60 km/h, 90 km/h and 120 km/h, and, two water film thicknesses, 2.5mm and 5 mm were adopted for the determination of their inherent influence on the wet friction. For both field and numerical modeling investigations, the tire was tested at an inflation pressure of 220 kPa, and a tire load of 4.29 kN. On the basis of these variables, total 32 scenarios (2 pavement surfaces \times 4 speeds \times 2 slip ratios \times 2 water films) were considered to validate the wet friction results obtained by FE model against field measurements.

Figure 7.11 summarizes the results of the validation analysis. Figure 7.11 (a) to Figure 7.11 (d) shows the plots of wet friction against speed for PA surface and Figure 7.11 (e) to Figure 7.11 (h) shows the wet friction against speed for AC-10 surface. It is observed that the numerical differences between the predicted and measured wet friction coefficient values are at most 0.106. In fact, only 6 of the 30 test cases studied have a difference in wet friction coefficient larger than 0.05. In terms of percentage error, except for one case with 14% error, all the remaining 29 cases have errors of 11% or less.

For all cases tested, the comparison of the measured and predicted results in Figure 7.10 shows very good agreement, considering the unavoidable variations of field conditions and possible measurement errors. By examining both experimental and numerical modeling results, there are some observations made and can be summarized as following:

- wet friction is highly dependent on the wheel slip ratio. The friction decrease is more pronounced for locked wheel
- thickness of water has great effect on wet friction. Both of frictions (ABS and locked) decrease when the water thickness increases, irrespective of the pavement surfaces and velocities
- if one takes 0.1 of friction coefficient as being the threshold of hydroplaning onset, most of the locked wheel scenarios at 120 km/h show indications of hydroplaning on water depth of 6mm

Due to safety reasons, the field tests cannot be conducted until the total hydroplaning of tire occurs. However, the total hydroplaning situations can be simulated by using the developed FE model after it is being duly validated with the experimental data of lowest friction values under the same test conditions and continuing the analysis for higher speeds until there is hardly any friction is available between the tire and the pavement surface.

FINITE ELEMENT SIMULATIONS OF TIRE-WET PAVEMENT INTERACTION

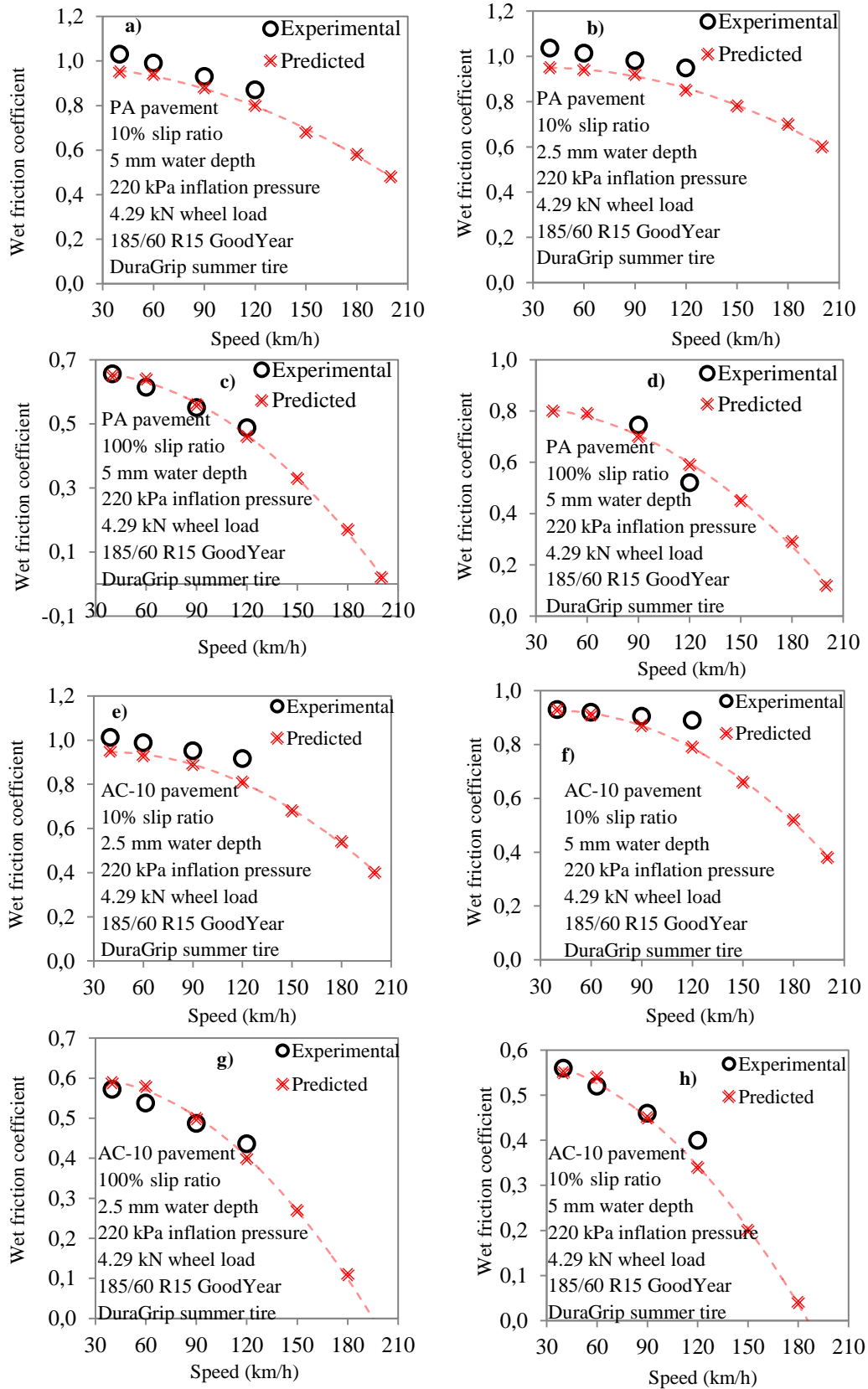


Figure 7.11 Verification of simulation model against experimentally measured data

7.5.5 Results and Discussion

In this section, the effect of MPD and pavement mix design on wet friction coefficient is investigated using the developed FE model. Also the effect of factors like water depth, slip ratio and tread pattern on wet friction is also investigated.

7.5.5.1 Effect of MPD and other factors on wet friction coefficient and hydroplaning

In this section, lasers cans of a PA surface was taken at different polishing levels to represent different MPD values. These surface scans were then converted into FE pavement meshes as explained in the previous section. Then FE simulation runs of pneumatic tires rolling/skidding over the same FE pavement surface meshes were performed in the presence of water films and the wet friction coefficients were computed. The computed wet friction coefficients for 196 cases (7 MPD \times 7 speeds \times 2 water depths \times 2 slip ratios) of simulation analyses of a PIARC smooth tire and a GOODYEAR patterned tire are presented in Figure 7.12. Each figure plots the computed wet friction coefficients against MPD. To evaluate the relative effectiveness of the different factors influencing the wet friction, the following analyses are made in the following paragraphs:

- Evaluation of the effect of MPD on wet friction for a given slip ratio; water depth and tread pattern
- Assessment of the effect of ABS and locked wheel operating conditions on wet friction for a given MPD; water depth and tread pattern
- Evaluation of the effect of a given tread pattern on wet friction for a given MPD; water depth and slip ratio
- Evaluation of the effect of water depth on wet friction for a given MPD; slip ratio and water depth
- Combined effect of MPD and tread pattern on wet friction for a given water depth and tire slip ratio

In order to assess the effect of pavement macrotexture on wet friction, curves in the Figure 7.12 are plotted to represent the changes of wet friction coefficient as the MPD increases from 0.2 to 1.4 mm. It indicates that at a constant surface water depth, the wet friction coefficient increases with MPD. The wet friction at the MPD of 1.4 mm is higher than the value at the MPD of 0.2 by 0.27 to 0.45 for a patterned tire and 0.01 to 0.42 for a smooth tire, depending on surface water depth and slip ratio. An examination of the simulation results shows that with a deeper MPD which offers a more effective channel for water flow, results in higher wet coefficients of friction.

The simulation model provides a useful tool to evaluate the effect of slip ratios on wet friction. Results from Figure 7.12 shows that with increase in slip ratio from 10% to 100% the wet friction values decrease. Although, a marginal decrease in wet friction values can be observed between 10% and 100% slip ratios at lower speeds, but the effect of slip ratio on wet friction is more pronounced at higher speeds. The rate of decrease in wet friction with speed is more pronounced for locked wheel than ABS wheel for both smooth and patterned tires. Lower wet friction values are observed at locked wheel condition which increase the probability of accidents. The average percentage decrease in wet friction value between an ABS wheel to a locked wheel was observed to be 19.8% and 23.2% respectively for a patterned tire and a smooth tire.

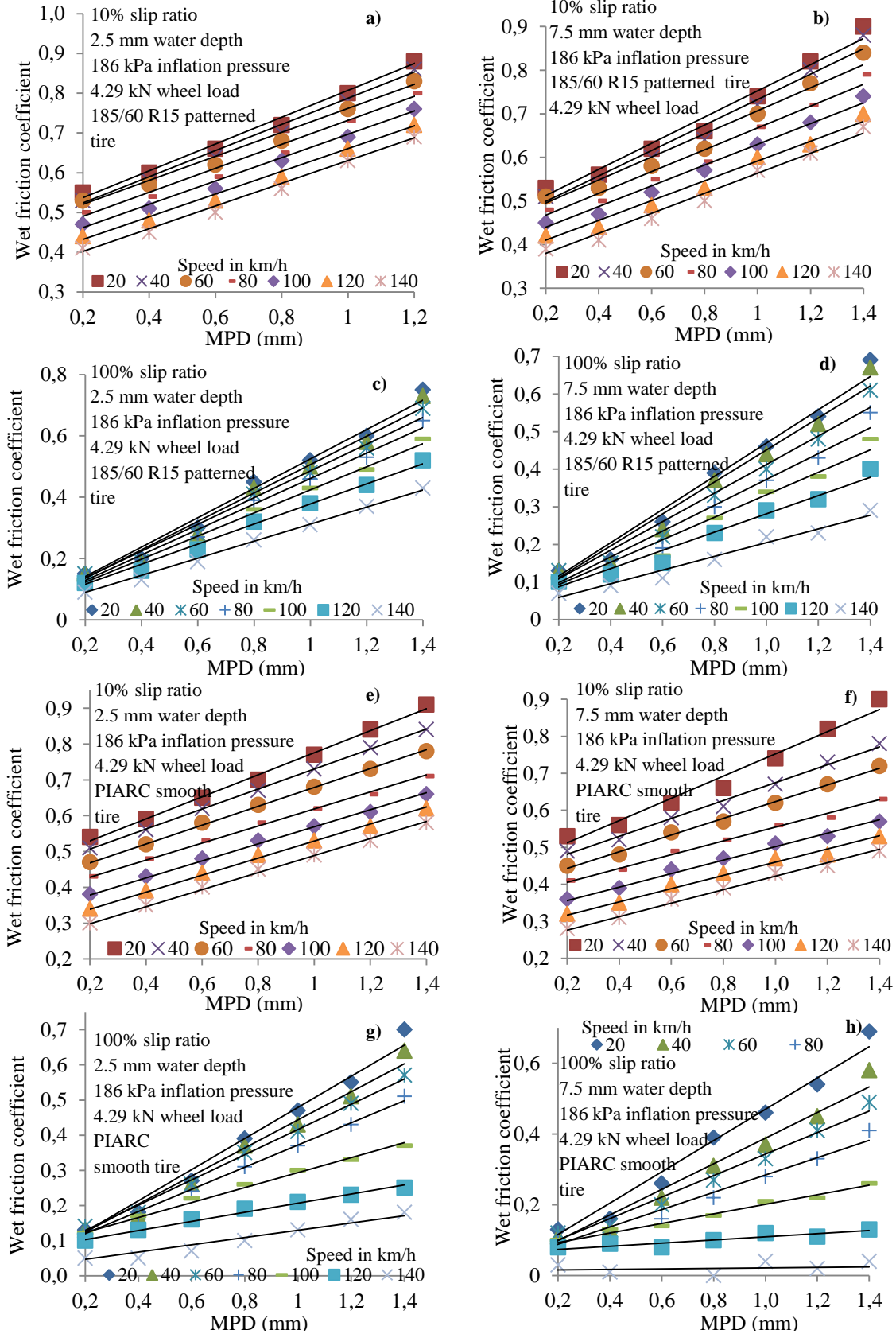


Figure 7.12 Wet friction coefficient vs. MPD

The analysis also presents the effect of tread pattern on wet friction phenomena by simulating smooth and patterned tires rolling/skidding over a given asphalt surface in the presence of water. Figure 7.12 shows that, for all speeds, wet friction values for a patterned tire are observed to be more than the friction values of a smooth tire for a given MPD of pavement. Figure 7.12 also shows that smooth tire skidding at higher speed over a pavement with thick water has registered negligible wet friction and therefore it is highly susceptible to hydroplaning. But for the same speed, water depth and pavement conditions, patterned tire still performs well. This proves the common practice of controlling tire tread depth and proper tread pattern to maintain sufficient skid resistance and delay the onset of hydroplaning for wet-weather driving.

Figure 7.12 also depicts the trends of wet friction variation with water-film thickness. The general falling trend of wet friction when the water-film thickness increases is common to all MPDs. This is in agreement with observations made in experimental studies by past researchers that loss of wet friction and hence hydroplaning risk rises with increasing surface water depth. It is observed that the effect of water depth on wet friction is marginal for tires rolling/skidding at lower speeds. But the effect of water thickness is more pronounced for tires rolling/skidding at higher speeds which causes an abnormal drop in the wet friction and leads to hydroplaning. Also the effect of water depth on the loss of wet friction is minimal for tires rolling at 10% slip ratio and higher macrotexture depths which shows the necessity to maintain proper pavement macrotexture and to use ABS system for wet weather driving.

For a case of asphalt pavement surface with lower MPD (0.2 mm) and higher speed (140 km/h) with 100% slipping GOODYEAR patterned tire, the wet coefficient of friction is observed to be very low (<0.1) such that even a patterned tire with good tread depth can show the indications of hydroplaning under adverse pavement and braking conditions.

This situation is true even for a lower water depth (2.5 mm) under consideration (Figure 7.12c and Figure 7.12d). This situation is even worse, if the tire is completely worn (smooth) for which it experiences hydroplaning even at normal driving speeds (<90 km/h) of passenger cars (Figure 7.12g and Figure 7.12h). On contrary, a good pavement with macrotexture depth, can offer adequate wet friction even for a full skidding smooth tire under higher water depths (Figure 7.12e and Figure 7.12f).

7.5.5.2 Effect of pavement mix design on wet friction coefficient and hydroplaning

The main intention of providing better surface macrotexture is to serve as flow channels to facilitate drainage and discharging of the water trapped within the tire-pavement contact area. Hence, the provision of better macrotexture of pavement surface has been accepted as good practice to enhance road travel safety against wet weather skidding and hydroplaning. The surface macrotexture of asphalt pavement varies with mix design. Therefore, in this analysis, four types of mix designs, PA, UTS, SMA and AC-10 were examined for a standard PIARC Smooth tire and a GOODYEAR Summer patterned tire at two slip ratios (10% and 100%) in the presence of a thick film of water (7.5 mm).

Figure 7.13 shows the variation of wet friction coefficient for different asphalt pavements under consideration with speed, slip ratio and tread pattern. For all the cases, wet friction coefficient decreases with increase in speed.

FINITE ELEMENT SIMULATIONS OF TIRE-WET PAVEMENT INTERACTION

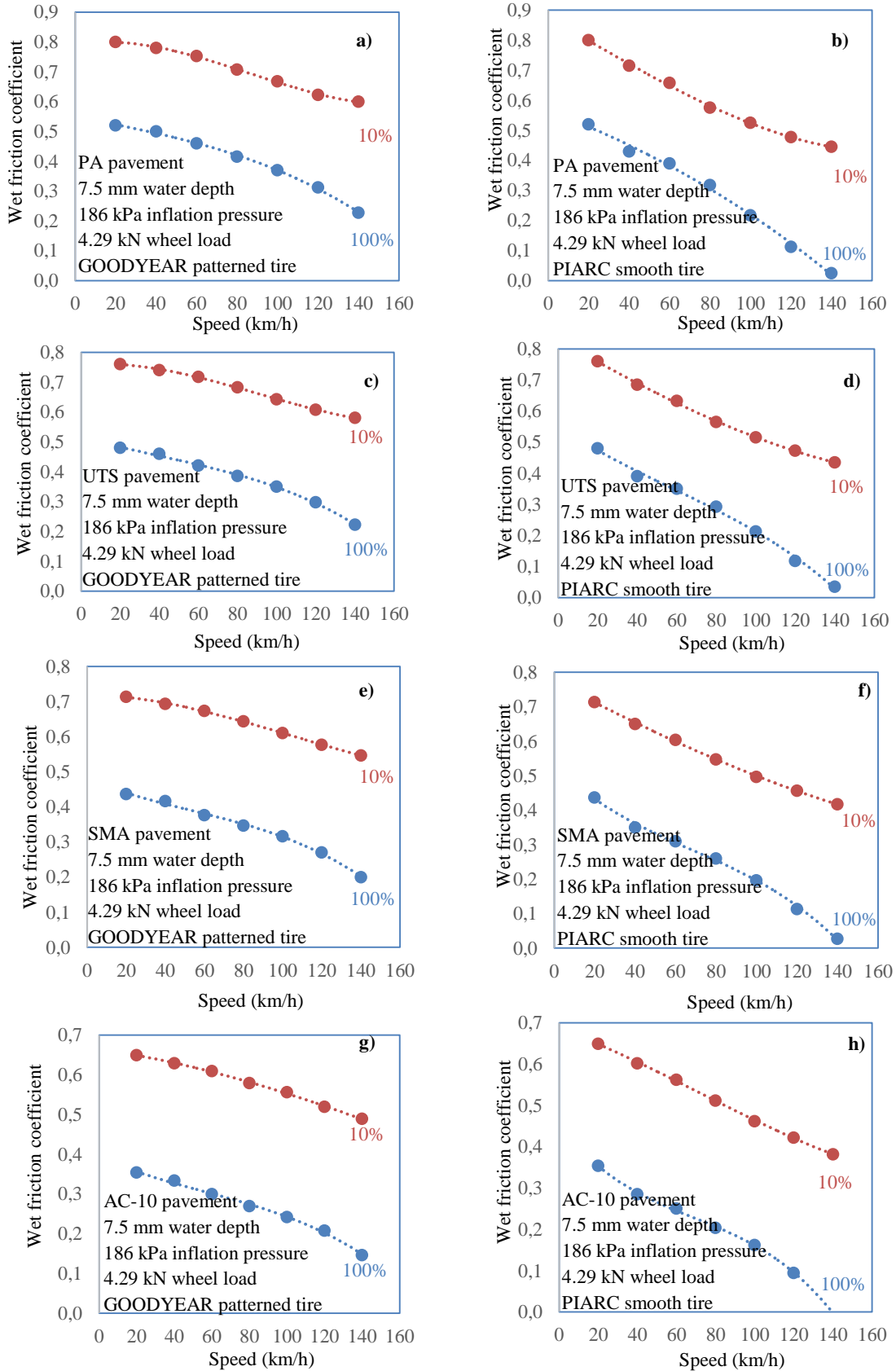


Figure 7.13 Wet friction coefficient vs. mix design

However, for the same tire, slip ratio and surface water depth conditions, PA pavement surface gives the highest wet friction coefficient followed by UTS, SMA and AC-10 respectively.

For example, for the case of GOODYEAR patterned tire rolling with 10% slip ratio at a speed of 100 km/h, the percentage decrease in wet skid resistance from PA to UTS was observed to be 4% and PA to SMA and PA to AC-10 were found to be 9% and 18% respectively. This affect is more pronounced for higher speeds and full skidding cases where the percentage decrease in wet friction from PA to UTS, SMA and AC-10 were found to be 6%, 15% and 35% respectively. This scenario shows that the pavement with open graded mix design gives better wet skid resistance than other mix designs.

Figure 7.13 also shows that the combination of all asphalt pavement surfaces with patterned tire, even at 100% skid ratio, always produce better wet friction coefficients even at high design speeds of highways. But this scenario is completely opposite in the case of their combination with smooth tire. In that case, wet friction coefficient drops to very lower values beyond 100 km/h showing the propensity of hydroplaning except for the case of PA. Beyond, 120 km/h almost all the pavement surfaces show negligible wet friction values with smooth tire. Therefore, it can be concluded that, although pavement macrotexture and pavement mix design alone alleviates the hydroplaning to a large extent for the case of worn-out tires, proper tire design with proper groove depth should also be maintained in order to avoid wet weather accidents.

7.6 Conclusions

The applications of the developed FE simulation model to study the phenomenon of hydroplaning and the effect of pavement macrotexture and mix design on the wet friction is described in this Chapter. The study has clearly demonstrated the capability of the FE model supported by field investigation data to evaluate the effectiveness of MPD and different pavement surface morphologies to combat the loss of wet friction. The MPDs examined cover the common macrotextures from highly polished surfaces i.e. 0.2 mm to highly textured surface i.e. 1.4 mm. Similarly, PA, UTS, SMA and AC mix designs examined cover open-graded mix to close- graded mix. Analyses have been presented to examine how changes in slip ratio, water depth and spacing, respectively, would affect the wet skid resistance. It was found that, in general, a larger MPD would increase the wet skid resistance and thus reduce the risk of wet weather accidents. It was also found that open grade mix design surface like PA results in highest wet friction coefficient followed by UTS, SMA and AC-10. The results also suggest that lower slip ratio, lower water depth and patterned tire would result in better wet friction coefficients. Overall, the model was found to be a very effective and efficient tool capable of computing friction on wet asphalt pavement surfaces under different operating conditions.

8 Conclusions and Recommendations

8.1 FE Modeling of Tire-Pavement Interaction

Two FE tire-pavement interaction model have been developed:

1. A FE thermo-mechanical tire-asphalt pavement interaction model to determine the effect of tire operating temperatures on the hysteretic friction
2. A FE tire-water-pavement interaction model to evaluate the effectiveness of mean profile depth and different pavement surface morphologies to combat the loss of wet friction and hydroplaning

8.2 FE thermo-mechanical tire-asphalt pavement interaction model

8.2.1 Model Development

The development of FE thermo-mechanical tire-asphalt pavement interaction model involved three stages:

- In the first stage, a PIARC smooth tire was tested under static loading conditions to obtain its overall deformational characteristics and in particular the relation between tire load - inflation pressure – foot print;
- In the second stage, Dynamic Shear Rheometer tests were performed to determine the material characteristics in terms of Prony’s series of the tire tread rubber. The material characteristics of tire rubber were utilized in 3D FE simulations of the test tire. Determination of the material parameters of the reinforcing materials of tire was performed on the basis of tire loading tests of first stage;
- In the third stage, emphasis was placed on the FE simulations of the progressive development of tire temperature and its effect on the mechanical response of test tire and hence on the measured friction at the tire–pavement interface. In this stage, the FE simulations were performed on simulated asphalt pavement surfaces. The FE model results were calibrated against (a) the actual temperature measurements in different components of the instrumented test tires, performed by past researchers, and, (b) the experimental results obtained by ADHERA friction measuring operating under continuous field measurement conditions. Processing of the results enabled the quantification of the role of test tire temperature increase on skid resistance measurements.

8.2.2 Model Capabilities

The developed FE model has the capability to

- determine the temperature distribution of tire at steady state conditions and the time required to warm up and cool down of tire;

- compute the time required for different regions of a rolling tire to reach an effective temperature equilibrated state while a traversing on an asphalt pavement surface;
- evaluate the effects of tire tread temperature, pavement temperature, ambient temperature, contained air temperature, pavement surface texture and tire slip ratio on the hysteretic friction;
- evaluate braking, rolling and cornering performances of a test tire traveling on different asphalt pavement surfaces.

8.2.3 Conclusions

- In general, it was observed that increase in tire tread, ambient and pavement temperatures decrease the hysteretic friction, while the CAT has a minimal effect on the hysteretic friction within the considered temperature range.
- It was observed that the tire temperature increases with increase in pavement texture. However, pavement high macrotexture offers more skid resistance.
- It was observed that increase in tire slip ratio from 20% to 100% causes the hysteretic friction to decrease appreciably
- It was observed from the tire cornering simulations that the change in the load and the inflation pressure changes the temperature in the tire cross section. The tire temperature was found to increase with increase in load and to decrease with the inflation pressure.
- It was also noted that the rate of increase in the tire temperature is not uniform throughout the tire cross section. The study showed that because of the change in the temperature, material properties of tire rubber also changes and thus the anti-skidding forces developed beneath the tire also vary. The cornering friction coefficients were found to decrease with the increase in the loads and the speeds. On the other hand, the cornering friction coefficients were found to increase with the increase in inflation pressures, sideslip angles and pavement surface texture depths.

From the above, it can be deduced that the developed frame work was found to be very useful in predicting the effect of temperature on the skid resistance measurements. Here it is worth mentioning that the following future works need to be carried out to calibrate the developed model for more accurate prediction of the results.

8.2.4 Recommendations

- Experimental measurements of temperature in the sidewall, belt edges, bead, apex etc. at different time spans should be considered for the accurate prediction of the effect of temperature on the skid resistance.
- Heat convection coefficients applied in this analysis are taken from the studies of past researchers (Ebbott et al., 1999). These coefficients should be computed on the basis of field experiments.
- Complex tire operating conditions result in complex wear mechanisms which affect various tire response characteristics. Simulation of such conditions will require the next level of FE tire-pavement interaction model to simulate typical patterns of tire tread wear under hot weather conditions.

- By utilizing the developed tire-pavement thermo-mechanical contact algorithm, a micromechanics based harmonization of pavement friction measuring equipment can be performed taking into account all major physical processes and mechanisms contributing to friction in the interfacial zone between the pavement surface and the tire.
- Issues related to the rolling resistance of a pneumatic tire rolling on asphalt pavement surface can be addressed by utilizing the developed tire-pavement thermo-mechanical contact algorithm.

8.3 FE tire-water-asphalt pavement interaction model

8.3.1 Model Development

The development of FE tire-water-asphalt pavement interaction model involved two stages:

- In the first stage, a steady state analysis of a 3D pneumatic tire rolling over a smooth plane pavement surface was performed. In this stage tire deformation and footprint analysis, rolling radius analysis and steady state braking/rolling analyses were carried out. The history of stresses, strains and displacements obtained from this stage were transferred to the subsequent transient analysis step
- In the second stage, an equivalent translation velocity was given to the water and the smooth or asphalt pavement in the longitudinal direction. At the same time, an angular velocity of the tire was specified in such a way that it can produce required slip ratio. Depending on the pavement surface and (or) tread pattern capability to drain water, part of the water volume can flow into the tire grooves and pavement macrotexture; at the same time, due to the dynamic water pressure against the deformable tire structure, a lift force arises; therefore water can also progressively penetrate under the tire footprint area, thus reducing the original contact area between tire and pavement surface. The resulting horizontal force can be utilized to compute the wet friction coefficient. On the other hand, the hydroplaning is assumed to occur at the striking velocity of water at which there is no or relatively very low contact force between the tire and asphalt pavement surface

8.3.2 FE Model Capabilities

The developed FE model has the capability to

- compute the hydroplaning speed at different slip ratios and yaw angles;
- evaluate the effectiveness of mean profile depth and different pavement surface morphologies to combat the loss of wet friction and hydroplaning
- examine the effect of water depth and tread pattern on the wet friction and hydroplaning

8.3.3 Conclusions

- It was found that a deeper tire groove and lower water depth reduces the risk of hydroplaning

- It was found that higher MPDs and open grade mix design surfaces increase the wet friction coefficient and thus reduce the risk of wet weather accidents
- It was found that a patterned tire results in higher wet friction coefficient than a worn tire

Overall, the model was found to be a very effective and efficient tool, capable of computing friction and hydroplaning on wet smooth or asphalt pavement surfaces under different operating conditions.

8.3.4 Recommendations

- By improvising the tire-wet pavement interaction model, the simulation of flow of water through the voids of the of different asphalt pavement mixes can be performed. Such simulations shall determine magnitude of moisture induced stresses on the pavement internal structure. Also such simulations shall ascertain the drainage properties of asphalt mix which has influence on the wet frictional performance at the tire-pavement interface
- By improvising the model, the effect of asphalt pavement groove patterns on wet friction and hydroplaning can be determined
- By improvising the model, the effect of wide base tires in comparison with the conventional tires on the wet skid resistance and hydroplaning

Appendices

Appendix-2.1 Determination of G^* at zero angular frequency

For a relaxation test, the value of G^* for $\omega = 0$ is defined as:

$$G_0^* = \lim_{\omega \rightarrow 0} G^* = G_\infty + \sum_{k=1}^m \lim_{\omega \rightarrow 0} \left(\frac{\omega^2 \rho_k^2 G_k}{\omega^2 \rho_k^2 + 1} \right) + i \sum_{k=1}^m \lim_{\omega \rightarrow 0} \left(\frac{\omega \rho_k G_k}{\omega^2 \rho_k^2 + 1} \right) = G_\infty \quad (\text{A-2.1.1})$$

where, G_∞ is the modulus of the single spring and G_k and ρ_k are respectively the moduli and relaxation times associated with the springs in the m viscoelastic components.

The value of G_0^* is determined by taking the n experimental data points $(\omega_i, G^*(\omega_i))$ closest to $\omega = 0$ and perform a linear regression analysis $G^* = a\omega + b$.

Then G_0^* will be equal to b , because $\omega = 0$. The linear regression is governed by the following over-determined system of equations:

$$\begin{bmatrix} G^*(\omega_1) \\ G^*(\omega_2) \\ \vdots \\ G^*(\omega_n) \end{bmatrix} = \begin{bmatrix} \omega_1 & 1 \\ \omega_2 & 1 \\ \vdots & \vdots \\ \omega_n & 1 \end{bmatrix} \begin{bmatrix} a \\ b \end{bmatrix} \quad (\text{A-2.1.2})$$

where a and b are the regression unknowns.

The least squares solution for a and b can be found from:

$$\begin{bmatrix} \omega_1 & \omega_2 & \cdots & \omega_n \\ 1 & 1 & \cdots & 1 \end{bmatrix} \begin{bmatrix} G^*(\omega_1) \\ G^*(\omega_2) \\ \vdots \\ G^*(\omega_n) \end{bmatrix} = \begin{bmatrix} \omega_1 & \omega_2 & \cdots & \omega_n \\ 1 & 1 & \cdots & 1 \end{bmatrix} \begin{bmatrix} \omega_1 & 1 \\ \omega_2 & 1 \\ \vdots & \vdots \\ \omega_n & 1 \end{bmatrix} \begin{bmatrix} a \\ b \end{bmatrix} \quad (\text{A-2.1.3})$$

This system of equations can be rewritten as:

$$\begin{bmatrix} \sum_{i=1}^n \omega_i G^*(\omega_i) \\ \sum_{i=1}^n G^*(\omega_i) \end{bmatrix} = \begin{bmatrix} \sum_{i=1}^n \omega_i^2 & \sum_{i=1}^n \omega_i \\ \sum_{i=1}^n \omega_i & n \end{bmatrix} \begin{bmatrix} a \\ b \end{bmatrix} \quad (\text{A-2.1.4})$$

The values for the regression parameters a and b are now defined as:

$$\begin{bmatrix} \mathbf{a} \\ \mathbf{b} \end{bmatrix} = \frac{1}{n \left(\sum_{i=1}^n \omega_i^2 \right) - \left(\sum_{i=1}^n \omega_i \right)^2} \begin{bmatrix} n \left(\sum_{i=1}^n \omega_i G^*(\omega_i) \right) - \left(\sum_{i=1}^n \omega_i \right) \left(\sum_{i=1}^n G^*(\omega_i) \right) \\ \left(\sum_{i=1}^n \omega_i^2 \right) \left(\sum_{i=1}^n G^*(\omega_i) \right) - \left(\sum_{i=1}^n \omega_i \right) \left(\sum_{i=1}^n \omega_i G^*(\omega_i) \right) \end{bmatrix} \quad (\text{A-2.1.5})$$

This means that:

$$G_0^* = \mathbf{b} = \frac{\left(\sum_{i=1}^n \omega_i^2 \right) \left(\sum_{i=1}^n G^*(\omega_i) \right) - \left(\sum_{i=1}^n \omega_i \right) \left(\sum_{i=1}^n \omega_i G^*(\omega_i) \right)}{n \left(\sum_{i=1}^n \omega_i^2 \right) - \left(\sum_{i=1}^n \omega_i \right)^2} \quad (\text{A-2.1.6})$$

The quality of the G_0^* solution can be checked by its R^2 value, which should be close to 1, and is defined as:

$$R^2 = \frac{\left(n \left(\sum_{i=1}^n \omega_i G^*(\omega_i) \right) - \left(\sum_{i=1}^n \omega_i \right) \left(\sum_{i=1}^n G^*(\omega_i) \right) \right)^2}{\left(n \left(\sum_{i=1}^n \omega_i^2 \right) - \left(\sum_{i=1}^n \omega_i \right)^2 \right) \left(n \left(\sum_{i=1}^n (G^*(\omega_i))^2 \right) - \left(\sum_{i=1}^n G^*(\omega_i) \right)^2 \right)} \quad (\text{A-2.1.7})$$

Appendix-2.2 Minimizing function with constraints on variables

The basis for the parameter back-calculation described in the next section is the ability to minimize functions representing the difference between model and experimental parameter values.

The mathematical form for such a minimization is stated as:

$$\min f(\underline{x}), \quad \text{where } \underline{\ell} \leq \underline{x} \leq \underline{u} \quad (\text{A-2.2.1})$$

where f is the function to be minimized, \underline{x} is the vector of variables and $\underline{\ell}$ and \underline{u} are the vectors of lower and upper bounds for \underline{x} respectively.

The vector of variables is defined as:

$$\underline{x} = (G_\infty \quad G_1 \quad G_2 \quad \cdots \quad G_m \quad \rho_1 \quad \rho_2 \quad \cdots \quad \rho_m)^T \quad (\text{A-2.2.2})$$

with G_∞ is the modulus of the single spring and G_i and ρ_i are respectively the moduli and relaxation times associated with the springs in the m viscoelastic components.

To solve this problem, a Lagrangian L is setup

$$L(\underline{x}, \underline{\alpha}, \underline{\beta}) = f(\underline{x}) + \underline{\alpha} \cdot (\underline{\ell} - \underline{x}) + \underline{\beta} \cdot (\underline{x} - \underline{u}) \quad (\text{A-2.2.3})$$

Here $\underline{\alpha}$ and $\underline{\beta}$ are vectors of Lagrange multipliers for the lower and upper bound constraints.

The Karush-Kuhn-Tucker conditions are now defined as:

$$\begin{aligned} \frac{\partial L}{\partial \underline{x}} &= \frac{\partial f}{\partial \underline{x}} - \underline{\alpha} + \underline{\beta} = 0 \\ \underline{\alpha} \cdot (\underline{\ell} - \underline{x}) &= 0 \quad , \quad \underline{\alpha} \geq 0 \\ \underline{\beta} \cdot (\underline{x} - \underline{u}) &= 0 \quad , \quad \underline{\beta} \geq 0 \end{aligned} \quad (\text{A-2.2.4})$$

Solving this non-linear system of equations is done by successive Newton-Raphson iterations until convergence. The linearized system of equations solved within a Newton-Raphson iteration is posed as:

$$\begin{bmatrix} \frac{\partial^2 f}{\partial \underline{x} \partial \underline{x}} & -\underline{I} & \underline{I} \\ -\underline{I} & \underline{O} & \underline{O} \\ \underline{I} & \underline{O} & \underline{O} \end{bmatrix} \begin{bmatrix} \Delta \underline{x} \\ \Delta \underline{\alpha} \\ \Delta \underline{\beta} \end{bmatrix} = - \begin{bmatrix} f(\underline{x}) - \underline{\alpha} + \underline{\beta} \\ \underline{\ell} - \underline{x} \\ \underline{x} - \underline{u} \end{bmatrix} \quad (\text{A-2.2.5})$$

Convergence is reached when the 2-norm of the increment vector $[\Delta \underline{x} \quad \Delta \underline{\alpha} \quad \Delta \underline{\beta}]^T$ is smaller than a specified small number. The above Newton Raphson scheme is the core of many non-linear programming (NLP) algorithms, amongst which Generalized Reduced Gradient (GRG)

method and Successive Quadratic Programming (SQP) are the most popular ones.

Appendix-2.3 Back calculation procedure based on successive constraint optimization

The methodology for back-calculating the shear moduli and relaxation times for a Generalized Maxwell model from the experimental data retrieved from DSR tests is split into four stages:

The first stage deals with finding an appropriate value for the shear modulus of the single spring $G_\infty = G_0^* = G^*(\omega=0)$. From the plot of the shear modulus magnitude G^* as a function of angular frequency ω the intersection point with the $\omega=0$ axis is determined by one or more linear regression analyses. Also initial values for the other parameters (G_i and ρ_i , $i=1..m$) have to be chosen within their admissible range of values. This part is done only once at the beginning of the back-calculation process.

The other three stages are each performing a constraint optimization step on the basis of the solution of the previous stage. The minimizations for G' , G'' and G^* are defined as:

$$\text{STAGE2 : } \min f_2(\underline{x}) = \sum_{j=1}^n \left(\frac{G'(\omega_j, \underline{x})}{G'_{\text{meas}}(\omega_j)} - 1 \right)^2, \quad \text{where } \underline{\ell} \leq \underline{x} \leq \underline{u} \quad (\text{A-2.3.1})$$

$$\text{STAGE3 : } \min f_3(\underline{x}) = \sum_{j=1}^n \left(\frac{G''(\omega_j, \underline{x})}{G''_{\text{meas}}(\omega_j)} - 1 \right)^2, \quad \text{where } \underline{\ell} \leq \underline{x} \leq \underline{u} \quad (\text{A-2.3.2})$$

$$\text{STAGE4 : } \min f_4(\underline{x}) = \sum_{j=1}^n \left(\frac{G^*(\omega_j, \underline{x})}{G^*_{\text{meas}}(\omega_j)} - 1 \right)^2, \quad \text{where } \underline{\ell} \leq \underline{x} \leq \underline{u} \quad (\text{A-2.3.3})$$

Here the subscript 'meas' stands for the values coming from the DSR tests, j is the angular frequency index, n is the maximum number of frequencies taken into account and $\underline{\ell}$ and \underline{u} are the vectors of lower and upper bounds for the parameter vector \underline{x} respectively.

The parameter values found at stage 4 are substituted into the 3 minimization functions. If the resulting values are close enough to zero, a valid parameter set has been found. If not, stages 2 to 4 are repeated again until a valid parameter set has been found.

It turns out that the procedure is very stable and converges to a plausible parameter set for arbitrary initial guesses within the admissible parameter value ranges.

Appendix-4.1 Procedure to determine the rate of viscous strain

$$\sigma_i = \eta_i \dot{\epsilon}_{vi} \quad (\text{A-4.1.1})$$

$$\begin{aligned} \dot{\epsilon}_{vi} &= \frac{d}{dt} \left(\epsilon - \int_0^t e^{-\frac{E_i}{\eta_i}(t-s)} \dot{\epsilon}(s) ds \right) \\ &= \frac{d}{dt} \left(\epsilon - \int_0^t e^{-\frac{1}{\tau_i}(t-s)} \dot{\epsilon}(s) ds \right), \text{ where } \tau_i = \frac{E_i}{\eta_i} \end{aligned} \quad (\text{A-4.1.2})$$

$$\begin{aligned} \dot{\epsilon}_{vi} &= \dot{\epsilon} - \frac{d}{dt} \left(e^{-\frac{1}{\tau_i}t} \int_0^t e^{\frac{1}{\tau_i}s} \dot{\epsilon}(s) ds \right) \\ &= \dot{\epsilon} - \left(-\frac{1}{\tau_i} e^{-\frac{1}{\tau_i}t} \int_0^t e^{\frac{1}{\tau_i}s} \dot{\epsilon}(s) ds + e^{-\frac{1}{\tau_i}t} e^{\frac{1}{\tau_i}t} \dot{\epsilon}(t) \right) \\ &= \dot{\epsilon} + \frac{1}{\tau_i} \int_0^t e^{-\frac{1}{\tau_i}(t-s)} \dot{\epsilon}(s) ds - \dot{\epsilon} \\ &= \frac{1}{\tau_i} \int_0^t e^{-\frac{1}{\tau_i}(t-s)} \dot{\epsilon}(s) ds \\ &= \frac{1}{\tau_i} \epsilon_{ei} \end{aligned} \quad (\text{A-4.1.3})$$

Appendix-4.2 Sigmoidal fitted function

The proposed form to fit the data in Figure A-1.1 can be defined as:

$$y = (c_1 x + d_1) \exp(-a x) + (c_2 x + d_2) (1 - \exp(-a x)) \quad (\text{A-4.2.1})$$

The parameters c_1 , c_2 , d_1 and d_2 are determined from linear data fits at the boundaries of the x interval. The parameter a is used to control the curvature of the fitted function.

Assume that the linear fits (or tangents) at the two boundaries of the x interval are defined as:

$$\begin{aligned} z_0 &= a_1 x + b_1 \quad \text{at } x = 0 \\ z_{\max} &= a_2 x + b_2 \quad \text{at } x = x_{\max} \end{aligned} \quad (\text{A-4.2.2})$$

Furthermore it is assumed that the term $a x_{\max}$ is large enough, so that $\exp(-a x_{\max})$ is close to zero.

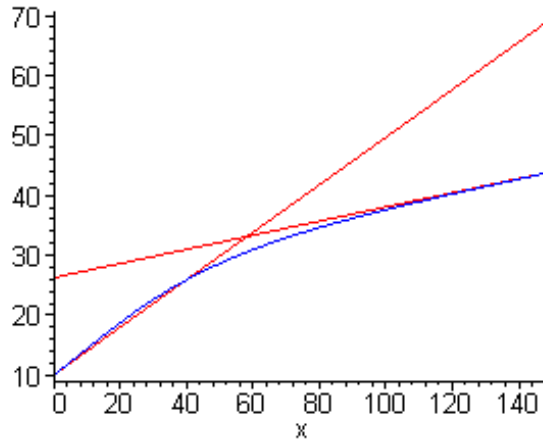


Figure A-1.1 The proposed fitted function

The parameters c_1 , c_2 , d_1 and d_2 are now calculated from the following 4 equations:

$$\begin{aligned} z_0 \Big|_{x=0} &= y \Big|_{x=0} \\ \frac{dz_0}{dx} \Big|_{x=0} &= \frac{dy}{dx} \Big|_{x=0} \\ z_{\max} \Big|_{x=x_{\max}} &= y \Big|_{x=x_{\max}} \\ \frac{dz_{\max}}{dx} \Big|_{x=x_{\max}} &= \frac{dy}{dx} \Big|_{x=x_{\max}} \end{aligned} \quad (\text{A-4.2.3})$$

Substituting Equation (A-2.2) and (A-2.3) into Equation (A-2.1) gives:

$$\begin{aligned}
 b_1 &= d_1 \\
 a_1 &= c_1 - a d_1 + a d_2 \\
 a_2 x_{\max} + b_2 &= c_2 x_{\max} + d_2 \\
 a_2 &= c_2
 \end{aligned}
 \tag{A-4.2.4}$$

Therefore it holds:

$$\begin{aligned}
 d_1 &= b_1 \\
 c_2 &= a_2 \\
 d_2 &= b_2 \\
 c_1 &= a_1 + a(b_1 - b_2)
 \end{aligned}
 \tag{A-4.2.5}$$

So that:

$$y = \left((a_1 + a(b_1 - b_2))x + b_1 \right) \exp(-a x) + (a_2 x + b_2)(1 - \exp(-a x))
 \tag{A-4.2.6}$$

Coefficients are determined except the parameter a .

This parameter can be found by linear regression analysis.

Nomenclature

λ	wavelength
A	peak-to-peak amplitude
μ	coefficient of friction
F	tangential friction force between the tire tread rubber and the horizontal travelled surface
F_W	perpendicular force or vertical load
S	slip speed
V	vehicle speed
V_P	average peripheral speed of the tire
SR	slip ratio
SFC	side-force coefficient
α	angle between the plane of the test tire and the forward velocity vector
F_s	force perpendicular to the plane of the rotating tire
R_N	normal reaction force
R_T	tangential reaction force
λ_N, λ_T	Lagrange multipliers
g_N, g_T	normal and tangential gap functions
$\mathcal{E}_N, \mathcal{E}_T$	penalty parameters
ΔW	energy loss per unit volume per cycle
\dot{Q}	rate of heat generation per unit volume
T_r	elapsed time for one revolution
$\sigma(\tau), \varepsilon(\tau)$	stress component and strain components with respect to time in a cycle extracted from the deformation of tire against pavement surface

δ	Phase lag
k	thermal conductivity ($\text{Wm}^{-1}\text{K}^{-1}$)
T	temperature (K)
Q	internal and external heat sources (Wm^{-3})
h	heat transfer coefficient ($\text{W}/\text{m}^2 \cdot \text{K}$)
t	time (sec.)
SN_v	skid number at vehicle speed v
SN_0	fictional skid number at zero vehicle speed
PNG	percentage normalized gradient of the SN versus v curve
v_0	speed constant
μ_{\max}	maximum friction value
S_{MAX}	slip speed at maximum friction value
S_p	speed number
MTD	mean texture depth
MPD	mean profile depth
S'	elastic torque
S''	viscous torque
$\text{Tan}\delta$	phase angle
G'	storage modulus
G''	loss (viscous) modulus
G^*	complex modulus
η	dynamic viscosity
ω	frequency (rad/sec.)
T_g	glass transition temperature

a_t	shift factor value
$G_{rel}(t)$	linear relaxation (shear) modulus
G_∞	modulus of the single spring
G_k, ρ_k	moduli and relaxation times associated with the springs in the m viscoelastic Components
R_e	effective rolling radius
R_u	unloaded radius
ρ	mass density
b	body force
σ	Cauchy stress
n	outward unit vector normal to the boundary
\hat{t}	external traction
\mathbf{F}	deformation gradient
J	Jacobian determinant ($J = \det(\mathbf{F})$)
\mathbf{S}	second Piola-Kirchhoff stress
ε	total strain
ε_v	inelastic strain
E_∞ and E_i	stiffness moduli of infinite spring and Maxwell springs
$\dot{\varepsilon}_v$	inelastic strain rate
W	total energy dissipation
\dot{Q}	rate of heat generation
q	heat flux per unit area of the body flowing into the body
k	thermal conductivity
T_0	reference temperature

ν	Stefan-Boltzmann constant
ξ	emissivity
TT	tire temperature
PT	pavement temperature
AT	ambient air temperature
μ_{wet}	measures traction coefficient,
μ_{BL}	pure boundary-layer wet friction or traction coefficient
F_{EHL}	fraction of footprint in hydrodynamic lubrication mode
v_h	hydroplaning speed
FAR	tire foot print aspect ratio
p	tire inflation pressure
t_w	water film thickness
$V_{h,\text{rolling}}$	hydroplaning speed for rolling tire
$V_{h,\text{locked}}$	hydroplaning speed for locked wheel
V_{spindown}	spin-down speed
SD	spin-down in percentage
f	volume fraction
u, v, w	Cartesian components of the velocity
C_{Lh}	hydrodynamic lift coefficient

References

1. ABAQUS (2010). ABAQUS User's Manual. Version 6.10, Hibbit, Karlson, and Sorensen, Pawtucket, RI, USA, 2010.
2. Agrawal, S. K. and Henry J. J. (1977). Technique for Evaluating Hydroplaning Potential of Pavements. Transportation Research Record 633, pp. 1-7.
3. American Concrete Pavement Association (ACPA), (2000), Concrete Pavement Surface Texture, Special report, Report No. ST902P, Report No. ST902P, American Concrete Pavement Association, Skokie, IL.
4. American Society for Testing and Materials. (2005h). ASTM Standard E 965-96. Standard Test Method for Measuring Pavement Macro-texture depth using a Volumetric Technique. ASTM Standards Sources, CD-ROM, Philadelphia.
5. American Society for Testing and Materials. (2006). "ASTM standard e 524-88, standard specification for standard smooth tire for pavement skid-resistance tests." ASTM Standards Sources (CD-ROM), ASTM, Philadelphia.
6. American Society for Testing and Materials. (2006). "ASTM standard e 501-94, standard specification for standard rib tire for pavement skid-resistance tests." ASTM Standards Sources (CD-ROM), ASTM, Philadelphia.
7. Anderson, D. A., R. S. Huebner, J. R. Reed, J. C. Warner and J. J. Henry. (1998). Improved Surface Drainage of Pavements: Final Report. National Cooperative Highway Research Program NCHRP Web Document 16, Pennsylvania State University.
8. Anderson, D. A., W. E. Meyer, and R. L. Rosenberger. Development of a Procedure for Correcting Skid-Resistance Measurements to a Standard End-of-Season Value. In Transportation Research Record: Journal of Transportation Research Board, no. 1084, Transportation Research board of the National Academies, Washington D.C, 1984, pp. 40-48.
9. Anupam, K., S.K. Srirangam, A. Scarpas, and C. Kasbergen. Influence of Temperature on the Tire-Pavement Friction-II : Analyses. Journal of Transportation Engineering, Transportation Reserach Record, 2013.
10. Baffet, G., A. Charara, and D. Lechner. Tire Force and Wheel Cornering Stiffness. Journal of Control Engineering Practice, Vol. 17, no. 11, 2009, pp. 1255-1264.
11. Baffet, G., A. Charara, and J. St'ephant. Sideslip angle, lateral force and road friction estimation in simulation and experiments. in IEEE International Conference on Control Applications, Munich, 2006, pp. 903-908.
12. Baffet, G., A. Charara, D. Lechner, and D. Thomas. Experimental evaluation of observers for tire-road forces, sideslip angle, and wheel cornering stiffness. Journal of Vehicle Syatem Dynamics, Vol. 46, no. 6, 2008, pp. 501-520.
13. Baffet, G.A., A.Charara, D. Lechner and D.Thomas (2008). Experimental Evaluation of Observers for Tire-Road Forces, Side-slip Angle and Wheel Cornering Stiffness, Vehicle System Dynamics, Vol.45, pp.191-216.
14. Balmer G. G. and Gallaway B. M. (1983). Pavement Design and Controls for Minimizing Automotive Hydroplaning and Increasing Traction. In Meyer W. E. and Walter J. D (eds.), Frictional Interaction of Tire and Pavement, ASTM STP 793, 167-190.
15. Bazlamit, Subhi M and Reza, Farhad, 2005. Changes in Asphalt Pavement Friction Components and Adjustment of Skid Number for Temperature. Journal of Transportation Engineering. Vol.131, pp 470-476.
16. Benson, D.J. Computational Methods in Lagrangian and Eulerian Hydrocodes. Computer Methods in Applied Mechanics and Engineering, Vol. 99, 1992, pp. 235-394.
17. Boffi, D. and Gastaldi, L. (2003). A Finite element approach for the immersed boundary method. Comput. & Structures, Vol. 81, pp. 491-501.

18. Bower, M. V. and Gant, F. S., 1994. Stress relaxation Functions: Methods of Approximation. NASA-CR-195830.
19. Bridgestone truck tyre. Bridgestone, Nov. 14, 2012. <http://www.bridgestonetrucktires.com/publications/02v7iss1/ra8.asp>. Accessed Nov. 10, 2012.
20. Browne, A. L. and D. Whicker. (1983). An Interactive Tire-Fluid Model for Dynamic Hydroplaning. In Friction Interaction of Tire and Pavement, ASTM STP 793, ed: by W. E. Meyer and J. D. Walters, pp. 130-150, Americal Society for Testing and Materials, Philadelphia.
21. Browne, A. L., D. Wicker, and D. J. Segalman. A General Model for Power Loss in Pneumatic Tires. GM Research Laboratories, Engineering Mechanics Department, GMR-4005, 1980.
22. Browne, A.L (1971). Dynamic Hydroplaning of Pneumatic Tires. PhD Thesis, North Western University, USA.
23. Bui, Q.V. and Ponthot, J.P. (2002). Estimation of Rubber Sliding Friction from Asperity Interaction Modeling. *Wear*, 252: 150-160.
24. Burchett, J. L., and R. L. Rizenbergs. Seasonal Variations in the Skid Resistance of Pavements in Kentucky. In Transportation Research Record: Journal of Transportation Research Board, no. 788, Transportation Research board of the National Academies, Washington D.C, 1980, pp. 6-14.
25. Chemical Rubber Company. Handbook of Chemistry and Physics, 69th ed. CRC press, Cleaveland, Ohio, USA, 1988.
26. Chen, T. Determining a Prony Series for a Viscoelastic Material From Time Varying Strain Data. NASA, TM-2000-210123., 2000.
27. Chenot, J. L. and L. Fourment (1998). Numerical formulations and algorithms for solving contact problems in metal forming simulation. In Computational Mechanics, New Trends and Applications.
28. Cho, J. C. and B. C. Jung (2007) Prediction of Tread Pattern Wear by an Explicit Finite Element Model. *Tire Science and Technology: December 2007*, Vol. 35, No. 4, pp. 276-299.
29. Cho, J. R., Lee, H. W., Sohn, J. S., Kim, G. J. and Woo, J. S. (2006). Numerical Investigation of Hydroplaning characteristics of Three-dimensional patterned tire, *European Journal of Mechanics A/Solids*, pp. 914-926.
30. Cho, J.R., Kim, K.W. and Jeong, H.S. (2007). Numerical investigation of tire standing wave using 3-D patterned tire mode. *Journal of Sound and Vibration*, Volume 305, Issues 4-5, pp. 795-807.
31. Cho, J.R., Kim, K.W., Jeon, D.H., Yoo, W.S., (2005). Transient dynamic response analysis of 3-D patterned tire rolling over cleat. *Eur. J. Mech. & Solids* 24 (3), 519-531.
32. Christensen, P.W., Klarbring, A., Pang, J.S. and Strömberg, N. (1998). Formulation and Comparison of Algorithms for Frictional Contact Problems. *International Journal for Numerical Methods in Engineering*, 42:145-173.
33. Clark, K. Mechanics of Pneumatic Tires. US DOT : NHTSA, 1981.
34. Clark, S.K (1982), Mechanics of pneumatic tires. Government Printing Office, Washington, DC.
35. Clark, S.K. and R. N. Dodge (1985). Tire Modeling And Contact Problems : Heat Generation In Aircraft Tires, *Computers& Structures*, Vol 20. No 1-3, pp. 535-544.
36. Close, W. Locked Wheel Friction Tests on Wet Pavements. Highway Research Board, 1961, p. 18.
37. Coleman, B. D. and Gurtin, M. E., 1967. Thermodynamics With Internal State Variables. *Journal of Chemical Physics* 47, pp. 597-613.

38. Comfort, G., (2001), Wet Runway Friction: Literature and Information Review, Fleet Technology Ltd. report TP14002E submitted to the Aerodrome Safety Branch of Transport Canada.
39. Cooley, L.J., and R. James. Micro-Deval Testing of Aggregates in the Southeast. Transportation Research Record, TRR, Vol. 1837, 2003, pp. 73-79.
40. Daughaday, H. and C.Tung (1969). A Mathematical Analysis of Hydroplaning Phenomena, CAL Report-AG-2495-S-1, Cornell Aeronautical Laboratory Inc., Buffalo, New York.
41. Davis, P. A. (1997). Quasi-Static and Dynamic Response Characteristics of F-4 Bias-Ply and Radial-Belted Main Gear Tires, NASA Technical Paper 3586, National Aeronautics and Space Administration, Langley Research Center, Hampton, Virginia.
42. Denhart, J. and Volk, H. An Approach to Predict Temperature Distribution in Rolling Tires Using Finite Element Methods. Presented at the 10 th Meeting of the Tire Society, Akron, Ohio, 1991.
43. Dick, J.S, 2003. Basic Rubber Testing: Selecting Methods For A Rubber Test Program. ASTM stock number: MNL 39.
44. Dijks, A. (1976). Influence of Tread Depth on Wet Skid Resistance of Tires. In Transportation Research Record: Journal of the Transportation Research Board, No. 621, TRB, National Research Council, Washington D.C., pp. 136-147.
45. Dixon, J.C. Tires, Suspension and Handling. Society of Automotive Engineers, 1996.
46. Ebbott, T. G., R. L. Hohman, J. P. Jeusette, and V. Kerchman. Tire Temperature and Rolling Resistance Prediction with Finite Element Analysis. Tire Science Technology, Vol. 27, 1999, pp. 2-21.
47. Elkin, B. L., K. J. Kercher, and S. Gullen. Seasonal Variation of Friction of Bituminous Surfaces in Indiana. In Transportation Research Record: Journal of Transportation Research Board, no. 777, Transportation Research board of the National Academies, Washington D.C., 1980, pp. 50-58.
48. Enhanced Driver Safety due to Improved Skid Resistance (SKIDSAFE). No. 234303.
49. Eshel, A. A (1967). Study of Tires on a Wet Runway, Report No. RR67-24, Ampex Corporation, Redwood City, California.
50. Federal Highway Administration (FHWA),(2002), ICH Performance Concrete Pavement, Pavement texturing and tire pavement Noises, Publication No.. FHWAIF-02-020.
51. Flintsch, G. W. , Luo, Y. , and Al-Qadi, I. L. (2005). "Analysis of the effect of pavement temperature on the frictional properties of flexible pavement surfaces." Proc., Transportation Research Board Annual Meeting , CD-ROM, Transportation Research Board, Washington, DC.
52. Forster, S. W. Pavement Microtexture and its Relation to Skid Resistance. In Transportation Research Record: Journal of Transportation Research Board, No.1215, Transportation Research Board of National Academies Washington D.C., 1989, pp. 151-164.
53. Fujikawa, T., Y. Uchiyama, and I. Yamaguchi (1999) Tire Model To Predict Treadwear. Tire Science and Technology: April 1999, Vol. 27, No. 2, pp. 106-125.
54. Fuller, K.N.G and Tabor, D. (1975). The effect of surface roughness on the adhesion of elastic solids. Proc.Roy. Soc. (Lond.) A345: 327-342.
55. Fwa T. F., Santosh S.K., Ong, G. P., and Huang, C.J.H. (2008). Analytical modeling of effects of rib tires on hydroplaning. Transportation Research Record: Journal of the Transportation Research Board, 109-118.
56. Fwa, T.F., Kumar, Santosh, Anupam, Kumar, Ong, Ghim, (2009). Effectiveness of Tire-Tread Patterns in Reducing the Risk of Hydroplaning. Transportation Research Record: Journal of the Transportation Research Board, 2094, pp 91-102.

57. Fwa, T.F., Kumar Anupam, G. P. Ong, (2010), Relative Effectiveness of Grooves in Tire and Pavement for Reducing Vehicle Hydroplaning Risk, Transportation Research Record: Journal of the Transportation Research Board, 2155/2010, 73-81.
58. Gal, A.L., Yang, X., and Klüppel, M, 2005. Evaluation Of Sliding Friction And Contact Mechanics Of Elastomers Based On Dynamic-Mechanical Analysis. Journal of Chemical Physics, 123, pp. 014704-1-11.
59. Gall, R., F. Tabaddor, D. Robbins, P. Majors, W. Sheperd, and S. Johnson (1995). Some notes on the finite element analysis of tires. Tire Science and Technology, 23(3):175–188.
60. Gallaway, B. M., D. L. Ivey, G. G. Hayes, W. G. Ledbetter, R. M. Olson, D. L. Woods and R. E. Schiller (1979). Pavement and Geometric Design Criteria for Minimizing Hydroplaning. Federal Highway Administration Report No. FHWARD-79-31, Texas Transportation Institute, Texas A&M University, USA.
61. Gallaway, B.M., Schiller, R.E., Jr., and Rose, J.G., 1971, The Effect of Rainfall Intensity, Pavement Cross Slope, Texture, and Drainage Path Length on Pavement Water Depths, Texas Transportation Institute, Texas A&M University Research report no. 138-5.
62. Gengenbach, W. Experimental investigation of Tires on Wet Tracks. Automobiltechnische Zeitschrift, Vol. 70, 1968, pp. 310-316.
63. Gough, V.E. (1959). Discussion of Paper by D. Tabor. Revue Generale Du Caoutchouc, Vol. 36, N0. 10, pp.1409.
64. Green, A.E, and P.M. Naghdi. Thermoelasticity Without Energy Dissipation. Journal of Elasticity, Vol. 31, 1993, pp. 189–208.
65. Green, M. S. and Tobolsky, A. V., 1946. A New Approach To The Theory Of Relaxing Polymeric Media. Journal of Chemical Physics 14, pp. 80-92.
66. Greenwood, J. A. and D. Tabor. (1958). The Friction of Hard Slider and Lubricatd Rubber: The Importance of Deformation Losses, Proceedings of the Physical Society, Vol. 71, No. 6, pp. 989-1001.
67. Grogger, H. and Weiss, M. (1996). Calculation of the Three-Dimensional Free Surface Flow around an Automobile Tire, Tire Science and Technology Vol.24, No.1, pp.39.
68. Grogger, H. and Weiss, M. (1997). Calculation of Hydroplaning of a Deformable Smooth-Shaped and Longitudinally-Grooved Tire", Tire Science and Technology Vol.25, No.4, pp.265.
69. Grosch, K. A. and A. Schallamach, Wear 4, (1961), 356.
70. Grosch, K. A. Rubber friction and traction, in The Pneumatic Tire, Gent, A. N., and J. D. Walter. Ed.NHTSA, US DoT, Washington D.C, ch. 11, 2005.
71. Grosch, K. A. The Relation between the Friction and Viscoelastic Properties of Rubber. in Rubber Society London, Ser. A 274, 1963, pp. 21–39.
72. Grosch, K. A., and A. Schallamach. The Load Dependence of Laboratory Abrasion and Tire Wear. Rubber Chemistry and Technology, Vol. 43, no. 4, July 1970, pp. 701-713.
73. Grosch, K.A., and G. Maycock. Influence of Test Conditions on Wet Skid Resistance of Tire Tread Compounds. Rubber Chemistry and Technology, Vol. 41, no. 2, 1968, pp. 477-493.
74. Hall, J. W., L. T. Glover, K. L. Smith, L. D. Evans, J. C. Wambold, Y. J. Yager, and Z. Rado (2009). Guide for Pavement Friction. National Cooperative Highway Research Program, Transportation Research Board, National Research Council, Washington, D.C., Web-Only Document. Final Guide Project No. 1-43.
75. Han, Y. H. (2003). Fatigue Life Prediction for Cord-Rubber Composite Tires Using a Global-Local Finite Element Method. PhD Thesis, University of Texas at Austin.
76. Haraldsson, A., P. Wriggers (2001). A strategy for numerical testing of frictional laws with application to contact between soil and concrete., Computer Methods in Applied Mechanics and Engineering, 190:963-978.

77. Harmonization of European Routine and Research Measuring Equipment for Skid Resistance (HERMES). FEHRL Report 2006/01, 153 p.
78. Harrin, E.N. (1958). Low Tire Friction and Cornering Forces on a wet Surface, NACA Technical Note 4406.
79. Harrin, E.N. (1960). Investigation of Tandem-Wheel and Air-Jets Arrangements for Improving Braking Friction on wet Surfaces, NACA Technical Note D-405.
80. Hayes, G. G., Ivey, D. L., and Gallaway, B. M. (1981). "Hydroplaning, hydrodynamic drag, and vehicle stability." ASTM Special Technical Report STP 793, American Society for Testing and Materials, 151-166.
81. Hegmon, R. R. and Henry, J., 1973. Thermal Analysis of a Skidding Tire. *Wear*, 24, pp. 361-380.
82. Heiing, B., and M. Ersoy. Chasis Hand Book: Fundamentals, Driving Dynamics, Components, Mechatronics, Perspectives., First edition, ATZ ed., 2011.
83. Henry, J. J. and W. E. Meyer. (1983). The Simulation of Tire Traction on Wet Pavements. In Proceedings of the 18th International Automobile Technical Congress, Report 369, Hamburg, Germany, pp. 121-128.
84. Henry, J.J. (2000). Evaluation of Pavement Friction Characteristics, NCHRP Synthesis 291, National Cooperative Highway Research Program (NCHRP), Washington, D.C.
85. Highway Research Board. (1972). Skid Resistance. National Cooperative Highway Research Program Synthesis of Highway Practice, No. 14, Highway Research Board, Washington, D. C.
86. Hill, B. J. and Henry, J. J. 1978. Short-Term, Weather-Related Skid Resistance Variation. In: Transportation Research Record: Journal of the Transportation Research Board, No. 836, 76-81, TRB, National Research Council, Washington, D.C., USA.
87. Hill, B. J., and J. J. Henry. Surface Materials and Properties Related to Seasonal Variations in Skid Resistance. Pavement Surface Characteristics and Materials. ASTM Special Technical Publication 763. American Society of Testing and Materials, Philadelphia, 763, 1982.
88. Hirt, C.W. and Nichols, B.D. (1981). Volume of fluid (VOF) method for the dynamics of free boundaries . *Journal of Computational Physics*, Volume 39, Issue 1, January 1981, pp. 201–225.
89. Holmes, K.E. Braking Force/Braking Slip Measurements over a Range of Conditions Between 0 and 100 per cent Slip. LR 292, 1970.
90. Holzapfel, G.A., Simo, J.C., 1996. A New Viscoelastic Constitutive Model For Continuous Media At Finite Thermomechanical Changes. *Int. J. Solid Struct.* 33, pp. 3019–3034.
91. Horne W. B. (1968). "Tire hydroplaning and its effects on tire traction." Transportation Research Board, Highway Research Record No. 214, Washington D.C., 24-33.
92. Horne, W. B. (1964). " Air jets – A possible solution to hydroplaning and other associated runway wetness problems." Proceedings of 17th Annual International Air Safety Seminar, flight Safety foundation, October 11-15, New York City, USA.
93. Horne, W. B. (1975). "Wet runways." NASA TM X-72650, NASA, USA.
94. Horne, W. B. (1976). "Status of runway slipperiness." NASA SP-416, NASA, USA.
95. Horne, W. B. and T. J. W. Leland. (1962). Influence of Tire Tread Pattern and Runway Surface Condition on Braking Friction and Rolling resistance of a Modern Aircraft Tire, NASA Technical Note D-1376, National Aeronautics and Space Administration, Washington D.C.
96. Horne, W. B., and Dreher, R. C. (1963). "Phenomena of pneumatic tire hydroplaning." NASA TN D-2056, NASA, USA.
97. Horne, W. B., and Joyner, U. T. (1965). "Pneumatic tire hydroplaning and some effects on vehicle performance." SAE International Automotive Engineering Congress, 11-15 Jan, Detroit, Michigan, USA.

98. Horne, W. B., Yager, T. J. and Ivey, D. L. (1986). "Recent studies to investigate effects of tire footprint aspect ratio on dynamic hydroplaning speed." The tire pavement interface, ASTM STP 929, American Society of Testing and Materials, 26-46.
99. Horne, W.B. (1974), Elements Affecting Runway Traction, presented at the SAE Transport Committee Meeting, April 30 - May 2, Dallas.
100. Horne, W.B. (1998), Correlation between Ground Vehicle Friction Measuring Equipment and Aircraft on Runways and Taxiways for Both Winter and Summer Conditions, draft report submitted to Transport Canada.
101. Horne, W., Yager, T., and Taylor, G. (1968). Review of Causes and Alleviation of Low Tire Traction on Wet Runways, NASA Technical Note TN D-4406.
102. Horne, W.B and T.J Leland (1962). Influence of Tire tread Pattern and Runway Surface Condition on Braking Friction and Rolling Resistance of a Modern Aircraft, NASA TN D-1376.
103. Horne, W.B. (1969). "Pavement grooving and traction studies." NASA SP-5073, NASA, 425-464.
104. Horne, W.B. (1984). Predicting the Minimum Dynamic Hydroplaning Speed for Aircraft, Bus, Truck, and Automobile Tires Rolling on Flooded Pavements. Presentation to ASTM Committee E-17 at College Station, June 5, Texas, USA.
105. <http://autopedia.com/TireSchool/TireA.html>
106. <http://www.steel-wireropes.com/>
107. <http://www.yokohamatire.ph/tire-basics/>
108. Huebner, R.S., Reed, J.R., and Henry, J.J. (1986). Criteria for Predicting Hydroplaning Potential, ASCE Journal of Transportation Engineering, Vol 12, No 5.
109. Ivey, D.L., T.M. Griffm, R.L. Lytton, and K.C. Hankins. Predicting wet weather accidents. Accident Analysis and Prevention, Vol. 13, 1981, pp. 83-99.
110. Jayawickrama, P. W., and B. Thomas. Correction of Field Skid Measurements For Seasonal Variation in Texas. In Transportation Research Record: Journal of Transportation Research Board, no. 1639, Transportation Research board of the National Academies, Washington D.C., 1998, pp. 147-154.
111. Jayawickrama, P. W., and B. Thomas. Correction of Field Skid Measurements For Seasonal Variation in Texas. In Transportation Research Record: Journal of Transportation Research Board, no. 836, Transportation Research board of the National Academies, Washington D.C., 1981, pp. 82-86.
112. Johnson K L, Kendall K, Roberts A D (1971). Surface energy and the contact of elastic solids. Proc.Roy. Soc. (Lond.) A324: 301-313.
113. Johnson, A. R., and Quigley, C. J., 1992. A Viscohyperelastic Maxwell Model for Rubber Viscoelasticity. Rubber Chemistry and Technology, Vol. 65, No. 1, pp 137-153.
114. Johnson, A. R., J. A. Tanner and A. J. Mason. (1999). Quasi-Static Viscoelastic Finite Element Model of an Aircraft Tire, NASA/TM-1999-209141, National Aeronautics and Space Administration, Langley Research Center, Hampton, Virginia.
115. Karrabi, M, Bakhshandeh, G and Ghoreishy, MHR., 2004. Rheological Study Of Tyre Tread Compound (Part II): A Method To Study The Relaxation Time And Viscosity Index Using Parallel Plate Rheometer. Italian polymer journal, pp. 397-404.
116. Klüppel, M., and Heinrich, G. 2000. Rubber friction on self-affine road tracks. Rubber Chemistry and Technology, Vol. 73, No. 4, pp 578-606. Heißing, B and Ersoy, M, 2011. Chassis Hand Book: Fundamentals, Driving Dynamics, Components, Mechatronics, Perspectives. First edition, ATZ.
117. Koishi, M., Kabe, K., Shiratori, M., 1998, "Tire Cornering Simulation Using an Explicit Finite Element Analysis Code", Tire Science and Technology, TSTCA, Vol26, No.2, April-June 1998, pp. 109-119.

118. Kokkalis, A. G., G. H. Tsohos, and O. K. Panagouli. Consideration of Fractals in Pavement Skid Resistance Evaluation. *Journal of Transportation Engineering*, Vol. 128, No. 6, American Society of Civil Engineering, 2002, pp 591-595.
119. Kondé, A.K, Rosu, I., Lebon, F., Seguin, L., Brardo, O., Troude, F. and Devésá, B. (2013). Thermomechanical couplings in aircraft tire rolling/sliding modeling, *Advanced Materials Research*, Vol. 274 (2011), pp 81-90.
120. Kulakowski, B.T. and Meyer, W.E. (1990). Skid Resistance of Adjacent Tangent and Nontangent Sections of the Roads. *Transportation Research Record 1215*, Transportation Research Board, TRB, National Research Council, Washington, D.C.
121. Kummer, H. W. (1966). *Unified Theory of Rubber and Tire Friction*, Engineering Research Bulletin, B-94, Pennsylvania State University.
122. Kummer, H.W. and Meyer, W.E. (1963). Penn State Road Surface Friction Tester as Adapted to Routine Measurement of Pavement Skid Resistance. *Road Surface Properties*, 42nd Annual Meeting, January. Choubane, B., Holzschuher, C.R., and Gokhale, S. 2004. Precision of Locked-Wheel Testers for Measurement of Roadway Surface Friction Characteristics. *Transportation Research Record 1869*, Transportation Research Board, TRB, National Research Council, Washington, D.C.
123. Laursen TA. (2002). *Computational Contact and Impact Mechanics*. Springer: Berlin, New York, Heidelberg.
124. Laursen, T.A. & J.C. Simo (1993), A Continuum-Based Finite Element Formulation for the Implicit Solution of Multibody, Large Deformation Frictional Contact Problems, *International Journal for Numerical Methods in Engineering*, 36, 3451-3485.
125. Leland, T.J.W., and Taylor, Glenn R., (1965). An Investigation of the Influence of Aircraft Tire-Tread Wear on Wet-Runway Braking, Langley Research Center, Langley Station, Hampton, Va., NASA Technical Note TN D-2770.
126. Leland, T.J.W., Yager, T., and Joyner, T., (1968), Effects of Pavement Texture on Wet Runway Braking Performance, NASA Technical Note TN D-4323.
127. Lim, G.T., (2005). *Scratch Behavior of Polymers*. PhD Thesis. Texas A&M University.
128. Lubliner, J., (1985). A Model Of Rubber Viscoelasticity. *Mechanics Research Communications* 12, pp. 93-99.
129. Luo, Y. Effect of Pavement Temperature on Frictional Properties of Hot-Mix-Asphalt Pavement Surfaces at the Virginia Smart Road. Virginia Polytechnic Institute and State University, Blacksburg, Virginia, Thesis, Master of Science 2003.
130. Luo, Y., Flintsch, G., and Al-Quadi, L. (2004). "Analysis of the Effect of Pavement Temperature on the Frictional Properties of Flexible Pavements Surface." *Transportation Research Board 2005*, TRB Annual Meeting of the Transportation Research Board.
131. Martin, C. S. (1966). *Hydrodynamics of Tire Hydroplaning*, Final Report, Project B-608, Georgia Institute of Technology.
132. Martin, C.S. (1966). *Hydroplaning of Tire Hydroplaning Final Report*, Project B-608, Georgia Institute of Technology.
133. Maycock, G. (1965). Studies of the Skidding Resistance of Passenger Car Tires on Wet Surfaces, *Proceedings of the Institute of Mechanical Engineers*, Vol. 180, Pt.2A, pp 122 – 141.
134. Maycock, G. Studies of the Skidding Resistance of Passenger Car Tires on Wet Surfaces. in *Proceedings of Institute of Mechanical Engineers*, Vol. 180, 1965, pp. 122-141.
135. Mercer, S.. Locked wheel Skid Performance of Various Tires on Clean, Dry Road Surfaces. *Highway Research Board*, 1958, pp. 8-25.
136. Meschke, G., Payer, H. J. and Mang, H. A. (1997). 3D Simulations of Automobile Tires: Material Modeling, Mesh Generation, and Solution Strategies. *Tire Science and Technology*: July 1997, Vol. 25, No. 3, pp. 154-176.

137. Meyer, W. E. (1991). Pavement Surface Texture and Measurement, ASTM Standardization News, pp. 28 – 31.
138. Meyer, W. E. “Synthesis of Frictional Requirements Research.” Federal Highway Administration (FHWA), Report No. FHWA/RD-81/159, Washington, DC, 1982.
139. Meyer, W.E., Kummer, H.W., 1964. Die Kraftübertragung zwischen Reifen und Fahrbahn. *Automobiltechnische Zeitschrift* 66(9), pp. 245–250.
140. Miehe, C., 1995. Entropic Thermoelasticity At Finite Strains. Aspects Of The Formulation And Numerical Implementation. *Computer Methods in Applied Mechanics and Engineering* 120, pp. 243-269.
141. Milliken, W.F., and D.L. Milliken (1995). Race car vehicle dynamics. Society of Automotive Engineers.
142. Moore, D. F (1967). Prediction A Theory of Viscous Hydroplaning, *International Journal of Mechanics Science*, Vol. 9, pp. 797-810.
143. Moore, D. F. (1966). Prediction of Skid-resistance Gradient and Drainage Characteristics for Pavements, *Highway Research Record* 131, pp.181-203.
144. Moore, D.F. (1969). Recommendations for an International Minimum Skid-Resistance Standard for Pavements. Highway Research Board Special Report 101, Highway Research Board, National Research Council, Washington, D.C.
145. Moore, D.F. (1972). *The Friction and Lubrication of Elastomers*. Pergamon Press LTD., Oxford, Great Britain.
146. National Cooperative Highway Research Program, (2009). NCHRP Web-Only Document 108: Guide for Pavement Friction. Accessed on March 5, 2010. http://onlinepubs.trb.org/onlinepubs/nchrp/nchrp_w108.pdf
147. Noyce, D.A., Bahia, H.U., Yambó, J.M., and Kim, G. (2005). Incorporating Road Safety into Pavement Management: Maximizing Asphalt Pavement Surface Friction for Road Safety Improvements. Midwest Regional University Transportation Center Traffic Operations and Safety (TOPS) Laboratory.
148. Oden J.T., and Martins J.A.C. (1985). "Models and computation methods for dynamic friction phenomena." *Comput. Methods Appl. Mech. Eng.*, 52, 527–634.
149. Oden, J.T. (1981). Exterior penalty methods for contact problems in elasticity. In *Nonlinear Finite Element Analysis in Structural Mechanics*, Wunderlich W, Stein E and Bathe KJ (eds). Springer: Berlin, ; 655–665.
150. Oh, B. S., Y. N. Kim, N. J. Kim, H. Y. Moon, and H. W. Park (1995) Internal Temperature Distribution in a Rolling Tire. *Tire Science and Technology: January 1995, Vol. 23, No. 1*, pp. 11-25.
151. Okano, T. and M. Koishi. (2000). A New Computational Procedure to Predict Transient Hydroplaning on a Tire. Presented in the 19th Annual Meeting and Conference on Tire Science and Technology, Akron, Ohio, USA.
152. Oliver, J.W.H. (1989). Seasonal Variation of Skid Resistance in Australia. Australia Road Research Board, Special Report 37.
153. Ong G. P., and Fwa T. F. (2007). “Prediction of wet-pavement skid resistance and hydroplaning potential.” *Transportation Research Record: Journal of the Transportation Research Board*, 160-171.
154. Ong G.P., and Fwa T.F. (2007). “Modeling hydroplaning and effects of pavement microtexture.” *Transportation Research Record: Journal of the Transportation Research Board*, 166-176.
155. Ong, G. P. and Fwa, T. F. (2007). Effectiveness of Transverse and Longitudinal Pavement Grooving in Wet-Skidding Control. In *Transportation Research Record: Journal of the Transportation Research Board*, No. 2005, TRB, National Research Council, Washington D.C., pp. 172-182.

156. Ong, G.P and Fwa, T. F. (2006a). Transverse Pavement Grooving against Hydroplaning, I – Simulation Model. ASCE Journal of Transportation Engineering, Vol 132 No6 pp 441 – 448.
157. Ong, G.P and Fwa, T.F (2006b). Transverse Pavement Grooving against Hydroplaning, II – Design. ASCE Journal of Transportation Engineering, Vol 132, No6, pp 449 – 457.
158. Ong, G.P., and T.F. Fwa. Modeling Skid Resistance of Commercial Trucks on Highways. ASCE Journal of Transportation Engineering, Vol. 136, no. 6, 2010, pp. 510–517.
159. Ong, G.P., T.F. Fwa and J. Guo. (2005). Modeling Hydroplaning and the Effects of Pavement Micro-Texture. In Transportation Research Record: Journal of the Transportation Research Board, No. 1905, TRB, National Research Council, Washington D.C., pp. 166-176.
160. Pacejka, H.B. Tyre and Vehicle Dynamics. Oxford : Elsevier Ltd., 2006.
161. Padovan, J. Finite Element Analysis of Steady and Transiently Moving/Rolling Viscoelastic Structure – I. Theory, Computers and Structures, Vol. 27, 1987, pp. 249-257.
162. Palasantzas, G. (2003), J. Appl. Phys. 94, 5652.
163. Panagouli, O.K., and Kokkalis, A.G. (1998). Skid Resistance and Fractal Structure of Pavement Surface. Chaos, Solutions & Fractals, 9(3), 493-505.
164. Parikh, P.D. (1977), A finite element analysis of the static and dynamic behavior of the automobile tire. PhD Thesis. Texas Tech University, USA.
165. Park, H. C., S. K. Youn, T. S. Song and N-J. Kim (1997). Analysis of Temperature Distribution in a Rolling Tire Due to Strain Energy Dissipation, Tire Science and Technology Jul 1997, Vol. 25, No. 3 (July 1997), pp. 214-228.
166. Permanent International Association of Road Congresses. (1995). “International PIARC experiments to compare and harmonize texture and skid resistance measurements.” PIARC Report 01.04T, PAIRC, Paris, France.
167. Person, B.N.J. (1998). Sliding Friction: Physical Principles and Applications. Springer, Berlin, Germany.
168. Persson, B. N. J. (1998). On the Theory of Rubber Friction, Surface Science, Vol. 401, Issue 3.
169. Persson, B. N. J. and Volokitin, A, (2002). Theory of Rubber Friction: Nonstationary Sliding. Physical Review B, Volume 65, 134106, pp. 1-11.
170. Persson, B. N. J., Albohr, O., Creton, C. and Peveri, V, (2004). Contact Area Between A Viscoelastic Solid And A Hard, Randomly Rough, Substrate. Journal of Chemical Physics, Volume 120, pp. 8779-8793.
171. Persson, B. N. J., Albohr, O., Creton, C. and Peveri, V. (2004). Contact Area Between A Viscoelastic Solid And A Hard, Randomly Rough, Substrate. Journal of Chemical Physics, Volume 120, pp. 8779-8793.
172. Persson, B.N.J. (1998). On the theory of rubber friction. Surface Science, Vol. 401, No. 3.
173. PIARC (1995). International PIARC Experiment to Compare and Harmonize Texture and Skid Resistance Measurements. Technical Committee on Surface Characteristics , Paris, France.,.
174. PIARC Technical Committee on Surface Characteristics (1987). Road Traffic Noise and Surface Characteristics Optimization. Report to the XVIIIth PIARC World Congress, P.I.A.R.C. reference 18.01.E, Brussels.
175. PIARC, (2004). Specifications For A Standard Test Tyre For Friction Coefficient Measurement Of A Pavement Surface, PIARC technical committee 1 surface characteristics.
176. Pietrzak, G and Curnier, A. (1999). Large deformation frictional contact mechanics: continuum formulation and augmented Lagrangian treatment. Computer Methods in Applied Mechanics and Engineering, 177: 351–381.

177. Priyantha, W. J. and L. G. Gary. (1995). Use of Skid Performance History as Basis for Aggregate Qualification for Seal Coats and Hot-Mix Asphalt Concrete Surface Courses, Transportation Research Record, No. 1501, pp. 31-38.
178. Rado, Z. (1994). "Analysis of Texture Models," PTI Report No. 9510, Pennsylvania Transportation Institute (PTI), Penn State University, State College, Pennsylvania
179. Rao, K.V.N, Kumar, R.K., Bohara, B.C., Mouli, C.P., (2002). Dynamic Analysis Of Tyre Cornering Behavior Using Explicit Finite Element Code, Proceedings of Twenty First Southeastern Conference On Theoretical And Applied Mechanics, Orlando, Florida.
180. Rao, K.V.N., Kumar, R. Krishna, Bohara, P. C., and Mukhopadhyay, R., (2006). A Finite Element Algorithm for the Prediction of Steady-State Temperatures of Rolling Tires. Tire Science and Technology, TSTCA, Vol. 34, No. 3, pp. 195-214.
181. Reese, S., Govindjee, S., 1998. A Theory Of Finite Viscoelasticity And Numerical Aspects. Int. J. Solid Struct. 35, pp. 3455-3482.
182. Research Framework 2007-2015, European Road Transport Research Advisory Council, 2006.
183. Rezaei, A. (2010). Development Of A Prediction Model For Skid Resistance Of Asphalt Pavements, PhD Dissertation, Texas A&M University, USA.
184. Roberts, A.D. 1988. Rubber Adhesion at High Rolling Speeds. Journal of Natural Rubbers Research, 3(4), pp. 239-260.
185. Rose, J.G., and B.M. Gallaway. Water Depth Influence on Pavement Friction. ASCE Journal of Transportation Engineering, Vol. 103, no. 4, 1977, pp. 491-506.
186. Rose, J.G., Hutchinson, J.W. and Gallaway, B.M. (1972). "Summary and analysis of the attributes of methods of surface texture measurement." ASTM, Spec. Tech. Publ. 53.
187. Runkle, S. N., and D. C. Mahone. Variation in Skid Resistance over Time. Virginia Highway & Transportation Research Council, pp.10-13, 1980.
188. Saka, H. and K. Araki (1999). Thermal Engineering Analysis of Rubber Vulcanization and Tread Temperatures During Severe Sliding of a Tire. Tire Science and Technology: January 1999, Vol. 27, No. 1, pp. 22-47.
189. Saka, H., and K. Araki (1998). Thermal engineering of rubber vulcanization and tread temperatures during severe sliding of a tire. in Seventh annual conference of the tire society, Akron, Ohio.
190. Sakai, H., and K. Araki (1998). Thermal engineering of rubber vulcanization and tread temperatures during severe sliding of a tire. in Seventh annual conference of the tire society, Akron, Ohio.
191. Sakai, H., Kanaya, O., and Okayama, T. (1978). "The effect of hydroplaning on the dynamic characteristics of car, truck, and bus tires." SAE, Paper No. 780195.
192. Sarkar, K., Y. D. Kwon and D. C. Prevorsek. A New Approach for the Thermomechanical Analysis of Tires by the Finite Element Method. Tire Science and Technology, Vol. 15, 1987, pp. 261-275.
193. Scarpas, A. (2004), A Mechanics Based Computational Platform for Pavement Engineering, TU Delft publication.
194. Scutte, A. (2011), Numerical Simulation of Tyre/Road Noise, PhD Dissertation, University of Twente.
195. Seta E, Nakajima Y, Kamegawa T and Ogawa H (2000). Hydroplaning Analysis by FEM and FVM: Effect of Tire Rolling and Tire Pattern on Hydroplaning, Tire Sci. and Technol., Volume 28, Issue 3, pp. 140-156.
196. Seta, E. (2000). Hydroplaning Analysis by FEM and FVM: Effect of Tire Rolling and Tire Pattern on Hydroplaning", JSAE SYMPOSIUM, No.01-00, Japan, pp.44.
197. Shah, V. R., Henry, J. J. (1978). Determination of Skid Resistance-Speed Behavior and Side Force Coefficients of Pavements, In Transportation Research Record: Journal of the

- Transportation Research Board, No. 666, TRB, National Research Council, Washington D.C., pp. 13-18.
198. Shimizu, T., T. Sano (1995). An application of a penalty method contact and friction algorithm to a 3-dimensional tool surface expressed by a B-spline patch. *J. Mater. Process. Technol.*, 48 (1995), pp. 207–213.
 199. Simo, J.C., Hughes, T.J.R. (1998). *Computational Inelasticity*, Springer.
 200. Simo, J.C., Pister, K. S. (1985): Remarks on rate constitutive equations for finite deformation problems. *Comput. Meth. Appl. Mech. Eng.* 48, 201-215.
 201. Simpleware, 2011. ScanIP 32-bit, Version 4.3. +CAD 32-bit, Version 1.3.
 202. Simulia, 2010. Abaqus Theory manual, version 6.10.
 203. Simulia, 2010. Tire and Vehicle Analysis, Example problems manual, volume 2, version 6.10.
 204. Sinnnamon, J. F., Tielking, J. K. (1974). Hydroplaning and tread pattern hydrodynamics, Report No. UM-HSRI-74-10, Highway Safety Research Institute, University of Michigan.
 205. Skerritt, W. H. Aggregate Type and Traffic Volume as Controlling Factors in Bituminous Pavement Friction. In *Transportation Research Record: Journal of Transportation Research Board*, No.1418, Transportation Research Board of National Academies, Washington, D.C., 1993, pp. 22-29.
 206. Srirangam, S. K., K. Anupam, A. Scarpas, and A. Köster (2013). Influence of Temperature on Tire-Pavement Friction: Laboratory Tests and Finite Element Modeling. *Transportation Research Board*.accepted for CD ROM., Washington, D.C.
 207. Srirangam, S. K., K. Anupam, A. Scarpas, and C. Kasbergen. Influence of Pavement Surface Texture Characteristics on Wet Friction Measurements: Field Tests and Finite Element Modeling Aspects. *International Journal of Pavement Engineering*, Accepted for Publication.
 208. Staughton, G .C. and Williams, T. (1970). Tyre Performance in Wet Surface Conditions, Road Research Laboratory Report LR 355.
 209. Subhi, M. B., and R. Farhad. Changes in Asphalt Pavement Friction Components and Adjustment of Skid Number for Temperature. *Journal of Transportation Engineering*, ASCE, Vol. 131, 2005, pp. 470-476.
 210. Tabor, D. The Importance of Hysteresis Losses in the Friction of Lubricated Rubber. in *Virginia Highway Research Council, Proc First INTL SKID PREV Part 1*, 1958, pp. 211-218.
 211. Tanner, J. A. (1996). *Computational Methods for Frictional Contact With Applications to the Space Shuttle Orbiter Nose-Gear Tire*, NASA Technical Paper 3573, National Aeronautics and Space Administration, Langley Research Center, Hampton, Virginia.
 212. Tanner, J. A., Stubbs, S. M., and McCarthy, J. (1981). “Mechanical properties of two, type vii, aircraft tires: static and yawed-rolling.” NASA TP-1863, NASA, USA.
 213. Tönük , E., and Y.S. Ünlüsoy. Prediction of Automobile Tire Cornering Characteristics by Finite Element Modeling and Analysis. *Journal of Computers and Structures*, Vol. 70, 2001, pp. 1219-1232.
 214. Tsakonas, S., C. J. Henry and W. R. Jacobs. (1968). Hydrodynamics of Aircraft Tire Hydroplaning, NASA CR-1125, National Aeronautics and Space Administration, Washington D. C.
 215. Tung, J. S.N., J. J. Henry, and S. H. Dahir. Statistical Analysis of Seasonal Variations in Pavement Skid Resistance. The Pennsylvania Transportation Institut Department of Transportation Bureau of Materials, Testing and Research, Research Report 75-10, 1977.
 216. TYROSAFE. Tyre and Road Surface Optimisation for Skid resistance and Further Effects. TYROSAFE, July 23, 2013. <http://tyrosafe.fehrl.org>.

217. Veith, A. G., "The Driving Severity Number (DSN) – A Step Toward Quantifying Treadwear Conditions," *Tire Science and Technology*, TSTCA, Vol. 14, No. 3, July-September 1986, pp.129-159.
218. Wambold, J.C., Henry, J.J. and Yeh, E.C. (1984). Methodology for Analyzing Pavement Condition Data, report FHWA/RD-83/094 prepared by the Pennsylvania Transportation Institute.
219. Wambold, J.C., J.J. Henry, and R.R. Hegmon. Skid Resistance of Wet-Pavement Accidents Sites. ASTM, 1986, pp. 47-60.
220. Wang, H. and Flintsch, G. W. (2007). Investigation of Short-and Long-Term Variations of Pavement Surface Characteristics at the Virginia Smart Road. CD-ROM. Transportation Research Board, National Research Council, Washington, D.C., USA.
221. Wei, Y.T., Z.H. Tian, and X. W. Du. A Finite Element Model for the Rolling Loss Prediction and Fracture Analysis of Radial Tires. *Tire Science and Technology*, Vol. 27, 1999, pp. 250-276.
222. Whicker, D., Browne A. L., Segalman, D. J., and Wickliffe, L. E. (1981). A Thermomechanical Approach to Tire Power Loss Modeling. *Tire Science Technology*, Vol. 9 (1981), pp. 3-18.
223. Wilburn, D.K. A Temperature Study of Pneumatic Tires during Highway Operation. 11716, 1972.
224. Williams, T. The Relation between Braking Force Coefficient and Slip for an Aircraft Tire Braked on Four Wet Surfaces. 50, 1966.
225. Wriggers P and Panagiotopoulos P. *New Developments in Contact Problems*. Springer: Wien, 1999.
226. Wriggers P. *Computational Contact Mechanics*. Wiley: Chichester, 2006
227. Wriggers P.; Zavarise G. (2004). Computational contact mechanics. In: *Encyclopedia of Computational Mechanics* / E. STEIN; R. DE BORST; T.J.R. HUGES. John Wiley & Sons, CHICHESTER, pp. 195-226.
228. Yager, T., 1983, Factors Affecting Aircraft Ground Handling Performance, NASA Technical Memorandum 85652.
229. Yager, T., Phillips, W.P., and Horne, W., (1970). A Comparison of Aircraft and Ground Vehicle Stopping Performance on Dry, Wet, Flooded, Slush-, Snow-, and Ice-Covered Runways, NASA Technical Note TN D-6098.
230. Yager, T.J. Comparative Braking Performance of Various Aircraft on Grooved and Ungrooved Pavements at the Landing Research Runway. Washington D.C., USA, In *Pavement Grooving and Traction Studies* NASA SP-5073, 1969.
231. Yan, X (2001), Non-linear three-dimensional finite element modeling of radial tires. *Journal of Mathematics and Computers in Simulation*, Vol-58, pp.51–70.
232. Yandell, W. O. ,P. Taneerananon and V. Zankin. Frictional Interaction of Tire and Pavement: Prediction Of Tire-Road Friction from Surface Texture and Tread Rubber Properties." ASTM special technical publication 793 , 1983, pp. 304–322.
233. Yandell, W. O., and S. Sawyer (1994). Prediction of Tire-Road Friction from Texture Measurements. In *Tranportation Research Record: Journal of Transportation Research Board*, no. 1435, Transportation Research board of the National Academies, Washington, D.C.
234. Yavari, B., W. W. Tworzydlo and J. M. Bass. A Thermomechanical Model to Predict the Temperature Distribution of Steady State Rolling Tires. *Tire Science and Technology*, Vol. 21, 1993, pp. 163-178.
235. Yeager R. W. and Tuttle. J. L. (1972). Testing and Analysis of Tire Hydroplaning. In *SAE National Automobile Engineering Meeting*, Detroit, Michigan.

236. Yeager, R.W., (1974), Tire Hydroplaning: Testing, Analysis and Design, in *The Physics of Tire Traction: Theory and Experiment*, edited by D. Hays and A. Browne, published by Plenum Press, pp. 25-58.
237. Zavarise G and Wriggers P. A superlinear convergent augmented Lagrangian procedure for contact problems. *Engineering with Computers* 1999; 16: 88–119.
238. Zavarise, G., P. Wriggers, and B. A. Schrefler (1998). A method for solving contact problems *International Journal for Numerical Methods in Engineering* 42, 473–498.
239. Zheng, D.: Prediction of tire tread wear with FEM steady state rolling contact simulation. *Tire Science and Technology* 31(3), 189–202 (2003).

Publications

Peer Reviewed Journals

1. **S.K. Srirangam**, K. Anupam, A. Scarpas & C. Kasbergen (2014): Development of a thermomechanical tyre–pavement interaction model, *International Journal of Pavement Engineering*, DOI: 10.1080/10298436.2014.946927.
2. K. Anupam, **S.K. Srirangam**, A. Scarpas and C. Kasbergen (2014): Influence of Temperature on Tire-Pavement Friction: Analysis, Volume 2369 / Pavement Management 2013, Vol. 4, *Transportation Research Record: Journal of the Transportation Research Board*, DOI: 10.3141/2369-13, pp. 114-124.
3. K. Anupam, **S.K. Srirangam**, A. Scarpas, C. Kasbergen and M. Kane (2015) : Study of Cornering Maneuvers of a Pneumatic Tire on Asphalt Pavement Surfaces Using the Finite Element Method, Volume 2457 / Pavement Management 2014, Vol. 3, *Transportation Research Record: Journal of the Transportation Research Board*, DOI: 10.3141/2457-14, pp. 129-139.
4. **S.K. Srirangam**, K. Anupam, A. Scarpas, C. Kasbergen and M. Kane (2015) : Safety Aspects of Wet Asphalt Pavement Surfaces Through Field and Numerical Modeling, Volume 2446 / Asphalt Materials and Mixtures, Vol. 3, *Transportation Research Record: Journal of the Transportation Research Board*, DOI: 10.3141/2446-05, pp. 37-51.
5. **S.K. Srirangam**, K. Anupam, C. Kasbergen, A. Scarpas, and V.Cerezo (2015) : Study of Influence of Operating Parameters on Braking Friction and Rolling Resistance, *Transportation Research Record: Journal of the Transportation Research Board* (Accepted for publication).

Publications in International Conference Proceedings

6. **Srirangam Santosh Kumar**, Kumar Anupam, Tom Scarpas and Cor Kasbergen (2012): Study of Hydroplaning Risk on Rolling and Sliding Passenger Car, Presented at *SIIV-5th International Congress - Sustainability of Road Infrastructures 2012*, Rome, Italy, October 29-31, Published in *Procedia - Social and Behavioral Sciences*, Volume 53, pp. 1019–1027.
7. **Srirangam, S.**, Anupam, K., Scarpas, A., and Kasbergen, C. (2013): Hydroplaning of Rolling Tires under Different Operating Conditions, Presented at *Airfield & Highway Pavement Conference-2013*, Los Angeles, California, United States, June 9-12, 2013, DOI: 10.1061/9780784413005.045, pp. 561-572.
8. **S.K. Srirangam**, K. Anupam, A. Scarpas and A. Kusters (2013): Influence of Temperature on Tire-Pavement Friction-I: Laboratory Tests and Finite Element Modeling, Presented at *Transportation Research Board (TRB) 92nd Annual meeting*, Washington D.C., USA, Jan 13-17, 2013, paper no. #13-4260.
9. **Srirangam, S.K.**; Scarpas, A.; Kasbergen, C.; Anupam, K (2012), Numerical investigation of the effect of hydroplaning on braking and directional stability of

passenger car tires, Presented at *ECCOMAS-2012 conference*, Vienna, Austria, Sep 10-14.

10. **Santosh Kumar Srirangam**, Kumar Anupam, Tom Scarpas, Cor Kasbergen, Peter The (2015): A Durability Analysis of Super-Quiet Pavement Structures, Presented at *Middle East - Mediterranean Materials Congress (MEMA 2015)*, Doha, Qatar, Jan 11-14.

Summary

Good skid resistance of a pavement surface is essential for road safety. Loss of skid resistance can lead to property damage and loss of lives. Ever increasing need of driver safety poses challenges to the highway authorities to evaluate pavement conditions even more precisely under different conditions. Environmental variables like temperature, water, snow etc. can have a significant effect on the skid resistance apart from the vehicle and pavement related factors. The temperature increase in the tire-pavement contact region results in a complex relationship between the temperature and the friction and constitutes one of the main sources of uncertainty in interpreting the data of continuous field measurements. Likewise, very low friction coefficients can be observed between the tire and pavement surface under wet conditions. Nevertheless, the phenomena have not been adequately quantified yet within the skid resistance evaluation engineering community. The road agencies use correlation factors to estimate frictional characteristics of the road. These correlation factors are based on the experience and field test measurements which have a very limited scope in terms of reliability and transferability. It is the aim of this research is to study the effect of temperature and water on the frictional performance of the asphalt surface, when a pneumatic tire is traversing at given operating conditions.

The tire operating temperature is a very important concern to the tire manufacturers, highway agencies and users due to its major influence on the traction performance of a tire. Tire rubber hysteresis is considered to play a major role in countering skidding of a vehicle travelling at high speed. Past studies showed that the contribution from the hysteresis component in comparison to adhesion has a larger influence on the friction measurements. This research aims to develop a sequentially coupled thermo-mechanical model in the finite element (FE) framework to determine the progressive temperature development in a pneumatic tire rolling over a simulated asphalt pavement surface mesh and its eventual effect on the hysteretic friction. This research also studies the hysteretic frictional behavior of a test tire under different surrounding temperature conditions.

In this methodology, first, the tire is tested under static loading conditions to obtain its overall deformation characteristics and in particular the relation tire load - inflation pressure – foot print. In the second step, rubber material tests are performed to determine the rheological characteristics of the tire tread rubber. The test results are used for the determination of rheological parameters of a tire rubber material in the form of Prony's coefficients. The Prony's coefficients are later utilized in the development of a 3D FE test tire. In the third step, the tire is modelled in the FE framework, accounting for the different components of a tire like tread, side wall, carcass, belts, plies, inner liner, rim etc. The FE simulation results corresponding to the footprint and the deformation are compared with the measurements of static load deflection tests. The FE mesh of a given asphalt pavement surface is developed based on scanned asphalt surface data obtained by a Laser Profilometer and an X-ray tomographer. A dynamic analysis of a tire rolling at a definite slip ratio over a simulated asphalt pavement surface is performed. The results obtained from this analysis are used in the subsequent energy dissipation analysis to determine the heat fluxes. These heat fluxes are the input of a heat transfer analysis to determine the temperature development in the body of a tire.

Many past experimental studies showed that the tire-pavement friction values are related to the tire surrounding conditions such as pavement temperature, ambient temperature, contained air temperature and surface characteristic of pavement. Therefore, in this research, the effect of pavement temperature, ambient temperature and contained air temperature on friction

measurements is studied. By using the developed FE model, practical test conditions of fully and partially skidding tires traversing over different asphalt pavement surfaces, namely, Porous Asphalt, Ultra-Thin Surface and Stone Mastic Asphalt and AC-10 are analysed. Emphasis is placed on the determination of tire tread temperature as a critical combination of pavement temperature and ambient temperature. An attempt has also been made to determine the time required for different regions of a rolling tire to reach an effective temperature equilibrated state. Such kind of analysis gives insight into the effect of thermal behaviour of different components of tire on the tire hysteresis which eventually decides its frictional performance. This research also deals with the cornering frictional behaviour of a pneumatic tire. By utilizing the developed FE model, the cornering friction was computed for inflation pressure, wheel load, vehicle speed, side-slip angle, surface texture and mix design.

Good pavement macrotexture has a direct influence on the vehicle safety during wet weather conditions by improving its traction/braking ability. Apart from the macrotexture, there are several factors that affect the wet friction, such as, environmental, tire and pavement related characteristics. In recent years, development of powerful finite element tools made it possible to simulate complex wet tire-pavement interaction as close as possible to the actual field conditions. However, to the best of the author's knowledge, none of the past analytical/numerical studies were able to include the asphalt pavement surface texture in their analysis.

In the next part of this thesis, the loss of friction under wet/flooded pavement conditions is studied. This research presents an FE approach to study the effect of surface morphology of asphalt pavements on the wet friction coefficient. The wet friction performance of different asphalt surface morphologies of open-graded mix to close-graded mix are studied by using the developed FE model. The tire-wet asphalt surface interaction FE model is duly calibrated with the field investigations conducted by using the state-of-art field equipment. The extreme loss of wet friction which ultimately leads to risk of hydroplaning is also studied. The FE simulations are performed on different water film thicknesses, tread pattern and different tire slip ratios and yaw angles. The results from the current study can be used as safety indicators of in-service asphalt pavements under wet/flooded conditions.

Samenvatting

Goede wegdekstroefheid is van essentieel belang voor de verkeersveiligheid. Verlies van stroefheid kan leiden tot materiële schade en verlies van levens. De steeds toenemende behoefte aan veiligheid van de bestuurder vormt uitdagingen voor autoriteiten om de wegdekcondities nog nauwkeuriger te evalueren onder verschillende omstandigheden. Milieuv variabelen zoals temperatuur, water, sneeuw etc. kunnen een significant effect op de stroefheid hebben, afgezien van de factoren gerelateerd aan voertuig en wegdek. De temperatuurstijging in het band-wegdek contactgebied resulteert in een complexe relatie tussen de temperatuur en de wrijving en vormt één van de belangrijkste bronnen van onzekerheid in de interpretatie van de gegevens van continue veldmetingen. Evenzo kunnen zeer lage wrijving coëfficiënten worden waargenomen tussen band en wegdek onder natte omstandigheden. Niettemin, de verschijnselen zijn nog niet voldoende gekwantificeerd binnen de gemeenschap, die zich met stroefheidsevaluatie bezig houdt. De wegagenschappen gebruiken correlatiefactoren om de wrijvingskarakteristieken van de weg te schatten. Deze correlatiefactoren zijn gebaseerd op ervaring en praktijktestmetingen die een zeer beperkt zijn wat betreft betrouwbaarheid en overdraagbaarheid. Het is het doel van dit onderzoek om het effect van de temperatuur en water op de wrijvingsprestaties van het asfaltoppervlak te bestuderen, wanneer een luchtband onder gegeven omstandigheden hier overheen beweegt..

De bandtemperatuur is een zeer belangrijke zorg voor de bandenfabrikanten, snelwegagenschappen en gebruikers vanwege zijn grote invloed op de tractieprestaties van een band. Bandrubberhysteresis wordt geacht een belangrijke rol te spelen bij het tegengaan van het slippen van een voertuig met hoge snelheid. Eerdere studies toonden aan dat de bijdrage van de hysteresiscomponent in vergelijking met adhesie een grotere invloed op wrijvingsmetingen heeft. Dit onderzoek heeft tot doel om een sequentieel gekoppeld thermo-mechanisch model in een eindige elementen (FE) kader te ontwikkelen om de progressieve temperatuurontwikkeling in een rollende luchtband over een gesimuleerd mesh van een asfaltoppervlak te bepalen en daarmee het uiteindelijke effect op de hysteresiswrijving. Dit onderzoek bestudeert ook het hysteresiswrijvingsgedrag van een testband onder verschillende omgevingstemperatuurcondities.

In deze methodologie wordt de band allereerst getest onder statische belastingscondities om de totale vervormingskenmerken te krijgen en in het bijzonder de relatie bandbelasting - bandenspanning - footprint. In de tweede stap worden rubbermateriaaltesten uitgevoerd om de reologische eigenschappen van het bandloopvlakrubber te bepalen. De testresultaten worden gebruikt voor het bepalen van de reologische parameters van een bandrubbermateriaal in de vorm van Prony coëfficiënten. De Prony coëfficiënten worden later gebruikt bij het ontwikkelen van een 3D FE testband. In de derde stap wordt de band gemodelleerd in het FE-kader, rekening houdend met de verschillende onderdelen van een band zoals loopvlak, zijwand, geraamte, riemen, coating, binnenbekleding, rand etc. De FE simulatieresultaten gerelateerd aan de footprint en de vervorming worden vergeleken met de metingen van buigingsproeven onder statische belasting. De FE mesh van een bepaald asfaltwegdek is ontwikkeld op basis van een gescand asfaltoppervlak verkregen door een laser Profilometer en een

X-ray tomographer. Een dynamische analyse van een rollende band onder een bepaalde slipratio over een gesimuleerd asfaltwegdek is uitgevoerd. De resultaten van deze analyse worden gebruikt in een eropvolgende energiedissipatieanalyse om de warmtefluxen te bepalen. Deze warmtefluxen zijn de input voor een warmteoverdrachtsanalyse om de temperatuurontwikkeling aan de binnenkant van een band te bepalen.

Vele vroegere experimentele studies toonden aan dat de band-wegdek wrijvingswaarden betrekking hebben op de bandomgevingsomstandigheden zoals wegdektemperatuur, omgevingstemperatuur, luchttemperatuur en de oppervlakkenmerken van het wegdek. Daarom is in dit onderzoek het effect van wegdektemperatuur, omgevingstemperatuur en luchttemperatuur op frictiemetingen onderzocht. Door middel van het ontwikkelde FE-model, praktische testomstandigheden van volledig en gedeeltelijk slippende banden die bewegen over verschillende asfaltwegdekoppervlakken, namelijk ZOAB, Ultra-Thin Surface en Stone Mastic Asphalt en AC-10 zijn geanalyseerd. De nadruk ligt op de bepaling van de bandprofieltemperatuur als een kritische combinatie van wegdektemperatuur en omgevingstemperatuur. Eveneens is een poging gedaan om de tijd, die nodig is voor verschillende delen van een rollende band om een effectieve temperatuurbalanstoestand te bereiken, te bepalen. Een dergelijke vorm van analyse geeft inzicht in het effect van het thermisch gedrag van de verschillende bandcomponenten op de bandhysteresis, wat uiteindelijk de wrijvingsprestaties bepaalt. Dit onderzoek gaat ook over het wrijvingsgedrag van een luchtband in bochten. Door gebruik te maken van het ontwikkelde FE-model, werd de wrijving in bochten berekend voor bandenspanning, wiel belasting, snelheid, side-slip hoek, oppervlaktestructuur en mengsel design.

Goede wegdekmacrotextuur heeft een directe invloed op de veiligheid van een voertuig tijdens natte weersomstandigheden door de verbetering van het tractie/remvermogen. Naast de macrotextuur zijn er verschillende factoren die de natte wrijving beïnvloeden, zoals milieu-, band en wegdek verwante eigenschappen. In de afgelopen jaren, maakte de ontwikkeling van krachtige eindige elementen gereedschappen het mogelijk om complexe natte band-wegdek interactie, zo dicht mogelijk bij de feitelijke veldomstandigheden, te simuleren. Echter, voor zover de auteur weet, zijn er geen van eerdere analytische / numerieke studies gedaan, die de wegdektextuur in een analyse meenemen.

In het volgende deel van dit proefschrift wordt het verlies van wrijving onder natte / ondergelopen wegdekomstandigheden bestudeerd. Dit onderzoek bevat een FE aanpak om het effect van oppervlaktemorfologie van asfaltwegdekken op de natte wrijvingscoëfficiënt te bestuderen. De natte wrijvingsprestaties van verschillende asfaltoppervlaktemorfologieën van open tot dichte asfaltmixen worden bestudeerd met behulp van het ontwikkelde FE-model. Het band-nat wegdek interactie FE model is naar behoren gekalibreerd door middel van veldonderzoeken gebruikmakend van state-of-art veldapparatuur. Het extreme verlies van natte wrijving, wat uiteindelijk leidt tot het risico van aquaplaning, is ook bestudeerd. De FE simulaties zijn uitgevoerd voor verschillende waterlaagdiktes, loopvlakprofielen, verschillende bandenslipratios en afwijkhoeken. De resultaten van de huidige studie kunnen worden gebruikt als veiligheidsindicatoren voor asfaltlagen onder natte / overstroomde omstandigheden.

Curriculum Vitae

Name	Santosh Kumar Srirangam
1979	Born in Kakinada, A.P., India
1999- 2003	Bachelor of Technology in Civil Engineering, Jawaharlal Nehru Technological University, Kakinada, A.P., India
2003-2004	Design Engineer, SCECON Architectures and Structures, Kakinada, A.P., India
2004 – 2006	Master of Technology in Transportation Engineering, Indian Institute of Technology, Kharagpur, W.B., India
2006-2007	Management Trainee, IJM (India) Infrastructure Pte. Ltd., Hyderabad, A.P., India
2007-2008	Master of Engineering in Infrastructure Systems and Management, National University of Singapore, Singapore
2008-2010	Planning Engineer, HSL Constructor Pte. Ltd., Singapore
2010-Present	PhD candidate, Section of Pavement Engineering, Faculty of Civil Engineering and Geosciences, TU Delft

